Faculty of Engineering and Science
Department of Mechanical Engineering

Design Optimization of Guided Flow Augmenters for Exhaust Air Energy Extraction

Enderaaj Singh

0000-0001-6664-1167

This thesis is presented for the Degree of
Master of Philosophy
of
Curtin University

July 2024

Declaration

To the best of my knowledge and belief, this thesis contains no material previously published by any other person except where due acknowledgement has been made.

This thesis contains no material which has been accepted for the award of any other degree or diploma in any university.

Signature: ……

Date:

ACKNOWLEDGEMENT

Throughout the writing of this dissertation, I have received an incredible amount of support and assistance from various individuals.

I want to extend my warm and sincere gratitude to my supervisory team, Associate Prof. Law Ming Chiat, Associate Prof. Sukanta Roy, and Dr. Yam Ke San, for their continuous support, invaluable advice, and patience throughout my research study. It has been an enormous honour and privilege to be under their supervision. Their immense knowledge and experience have guided and encouraged me throughout my academic research, where I have acquired significant knowledge in carrying out research and strengthened my expertise in Computational Fluid Dynamics, especially those related to wind turbines.

I would also like to sincerely thank my thesis chairperson, Associate Prof. Moola Mohan Reddy, for his insightful comments and suggestions at each stage of my research journey. Besides my supervisors, I must thank Curtin University Malaysia for providing the necessary facilities for my research.

In addition, I would like to thank my parents for their constant love, support, and prayers. My parents' unwavering support and belief have pushed me to keep believing in myself to complete my research by giving all my heart and dedication. Finally, I could not have finished this dissertation without the support of my wife, Pearl Teo, who was influential in shaping my thesis and providing constructive feedback. She was also the cornerstone, which allowed me to be consistent and focused throughout the writing of this dissertation.

ABSTRACT

Non-renewable fossil fuels are heavily relied on to meet energy demand, which has increased exponentially due to population and industrial growth. Continuous efforts to increase renewable energy growth are vital to reduce dependency on fast-depleting, carbon-based energies that are harmful to the environment. Wind energy is one of the fastest-growing renewable energies, thanks to research and advances in wind turbines, which convert wind energy to electrical energy. Large-scale power production from wind energy is done using conventional horizontal axis wind turbines (HAWTs) in remote areas. In contrast, vertical-axis wind turbines (VAWTs) are more suited to be used in urban areas. Harnessing wind energy closer to the end-user by distributed power generation in populated urban areas is beneficial as it lowers cable costs and power transmission loss. The H-Darrieus type VAWT (HDWTs) have received much interest for their feasibility in urban areas. Much research on HDWT in free-stream conditions can be found in the open literature. However, the unpredictable wind conditions in urban areas and the low average wind speed experienced by some countries throughout the year limit the ability for efficient energy generation. Another possibility to increase distributed energy generation is available by harnessing man-made or unnatural wind sources from the exhaust air of cooling towers, especially from mechanical cooling towers, which can be found on top of buildings with heating, ventilation, and air-conditioning (HVAC) systems used to remove heat waste.

In this study, three-dimensional numerical simulations were conducted using STAR CCM+ by solving the unsteady Reynolds Averaged Navier Stokes (URANS) equation with shear stress transport (SST) k-ω turbulence model to measure and enhance the performance of a 3-bladed S-1046 airfoil HDWT under exhaust air of a cooling tower. The HDWT was placed at the centre of the cooling tower outlet, where it rotates using sliding mesh. First, parametric studies on the bare HDWT AR and solidity were done. The HDWT with an AR of 0.44 and solidity of 0.450 produced the highest power coefficient (C_p) of 0.3196 at TSR 2.0. Next, cycloidal diffusers were added and optimized to augment the HDWT performance. The cycloidal diffuser was defined by four parameters: diffuser length, diffuser angle, shroud length and shroud angle, which are the variable factors. The power coefficient is the response factor and the optimization objective. The cycloidal diffuser parameters were first studied by one factor at a time (OFAAT) to determine the range of the parameters to be optimized.

Then, the cycloidal diffuser design was optimized at TSR 2.0 by Response Surface Methodology (RSM) using Design Expert. The analysis of variance (ANOVA) showed that the shroud length has the most substantial impact on the HDWT performance, and the strongest interaction was shown to occur between the diffuser angle and the shroud angle. The optimization result shows that the optimum cycloidal diffuser parameters are a diffuser length of 114 mm, diffuser angle of 36.1°, shroud length of 218 mm and shroud angle of 7.4°. The optimized result was validated by numerical simulation, which gives C_p of 0.4232, a 0.05% difference from the predicted value, and a 32.42% improvement compared to the bare HDWT design. Furthermore, an analysis of the flow physics around the HDWTs was done throughout this study, and the comparison of flow structures between the optimal design and bare HDWTs is presented and discussed in detail. The optimized HDWT can generate 16.66 W of power. It is estimated that a scaled-up model of the HDWT and cycloidal diffuser from this study can recover 3.93% of energy from an actual mechanical cooling tower whilst only reducing the cooling tower efficiency by 0.33%.

Overall, this thesis explored and showed how optimizing the guided flow HDWT setup can improve the performance of HDWT under the cooling tower's exhaust air. Moreover, insights into the aerodynamics of the HDWT under the accelerated flow condition were also provided to understand the reasons behind the performances obtained. The effect of the HDWT on the cooling tower performance and outlet water temperature can be studied in the future. Moreover, experimental work can be conducted to calculate the turbine power output of the guided flow augmented HDWT under the cooling tower setup for more accurate results. The findings from this study are expected to guide future research in investigating other HDWT parameters or operational parameters with the combination of different types and designs of guided flow augmenters to further optimize the exhaust air extraction efficiency of the HDWT in cooling towers.

TABLE OF CONTENTS

Declaration i

ACKNOWLEDGEMENT ii

ABSTRACT iii

LIST OF FIGURES ix

LIST OF TABLES xvi

NOMENCLATURE xvii

CHAPTER 1: INTRODUCTION 1

1.1 Background 1

1.1.1 Fossil fuels and renewable energy 1

1.1.2 Wind energy and wind turbines 3

1.1.2.1 Savonius VAWT 5

1.1.2.2 Darrieus VAWT 6

1.2 Problem Statement 8

1.3 Research Aim & Objectives 9

1.4 Research Questions 10

1.5 Research Scope 10

1.6 Significance of Research 11

CHAPTER 2: LITERATURE REVIEW 12

2.1 Fundamental Principle and Aerodynamics of HDWT 12

2.1.1 Static stall 13

2.1.2 Dynamic stall 14

2.1.3 Key operational parameters of HDWT 16

2.2 Enhancement Study on HDWT Parameter 18

2.2.1 Airfoil type and design 18

2.2.2 Solidity 21

2.2.3 Aspect ratio 22

2.2.4 Effect of interaction between parameters 23

2.3 Performance Enhancement of VAWT using Wind Augmenter 24

2.3.1 Diffusers with shroud and flange 24

2.3.2 Guide vanes 29

2.3.3 Deflectors 31

2.3.4 Other designs 34

2.4 Exhaust Air Energy Recovery 35

2.5. Cooling Tower Types & Working Principles 38

2.5.1 Important cooling tower parameters and performance measure of cooling tower 42
2.5.1.1 Wet-bulb temperature, range, and approach 42
2.5.1.2 Performance measure of a cooling tower 43
2.6 Research Gap 45
CHAPTER 3: METHODOLOGY 47
3.1 Overview 47
3.2 Cooling Tower Model for Computational Domain 47
3.3 Design Selection and Study of HDWT under Cooling Tower Exhaust Air 49
3.3.1 Study on the HDWT aspect ratio 50
3.3.2 Study on the HDWT solidity 51
3.4 Performance Enhancement using Wind Augmenters 52
3.4.1 Cycloidal diffusers design and parametric study 53
3.5 Analysis Methods 56
3.5.1 Azimuthal angle discussion 58
3.6 Computational Methodology 58
3.6.1 Boundary condition & flow physics setup 59
3.6.2 Governing equations and turbulence model 61
3.6.3 Mesh generation 63
3.6.4 Grid sensitivity and time-step 66
3.7 Model Validation 68
CHAPTER 4: RESULTS & DISCUSSION 71
4.1 Effect of Aspect Ratio on HDWT Performance 71
4.1.1 The performance comparison of HDWT aerodynamics with aspect ratios of 0.35 and 0.70 at TSR of 2.5 77
4.1.2 Influence of TSR on the performance of HDWT with an aspect ratio of 0.44 81
4.1.3 Analysis of the aerodynamic performance between HDWT of aspect ratio 0.35 and 0.44 at TSR 1.5 & 2.5 85
4.1.4 Comparative study between the present HDWT to past studies 89
4.2 Effect of Solidity on HDWT Performance for Cooling Tower Exhaust Air Energy Extraction 90
4.2.1 Pressure and streamlines comparison between HDWT of solidity 0.225 and 0.450 at TSR 2.0 and TSR 3.0 94
4.2.2 Vorticity comparison between HDWT of solidity 0.225 and 0.450 at TSR 2.0 98

4.3 Cycloidal Diffusers Parametric Study for HDWT Performance Enhancement under Cooling Tower Exhaust Air 100
4.3.1 Parametric study of diffuser length and diffuser angle 100
4.3.1.1 Flow analysis of the cycloidal diffusers with diffuser angles of 15°, 35°, and 40° with constant diffuser length of $0.5D$ 103
4.3.1.2 Flow analysis of the cycloidal diffusers with diffuser lengths of $0.25D$, $0.5D$, and $1.25D$ with constant diffuser angle of 35° 108
4.3.2 Parametric study of shroud length 112
4.3.3 Parametric study of shroud angle 118
CHAPTER 5: DESIGN OPTIMIZATION OF CYCLOIDAL DIFFUSERS FOR EXHAUST AIR ENERGY EXTRACTIONS 122
5.1 Optimization using Response Surface Methodology 122
5.1.1 Diffuser design parameters selection 123
5.1.2 Computational fluid dynamics study 124
5.2 Optimization Results And Discussion 124
5.2.1 Statistical analysis 125
5.2.2 Prediction equation 129
5.2.3 Interaction effect between independent variables 130
5.2.4 Optimized design 133
5.2.5 Validation of optimization result 134
5.3 Flow Analysis of Optimized Design 135
5.4 Analysis of the Cooling Tower Velocity Profile with Energy Recovery System for Performance Evaluation 141
5.5 Analysis of the Power Produced by the HDWT Exhaust Air Energy Recovery and its Effect on the Cooling Tower Performance 144
5.5.1 HDWT exhaust air power generation and its effect on the cooling tower mass flow rate 144
5.5.2 Analysis of the cooling tower flow 147
5.5.3 Expected energy recovery from cooling tower exhaust air 156
5.5.4 Impact of the blockage caused by the exhaust air energy recovery on cooling tower performance 157
CHAPTER 6: CONCLUSIONS AND RECOMMENDATIONS 161
6.1 Findings and Contributions 161
6.2 Recommendations for Future Work 163
REFERENCES 164
APPENDICES 176

A1) Cooling tower specifications for model T-2800 by Cooling Tower Systems, Inc. 176
A2) Conversion and calculation for cooling tower estimated power recovery 177
B) Publications resulting from this study 178
C) Author copyright statement 180
D) Best presenter award..... 181

LIST OF FIGURES

Figure 1.1. World energy consumption by fossil fuel type [2]. 2
Figure 1.2. Global wind power capacity and annual additions from 2010 to 2021 [7]. 4
Figure 1.3. Projected Wind Energy Capacity by 2030 to Meet Net Zero 2050 Scenario [11]. 4
Figure 1.4. Wind turbine classifications [16]. 5
Figure 1.5. Savonius style VAWT [15]. 6
Figure 1.6. Darrieus VAWT configurations (a) Straight-bladed “Musgrove H-Rotor”, (b) Curve-bladed “eggbeater Darrieus”, (c) Helical-blade “Gorlov” [47]. 7
Figure 1.7. Development of Darrieus-type turbine over the years [45]. 7
Figure 2.1. Forces and velocities on HDWT blade. 12
Figure 2.2. The azimuthal angle of attack for one complete rotation at different TSRs [60]. 13
Figure 2.3. Deep stall experienced by NACA 0018 airfoil [62]. 14
Figure 2.4. Flow physics and unsteady air loads diagrams of an airfoil experiencing dynamic stall [65]. 16
Figure 2.5. Flow around VAWT with a shrouded and flanged diffuser [77]. 24
Figure 2.6. Experiment setup of VAWT with diffusers [80]. 26
Figure 2.7. Velocity magnitude contour of the flow field around diffusers with flange angle $\theta = +15°$ [81]. 26
Figure 2.8. Wind lens configurations for Darrieus VAWT performance enhancement (a) Flat-panel type diffuser, (b) Curved-surface type diffuser, (c) Cycloidal-surface diffuser [42], [83]. 28
Figure 2.9. VAWT with a diffuser at location X/D= -0.3 [84]. 28
Figure 2.10. Omnidirectional guide vanes with four pairs of guide vanes [91]. 31
Figure 2.11. Augmented wind turbine design with omnidirectional stator [50]. 31
Figure 2.12. Deflector parameter specifications (a) Top view, (b) Front view [99]. 33
Figure 2.13. Parameter optimization of the flat plate deflector [100], [101]. 33
Figure 2.14. Schematic of cooling tower working principles (a) Wet cooling tower (b) Dry cooling tower [115]. 39
Figure 2.15. Forced cooling tower [119]. 40
Figure 2.16. Induced wet cooling tower (a) Crossflow vs (b) Counterflow [121]. 41

Figure 2.17. Recirculation in cooling towers [119]. 41
Figure 3.1. Cooling tower model. 48
Figure 3.2. Two-dimensional velocity contour of the cooling tower flow without HDWT from (a) Side view, (b) Top view. 49
Figure 3.3. Geometry of the S-1046 airfoil. 50
Figure 3.4. Three-bladed HDWT with S-1046 airfoil. 50
Figure 3.5. Proposed cycloidal diffuser design. 55
Figure 3.6. Two-dimensional view of cycloidal diffusers parameter and location. .. 55
Figure 3.7. Wind turbine path relative to the direction of the wind. 58
Figure 3.8. Computational methodology flow chart. 59
Figure 3.9. Three-dimensional view of the computational domain. 61
Figure 3.10. Two-dimensional view of the meshed computational domain. 64
Figure 3.11. Three-dimensional mesh view for the (a) Whole computational domain, (b) HDWT rotating region, (c) HDWT blade. 64
Figure 3.12. Two-dimensional view of the meshed computational domain with HDWT and cycloidal diffusers. 65
Figure 3.13. Three-dimensional view of the meshed diffusers around HDWT. 65
Figure 3.14. Contour of wall y+ value on the surface of (a) HDWT blade, (b) HDWT blades and cycloidal diffusers. 66
Figure 3.15. Grid independence study for AR 0.35 HDWT (D=570mm). 67
Figure 3.16. Grid independence study for AR 0.70 HDWT (D=285mm). 67
Figure 3.17. Time step size test. 68
Figure 3.18. The boundary condition for the validation study. 69
Figure 3.19. Validation of the current model against other studies. 70
Figure 4.1. Effect of AR on HDWT moment coefficient under accelerated cooling tower exhaust air. 71
Figure 4.2. Effect of AR on HDWT power coefficient under accelerated cooling tower exhaust air. 71
Figure 4.3. Instantaneous Cm against azimuthal angles of HDWT with ARs of 0.35, 0.44, 0.54 and 0.70 at TSR 1.5. 74
Figure 4.4. Single blade instantaneous Cm against azimuthal angles for HDWT with ARs of 0.35, 0.44, 0.54 and 0.70 at TSR 1.5. 74
Figure 4.5. Instantaneous Cm against azimuthal angles of HDWT with ARs of 0.35, 0.44, 0.54 and 0.70 at TSR 2.5. 75

Figure 4.6. Single blade instantaneous Cm against azimuthal angles for HDWT with ARs of 0.35, 0.44, 0.54 and 0.70 at TSR 2.5. 75
Figure 4.7. Instantaneous Cm against azimuthal angles of HDWT with ARs of 0.35, 0.44, 0.54 and 0.70 at TSR 3.5. 76
Figure 4.8. Single blade instantaneous Cm against azimuthal angles for HDWT with ARs of 0.35, 0.44, 0.54 and 0.70 at TSR 3.5. 76
Figure 4.9. Vorticity contour comparison at a complete rotation between HDWT of aspect ratios 0.35 (left) and 0.70 (right) at TSR 2.5. 79
Figure 4.10. Static pressure contour and streamlines around a blade during one full rotation for HDWT of 0.35 AR at TSR 2.5. 80
Figure 4.11. Static pressure contour and streamlines around a blade during one full rotation for HDWT of 0.70 AR at TSR 2.5. 80
Figure 4.12. Single blade instantaneous Cm against azimuthal angles for HDWT with ARs of 0.44 at TSR 1.5, 2.5 and 3.5. 81
Figure 4.13. Vorticity contour comparison at a complete rotation for HDWT of AR=0.44 (D=456mm) at TSRs 1.5 and 2.5. 82
Figure 4.14. Static pressure comparison at a complete rotation for HDWT of AR=0.44 (D=456mm) at TSRs 1.5 and 2.5. 83
Figure 4.15. Drag coefficient versus angle of attack during a complete rotation of the AR 0.44 HDWT at TSRs 2.5 and 3.5. 84
Figure 4.16. Wall shear stress contour comparison for AR 0.44 HDWT blades at blade azimuth angles of θ=65° and 105° at TSRs 2.5 and 3.5. 85
Figure 4.17. Three-dimensional volumetric vorticity contour at a complete rotation for HDWT of AR=0.35 (left) and AR=0.44 (right) at TSR 1.5. 87
Figure 4.18. Three-dimensional volumetric vorticity contour at a complete rotation for HDWT of AR=0.35 (left) and AR=0.44 (right) at TSR 2.5. 88
Figure 4.19. Comparative study on the drag coefficients produced by the turbine blades with other studies 89
Figure 4.20. Effect of solidity on HDWT moment coefficient under accelerated cooling tower exhaust air. 91
Figure 4.21. Effect of solidity on HDWT power coefficient under accelerated cooling tower exhaust air. 91

Figure 4.22. Instantaneous Cm against azimuthal angles for HDWT of solidities 0.225, 0.3, 0.375, 0.45 at TSR 2.0..... 93
Figure 4.23. Instantaneous Cm against azimuthal angles for HDWT of solidities 0.225, 0.3, 0.375, 0.45 at TSR 3.0..... 93
Figure 4.24. Single blade instantaneous Cm against azimuthal angles for HDWT of solidities 0.225, 0.30, 0.375 and 0.45 at TSR 2.0. 94
Figure 4.25. Single blade instantaneous Cm against azimuthal angles for HDWT of solidities 0.225, 0.30, 0.375 and 0.45 at TSR 3.0. 94
Figure 4.26. Static pressure contour and streamlines around the blade during one full rotation at TSR 2.0 for HDWT of solidity: (a) 0.225 & (b) 0.450..... 96
Figure 4.27. Static pressure contour and streamlines around the blade during one full rotation at TSR 3.0 for HDWT of solidity: (a) 0.225 & (b) 0.450..... 97
Figure 4.28. Three-dimensional volumetric vorticity contour at a complete rotation for HDWT of σ=0.225 (left) and σ= 0.450 (right) at TSR 2.0..... 99
Figure 4.29. Moment coefficient for HDWT using cycloidal diffusers of different diffuser lengths and with diffuser angles of 15°, 20°, 30°, 35° and 40° at TSR 1.5. 102
Figure 4.30. Power coefficient for HDWT using cycloidal diffusers of different diffuser lengths and with diffuser angles of 15°, 20°, 30°, 35° and 40° at TSR 1.5.102
Figure 4.31. Single blade instantaneous Cm against azimuthal angles for HDWT using cycloidal diffusers with diffuser angles of 15°, 35°, and 40° with a constant diffuser length of $0.5D$..... 104
Figure 4.32. Instantaneous Cm against azimuthal angles for HDWT using cycloidal diffusers with diffuser angles of 15°, 35°, and 40° with a constant diffuser length of $0.5D$..... 105
Figure 4.33. Velocity contour comparison around the augmented HDWT using cycloidal diffusers with angles of 15°, 30°, and 45° with a constant diffuser length of $0.5D$ at θ = 90°..... 106
Figure 4.34. Pressure contour with velocity streamline comparison around the augmented HDWT using cycloidal diffusers with angles of 15°, 30°, and 45° with a constant diffuser length of $0.5D$ at θ = 90°..... 107
Figure 4.35. Single blade instantaneous Cm against azimuthal angles for HDWT using cycloidal diffusers with diffuser lengths of $0.25D$, $0.5D$, and $1.25D$ with a constant diffuser angle of 35°..... 110

Figure 4.36. Instantaneous Cm against azimuthal angles for HDWT using cycloidal diffusers with diffuser lengths of $0.25D$, $0.5D$, and $1.25D$ with a constant diffuser angle of 35°. 110
Figure 4.37. Velocity contour comparison around the augmented HDWT using cycloidal diffusers with diffuser lengths of $0.25D$, $0.5D$, and $1.25D$ with a constant diffuser angle of 35° at θ = 90°. 111
Figure 4.38. Pressure contour with velocity streamlines comparison around the augmented HDWT using cycloidal diffusers with diffuser lengths of $0.25D$, $0.5D$, and $1.25D$ with a constant diffuser angle of 35° at θ = 90°. 112
Figure 4.39. Moment coefficient of HDWT using cycloidal diffusers with shroud lengths of 0D, 0.25D, 0.35D and 0.48D. 113
Figure 4.40. Power coefficient of HDWT using cycloidal diffusers with shroud lengths of 0D, 0.25D, 0.35D and 0.48D. 114
Figure 4.41. Single blade instantaneous Cm against azimuthal angles for HDWT using cycloidal diffusers with shroud lengths of $0D$, $0.35D$, and $0.48D$. 115
Figure 4.42. Instantaneous Cm against azimuthal angles for HDWT using cycloidal diffusers with shroud lengths of $0D$, $0.35D$, and $0.48D$. 115
Figure 4.43. Velocity contour comparison around the augmented HDWT using cycloidal diffusers with shroud lengths of $0D$, $0.35D$, and $0.48D$ at θ = 45°. 116
Figure 4.44. Pressure contour comparison around the augmented HDWT using cycloidal diffusers with shroud lengths of $0D$, $0.35D$, and $0.48D$ at θ = 45°. 117
Figure 4.45. Moment coefficient of HDWT using cycloidal diffusers with shroud angles of 0°, 2°, 4°, 7° and 10°. 118
Figure 4.46. Power coefficient of HDWT using cycloidal diffusers with shroud angles of 0°, 2°, 4°, 7° and 10°. 119
Figure 4.47. Single blade instantaneous Cm against azimuthal angles for HDWT using cycloidal diffusers with shroud angles of 0° and 7°. 120
Figure 4.48. Instantaneous Cm against azimuthal angles for HDWT using cycloidal diffusers with shroud angles of 0° and 7°. 120
Figure 4.49. Pressure contour with velocity streamline comparison around the augmented HDWT using cycloidal diffusers with shroud angles of 0° and 7° at θ = 30°. 121

Figure 5.1. Normal probability plot of externally studentized residuals for the coefficient of power of the quadratic model. 128
Figure 5.2. Predicted values against actual values for the coefficient of power of the quadratic model. 128
Figure 5.3. Externally studentized residuals vs. predicted values diagnostic plot for the coefficient of power of the quadratic model. 129
Figure 5.4. Externally studentized residuals vs. runs diagnostic plot for the coefficient of power of the quadratic model. 129
Figure 5.5. Three-dimensional surface response plot of the effect of interaction between diffuser length (A) and diffuser angle (B) on the coefficient of power. 131
Figure 5.6. Three-dimensional surface response plot of the effect of interaction between diffuser length (A) and shroud length (C) on the coefficient of power. 131
Figure 5.7. Three-dimensional surface response plot of the effect of interaction between diffuser length (A) and shroud angle (D) on the coefficient of power. 132
Figure 5.8. Three-dimensional surface response plot of the effect of interaction between diffuser angle (B) and shroud length (C) on the coefficient of power. 132
Figure 5.9. Three-dimensional surface response plot of the effect of interaction between diffuser angle (B) and shroud angle (D) on the coefficient of power. 133
Figure 5.10. Three-dimensional surface response plot of the effect of interaction between shroud length (C) and shroud angle (D) on the coefficient of power. 133
Figure 5.11. Suggested optimum design based on numerical optimization. 134
Figure 5.12. Radar plot of instantaneous Cm against azimuthal angles of Bare HDWT and HDWT with optimized cycloidal diffusers at TSR 2.0. 136
Figure 5.13. Single blade instantaneous Cm against azimuthal angles of Bare HDWT and HDWT with optimized cycloidal diffusers at TSR 2.0. 136
Figure 5.14. Streamlines coloured by velocity magnitude and 3D pressure contour on blade surfaces at θ=30° of the (a) Bare HDWT and (b) HDWT with optimized cycloidal diffusers. 138
Figure 5.15. Streamlines coloured by velocity magnitude and 3D pressure contour on blade surfaces at θ=0° of the (a) Bare HDWT and (b) HDWT with optimized cycloidal diffusers. 139
Figure 5.16. The pressure contour and streamlines comparison at θ=30° between (a) Bare HDWT and (b) HDWT with optimized cycloidal diffusers. 140

Figure 5.17. Characteristics of the airflow in the cooling tower with and without HDWT placed at the outlet. 143
Figure 5.18. XY-midplane velocity contour comparison for the cooling tower air flow with HDWT of (a) AR=0.35, (b) AR=0.44, and (c) AR=0.70 placed at the outlet at TSR 2.5. 148
Figure 5.19. YZ-midplane velocity contour comparison for the cooling tower air flow with HDWT of (a) AR=0.35, (b) AR=0.44, and (c) AR=0.70 placed at the outlet at TSR 2.5. 149
Figure 5.20. XY-midplane velocity contour comparison for the cooling tower air flow with AR 0.44 HDWT of σ = 0.225 (left) and σ = 0.450 (right) placed at the outlet at TSR 2.0. 151
Figure 5.21. YZ-midplane velocity contour comparison for the cooling tower air flow with AR 0.44 HDWT of σ = 0.225 (left) and σ = 0.450 (right) placed at the outlet at TSR 2.0. 152
Figure 5.22. XY-midplane velocity contour comparison for the cooling tower air flow with AR 0.44 HDWT of σ = 0.225 (left) and σ = 0.450 (right) placed at the outlet at TSR 3.0. 153
Figure 5.23. YZ-midplane velocity contour comparison for the cooling tower air flow with AR 0.44 HDWT of σ = 0.225 (left) and σ = 0.450 (right) placed at the outlet at TSR 3.0. 154
Figure 5.24. XY-midplane velocity contour comparison for the cooling tower air flow with HDWT of AR 0.44 and solidity of 0.450 augmented by cycloidal diffusers placed at the outlet at (a) TSR 1.5, (b) TSR 2.0, and (c) TSR 3.0..... 155
Figure 5.25. YZ-midplane velocity contour comparison for the cooling tower air flow with HDWT of AR 0.44 and solidity of 0.450 augmented by cycloidal diffusers placed at the outlet at (a) TSR 1.5, (b) TSR 2.0, and (c) TSR 3.0..... 156

LIST OF TABLES

Table 3.1. Cooling tower parameter. 48
Table 3.2. Main HDWT parameter used for this study. 50
Table 3.3. HDWT parameters for the effect of AR study. 51
Table 3.4. HDWT parameters for the effect of solidity study. 52
Table 3.5. Optimized HDWT parameters for wind augmenter study. 53
Table 3.6. Cycloidal diffuser dimensions for parametric study. 55
Table 3.7. Cycloidal diffusers parametric study steps. 56
Table 3.8. Validation reference parameters. 70
Table 4.1. Moment and power coefficients of HDWT using cycloidal diffusers with different diffuser lengths and diffuser angles at TSR 1.5. 101
Table 5.1. Independent variables and their levels. 123
Table 5.2. Optimal RSM runs conditions with the observed and predicted responses. 124
Table 5.3. ANOVA for power coefficient response of the optimal RSM design using a quadratic model. 126
Table 5.4. The goodness of fit for the regression model of the quadratic model. ... 127
Table 5.5. Criteria for the numerical optimization constraints. 134
Table 5.6. Validation of the numerical optimization predicted results by the computational result. 135
Table 5.7. The velocity of the air in the cooling tower at various positions, with and without the exhaust air energy extraction system. 142
Table 5.8. Cooling tower outlet mass flow rate and the power generated by the HDWT for selected HDWT cases. 145

NOMENCLATURE

A	Swept area	m^2
c	Chord length	m
C_m	Moment coefficient	-
C_p	Power coefficient	-
D	Turbine diameter	m
D_o	Cooling tower outlet diameter	m
D_{dt}	Throat width	m
H	Turbine height	m
H_{df}	Diffuser height	m
L_f	Shroud length	m
L_b	Diffuser length	m
L_t	Total length	m
N	Number of blades	-
p	Pressure	N/m^2
$P_{available}$	Wind power input	W
$P_{turbine}$	Turbine output power	W
R	Turbine radius	m
T	Torque	N/m
V_{in}	Wind speed	m/s
W	Flange width	m

Greek Symbols

σ	Turbine solidity	-
ω	Rotor rotational speed	rad/s
ρ	Density	kg/m^3
λ	Tip speed ratio	-
α	Angle of attack	°
θ	Azimuth angle	°
ϕ	Diffuser exit angle	°
γ	Shroud inlet angle	°

Abbreviations

VAWT	Vertical Axis Wind Turbine
HDWT	H-Darrieus Wind Turbine
URANS	Unsteady Reynolds Averaged Navier-Stokes
SIMPLE	Semi-Implicit Method for Pressure-Linked Equations
NACA	National Advisory Committee for Aeronautics
SST	Shear Stress Transport
CFD	Computational Fluid Dynamics
RSM	Response Surface Methodology
AR	Aspect Ratio
TSR	Tip Speed Ratio

CHAPTER 1: INTRODUCTION

1.1 Background

1.1.1 Fossil fuels and renewable energy

The annual growth in population and the economy has increased the need for energy production to meet the ever-increasing global energy demand. Non-renewable fossil fuels such as oil, gas, and coal are still the largest primary energy sources. Fossil fuel contributes 82% of the primary energy usage in 2021, down from 83% in 2019 and 85% in 2017 [1]. Even though the percentage of primary energy that comes from fossil fuels dropped, the CO2 emissions from the combustion of this type of energy source are still high due to the ever-increasing energy demand. Primary energy usage in 2021 increased by 5.8%, exceeding 2019's level by 1.3% [1]. The energy generated from fossil fuels for global energy consumption in 2021 is 136,018 terawatt-hours (TWh) [2], only 0.08% behind 2019 levels, as shown in Figure 1.1.

Environmental problems such as global warming are caused by the release of carbon dioxide (CO_2) from the excessive combustion of fossil fuels, which is a major issue. In 2019, CO_2 emission was recorded at 36.2 $GtCO_2$ [3]. CO_2 emission dropped by 1.9 $GtCO_2$, a 5.26% decrease in 2020 [3] since the consumption of fossil fuels was reduced to 128,800 TWh [2], the lowest reported since 2013 as nations were in lockdown and economies were halted due to the Covid-19 pandemic. With restrictions loosening and the economy resuming as usual, CO_2 emissions in 2021 and 2022 were recorded at 36.5 $GtCO_2$ and 36.8 $GtCO_{2,}$ respectively. This is a 0.83% increase in 2021 and a 1.66% increase in 2022 compared to 2019 [4]. With the current energy trend, CO_2 emission is predicted to rise to 43.2 $GtCO_2$ by 2040 [5].

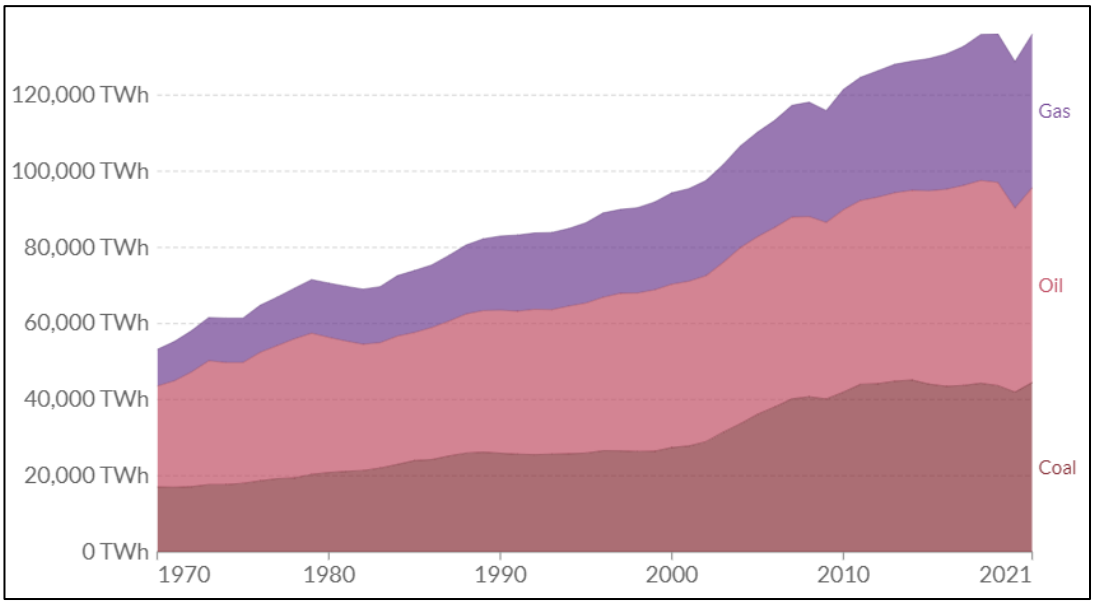

Figure 1.1. World energy consumption by fossil fuel type [2].

Fossil fuel resources are limited, and the ever-growing rate of fossil fuel usage is draining the available reserve with a high chance of completely depleting, as it is reported that only about 50 years of natural gas and oil reserves and 130 years of coal reserves are left [6]. Issues regarding energy demands and fossil fuel usage have raised global awareness to seek alternative ways to provide greener energy and control the emission of greenhouse gases. Cleaner and sustainable energy sources have become increasingly crucial, and continuous work to develop this energy source needs to be done immensely. Renewables 2022 Global Status Report [7] has reported that renewable sources such as solar, wind, hydropower, geothermal and biomass have all shown increased capacity growth in 2021. However, the renewable energy addition rate is not high enough compared to the increasing energy demand to reduce the reliance on fossil fuels, as the world's energy consumption is predicted to increase by 28% between 2015 and 2040 [8]. Globally, policies such as the Paris Agreement 2015 have been made to control the rise in global temperature by reducing greenhouse gas emissions and encouraging nations to help each other share the burden of promoting renewable energy by providing financial aid to less developed countries [9]. The Paris Agreement aims to keep the global average temperature rise below 2°C above the pre-industrial level, ideally limiting it to 1.5°C, reduce global emission by half by 2030, and reach net-zero emission by 2050 [9]. Based on the current global greenhouse gas emissions trend, the projected warming scenario would reach 2.9°C by 2100 with the current climate policies in place [10]. However, if all countries were to deliver their

reduction pledges made within the Paris climate agreement, the estimated warming would be at 2.1°C by 2100 [10]. Therefore, continuous development, the addition of clean energy production, and the reduction of fossil fuel usage are essential in addition to the current pledges made to realise the 1.5°C climate goals.

1.1.2 Wind energy and wind turbines

Wind energy comes second to solar energy as the largest renewable energy source. It shows a promising increase in generating clean energy with a consistent annual addition of 50 to 60 gigawatts from 2014 to 2019, with huge growth in 2020 and 2021 with additions of 95 GW and 102 GW, respectively, as shown in Figure 1.2 [7]. However, it is observed from Figure 1.3 that more than this growth is needed to achieve net-zero global emissions by 2050. The current wind energy growth needs to be faster for a robust global energy transition. GWEC Market Intelligence predicts that the total installed wind energy capacity will be around 1300 GW by 2030 [11]. This prediction means we will only have two-thirds of the wind energy required in 2030 to stay on track for the net zero and 1.5°C pathway set by IRENA [12] to meet the 2050 climate goals. Based on this, wind energy installation needs to be quadrupled to achieve the wind energy capacity target for 2030.

Wind turbines harness wind energy by capturing wind flow over specially curved turbine blades, producing lift force that spins the turbine shaft that converts kinetic energy to mechanical power by the rotor spinning motion and fed to a generator to generate electricity in significant amounts [13]. These turbines come in many sizes and power ratings and are classified into micro, small, medium, and large turbines, as shown in Figure 1.4. There are two main categories of wind turbines: horizontal axis wind turbines (HAWT) and vertical axis wind turbines (VAWT) [13]. Years of research and development on HAWT have enabled vast harnessing of wind energy for large-scale energy production in open fields with steady wind speed [14]. However, due to limited land space, VAWT is more suitable for use in urban areas as it has a lower noise level, smaller design, omnidirectional properties, and can adapt to high turbulent wind conditions [15], [16]. Moreover, VAWT has a simpler design and low maintenance cost, encouraging more interest in developing this turbine for small-scale power production [16]. These VAWTs can be further classified into Darrieus wind turbine, a lift-type turbine, and Savonius rotor, a drag-type turbine [13].

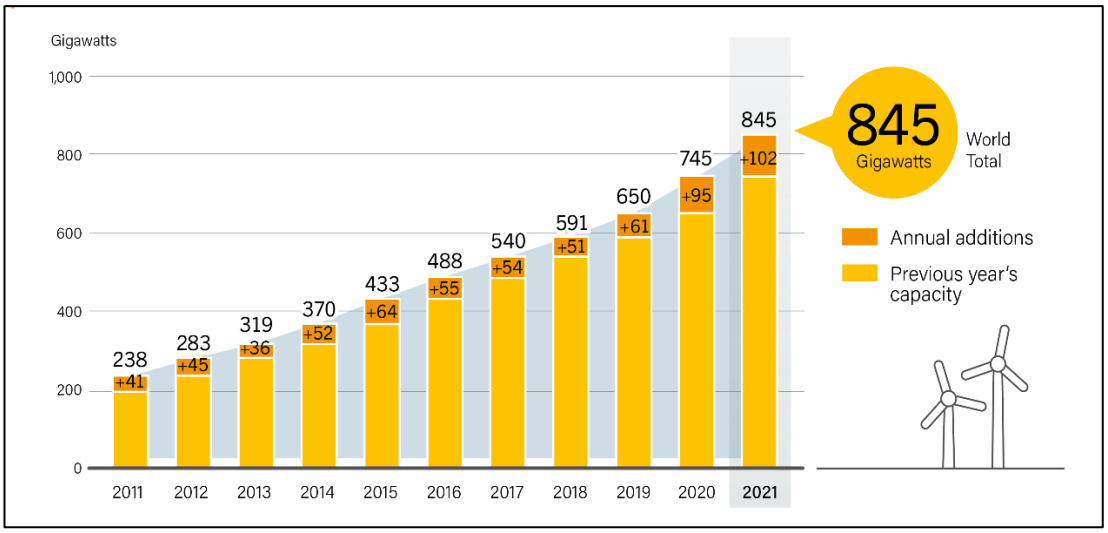

Figure 1.2. Global wind power capacity and annual additions from 2010 to 2021 [7].

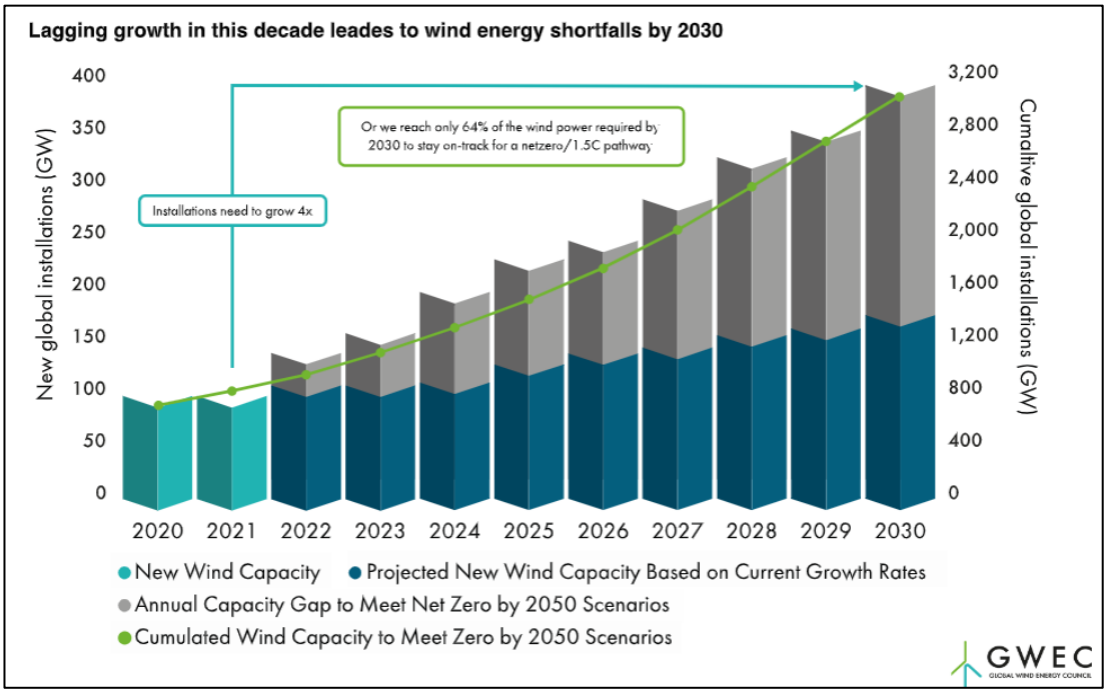

Figure 1.3. Projected Wind Energy Capacity by 2030 to Meet Net Zero 2050 Scenario [11].

Many studies have been conducted on the H-Darrieus wind turbine (HDWT) as it has greater potential in providing higher efficiency and wider tip speed ratio (TSR) working conditions over Savonius turbines [13], [16], [17], [18], [27]–[36], [19], [37]–[41], [20]–[26]. Some VAWTs are continuously being implemented in rural and urban areas for electricity generation at locations with medium to high wind speeds, such as along roadside dividers and railway tracks, on top of lamp posts and tall buildings [15],

[16]. However, this method of energy production is not cost-effective in places or countries with low and unstable wind conditions throughout the year.

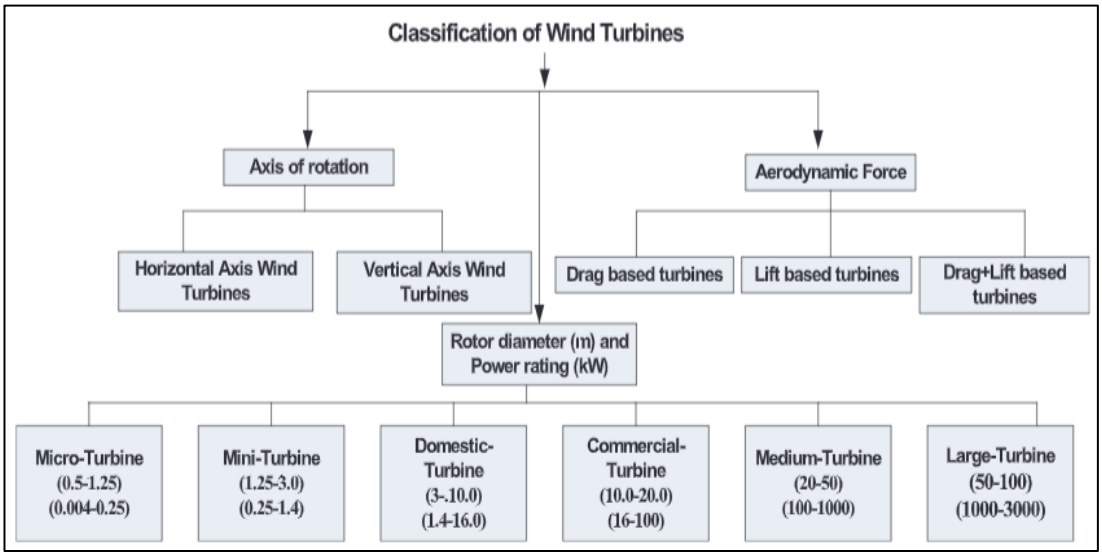

Figure 1.4. Wind turbine classifications [16].

1.1.2.1 Savonius VAWT

Savonius VAWT, a pure drag-type rotor, was the first type of VAWT built in the 1920s [42]. Figure 1.5 illustrates the design of a Savonius rotor consisting of turbine blades made of two half cylinders facing the opposite direction, creating a cross-section shaped like a letter “S”, which rotates around a shaft. This turbine rotates due to the difference in drag force the blades make. The advancing blade experiences more drag as the concave side moves with the wind. The returning blade pushes against the wind and experiences less drag force due to the curvature of the blade surface [43]. Savonius VAWT has excellent start-up characteristics. However, it is less efficient than other turbine types. A study by Sandia Laboratory, USA, has reported that a semi-circular Savonius wind turbine can achieve a maximum power coefficient of 0.24 [15]. Various studies have shown that the Savonius rotors’ performance in converting wind energy to mechanical power is still 20% lower than Darrieus rotors [44].

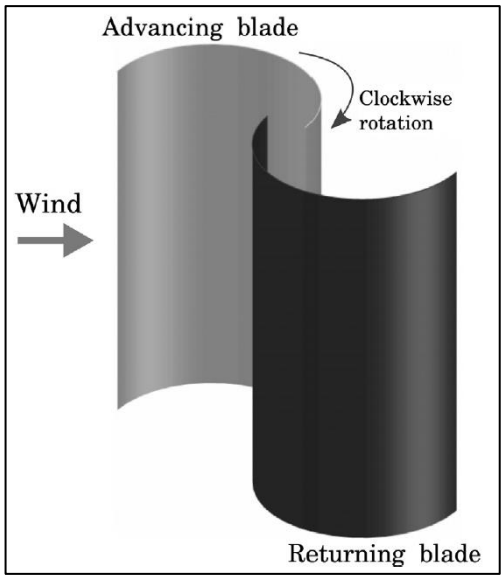

Figure 1.5. Savonius style VAWT [15].

1.1.2.2 Darrieus VAWT

The Darrieus VAWT is a lift-type turbine named after the French engineer Georges Darrieus, who designed it in 1925. The airfoil of a Darrieus VAWT generates a small net lift force in a forward direction as it moves through the air in a circular motion relative to the direction of the wind and creates positive rotor torque [16]. Early designs of the Darrieus VAWT consist of complex curve blades, also known as the egg-beater design, that rotates in a troposkein manner [42]. The egg-beater has drawbacks, such as challenges in manufacturing, low self-starting characteristics, and difficulty controlling turbine speeds and output power. Modifications were made to the Darrieus VAWT, and many variations were created, as shown in Figure 1.7, to overcome the shortcomings of the earlier designs. The introduction of the Giromill turbine or the straight-bladed Darrieus, also known as the HDWT, has a simpler design, and the turbine blades are easier to manufacture. Moreover, the HDWT has a better power coefficient than the egg-beater design, and therefore, many studies have been done to maximize its potential [45]–[48]. The Helical blade type Darrieus VAWT has been mainly studied as it offers better performance characteristics than HDWT; however, it is more expensive to manufacture. Figure 1.6 shows the eggbeater, H-Darrieus and Helical blade Darrieus VAWT. More details about the working principles of Darrieus VAWT and its aerodynamics are discussed in Section 2.1.

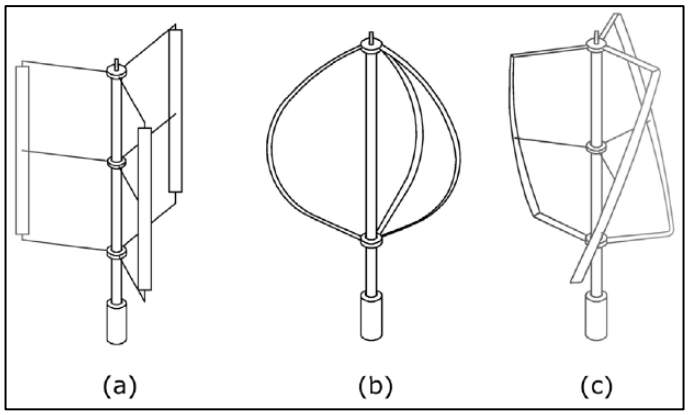

Figure 1.6. Darrieus VAWT configurations (a) Straight-bladed "Musgrove H-Rotor", (b) Curve-bladed "eggbeater Darrieus", (c) Helical-blade "Gorlov" [47].

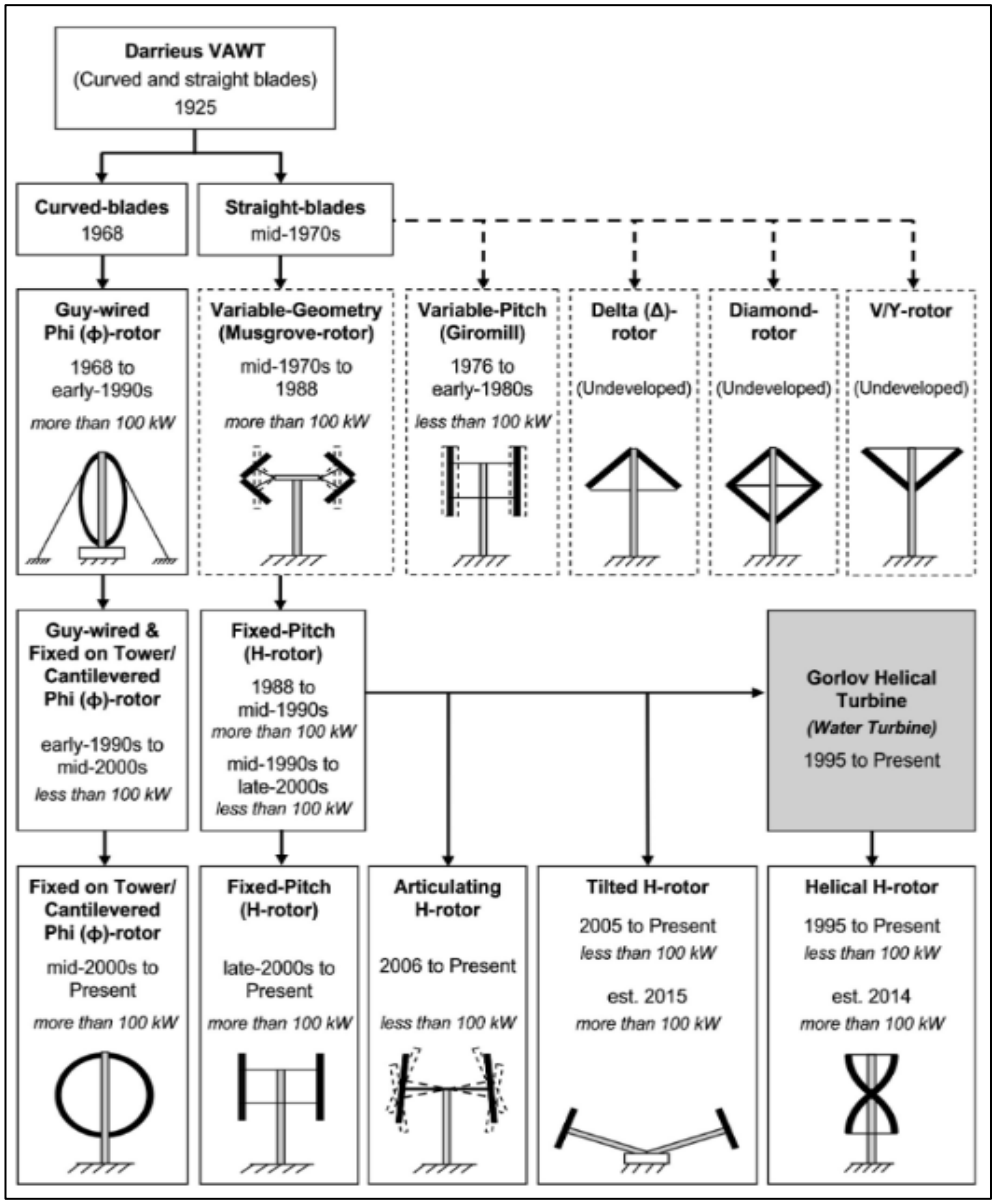

Figure 1.7. Development of Darrieus-type turbine over the years [45].

1.2 Problem Statement

Strong wind speeds, which are the best for generating wind power, are available mainly in remote locations like rural and open areas [49], [50]. More effort is needed to bring renewable technology closer to urban areas with higher population density and energy use, as on-site installation provides benefits such as lower cable costs and transmission losses [50]. Over the past few years, much research has been done on integrating VAWT in built environments to harness natural wind sources. However, field experiments drastically produce low power output due to turbulence and constantly changing wind direction caused by the complexity of building architectures in urban areas [51]. Turbulence in urban areas contributes about 15% to 30% decrease in power output [51]. Few on-site experiments, lab experiments, and simulation studies on the optimum configuration of VAWT, including the integration of augmentation methods for high-rise buildings, have been studied and discussed, and these are available in the open literature [51]–[53]. Countries with either low wind speed or fluctuating wind conditions throughout the year face difficulties in harnessing this renewable energy source to produce power [53]. For example, Malaysia's average annual wind speed is 2m/s [54]. Alternative ways to use wind turbines for clean energy production are available by utilising unnatural wind sources such as the strong and consistent exhaust air of cooling towers, which releases about 5m/s to 16m/s of airspeed [55]. Mechanical and atmospheric-induced cooling towers are abundantly used, which allows the accelerated wind source to be harnessed through its outlet air using wind turbines for clean energy generation. This idea is relatively new, with very few studies on the feasibility of harnessing cooling tower exhaust air to produce energy using VAWT, which was recently presented as discussed in the literature review in Section 2.4 [53], [56]–[59].

From previous studies, optimization of VAWTs through computational and experimental investigations under free stream flow conditions has proven that with better designs, the efficiency of the VAWT can be increased [44], [45]–[48]. However, the maximum efficiency achieved is only 13% for VAWT in cooling tower applications using guide vanes [58]. Free stream flow physics and aerodynamics of wind turbines are significantly different than accelerated flow of nozzle or guided flow, as in the case of cooling towers. Chong et al. [53] suggested that further optimization is needed for the cooling tower air energy extractor to maximize energy

extraction from the exhaust air. Minimal works of literature on the cooling tower energy recovery system have been observed [53], [56]–[59], with the flow physics and aerodynamics of cooling towers not fully explored to date. Understanding the fundamental flow physics and aerodynamics of the accelerated wind condition of the cooling tower will help determine the reasoning behind the low efficiency of the VAWT in cooling tower applications, and improvements to the turbine design can be made based on the associated flow physics and aerodynamics of the cooling tower system. Therefore, wind augmentation techniques can be optimized and added to the energy recovery system to maximize energy recovery from the exhaust of cooling towers. Hence, a detailed study of flow physics and aerodynamics in cooling tower applications and augmentation methods is needed to optimize the energy recovery system.

1.3 Research Aim & Objectives

This study aims to maximize energy extraction from the exhaust system of cooling towers through a three-dimensional numerical study by first studying the bare HDWT aspect ratio (AR) and solidity, followed by adding and optimizing the cycloidal diffuser design by using the design of experiment method and analysing the flow physics of the whole system. The objectives of this research are as follows.

- To determine the best AR and solidity of the HDWT for maximum power coefficient from cooling tower exhaust air and calculate the aerodynamic moments and power generated by the HDWT from cooling tower exhaust air.
- To study the flow physics via velocity, pressure, and vorticity around the bare HDWT energy extractor of the various ARs and solidities in cooling tower application.
- To conduct a parametric study on the cycloidal diffuser design parameters and analyse how each independent variable affects the HDWT power coefficient under cooling tower exhaust air.
- To optimize the design of the cycloidal diffuser using response surface design for maximum power generation and calculate the percentage increase of power coefficient obtained from the optimized system.

- To study how the flow around HDWT is enhanced using cycloidal diffusers and compare the flow characteristics of bare HDWT and the optimized augmented HDWT under cooling tower exhaust air.

1.4 Research Questions

- What is the best size and solidity of HDWT to improve energy extraction from the cooling tower outlet, and how much of a moment and power coefficient can be achieved?
- How does the associated flow physics in terms of the blade solid-fluid interaction and separation in the exhaust air energy extractor affect the performance of HDWT at different azimuthal positions?
- How do the cycloidal diffusers with different design parameters affect the performance of HDWT under accelerated flow conditions of the cooling tower?
- What will be the optimal cycloidal diffuser design to maximize the power coefficient of the HDWT from cooling tower exhaust air?
- How will the cycloidal diffusers improve the flow around HDWT in terms of blade vortex interaction, near wake region, vorticity, and separation under an accelerated cooling tower flow?

1.5 Research Scope

This research focuses on maximizing the power coefficient of HDWT in cooling tower applications by first investigating the best HDWT AR and solidity before integrating cycloidal diffusers into the computational setup. Then, a parametric study on the diffuser length, diffuser angle, shroud length, and shroud angle was studied to determine the range of parameters appropriate for HDWT performance enhancement under accelerated cooling tower exhaust air. Finally, design optimization of the cycloidal diffusers was done to optimize the cycloidal diffuser parameters to maximize the coefficient of power of HDWT. Analysis of the HDWT performance was done throughout this study by plotting the coefficient of moment and coefficient of power graph to measure and compare the performance of the HDWT for the different parameters stated. This study was conducted using computational fluid dynamics (CFD) in STAR CCM+ software as part of the aim of the study is to analyse the flow

behaviour of the system to discuss the reasons behind the performance achieved for the different AR, solidity, and cycloidal diffusers parameter. This was done by looking at various flow figures such as velocity, pressure, vorticity, streamlines and drag. In total, 131 simulation runs were completed to achieve this study's objectives. Since this is a simulation-heavy work, experimental work was not conducted due to time constraints. In addition, the effect of the exhaust air temperature was not considered, and it was set to constant as this work focuses on the air-blade interaction and how the cycloidal diffuser enhances HDWT performance under the accelerated cooling tower exhaust air. This work aims to build a foundation on the energy extraction of exhaust air using wind-augmented HDWT and opens the possibility for further studies to be conducted.

1.6 Significance of Research

This proposed research is expected to improve the cooling tower exhaust air energy extractor system by optimizing cycloidal diffusers specifically for the application of cooling towers. Cycloidal diffusers with proper shape and parameter optimization will improve turbine power generation by accelerating and guiding the air towards the turbine for higher power generation. The new design’s flow physics will be investigated to understand the cause of low efficiency at certain azimuthal rotation angles for each proposed design and discuss how the power coefficient varies for different cycloidal diffuser parameters. This information will be necessary for future research as the flow diagrams, with their discussions, are expected to guide future research to improve further the flow augmenters design and the overall cooling tower exhaust air energy extractor system. This project will contribute quantitative data for the analysis and provide a benchmark for numerical simulations for the relative scientific community. This will provide an understanding for future works on how the guided flow augmenters’ turbine aerodynamics behave under accelerated wind conditions of the cooling tower.

CHAPTER 2: LITERATURE REVIEW

2.1 Fundamental Principle and Aerodynamics of HDWT

The velocity and force that act on the Darrieus VAWT blades during operation are shown in Figure 2.1. The rotor tangential velocity ($\omega_r \times R$) is given as ($\vec{U}$). ($\vec{W}$) is the resultant velocity vector, which is the resultant sum of the induced velocity ($\vec{V_\infty}$) and tangential velocity ($\vec{U}$). The angle between relative velocity, W and the blade's chord line is called the angle of attack (α) of the blade. The relative wind speed and angle of attack of the blade change during each cycle. Therefore, at every different azimuthal position (θ), the magnitude and direction of the lift and drag forces change frequently throughout the VAWT rotation. The dynamic stall, which occurs at a relatively high angle of attack, is associated with the variation in the angle of incidence. The angle of attack (α) of a VAWT blade is expressed as [36]:

$$\alpha = arctan\frac{sin\theta}{\lambda + cos\theta} \tag{2.1}$$

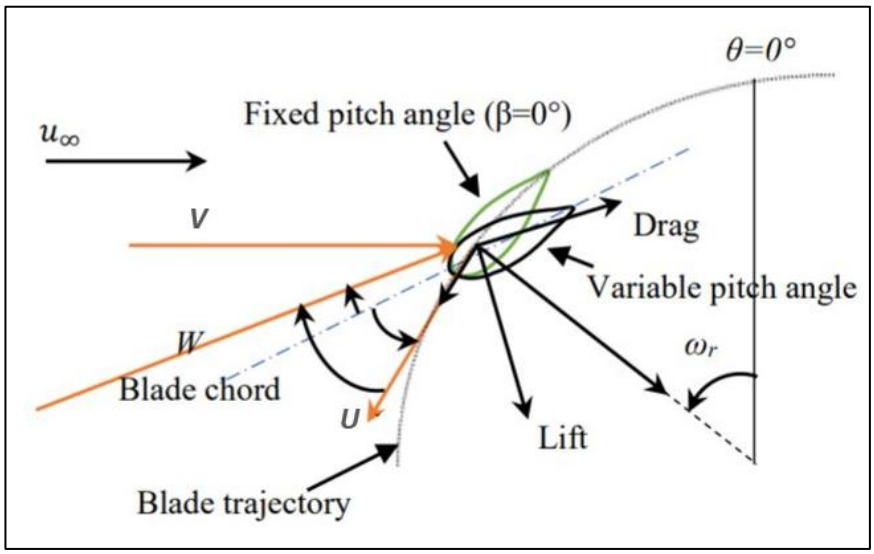

Figure 2.1. Forces and velocities on HDWT blade.

At low TSR, beyond the stall angle, VAWT blades frequently experience a high angle of attack, as shown in Figure 2.2, which causes the blade to stall at most of its trajectories. This stall leads to a sudden decrease in the lift and a rapid increase in drag, consequently decreasing the rotor torque. Increased development of blade vortex formation is another consequence of the large variation of the angle of attack, which

causes flow separation on the blade surface. The static stall and dynamic stall phenomenon are described in detail in Subsections 2.1.1 and 2.1.2.

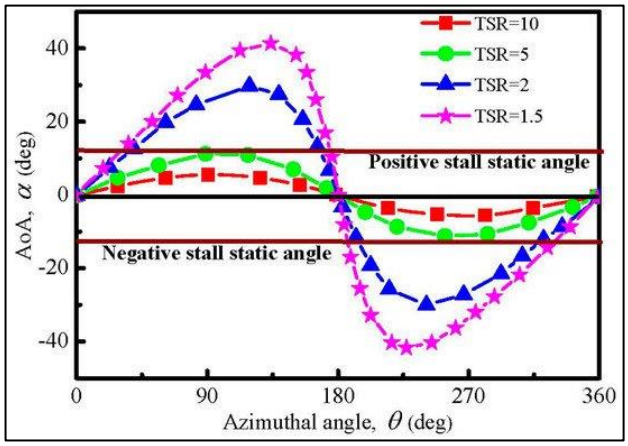

Figure 2.2. The azimuthal angle of attack for one complete rotation at different TSRs [60].

2.1.1 Static stall

The stall is a common phenomenon in HDWT airfoil aerodynamics. The static stall develops around the airfoil when the angle of attack reaches a critical value, causing it to lose lift and dramatically increase its drag [61]. In static or deep stalls, the flow separation begins at the airfoil's trailing edge, shifting to the leading edge as the angle increases. If Reynold's number is too low, separation may occur immediately at the leading edge, negatively affecting the HDWT's self-starting ability. Whenever the airfoil is in a deep stall, it will continue experiencing it for some time, even after the angle decreases again, creating a hysteresis loop. When the airfoil is in this loop, its performance is unfavourable as it suffers from low lift and high drag. The complete lift and drag curves of the HDWT airfoil are essential since the HDWT airfoil always operates outside of the design consideration. Figure 2.3 shows an example of the lift and drag curve of a NACA 0018 airfoil for a full range of angle of attack. At 9°, the lift increase is nonlinear as the flow separates from the airfoil's top surface. This angle is generally called static stall angle as it is at this point the dynamic stall begins. The deep stall angle is reached once the airfoil passes the maximum lift point, resulting in massive flow separation from the leading edge, causing a considerable drop of lift followed by a sudden drag increase. From here, when the airfoil's angle of attack decreases, it experiences the previously stated hysteresis loop, preventing flow from reattaching. The flow only re-attaches once the angle of attack becomes low enough.

The deep stall occurrence for airfoils depends on the airfoil's thickness and Reynolds number. In HDWT applications, large angles of attacks are common, and the optimum TSR is achieved when the influence of this stall phenomenon is small [62].

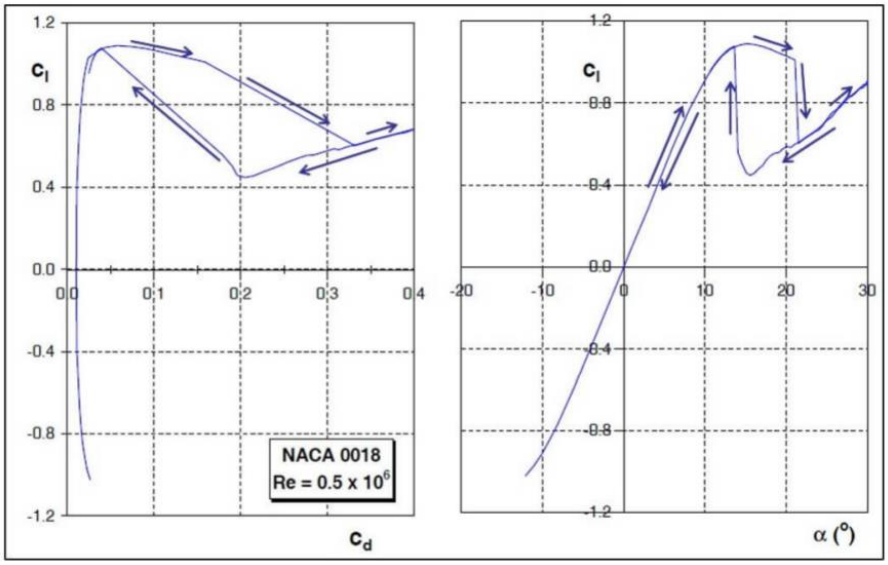

Figure 2.3. Deep stall experienced by NACA 0018 airfoil [62].

2.1.2 Dynamic stall

Dynamic stall occurs when the airfoil experiences rapid change in angle of incidence or motion which causes the airfoil's angle of attack to exceed the static stall angle. This dynamic stall effect is a time-varying phenomenon where flow separates from the airfoil lift-generating surface, causing it to stall, as McCroskey defined in an early experimental study in 1976 [63]. Regarding the oscillatory condition of VAWTs, Kramer observed that dynamic stalls could increase lift generation as flow separation occurs at a higher angle of attack compared to the static condition [64]. Leishman (2006) has given an overview of the dynamic stall process, which can be broken down into five stages, as shown in Figure 2.4. In the first stage, when the static stall angle is exceeded, lift continues increasing with the angle of attack as there is a delay in flow separation. The phenomenon is due to the equal and opposite circulation shedding into the wake at the airfoil's trailing when the airfoil experiences changes in circulation (lift increases). The wake counter-circulation causes the airfoil surface to experience a down-washing force, which delays the formation of a vortex, as Theodorsen's Theory and the two-dimensional thin airfoil theory explain. In addition, the pressure gradients

and leading-edge pressure are reduced by a positive pitch rate compared to the steady case [65].

In stage 2, when the leading-edge pressure gradient increases high enough, a vortex is formed due to the viscous shear forces, and the then separated flow rolls up at the leading edge of the airfoil, which moves down the chord towards the trailing edge of the airfoil at stage 3. Whilst the vortex is near the suction side of the airfoil, the lift increases, and the centre of pressure shifts towards the trailing edge as the vortex moves down the chord. Stage 4 begins once the vortex passes the trailing edge, causing the flow to be fully separated. This flow separation causes the blade section to have a nose-down pitching moment, sudden reduction in lift and increase in drag, which creates unwanted torsional loading as the flow separation over the blade's entire length is not uniform. Moreover, separated flow reduces the aerodynamic damping, potentially causing blade instabilities, known as stall flutter. The flow will begin to reattach once the airfoil's angle of attack decreases back below the static stall angle. However, there will be a delay in the flow reattachment caused by the flow reorganisation on the suction side of the airfoil [61]. The airfoil will also experience a negative pitching rate (opposite of the stage 1 effect), which reduces the lift force. For this reason, the angle of attack needs to decrease below the static stall angle so the flow can be fully attached again. Stage 5 happens once the flow fully reattaches to complete the cycle. The delay in flow separation and reattachment is known as the hysteresis effect, as described for the static stall in Subsection 2.1.1. Therefore, it is essential to consider dynamic stalls in design since flow separation results in the regular occurrence of peak loads and increases blade stresses and vibration, potentially exceeding the structure's fatigue limits.

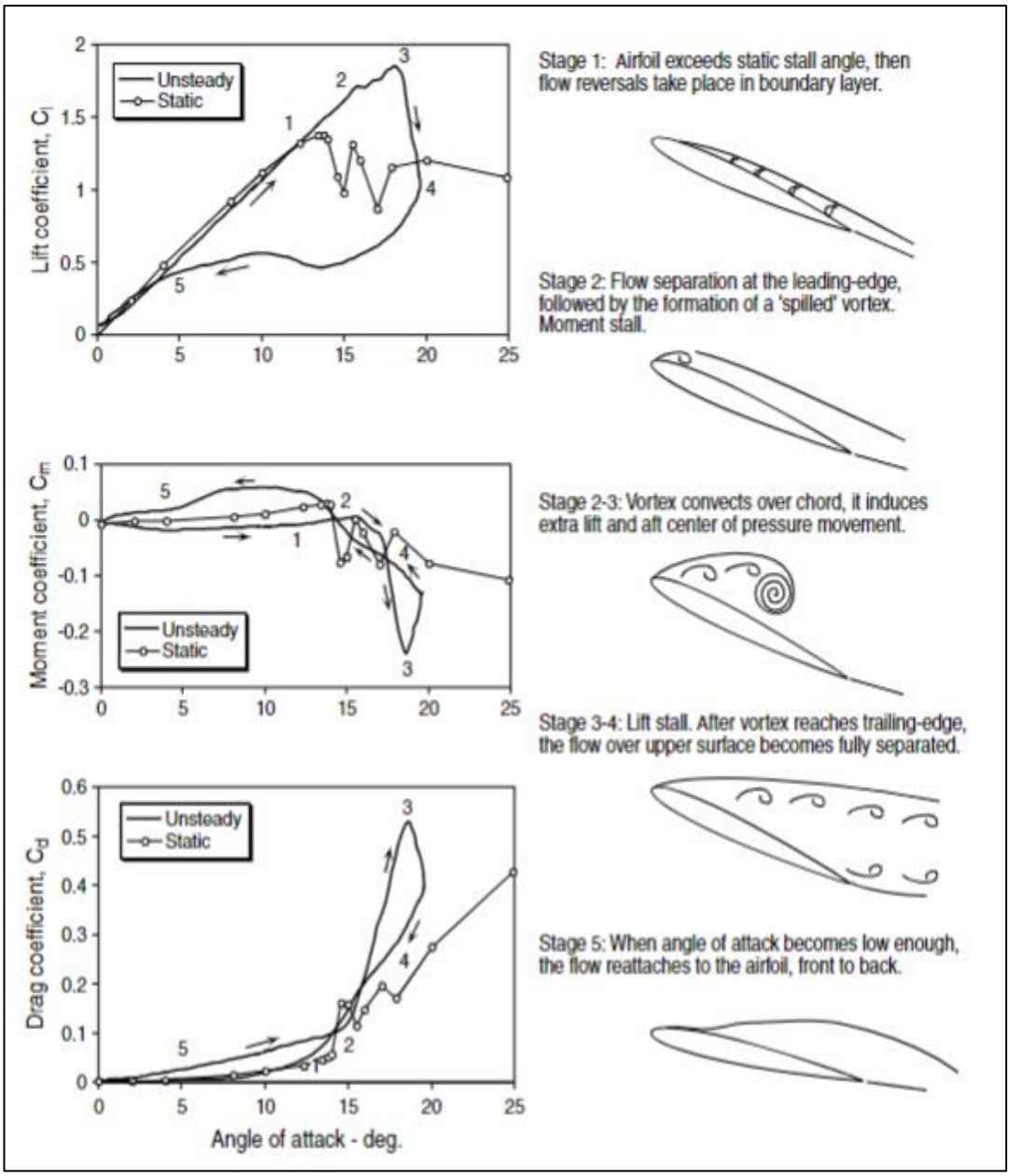

Figure 2.4. Flow physics and unsteady air loads diagrams of an airfoil experiencing dynamic stall [65].

2.1.3 Key operational parameters of HDWT

The design parameters of an HDWT significantly influence its performance. Therefore, paying attention to some of the most decisive HDWT parameters is critical in this study. These parameters include the rotor solidity, AR, TSR, chord-based Reynold's number, coefficient of moment and coefficient of power. All the equations in this section are the fundamental equations for the HDWT and have been described in all studies involving this turbine [17], [18], [27]–[36], [19], [37]–[41], [20]–[26].

HDWT solidity refers to the ratio of the total planform area of the rotor to the total swept area expressed as a function of the number of blades N, chord length of the blades c, (m), and diameter of turbine D, (m) as shown by Equation 2.2 below:

$$\sigma = \frac{Nc}{D} \tag{2.2}$$

The effect of AR on HDWT performance under cooling tower accelerated flow is one of the objectives of this study. The diameter-based AR and chord-based AR are given as a ratio to the height of the blade, H (m), as shown in Equation 2.3 and Equation 2.4 below:

$$AR = \frac{H}{D} \tag{2.3}$$

$$AR_c = \frac{H}{c} \tag{2.4}$$

The TSR is the most decisive parameter for HDWT design performance measure, and it is defined as the ratio between the transitional speed at the tip of the HDWT blades and free stream wind velocity U_∞, (m/s) as expressed in Equation 2.5 where ω is the angular velocity, (rad/s) and R is the radius of the HDWT, (m) respectively.

$$TSR = \frac{\omega R}{U_\infty} \tag{2.5}$$

Chord-based Reynold's number, Re_c has an important effect on smaller HDWT performance, as increasing this causes the lift coefficient to rise while the drag coefficient of the airfoil reduces [18], [24]. Equation 2.6 shows that the Re_c is directly proportional to the relative air speed of the airfoil w, (m/s) and blade chord length. The relative air speed is the sum of peripheral speed and free stream wind velocity reduced by induction factor a as expressed in Equation 2.7.

$$Re_c = \frac{wc}{U_\infty} \tag{2.6}$$

$$w = \omega R + U_\infty(1 - a) \tag{2.7}$$

The coefficient of moment, C_m and coefficient of power, C_p are calculated for HDWT performance measures and are widely used to measure the efficiency of wind turbines in wind power industries. The HDWT power performance is measured as the

ratio between the turbine's output electrical power and the input wind power. The moment coefficient and power coefficient are given as a function of average mechanical torque, T (Nm), density, ρ [kg/m^3], HDWT swept area, A [m^2], HDWT radius, R (m), and free stream wind velocity U_∞ [m/s]. Equation 2.8 shows the turbine's swept area, whereas Equation 2.9 and 2.10 show the moment and power coefficients, respectively.

$$Swept\ area\ (A) = H \times D \tag{2.8}$$

$$C_m = \frac{T}{0.5\rho A R U_\infty^2} \tag{2.9}$$

$$C_p = \frac{P_{turbine}}{P_{available}} = \frac{T\omega}{0.5\rho A U_\infty^3} = \frac{T}{0.5\rho A R U_\infty^2} \times \frac{R\omega}{U_\infty} = C_m \times TSR \tag{2.10}$$

2.2 Enhancement Study on HDWT Parameter

The advantages and potential of HDWT have attracted a large number of studies to continuously improve its performance for cost-effective energy production for various locations and conditions. Some studies were done on the geometric and operational parameters of the HDWT, such as the airfoil types, solidity, number of blades, AR, pitch angles, strut effect and Reynold's number effect with various design techniques and flow visualisation analysis [44], [47], [48].

2.2.1 Airfoil type and design

Blade airfoil is the most crucial selection for an HDWT as it has a significant impact on its performance aerodynamically, with many studies focused on the type and profile of airfoil available [26], [28], [33], [35], [37], [41], [42]. The geometry of the blade greatly influences the aerodynamic efficiency of HDWTs, as proven by many experimental and numerical studies over the years. Qamar and Janajreh [28] carried out a two-dimensional CFD simulation study using an eddy viscosity model to compare how three different airfoils affect the performance of a three-bladed HDWT at TSR of 1 to 7. The airfoils used were of a symmetrical geometry, NACA 0012 and two cambered airfoils of NACA 4512 and NACA 7512, where the results showed that the cambered airfoils gave approximately 42% increase in C_p and the maximum C_p is achieved at lower TSR compared to the symmetrical airfoil. A broader airfoil study using two-dimensional Unsteady Reynolds-Averaged Navier-Stokes (URANS)

simulation on 24 types of airfoils from 8 airfoil series for three-bladed HDWT was done by Hashem and Mohamed [42]. The HDWT of solidity 0.1 was tested at various TSRs, ranging from 2 to 8, and the result showed that the turbine using S1046 airfoils gave the highest C_p at most of the TSR with the maximum recorded to be C_p=0.3463 at TSR=4.0. Sun et al. [26] studied the effect of 6 different blade shapes, three of which are symmetric (NACA 0018, S-1046, DU 06-W-200)) and three asymmetrical airfoils (NACA 1425, NACA 4425 and EN 0005) on the power extraction performance, self-starting characteristics, and fatigue characteristics of a bowl-shaped straight-bladed VAWT [26]. The EN 0005 blade performed the best for the self-starting ability as it is asymmetrical. The airfoils with thicker camber (NACA 4425 and NACA 1425) give better power extraction performance at low wind speeds of less than 6 m/s. At higher wind speeds, the thin camber airfoil (S-1046) turbine gives the best power extraction performance. The turbine with S-1046 airfoils also performs best in terms of fatigue characteristics as it has the smallest deviation of aerodynamic force.

Changes to the airfoil design were also studied to improve the HDWT stall and dynamic performances further. Celik et al. [66] conducted a 2D CFD study on impact J-shaped airfoil with different opening ratios on 3-bladed HDWT self-starting performance. Firstly, the opening ratio at the inner surface of the airfoil is undesirable as it does not show good start-up characteristics. The J-shaped airfoil of NACA 0018, with the largest outer surface opening ratio of 90%, has a better torque coefficient at a lower TSR. Still, the airfoil with no opening produces higher torque at higher TSR. However, at optimum TSR, the larger opening ratio airfoil has the best start-up characteristics but at the cost of lower torque generation. The best opening ratio was reported to be 30%-40%, giving good start-up characteristics with maximum torque close to the airfoil with no opening. The optimum airfoil thickness of the J-shaped airfoil with different opening ratios was also investigated using six different airfoils. The thicker airfoil, NACA 0018 and reverse-cambered NACA 2518 produced the best self-starting performance for most of the opening ratios. Abdolahifar and Karimian [67] conducted a 3D CFD study on different slot designs on straight-bladed Darrieus VAWT to reduce flow separation by transferring the flow from the pressure side to the suction side of the blade at low TSR. The effect of slot width and outflow location was studied. Increasing the width of the inflow section (at the pressure side of the blade) and outflow section (suction side of the blade) results in a higher mass flow rate

through the slot, which improves the average torque coefficient by 36.2% due to postponement of the flow separation. The best outflow location was found to be $c/3$, which produced a 66.1% higher average torque coefficient and delayed the azimuthal angle of peak torque coefficient by 15.5° at TSR 1.0. However, at higher TSRs, the slot design delivers lower torque at the downwind region, resulting in the average torque coefficient only increasing by 10.5%. Another passive control method that is increasingly gaining attention in VAWT studies is the use of leading-edge serration or bionic blades, which is an airfoil design based on the pectoral fin of humpback whales, to study the effect on pressure distribution, stall, hysteresis loop and laminar separation bubble compared to baseline blade design [22], [31], [68]–[73]. Zhu et al. [73] conducted a numerical study comparing the aerodynamic characteristics between the 2-bladed HDWT with bionic and standard blades. It was found that the turbine with bionic blade produced a higher average power coefficient, and the difference between the value to the turbine with standard blades increases with TSR as bionic blades improve the average power coefficient by 1.83%, 2.62% and 4.06% at TSRs 1.38, 2.19 and 2.58, respectively. The result showed that at an azimuthal angle of $200° < \theta < 260°$, flow attachment at the wave crest section of the bionic blade produced better aerodynamic performance. Zhang et al. [71] further analysed the aerodynamic and flow characteristics of the HDWT with bionic airfoil from the study of Zhu et al. [73]. For the blade angle of attack up to 12°, the baseline airfoil shows a better lift coefficient with a maximum value of 0.723. However, for the 14° and higher angle of attack, the bionic airfoil showed better lift characteristics with a maximum lift coefficient of 0.743. The bionic airfoil improved power performance at the dynamic stall by delaying the stall and promoting the transition from laminar to turbulent.

There are other examples of airfoil design studies such as V-shape HDWT [36], slotted airfoil blades [25], the use of Gurney flaps [29], [39], passive flow control using leading edge slat [30] and trailing edge flaps [17]. However, most of these changes or additions to the airfoil are expensive to manufacture and be used in real applications. Therefore, the simple symmetrical S-1046 airfoil is the best choice for HDWTs as it has been demonstrated to perform best compared to many other symmetrical and asymmetrical airfoils [26], [42].

2.2.2 Solidity

The performance of turbines is mainly measured at different TSRs. An abundance of past research has shown that the solidity and number of blades of an HDWT affect the power coefficient at different TSR values [19]–[21], [27], [37], [38], [40]. Qamar and Janajreh [38] conducted a two-dimensional CFD study using NACA 4312 blades of three different chord lengths (c=0.2, 0.5 and 1.0) on a three-bladed HDWT at low and high TSR. The higher solidity turbine gave a much higher C_p over the lower solidity turbine at a lower TSR range of 1.0 to 3.5. In comparison, the lower solidity turbine has an advantage at higher TSR values and can operate at a wider TSR range. Qamar and Janajreh also compared using 2-bladed and 3-bladed HDWT, resulting in the 3-bladed HDWT producing better C_p. Next, a three-dimensional Transition shear stress transport (SST) model simulation study on different solidity by varying number of blades was done by Subramanian et al. [37] on 2,3 and 4-bladed HDWT using NACA 0012 and NACA 0030 airfoils. In their study, Subramanian et al. showed that the 2-bladed and 3-bladed turbines performed well, while the 4-bladed turbines did not perform satisfactorily. Overall results depict that the 2-bladed turbine performance is better at higher TSR but suffers from a low self-starting performance at lower TSR due to lower solidity. An experimental study on small HDWT by Li et al. [21] further proves that increasing the number of blades deteriorates the turbine power performance. Analysis of the rotor pressure distribution shows that the increasing number of blades reduces the pressure difference, which explains the drop in performance [21]. Sagharichi et al. [19] studied the effect of seven solidities, ranging from 0.20 to 0.80, on the fixed pitch and variable pitch 3-bladed HDWT using NACA 0021 airfoils. Results obtained indicated fixed pitch and variable pitch blades achieved maximum C_p at a solidity of 0.6 and 0.8, respectively. The difference between fixed and variable pitch blades increases with solidity, with the variable pitch showing greater performance. Overall, these studies showed that symmetry airfoils give good aerodynamic performance with lower solidity HDWT optimal at higher TSRs and higher solidity HDWT optimal at lower TSRs. The TSR that produces peak power coefficient varies according to the type of airfoil used.

2.2.3 Aspect ratio

The primary considerations for designing an HDWT are the size and parameters, as there are few studies conducted on the HDWT ARs [18], [23], [24], [32], [34] highlighting the importance of selecting a suitable blade span length, chord length, and diameter for maximizing the performance of the turbine. Li et al. [23] conducted a study using the panel method to study the effect of AR by changing the ratio of the blade span to the HDWT diameter (H/D) in two cases, one at fixed solidity, σ and the second at fixed rotor chord-based AR (blade span to blade chord ratio), H/c of a 2-bladed HDWT of NACA 0021 airfoils. The study by Li et al. [23] showed that at fixed solidity, there is an increase in the HDWT power coefficient as the height-to-diameter ratio gets bigger. However, at fixed rotor AR, the height-to-diameter ratio does not exhibit any significant effect on the power coefficient. The study by Li et al. indicates that the performance of HDWT depends on the rotor AR in the case of varying height-to-diameter ratio. It is noted that diameter was the fixed variable in the study done by Li et al. A thorough investigation on 3-bladed HDWT parameter optimization was studied by Bianchini et al. [18] using the Blade Element Momentum approach to maximize Reynold's number and keep the relative speed on the airfoil at a desirable value. In the study by Bianchini et al., 21600 total combinations cases were investigated on three uncambered airfoils (NACA 0012, NACA 0015 and NACA 0018) and one cambered airfoil (NACA 4415) to construct a design guideline to determine the best parameter by varying the chord-to-diameter ratio, c/D and height-to-diameter ratio of the HDWT for three rotor swept area and six wind speeds. The main findings from Bianchini et al. showed that as wind speed increases, the best solidity reduces; however, the best height-diameter ratio and chord-diameter ratio highly depend on the rotor swept area and the type of airfoil used. Zanforlin and Deluca [24] studied the effect of diameter-based AR on the Reynold's number and tip losses of a 2-bladed HDWT ranging from micro to large power generating turbine in a 3D CFD study using URANS with SST turbulence model. Zanforlin and Deluca highlighted that bigger AR are better suited for medium to large-size HDWTs, as this increases the efficiency by limiting the tip losses compared to increasing the chord-based Reynold's number. However, for microturbines, the difference reduces greatly, resulting in Reynold's number effect being increased significantly. In conclusion, choosing the right HDWT AR is a complex process as the diameter, chord length, and

height of the HDWT also directly affect the solidity, turbine's swept area, relative blade wind speed, and Reynold's number. Careful design consideration must be done based on its application to maximize wind energy extraction for cost-effectiveness.

2.2.4 Effect of interaction between parameters

Peng et al. [74] conducted wind tunnel testing to study the parametric effects of solidity, AR, and the blade pitch angle of a VAWT with three straight-bladed NACA 0018 airfoils in various turbulent environments of intensities, I_u=0.9%, 5.1%, 10.9% and 14.6%. It was found that as solidity increases, the performance of the VAWT increases for all turbulence levels, but the range of TSR is reduced, and at higher solidity, flow penetrating the turbine is reduced. The VAWT of solidity 0.69 produced the highest C_p at I_u of 10.9%. Next, the pitch angle which produced the highest performance is β=-6.5° at I_u= 5.1% and 10.9%. Lastly, the VAWT of AR 1.3 produced the highest performance when I_u=14.6%. Peng et al. [74] then implemented the Taguchi Method to investigate the impact of various parametric effects studied, which revealed that the most influential parameter for the VAWT efficiency is pitch angle followed by solidity, AR and turbulence intensity being the least influential.

Maloouly et al. [75] conducted a 2D CFD parametric study on the effect of the airfoil profile, chord length (solidity), angle of attack and cambered blade on the transient behaviour and steady-state performance of a three-bladed HDWT. For both transient and steady-state performance, the uncambered, symmetry NACA 0017 airfoil with an angle of attack of 4° was optimal [75]. The chord length showed the most significant effect on the VAWT performance, with the optimal chord length for steady-state performance and transient performance being c=0.3m (solidity, σ=0.53) and c=0.6m (solidity, σ=1.06), respectively [75]. However, lower solidity VAWT negatively affects the VAWT start-up performance, while higher solidity VAWT degrades its steady-state performance. Maloouly et al. [75] also investigated the performance of the two optimized VAWTs under four different wind profiles. The velocity magnitude of incoming wind does not affect the VAWT transient performance, but the higher velocity wind does result in the VAWT having a higher steady-state velocity.

2.3 Performance Enhancement of VAWT using Wind Augmenter

Throughout the years, HDWT performance improvements focused on turbine parameters such as blade profile, solidity, blade chord, and many more. Continuous efforts by researchers to improve the efficiency of wind turbines contributed to studies of flow properties and hence the study and use of augmentation methods such as diffusers, guide vanes, deflector plates and many more to maximize wind turbine generated power by increasing the wind speed and guiding the wind for a better angle of attack on the turbine blades [76]. Most of the research on augmentation methods focused on high-rise building applications in urban areas to improve VAWT performance.

2.3.1 Diffusers with shroud and flange

Diffusers, also known as wind-lens, are great augmenters as they create a pressure difference between the upstream and downstream of the turbine to accelerate the wind speed from high pressure to the lower pressure segment downstream of the turbine. This pressure difference exists because of the vortex formation at the flange, which has low pressure. The fundamental concept of the diffuser is shown in Figure 2.5. The nozzle and brim are also known as the shroud and the flange, respectively. The terms shroud and flange are used throughout this study.

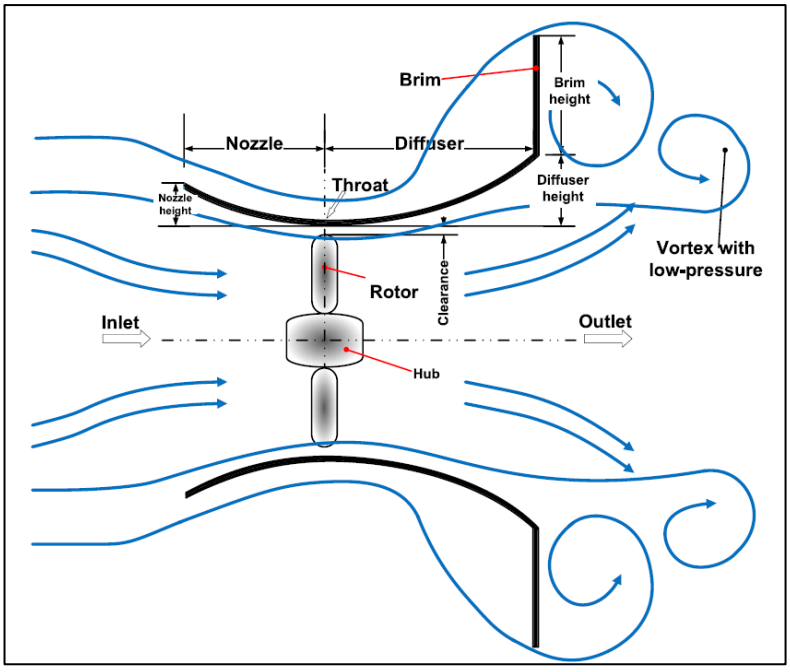

Figure 2.5. Flow around VAWT with a shrouded and flanged diffuser [77].

Ohya et al. [78] presented a new idea of a diffuser shroud with a broad ring flange exit to accelerate the approaching wind towards the turbine for increased power generation. A few design parameters of the flanged diffuser were examined. The final optimum design demonstrated a 4 to 5 times increase in output power compared to a bare HAWT. The flange helps generate a low-pressure region by vortex formation at the exit, drawing more air mass flow towards the turbine inside the diffuser [78]. Krishnan and Parachivoiu [79] used diffuser-shaped shrouds on building roofs in a simulation study to improve the performance of a Savonius turbine with cylindrical-shaped cup blades by studying the flow over the building, optimizing the turbine location on the building, varying inlet shroud angle, and some design improvements on the turbine which resulted in optimum configuration improving power coefficient by 2.5 times compared to the initial turbine. Dilimulati et al. [51] performed a CFD simulation study to optimize wind flow over a building using a diffuser shrouded with a cycloidal curved inlet geometry and flange at the outlet, guiding and accelerating the airflow to validate the advantage of using these augmenters and study the diffuser's flow interaction. The flange draws more air by creating suction and accelerates wind velocity by 1.6 times, potentially increasing wind power by up to 4 times [51].

Wang et al. [80] demonstrated that the diffuser is an excellent wind augmenter method to improve HDWT performance in a wind tunnel experiment study, as shown in Figure 2.6. The comparison of HDWT performance with and without the flat-panel diffuser showed that the diffuser managed to increase the power obtained for the HDWT by 26.3%. Moreover, the HDWT showed better self-starting ability, increasing its rotational speed by approximately 16.67% [80]. El-Zahaby et al. [81] investigated the influence of flange angles on the pressure drop and vortices created behind the flange of a flat-panel diffuser in a 2-dimensional CFD study. The result indicated that the 15° flange, as shown in Figure 2.7, can increase the mass flow rate through the diffuser and achieve maximum velocity, predicted to increase wind turbine power generated by 5% [81]. Watanabe et al. [82] optimized the flat-panel type diffuser parameters in a wind tunnel experimental study. Firstly, the larger semi-open angle (diffuser's exit angle) increases the HDWT performance, with the optimum angle found to be 20° with a recommended diffuser length of 0.5 of the HDWT diameter. Including a shrouded inlet in the diffuser design also produced some performance enhancements over a wide range of TSRs. Next, the diffuser is best located when the

throat is aligned with the centre of HDWT. This set-up of the flat-panel diffusers showed a power augmentation factor of 2.0 compared to the bare HDWT configuration. Lastly, the diffuser shape was changed to a curved type, which showed a power augmentation factor of 2.1, which was a better performance than the flat-panel type design [82].

Figure 2.6. Experiment setup of VAWT with diffusers [80].

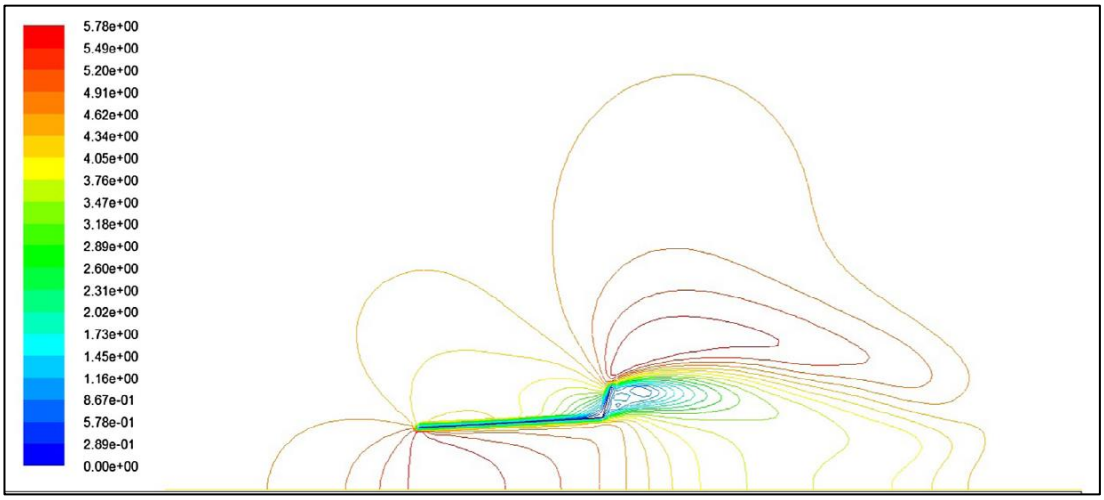

Figure 2.7. Velocity magnitude contour of the flow field around diffusers with flange angle θ = +15° [81].

Hashem and Mohamed [42], in an earlier study, concluded that the cycloidal surface diffuser performed better than the flat panel diffuser and curved surface diffuser as it

produces the best result with a power augmentation factor of 3.9 compared to a bare Darrieus turbine. Dessoky et al. [83] carried out 2D and 3D CFD simulation studies on optimizing the design parameters of the diffusers from Hashem and Mohamed's [42] study by varying diffuser lengths, diffuser angles, shroud lengths, shroud angles, and flange height to improve a 2-bladed HDWT performance. The diffuser parameters are shown in Figure 2.8. The optimization was focused on the flat-panel type diffuser. The best parameters obtained were diffuser length of 1D, diffuser angle of 29°, shroud length of 0.25D, shroud angle of 4° and flange height of 0.5D. These parameters produce the best aerodynamic performance, such as the least diffuser separation, the most positive impact from the vortical structure, which increases the axial flow velocity component, and the highest possible pressure difference from upstream to downstream of the turbine without much flow separation from the diffuser wall. These best parameters were chosen to compare the three different diffuser types [83]. The cycloidal diffuser still performs the best with all the parameter changes in terms of operating range and maximum power coefficient with up to 82% increase compared to the bare HDWT at TSR of 2.75, as the diffuser increases the torque over almost the complete revolution of the turbine compared to an open turbine [83]. Ghazalla et al. [84] conducted a similar study to optimize the flange height, shroud inlet angle, diffuser's outlet semi-open angle and location of the flat-panel type diffuser in a 2D CFD study. Ghazalla et al. [84] showed that the optimum location of the diffuser throat is ahead of the HDWT (X/D = -0.3), as shown in Figure 2.9. Increasing the size of the flange also increases the size of the vortex behind the flange, which aids in drawing more mass flow through the diffusers, thus improving the turbine's performance [84]. The best inlet and semi-open diffuser angles were found to be 0° and 8°, respectively. These angles are smaller compared to studies done by Watanabe et al. [82] and Dessoky et al. [83]. It was shown that at larger inlet and outlet angles, flow separation occurs near the diffuser wall, which causes its performance augmentation capability to be lower than the smaller angles [84].

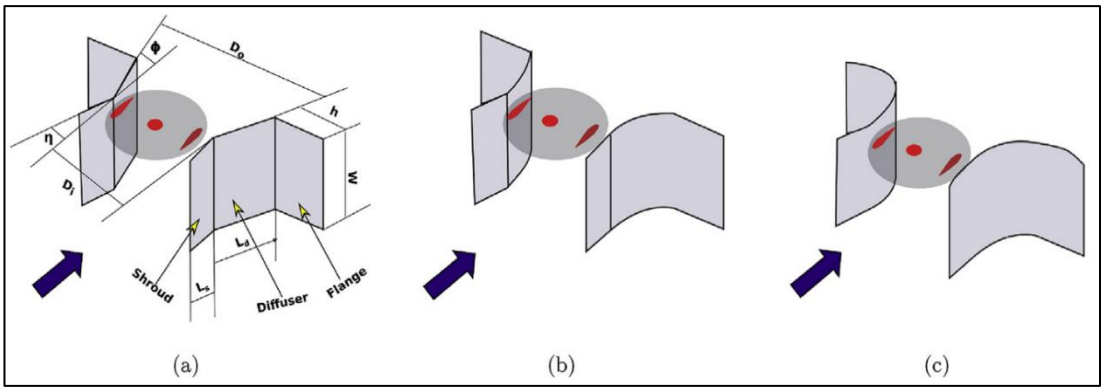

Figure 2.8. Wind lens configurations for Darrieus VAWT performance enhancement (a) Flat-panel type diffuser, (b) Curved-surface type diffuser, (c) Cycloidal-surface diffuser [42], [83].

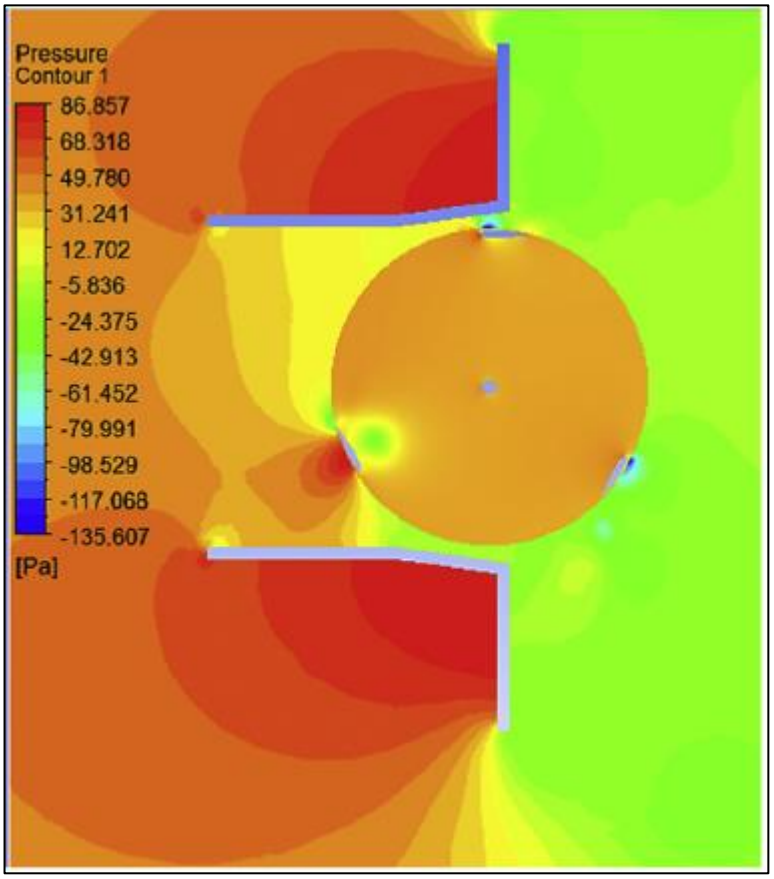

Figure 2.9. VAWT with a diffuser at location X/D= -0.3 [84].

A more comprehensive study on external diffuser systems was done by Kuang et al. [85] to explore the best fully enclosed curved inner surface diffuser parameters measurements in a 3D simulation study using Star CCM+ software. Results showed that a longer diffuser length (2 times the HDWT diameter) works best for the fully enclosed diffuser. Other diffuser parameters, such as the flange, work best with a width

of 0.5D and shroud length of 0.25D, a similar finding to the study by Dessoky et al. [83]. The best semi-open angle was found to be 20°. Next, the optimal flange angle is smaller at lower TSR, with 10° giving the best performance at TSR 1.5, while at TSR 2.5, a flange angle of 15° gave the best result. The ejector or shroud angle should be kept at 2.5° for optimum HDWT performance improvement, as larger angles would narrow the high-pressure region in front of the HDWT and deteriorate the wind acceleration through the diffuser [85].

The ability of the wind augmentation method to boost turbine performance has attracted many other studies that implement it on different turbine types, including the Archimedes wind turbine (AWT) type. AWTs are classified as a lift-drag type of turbine that has a screw design [86] or spiral design [87], with many studies available on the design of these types of turbines to improve their power performance [86]–[89]. Refaie et al. [86] studied the effect of using and optimizing wind concentrator configuration on the Archimedes Spiral wind turbine (ASWT) performance in a 3D numerical study. Refaie et al. [86] investigated a few parameters of the wind concentrator and obtained the optimum concentrator configuration at position Z= +0.1D, concentrator angle of 20°, tip clearance of 0.05D and length of 0.6D, where D is the rotor diameter which increases the maximum C_p obtained by 33.48% compared to bare ASWT. There is also another study done by Refaie et al. [87] on using a Shrouded Archimedes Spiral wind turbine (SASWT) where the optimized wind-lens duct length, diffuser length, diffuser angle and height of flange managed to improve the power performance of the SASWT by 2.1 times compared to bare ASWT.

2.3.2 Guide vanes

Guide vanes are also used as wind augmenters to guide approaching wind to an optimal angle of attack of the blade, creating higher lift force, particularly for Darrieus-type VAWT. Takao et al. [90] did a wind tunnel experiment on the geometry of a guide vane row with three arc plates by testing different setting angles and the gap between guide vanes and rotor blades on the performance of a 3-bladed HDWT. It was found that the best setting angle is between 37.5° and 45°, obtaining a 1.8 times higher maximum power coefficient than the turbine without guide vanes. However, the power coefficient is independent for different gaps and low TSRs of 1.25 and below; the performance is worse compared to without using guide vanes [90]. Since VAWT is

omnidirectional and most augmenters are limited to single-direction wind flow, many researchers worked on designs for the omnidirectional power augmentation method so that no yawing mechanism is needed. Chong et al. [91] introduced an omni-direction-guide-vane (ODGV) with four pairs of guide vanes (shown in Figure 2.10), each pair angled at $20°$ and $55°$ with an upper and lower wall duct that surrounds a 5-bladed HDWT. Results from the wind tunnel test using the Wortmann FX63-137 airfoil showed an 182% increase in turbine rotational speed, and power output at peak torque improved by 3.48 times. Simulations on a single-bladed NACA 0015 VAWT showed torque output at TSR=2.5 and TSR=5.1 increased by 58% and 39% respectively [91]. Wong et al. [52] further modified the previous design by Chong et al. [91] by using the same tilted angles pair of guide vanes but dividing each guide vane into two equal-length segments, bent at $10°$ angle in a CFD simulation study to compare the original and new design at TSR 5.1 for the wind turbine using single NACA 0015 airfoil. The C_P obtained for the new ODGV design showed 147.1% and 31.65% increases compared to the bare VAWT and original ODGV design [52]. Nobile et al. [50] examined the impact of an Augmented Wind Turbine (AWT) with an omnidirectional stator comprising eight straight vertical blades covered with two conical surfaces at the top and bottom (shown in Figure 2.11) on the performance of a 3-bladed NACA 0018 HDWT in a 2D simulation study. Three cases were studied. First, it was found that the omnidirectional stator increases the average torque and power coefficient by 30-35% at TSR 2.75 compared to the bare turbine. Second, three different pitch angles ($-30°, 0°$ and $30°$) of stator blades were examined, resulting in $0°$ orientation producing the greatest torque. Lastly, the average C_P is independent of the inlet wind speed [50]. Shahizare et al. [92] did a 3D simulation study for 52 different angles of the ODGV to optimize Chong et al. [91] design on the 5- straight bladed FX 63-137 lift type turbine at four different TSR. The simulation resulted with the ODGV angled $\beta = 20°$ and $\alpha = 55°$ performed the best with C_P increments of 40.9%, 36.5%, 35.3% and 33.2% at TSR 0.745, 1.091, 1.901 and 2.53 respectively [92]. These studies on guide vanes proved that it increases wind speed and guides it to a better angle of attack on the blades. It also reduces negative torque on the VAWT and the turbulence fluctuation, making it suitable for turbulence and weak wind flow conditions from any direction.

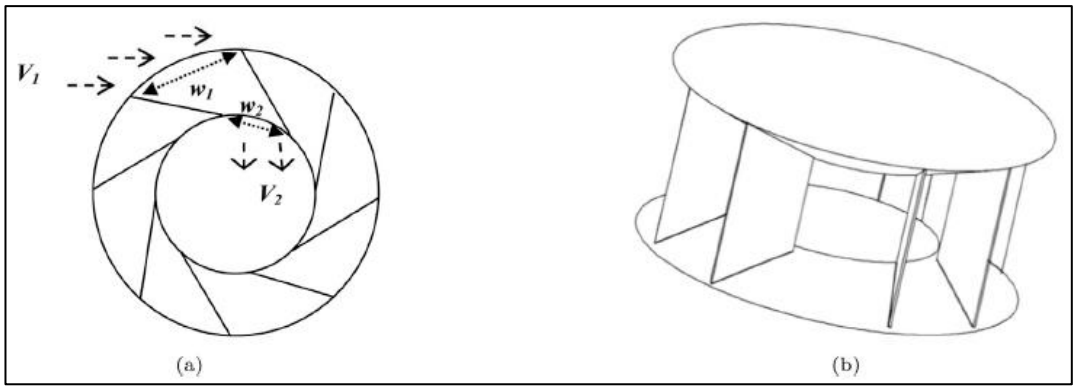

Figure 2.10. Omnidirectional guide vanes with four pairs of guide vanes [91].

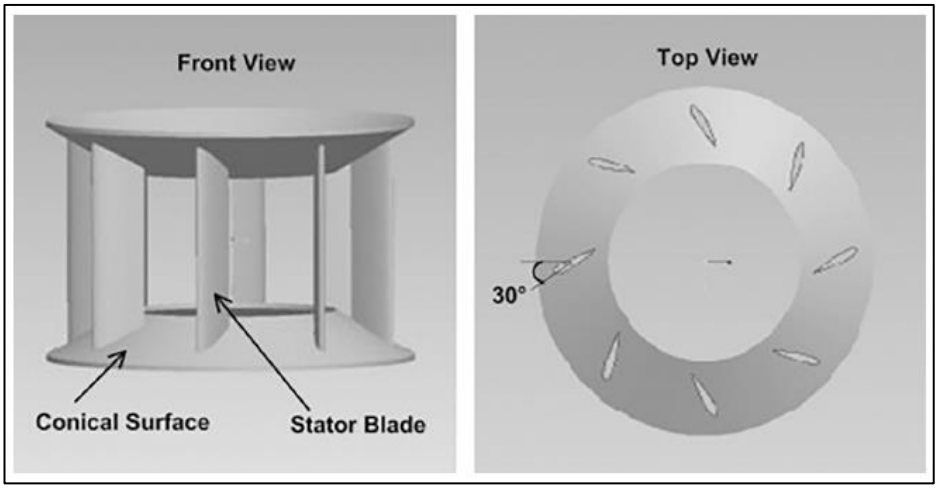

Figure 2.11. Augmented wind turbine design with omnidirectional stator [50].

2.3.3 Deflectors

Another type of augmenter is deflectors, mostly used to improve the drag type Savonius turbine by placing it upstream to shield wind flow on the returning blade and guide it to the advancing blade for higher positive torque. Plate deflectors are widely studied as they are the simplest power augmentation devices. In the early stages of this augmentation method, the straight-plate deflector was mainly focused on. Mohamed et al. [93] studied the effect of using an upstream plate deflector to shield the returning Savonius blade by first optimizing the position and angle of the deflector on a 2-bladed and 3-bladed rotor. The best configuration led to a 27% increase in power output and worked best with a 2-bladed rotor [93]. Other innovative designs like curtain plates [94], conveyor-deflector curtain systems [95], and guide plates [96] were used, which successfully improved Savonius VAWT performance compared to bare Savonius turbines. Fatahian et al. [97] used a rotating cylinder as a deflector in a 2D CFD, which

improved a Savonius VAWT power coefficient by 33% at TSR 1.3. Nimvari et al. [98] highlighted that most studies on the conventional solid deflector lack investigation on the turbulence and wake effect and proceeded with investigating the negative effect on a Savonius turbine performance to achieve a better design configuration by using a porous deflector to minimise the wake effect. Comparison of torque, power and flow structures for different deflector arrangements resulted in a maximum power increment of 10% at TSR 1, enhanced torque coefficient by two times at the start of the rotation, demonstrating self-starting ability and appropriate porosity value (of more than 0.9) caused wind flowing passed the porous zone able to breakdown the wake zone behind the deflector, showing better performance than using solid deflectors [98].

There are also performance improvements made on Darrieus VAWT using deflectors, and this was showed by Qasemi and Azadani [99] by a thorough study on flat plate diffusers with a Darrieus-type VAWT to study the effect of 5 different plate parameters, which are the horizontal distance of deflector to the turbine rotational axis, the vertical distance from the top edge of the plate to the bottom of the turbine blades, length, width, and angle of deflector respect to the axis of turbine rotation using Taguchi L_{16} orthogonal array method. Figure 2.12 shows the deflector parameter for the study by Qasemi and Azadani [99]. The turbine efficiency increased by 16.42%, and the angle of the plate diffuser was found to be the most influencing factor [99]. Wong et al. [100], [101] also demonstrated performance improvements of HDWT using flat plate deflectors by experimental and 3-dimensional CFD simulation studies. The performance of HDWT is highly dependent on the flat plat deflector positioning. The deflector X (horizontal distance) and Y (vertical distance) positioning, inclination angle and length were optimized in these studies by Wong et al. [100], [101] as shown in Figure 2.13. The optimal configuration was found to be at an upwind distance of $2R$ away from the rotor shaft, vertically $2/3H$ away from the edge of rotor blades, 0° inclination angle and with a deflector of length $1.5H$ where R is the HDWT radius and H is the blade length. Compared to the bare turbine, the maximum power coefficient increment using a deflector from the experiment was 7.4%, while the average C_p increased by 47.10% in the simulation study [100]. Placing the deflector too near to the HDWT causes the deflector's wake to reduce the HDWT performance. The proper positioning of the deflector increases the maximum Cp of the HDWT and improves the self-starting capability [101]. Chen et al. [102], [103] employed the Taguchi

method and modified additive method (MAM) to design two types of deflectors, an upper deflector and a lower deflector, to enhance the performance of a three-bladed HDWT. The factor of the distance of the deflector's top and bottom right corners from the centre of VAWT on the x-axis and y-axis was considered for each deflector case, totalling four factors, each for the upper deflector and lower deflector. The result showed that the optimum upper deflector location can increase the power coefficient of the VAWT by 20%, while the optimum lower deflector location increases the power coefficient by 17%. The most important influence on the VAWT performance was the distance between the centre of the VAWT to the bottom right corner of the upper deflector and to the top right corner of the bottom deflector.

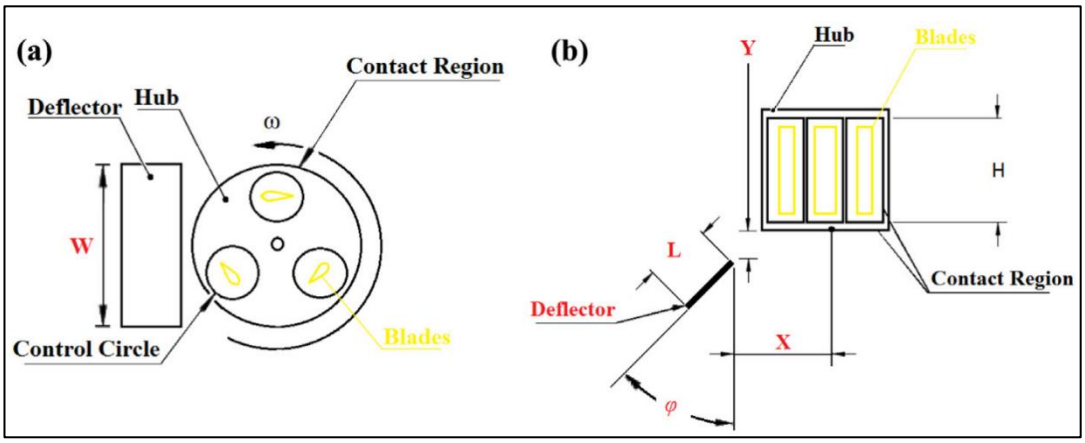

Figure 2.12. Deflector parameter specifications (a) Top view, (b) Front view [99].

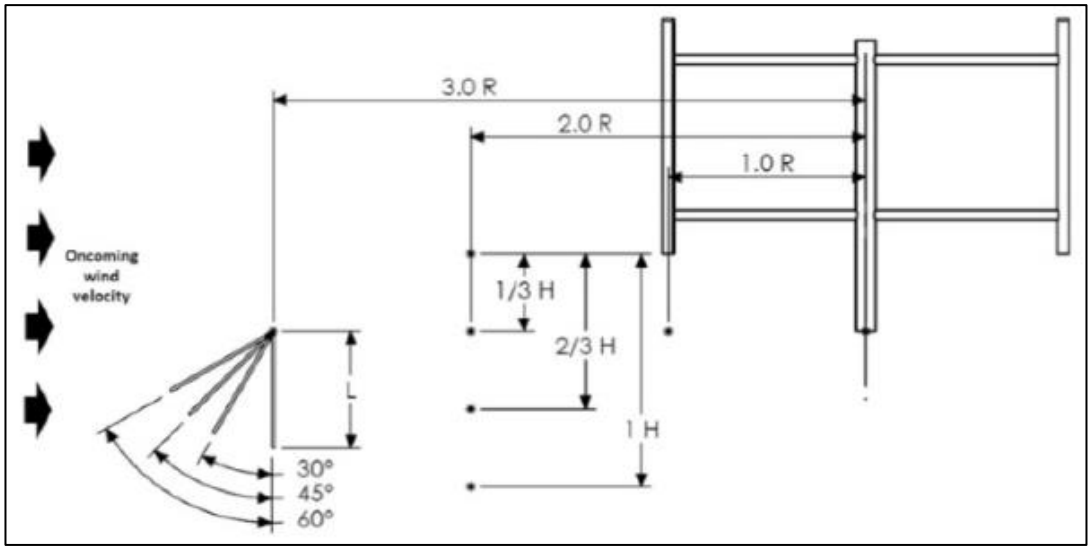

Figure 2.13. Parameter optimization of the flat plate deflector [100], [101].

2.3.4 Other designs

Other innovative wind augmenter designs have been introduced and researched to enhance the VAWT's performance. Li et al. [104] performed a study on a novel wind-gathering device (WGD) with a truncated cone shape placed at the top and bottom of the rotor to improve the performance of the HDWT. The study was designed to optimize the height, cone angle, and distance to the rotor using a quadratic orthogonal rotation combination design to predict the starting torque performance. The optimum design parameters obtained are the cone inner plate diameter equal to or a little bigger than the rotor, cone angle of 45°, cone height of less than 60% than the rotor height, and distance to the rotor should be at least two centimetres away. Wind tunnel tests and numerical simulations were carried out for static torque, rotational speed, and power characteristics performance. This optimum WGD shape showed performance improvements, with the maximum average coefficient of static torque of HDWT increased by 24.2% compared to bare HDWT [104]. Further study on the WGD with a curved outline, applying B-spline curve construction to study the parameters of upper and lower plan AR, inlet angle and outlet angle was done by Li et al. [105]. A similar design optimization method was used in the initial study [104], where the optimum parameters are a lower and upper radius ratio of 1.9, outlet angle of 4° and inlet angle of 16°. Wind tunnel and simulation on the optimized parameter showed that the maximum starting moment increased by 14.8%. The rotational speed of HDWT and self-starting ability can also be improved using this WGD, especially at low wind speeds [104], [105].

The crossflow wind turbine (CFWT), known as Banki Turbine VAWT, is suitable for low wind speed conditions [106]. Matias et al. [107] conducted a 2D CFD study to investigate the effect of using a circular arc-shaped windshield on the Banki VAWT performance for harnessing wind on highways using a car and a bus model as the passing vehicle. It was found that by varying the length of the arc windshield, the optimum case could increase the VAWT energy captured rate by 16.14% for the case of a passing car. However, in the case of a passing bus, all the arc windshield lengths tested reduced the energy captured rate of the turbine. It was suggested that this windshield device is good to use only at the roadside, adjacent to an overtaking lane where large vehicles are prohibited [107]. Heragy et al. [108] studied a wind concentrator's effect, consisting of two parallel plates with flanges added to an arc-

shaped windshield on a CFWT by wind tunnel experiments and 2D CFD simulation. The plates with flanges are based on the wind-lens concept, while the arc-shaped windshield is a deflection device. The experimental result from a study by Heragy et al. [108] shows that the wind concentrator increases the turbine's maximum power coefficient by 108%, higher than using only the arc-shaped windshield, which only improves the maximum power coefficient by 48%. The huge improvements in power coefficient from using the wind concentrator are due to the plates with flanges creating a high-pressure difference between the up and downwind regions of the turbine.

2.4 Exhaust Air Energy Recovery

As stated before, many studies have been conducted on building integrated wind recovery systems and using wind turbines on high-rise buildings. They showed potential to harness wind energy for electrical power generation, especially in urban areas with good natural winds. Wind augmentation methods were also used to enhance the recovery rate and produce higher power output. To further promote wind energy generation in urban areas, especially in places with low and unsteady wind conditions, a novel study on recovering wind energy from the exhaust air of a cooling tower was conducted by a group of researchers in a series of studies [53], [56]–[59]. These studies were done using a 5-bladed VAWT with FX63-137 airfoils placed at the outlet of a cooling tower. Investigations included measuring the effect of the VAWT on cooling tower performance, measuring VAWT performance, and using wind augmenters to improve VAWT performance. Initially, Chong et al. [53], [56] performed an experimental study by including one orientation of diffusers and straight guide vanes on a laboratory-scale cooling tower, which showed the VAWT rotational speed increased by 30.4% with the cost of 0.39% increment in cooling tower fan power consumption [53], [56]. Then, more focus was given to the straight guide vanes parameter, with 4 of them included and tested at different angles to maximize power. Each guide vane configuration gave different results, showing four guide vanes configured at ($40°, 70°, 70°$ and $40°$) gave an 8.38% increase in turbine rotational speed and decreased cooling tower power consumption by 1.98% [57]. Fazlizan et al. [58] then conducted a CFD study using the Double Multiple Stream Tube Theory to replicate non-uniform exhaust air velocity by inputting inlet velocity values obtained at various discharge outlet diameter measuring points from a lab experiment. The CFD

study was done to achieve optimum positioning of the turbine for best power extraction by investigating different locations from the cooling tower, both horizontally (different distances of turbine centre shaft to the centre of cooling tower outlet) and vertically (distance of the turbine nearest circumference to the discharge outlet of the cooling tower) [58]. It was found that the best location is horizontally further (X=250mm) from the cooling tower centre where discharge wind has higher speed and vertically higher positioned (Y=400mm), resulting in the highest reduction of fan motor power consumption, with the combination of both giving maximum C_p of 0.106, generating 1 kW power from a 7.5 kW fan motor resulting in 13% energy recovery [58]. The radius of the fan duct used in this CFD study was 365mm [58]. Tabatabaeikia et al. [59] then continued optimizing the design in a CFD study with two counter-rotating VAWTs of the same type by using three different modified plate diffusers with adjoining a semi-circular shape on the inner side of the diffuser facing the turbines to improve wind concentration. The effect of adding straight and modified separator plates was also studied and compared to the results of not using separator plates [59]. The final optimized augmented arrangement was achieved with a distance of X=250mm and Y=400m with a plate diffuser semi-circular shape angled at 30° using a modified separator. These optimized results improved the wind turbine generated power by 48.6% compared to the baseline design, obtaining a maximum C_p of 0.2210 and 0.2104 from the experiment and simulation, respectively [59]. These studies lack optimizing turbine parameters such as airfoil types, number of blades and solidity. Moreover, different augmenter types have not been examined, especially diffusers with shroud and flange incorporated. Computational studies are mostly focused on increasing the power generated by the turbine and increasing the pressure difference between the upstream and downstream of the turbine to increase its rotational speed. Flow properties on the blade, wake effect, flow separation and other flow properties have not been extensively studied to investigate why some designs do not maximize power output potential.

There are studies on other exhaust systems, such as using small-scale wind turbines (SSWTs) for electrical power generation from the high exhaust air speed of 16 m/s from bag filter ducts in a cement manufacturing plant done by Nimje and Gandhi [109]. In that study, a single hemispherical blade's distance, diameter, and depth were first optimized in a numerical study before numerically testing the 3-bladed and 6-

bladed drag-based turbine. The 6-bladed turbine showed better torque generation with a blade depth of 100mm and diameter constrained at 320mm, depending on the duct size [109]. The result was compared with the experiment study, indicating good agreement, which shows the 6-bladed set-up produced a generator power output of 35W, whereas the 3-bladed set-up only produced 12.22W [109]. Integrating more than one type of wind augmenters was studied by Park et al. [110] with the innovative designs of guide vane and diffusor integrated into a Venturi exhaust air duct cap with an on-field test done on exhaust air duct employed for high-rise residential buildings in Korea. The Venturi exhaust air duct cap was added to control the turbulent exhaust air, guide, and increase the exhaust air and external wind flow on the building. The integrated Venturi exhaust air ducts in high-rise residential buildings of 100m height generated 14.8 Wh average power over 13 days, 1.7 to 1.9 times higher than existing exhaust air duct caps and plain exhaust air duct dampers [110]. Furthermore, averaged wind flow data on 200- and 300-meter-high apartment rooftops were used to calculate the power generation capability, showing that the system power output can increase by 9.9% and 6.2%, respectively [110]. This study by Park et al. was conducted using a turbine with a combination of eggbeater Darrieus-type and Savonius-type blades. Using a better turbine shape like the H-Darrieus, which is well known for its higher rate of power generation and better optimization, would produce higher power output. Berhanu et al. [111] experimentally studied the energy recovery from a composite textile mill exhaust fan outlet using Savonius VAWT, drag force blocker and enclosure. The drag force blocker increased the exhaust wind speed by four times up to 55.5m/s, potentially increasing the overall system efficiency by 86.8%. The maximum power generated from the system was 140kW. Some numerical analysis was done on the VAWT blades for pressure distribution and maximum stress, but the power coefficient of the VAWT was not calculated.

Although very limited literature is available for wind turbine applications under unnatural wind conditions of cooling tower applications, it showed promising results in generating power in small-scale applications. Because of very limited investigations on the VAWTs for cooling tower applications with less variety of wind augmentation systems used, especially integration of more than one type of augmenters to guide the exhaust air for better performance, this area can be further explored to investigate the

feasibility of other designs of augmented flow diffuser and guide vanes for improving power generated by the VAWT in this concentrated wind flow condition.

2.5. Cooling Tower Types & Working Principles

Cooling towers are used to remove heat waste from industrial processes into the atmosphere through air through evaporative cooling [112]. This is done by channelling heated water from industrial buildings into the cooling tower using pipes. It is then cooled through heat transfer by contacting the ambient air, removing latent heat from vapour through evaporation [113]. This cools the water to a desired lower temperature, close to the wet bulb temperature. This water will then flow back into the industrial buildings to remove more heat, creating a continuous cycle. Depending on the mode of contact between the hot water and air, cooling towers can either be open-circuit (wet cooling towers) or closed-circuit (dry cooling towers) type [114]. as shown in Figure 2.14. In a wet cooling tower, water is distributed as droplets using spray nozzles to maximize contact with the fill material, where most of the heat transfer between the water and air happens through direct contact [115]. The fill material is used in wet cooling towers to increase the contact area and time between the air and the water [116]. The water does not directly contact the air in dry cooling towers. Heat transfer between air and water occurs using heat exchangers where the hot water flows in finned tubes or micro-channel coils and loses heat as air passes through them [115]. One of the advantages of wet cooling towers over dry cooling towers is that they can cool the water closer to the wet-bulb temperature instead of the dry-bulb temperature [115].

Many types of cooling towers are designed and used for different applications. These cooling towers can be differentiated into two main types: natural draft and mechanical draft cooling towers [117]. The natural draft cooling towers work by circulating air in the tower by natural convection, as it uses the difference in density between the less dense intake air and more dense heated air inside the tower [113]. The air in the natural draft cooling tower gets hotter as it comes into contact with the hot water, causing it to be denser. It will naturally rise and be replaced with the lower temperature intake air that is less dense, creating a continuous airflow cycle [118]. A natural draft cooling tower is typically large and can reach a height of up to 150 m [119].

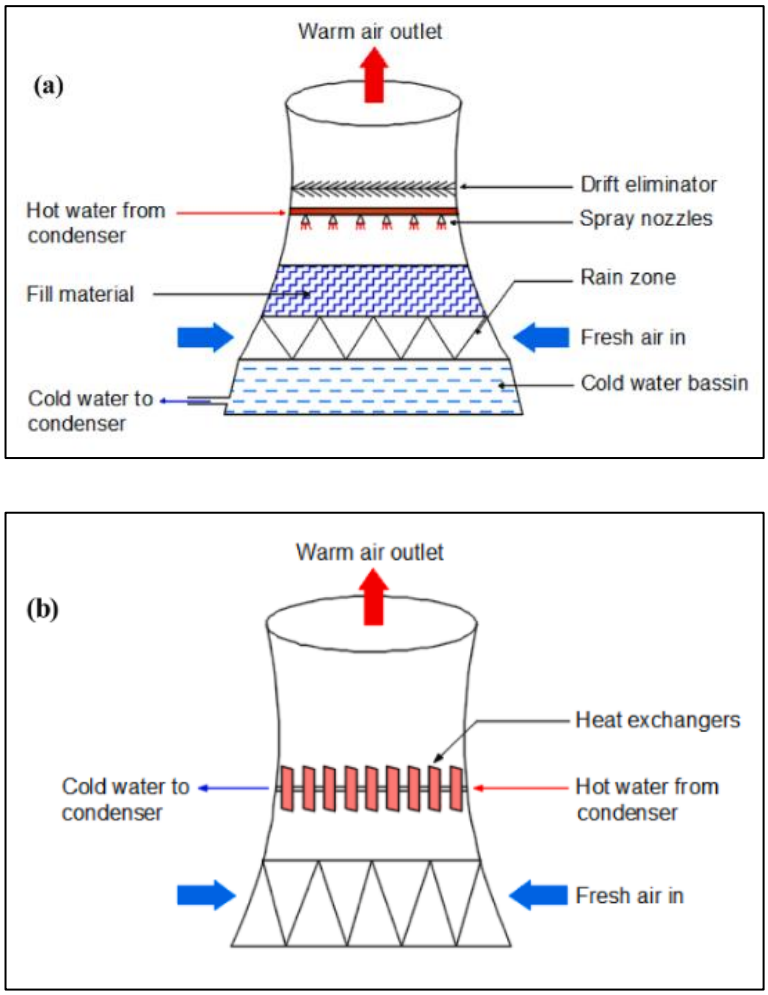

Figure 2.14. Schematic of cooling tower working principles (a) Wet cooling tower (b) Dry cooling tower [115].

Mechanical draft cooling towers, on the other hand, use mechanical devices such as propeller fans or blowers to push or draw the air out of the tower. There are two types of mechanical draft cooling towers: forced draft and induced draft [120]. In a forced draft cooling tower, the fan or blower is located near the air intake, either on the sides or at the bottom, to push air into the tower, as shown in Figure 2.15. Intake air is taken at high velocity in forced draft towers but discharged at a lower velocity. The low discharge air velocity makes the forced draft cooling tower susceptible to recirculation [121]. This tower type is costlier since it needs more power to run [119]. In an induced draft cooling tower, the fan is placed at the top of the unit, near the outlet, to pull air from inside the cooling tower to create air circulation, as shown in Figure 2.16 [122]. This induction force causes the air to exit the tower with high velocity, which helps prevent recirculation. Recirculation is a phenomenon where the discharge cooling tower air is pushed back into the cooling tower through the air inlet side due

to strong wind conditions, as shown in Figure 2.17. This is a major concern as it increases the air temperature in the tower, lowering the cooling performance and heat transfer between the water and air [119]. Mechanical cooling towers can also be classified into counterflow and crossflow based on the relative flow between the air and water in the tower [117]. In a crossflow tower, water flows vertically down the fill while the air flows across the flowing water in the fill horizontally, as shown in Figure 2.16 (a). On the contrary, water and air flow parallel to each other in counterflow cooling towers, as shown in Figure 2.16 (b). Water flows vertically downwards through the spray zone, fill zone, and rain zone, while the air flows vertically upwards from the bottom to the top of the tower to cool the water in all zones simultaneously [116]. Counterflow cooling towers are the most efficient method of evaporative heat transfer and are widely implemented to remove heat waste in industrial and thermal power plants [123].

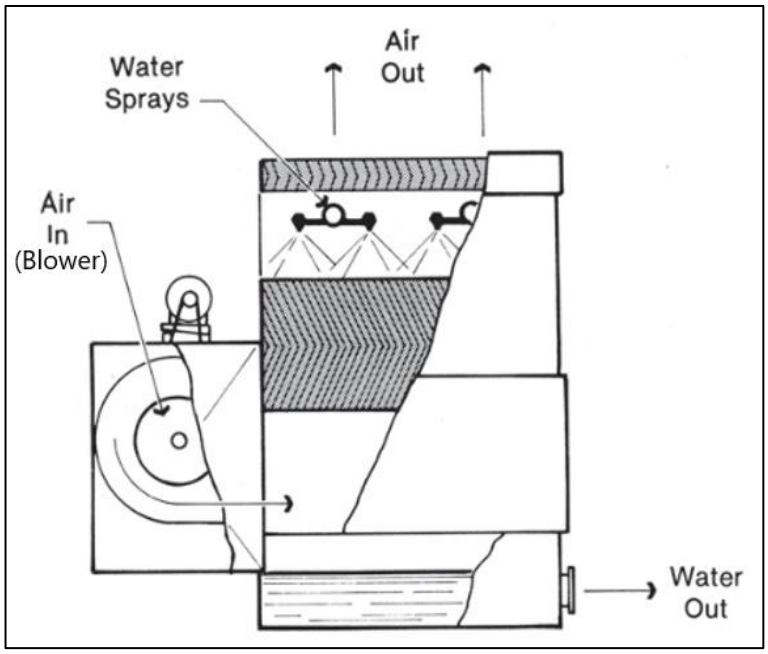

Figure 2.15. Forced cooling tower [119].

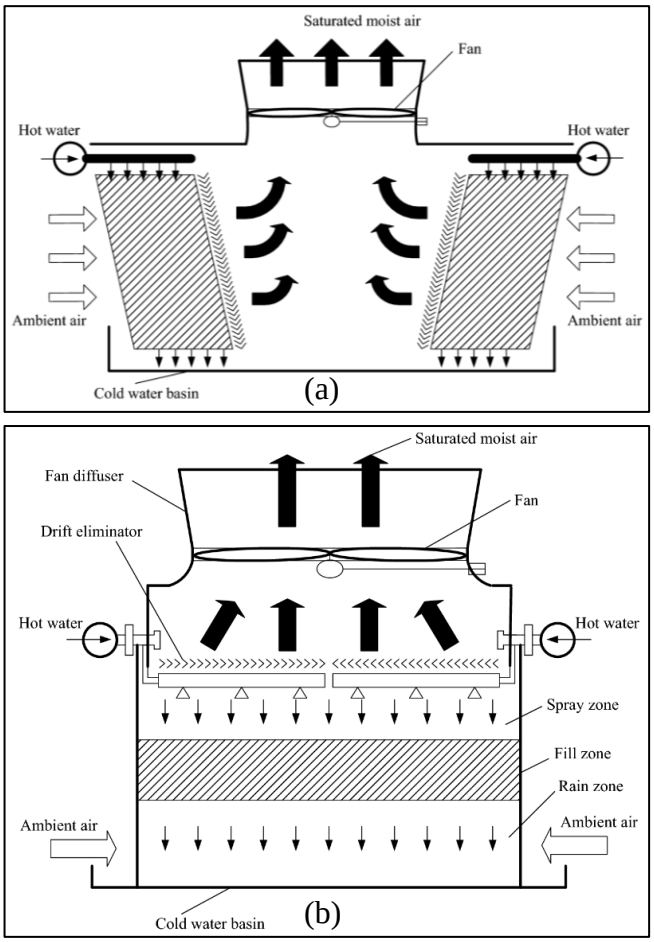

Figure 2.16. Induced wet cooling tower (a) Crossflow vs (b) Counterflow [121].

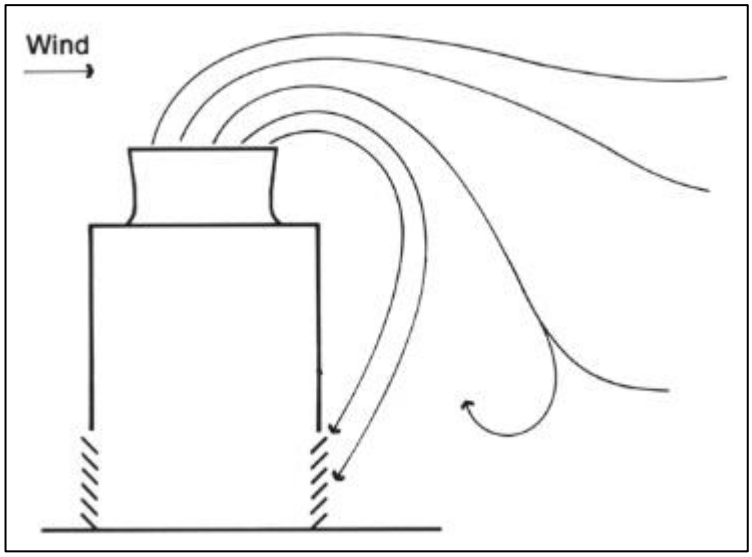

Figure 2.17. Recirculation in cooling towers [119].

2.5.1 Important cooling tower parameters and performance measure of cooling tower

Many factors can affect the operation of the cooling towers. These include the cooling tower components such as drift eliminators and fill, ambient conditions, mass flow rates of the air and water, and inlet temperature of the water, to name a few [124]. In this section, some of the most important parameters in cooling tower design, such as the wet-bulb temperature, range, approach, cooling tower efficiency and the heat load of the cooling tower is reviewed.

2.5.1.1 Wet-bulb temperature, range, and approach

The air wet-bulb temperature of a specific region is the most important parameter for selecting and designing cooling towers. Wet-bulb temperature refers to the air temperature when it is saturated with water (100% humidity), also known as a measure of relative humidity to the ambient temperature of the air. It shows how much water vapour can be stored in the atmosphere for a specific location. A low wet-bulb temperature indicates a drier surrounding air, which can hold more water vapour. In cooling tower operation terms, wet-bulb temperature is a measure of the lowest temperature obtainable by the evaporation of water under the current ambient state.

Range and approach are the other critical terms in cooling tower design and performance. The range of a cooling tower refers to the difference in temperature between the inlet and outlet water. In other words, it is the temperature drop of the hot water entering the tower. On the other hand, the approach is the difference between the outlet water and the ambient wet-bulb temperature. A small approach results in cooler water but requires higher cost and energy consumption as a larger tower is needed. Therefore, to optimize the selection of a cooling tower design, the amount of cooling required must be considered to achieve an approach that is neither too small nor too big [119]. The equation for range and approach are shown in Equations 2.11 and 2.12, respectively, where T_{wi} is the outlet temperature, T_{wo} is the inlet temperature, and T_{wb} is the air wet-bulb temperature, all in unit °C.

$$\Delta T = T_{wi} - T_{wo} \tag{2.11}$$

$$Approach = T_{wo} - T_{wb} \tag{2.12}$$

2.5.1.2 Performance measure of a cooling tower

The performance measure of a cooling tower includes the cooling effectiveness or efficiency of cooling towers, the thermal performance of a cooling tower, and the water loss of a cooling tower. Out of these three, the most important performance measure is the efficiency of the cooling tower [125]. Cooling tower efficiency (η) is the effectiveness in reducing the outlet temperature close to the air wet-bulb temperature and is expressed as shown in Equation 2.15 [114]. In practice, cooling towers normally have an efficiency of around 70% to 75%, but this may decrease due to changes in ambient air, such as higher wet-bulb temperatures in the summer compared to winter [126].

$$\eta = \frac{Range}{Range + Approach} \tag{2.13}$$

$$\eta = \frac{T_{wi} - T_{wo}}{(T_{wi} - T_{wo}) + T_{wo} - T_{wb}} \tag{2.14}$$

$$\eta = \frac{T_{wi} - T_{wo}}{T_{wi} - T_{wb}} \tag{2.15}$$

Next, the operation of a cooling tower involves removing heat waste, so the tower's efficiency in removing heat waste or thermal performance is also an important parameter. The heat load or cooling capacity of a cooling tower, Q is the amount of heat rejected by the circulating water in an hour and is given as in unit watts, W. The heat loss by the water, Q_w can be expressed as latent heat loss as shown in Equation 2.16 where $\dot{m}_w$ is the mass flow rate of water (kg/h), c_w is the specific heat capacity of water (J/ kg °C), and T_w is the temperature of water (°C). The air absorbs the heat removed from the water in the cooling tower. The heat gained by the air, Q_a can be expressed as the enthalpy gain as shown in Equation 2.17, where ma is the mass flow rate of air (kg/h), and h_a is the enthalpy of air (kJ/kg) [123].

$$dQ_w = \dot{m}_w c_{pw} dT_w \tag{2.16}$$

$$dQ_a = \dot{m}_a dh_a \tag{2.17}$$

The cooling tower does not produce or absorb any heat. It is simply a medium to cool the inlet water [123]. Therefore, the total heat in the cooling tower is balanced by the total heat coming out of it. Therefore, by accounting for the mass flow of the make-

up water supply due to evaporation loss, the energy balance of a cooling tower can be given by Equation 2.19 below [122]:

$$\Sigma Q_{in} = \Sigma Q_{out} \tag{2.18}$$

$$\dot{m}_w c_{pw} T_{wi} + \dot{m}_a h_1 + \dot{m}_{mw} h_3 = \dot{m}_w c_{pw} T_{wo} + \dot{m}_a h_2 \tag{2.19}$$

The enthalpy of the make-up water, inlet air, and outlet air is given as h_3, h_1 and h_2. The make-up water due to evaporation loss can be expressed as the difference between the vapour lost at the cooling tower outlet (ω_2) and the inlet vapour (ω_1), where ω_2 and ω_1 are the absolute humidity of the inlet and the outlet air as shown below [127]:

$$\dot{m}_{mw} = \dot{m}_a(\omega_2 - \omega_1) \tag{2.20}$$

Substituting Equation 2.20 into Equation 2.19 and rearranging the equation:

$$\dot{m}_w c_{pw} T_{wi} + \dot{m}_a h_1 + \dot{m}_a(\omega_2 - \omega_1) h_3 = \dot{m}_w c_{pw} T_{wo} + \dot{m}_a h_2 \tag{2.21}$$

$$\dot{m}_w c_{pw}(T_{wi} - T_{wo}) = \dot{m}_a[(h_2 - h_1) - (\omega_2 - \omega_1) h_3] \tag{2.22}$$

$$\dot{m}_a = \frac{\dot{m}_w c_{pw}(T_{wi} - T_{wo})}{(h_2 - h_1) - (\omega_2 - \omega_1) h_3} \tag{2.23}$$

One of the drawbacks of wet cooling towers is the water losses experienced through evaporation, drift, and blowdown losses [123]. Out of these three, evaporation loss contributes the most to water loss. Water used in cooling towers naturally contains dissolved minerals. During evaporation, the water becomes concentrated with dissolved minerals, solids, and microorganisms, leaving behind increasing amounts of calcium, chlorides, and biological contaminants, which can affect the operation of the cooling tower [115]. The concentrated water is continuously discharged from the cooling tower basin to solve this issue. This process is known as blowdown, which reduces the build-up of contaminants and ensures the efficiency and longevity of the cooling tower equipment [115]. The water lost through evaporation, drift and blowdown is continuously replaced by fresh make-up water.

2.6 Research Gap

Based on the literature discussed in Section 2.4, exhaust air recovery using VAWTs has shown the possibility of generating some power. The existing air energy extractor for cooling tower applications has been reported to have an efficiency as low as 13% using a 5-bladed HDWT with FX63-137 airfoils [58]. Even though the results indicated that the energy recovered is minimal, this application could work better with further improvements. The investigators reported that the air energy extractor's design needs to be optimized to maximize the energy extraction from the exhaust system, particularly focusing on the cooling tower applications [56], [58].

The types of turbines used in past exhaust air studies were mostly Savonius VAWT. Very few studies have used Darrieus VAWT, and parameters studies or optimization of this type of VAWT under exhaust air still need to be done. To the best of the author's knowledge, further study on the cooling tower exhaust air energy recovery system is yet to be done. Selecting HDWT with better airfoils and number of blades can significantly improve the energy recovered from exhaust air. In Section 2.2, studies on HDWT parameters showed that optimizing its design can improve the turbine's efficiency. Many optimization studies on the HDWT in free stream flow were done throughout the years. Still, less literature is found on AR compared to other parameters, such as HDWT blade design and solidity. Cooling towers come in many sizes. Thus, determining the best VAWT AR to maximize energy extraction would be crucial. As shown in Equation 2.3, the AR of a turbine is the ratio between its blade height and diameter. Since AR is a complex parameter to set for VAWT, this will be the first step in deciding the best size to harness energy from cooling tower exhaust air efficiently. Then, different solidities of the blades can also be tested using the best AR HDWT to further improve its performance.

In past studies, efforts to improve the VAWT performance for exhaust air recovery were made using the wind augmentation method and positioning the rotor for optimum power generation. Augmented flow guide vanes and diffusers have been proven to improve turbine efficiency in many applications. However, the cooling tower literature needs different types of guide vanes and diffusers, as only one type of guide vanes and straight plate diffuser has been used in past studies. Other guided augmented flows have yet to be tested for cooling tower applications, such as shrouded diffuser casing,

upstream deflector, and more diffuser designs. The cycloidal diffuser has been proven to be a great augmentation device for turbines in free stream flow conditions, as discussed in Section 2.3. From previous literature, studies on the diffuser's parameters were only done on the flat panel type design. Comparisons to curved and cycloidal diffusers were done by adopting the optimized parameter of the flat panel diffuser. For this reason, the second step of this study is focused on raising HDWT's performance under the cooling tower's accelerated flow by using cycloidal diffusers and optimizing its parameters.

Lastly, most of the past exhaust recovery studies were done experimentally, either in a lab or field test. Very few numerical studies were done on the whole system, especially on the aerodynamics flow analysis of the VAWT. By performing numerical studies, analysis of the fluid flow around the VAWT under cooling tower exhaust air can be done to understand the reason behind its low performance. Implementing the energy extraction system can be expensive, so experiments on the cooling tower are far-fetched in terms of cost and time. Planning the best possible conditions and configurations is essential to producing the best performance of the turbine, and this can be done by conducting a more feasible study in terms of cost and time. Simulation study allows more parameters to be altered and tested in a shorter time compared to experiments. Therefore, a 3D CFD study was conducted to optimize the cooling tower energy extraction system and analyse the flow physics throughout this study.

CHAPTER 3: METHODOLOGY

3.1 Overview

This study focuses on maximizing energy extraction from cooling tower exhaust air using the HDWT and wind augmenters in a three-dimensional numerical study using STAR CCM+, a CFD software. This chapter provides the research approach with detailed methodology and methods. Firstly, as this study is focused on cooling tower exhaust air energy extraction, the cooling tower model used as part of the computational domain is provided in Section 3.2. Next, the HDWT design and parameters used for this study are shown in Section 3.3, including the parameters of AR and solidity to be studied. The focus of this study is to optimize the wind augmenters' parameters to improve the performance of HDWT under the cooling tower accelerated air. The type of wind augmenters used and the strategy for the parametric study is provided in Section 3.4 before proceeding with the optimization study, which is discussed in Chapter 5. The methods and detailed steps of running the simulations, including the type of data collected and how the data were presented and analyzed, are shown in Section 3.5. Next, the flow of this numerical study, pre-processing steps and justification of techniques used are presented in detail in Section 3.6. Finally, the validation of this numerical study is provided in Section 3.7.

3.2 Cooling Tower Model for Computational Domain

This study involves modelling a cooling tower, which was used to form part of the computational domain to simulate the accelerated cooling tower exhaust air. An actual scaled-down model of a cooling tower, used in research conducted by Liu et al. [128], was adapted and used in this study. The cooling tower geometry is shown in Figure 3.1 with dimensions as stated in Table 3.1. The inlet velocity is set at the bottom of the cooling tower, which is then accelerated by the converging shape of the tower, as shown in Figure 3.2 (a). This cooling tower model was used to create a non-uniform cooling tower outlet velocity. The exhaust air has increasing velocity as it is further away from the centre of the cooling tower outlet, as shown in Figure 3.2 (b). The non-uniform increasing velocity profile from the centre of the cooling tower exhaust air was shown in experimental studies on an induced draft mechanical cooling tower to extract energy from the cooling tower exhaust air, conducted by Chong et al. [57] and Tabatabaeikia et al. [59]. The increasing exhaust air velocity was also shown by

Castiglione et al. [125] in their investigation of the part-load conditions of an induced cooling tower. The computational methodology for boundary condition and flow physics is discussed in detail in Section 3.6.1.

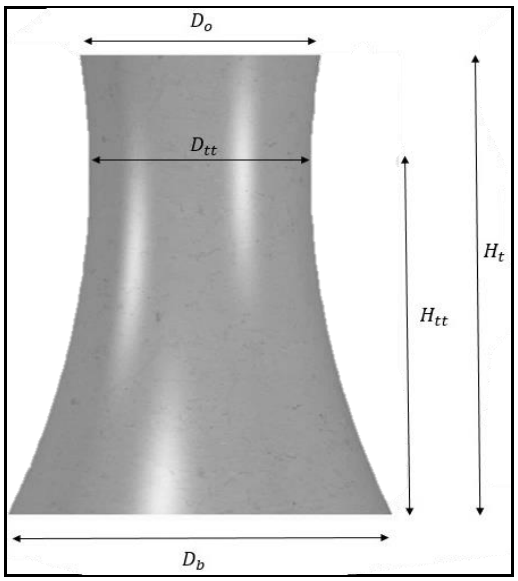

Figure 3.1. Cooling tower model.

Table 3.1. Cooling tower parameter.

Parameter	**Symbol**	**Dimension (mm)**
Total height	H_t	1175
Base diameter	D_b	910
Outlet diameter	D_o	570
Throat diameter	D_{tt}	525
Height of throat from base	H_{tt}	881

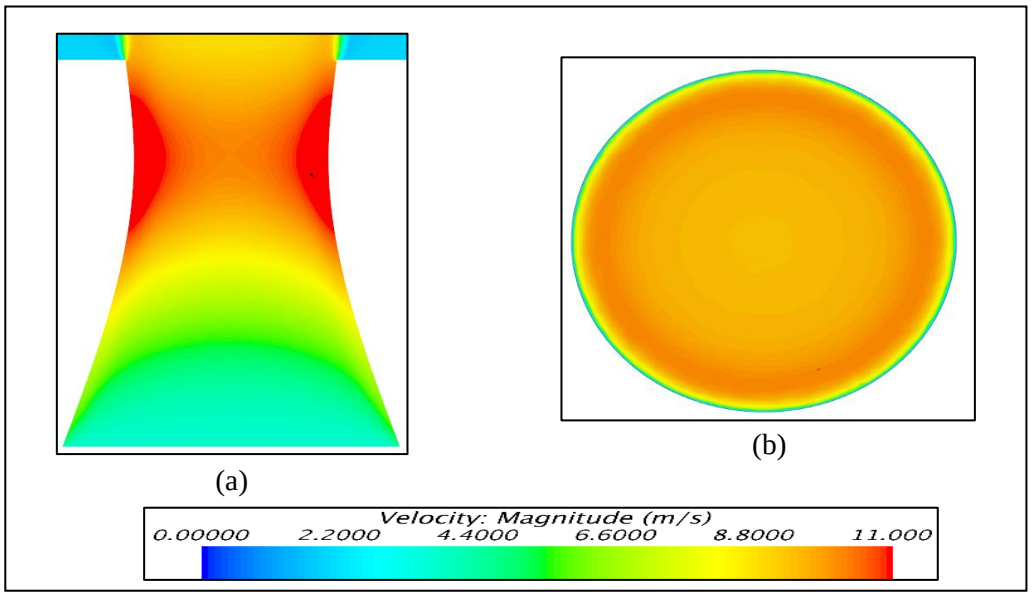

Figure 3.2. Two-dimensional velocity contour of the cooling tower flow without HDWT from (a) Side view, (b) Top view.

3.3 Design Selection and Study of HDWT under Cooling Tower Exhaust Air

The turbine chosen for this study is the HDWT with three blades using S1046 airfoils, as previous literature has demonstrated that this symmetrical airfoil produced the best C_p compared to other airfoils at a wide TSR range [42], [26]. Next, the 3-bladed HDWT produces good performance compared to a higher number of blades, and it has good start-up characteristics over 2-bladed HDWT, as shown in many studies in the past [20], [21], [37], [38]. For this study, before improving the HDWT performance using wind augmenters, the effects of the HDWT AR and solidity were studied under the accelerated flow of the cooling tower. The investigation of the HDWT AR and solidity for this study is discussed in Subsections 3.3.1 and 3.3.2, respectively. The blade length was kept constant at 200 mm throughout the study. All HDWT for this study was modelled using Solidworks, a computer-aided design (CAD) software. Figure 3.3 shows the S-1046 airfoil geometry, and Figure 3.4 shows an example of HDWT for this study. The effect of HDWT shaft and blade supporting arms is neglected throughout this study.

Table 3.2. Main HDWT parameter used for this study.

Parameter	Symbol	Value
Airfoil type	-	S-1046
Number of blades	N	3
Blade span	H	200 mm

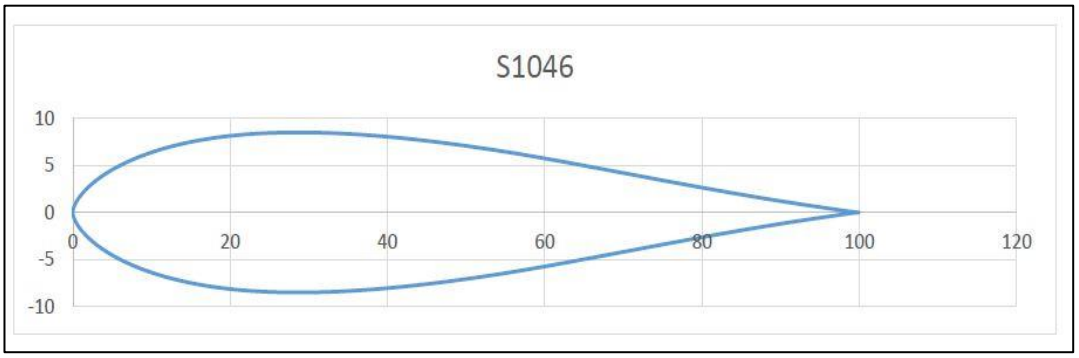

Figure 3.3. Geometry of the S-1046 airfoil.

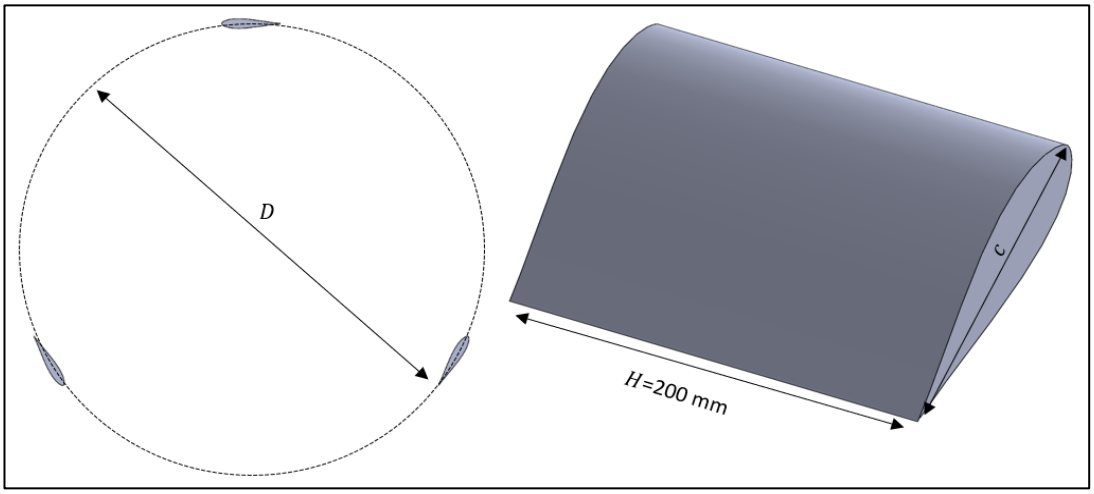

Figure 3.4. Three-bladed HDWT with S-1046 airfoil.

3.3.1 Study on the HDWT aspect ratio

This part of the study is focused on finding the best diameter-based AR of HDWT for exhaust air energy extractions. As discussed in the literature review, turbine sizing is a complex process that depends on factors like tip losses, chord-based Reynold's Number, and wind speed. As stated in Section 3.2, this study's cooling tower outlet diameter is 570 mm. Accordingly, the HDWT diameter must be within this outlet (≤ 570 mm) to maximize contact with the exhaust air for energy extractions. Previous studies have shown that increasing the AR while keeping the diameter fixed can

improve HDWT's performance as blade tip losses are limited, especially for cases using medium to large HDWT [23]. However, for micro-turbines, such is the case for this study, the influence of chord-based Reynolds' Number on HDWT performance is greater, as shown by Zanforlin and Deluca [24] in their study.

This study first investigated the performance of HDWT with different diameter-based AR under the cooling tower accelerated flow. The HDWT diameters chosen are $0.50D_o$ (285 mm), $0.65D_o$ (370.5 mm), $0.80D_o$ (456 mm), and $1D_o$ (570 mm), where D_o is the outlet diameter of the cooling tower to achieve HDWT with AR of 0.70, 0.54, 0.44 and 0.35, respectively. The HDWT was placed in the centre of the cooling tower, near the outlet. This is to ensure that the HDWT blades were fully within the boundary of the cooling tower outlet to allow the full length of blades to interact with the cooling tower exhaust air since the biggest diameter HDWT in this study has the same diameter as the cooling tower outlet. For each of the HDWT AR modelled, its chord lengths are set accordingly to ensure the solidities for each case were fixed at 0.3. The blade height, H, was kept constant throughout this study. A summary of the HDWT's parameters is listed in Table 3.3.

Table 3.3. HDWT parameters for the effect of AR study.

HDWT	Diameter, D (mm)	Chord length, c (mm)	Solidity, σ	Aspect ratio, AR	Chord-based aspect ratio, AR_c	TSR
Case 1	570	57.00	0.3	0.35	3.51	1.5, 2.0, 2.5, 3.0, 3.5
Case 2	456	45.60	0.3	0.44	4.39	
Case 3	370.5	37.05	0.3	0.54	5.40	
Case 4	285	28.50	0.3	0.70	7.02	

3.3.2 Study on the HDWT solidity

After the best AR is achieved, the best solidity for the HDWT was determined by measuring the power coefficient for the HDWT with four different solidities. The best AR obtained from Subsection 3.3.1 was 0.44, which is the 456mm diameter HDWT. Table 3.4 shows the HDWT parameters used to study the effect of different blade solidities by changing the chord length of the blades. These solidities were chosen

because, from studies available in the open literature, HDWT performance was reported to be optimal between solidities of 0.25 and 0.5 [40]. Moreover, the solidities were chosen to limit the c/D to 0.200, as anything higher than this will result in the 3-bladed HDWT solidity being higher than 0.6. Solidities higher than 0.6 are unsuitable as they make the HDWT comparable to a solid obstacle to the wind, which causes very strong interactions between the upwind and downwind blades and compromises the airfoil aerodynamics [18].

Table 3.4. HDWT parameters for the effect of solidity study.

Parameter	Symbol	Value
Number of blades	N	3
Diameter	D	456 mm
Blade span	H	200 mm
Chord length	c	34.2 mm, 45.6 mm, 57.0 mm, 68.4 mm
Solidity	σ	0.225, 0.300, 0.375, 0.450
Aspect ratio	AR	0.44
TSR		1.5, 2.0, 2.5, 3.0, 3.5

3.4 Performance Enhancement using Wind Augmenters

Once a study on the effect of the HDWT AR and solidity had been completed and the best parameters were found, the performance of the HDWT under cooling tower exhaust air was further improved by using wind augmenters. Table 3.5 shows the best HDWT parameters obtained from studies in Section 3.3 that were used for this part of the study. The wind augmentation method chosen was by adding cycloidal diffusers around the HDWT. A parametric study on the diffuser design was done using the parameters shown in Subsection 3.4.1, and the parametric study steps are discussed in Subsection 3.4.2. As discussed in the literature, diffusers with flange are great for improving HDWT's power coefficient. This parametric study was conducted to find the range of values for each factor that best enhances the HDWT performance under cooling tower exhaust air before carrying out an optimization study on the cycloidal diffuser, discussed in Chapter 5.

Table 3.5. Optimized HDWT parameters for wind augmenter study.

Parameter	Symbol	Value
Number of blades	N	3
Diameter	D	456 mm
Blade span	H	200 mm
Chord length	c	68.4 mm
Solidity	σ	0.45
Aspect ratio	AR	0.44

3.4.1 Cycloidal diffusers design and parametric study

Figure 3.5 shows the design of cycloidal diffusers with the parameters defined for this study. The cycloidal diffusers, modelled using Solidworks, were placed with the throat aligned to the centre of the HDWT rotor throughout this study, as shown in Figure 3.6. This positioning of the diffuser was chosen based on Watanabe et al. findings in their study to find the best diffuser positioning for improving HDWT performance, where the highest performance was achieved by aligning the throat of the diffuser to the centre of the HDWT. A parametric study on the cycloidal diffusers' outlet angle (diffusers' semi-open angle), inlet angle (shroud angle), back length (diffusers length), and front length (shroud length) was done with parameters shown in Table 3.6. The diffuser length, shroud lengths, and flange width were set with respect to the HDWT diameter, D. In past studies, the flat-panel type diffuser parameters were optimized [81]–[84]. Cycloidal diffusers have better performance, but optimization of their parameters has not yet been done. Moreover, there are mixed suggestions on the flat-panel diffuser's exit angle and diffuser length from works of literature. Watanabe et al. [82] suggested that the best diffuser length is $0.57D$ with a diffuser angle of 20° when the projection area of the diffusers needs to be kept small. However, Watanabe et al. only experimentally tested two diffuser's lengths, $0.57D$ and $1.14D$, with angles from 5° to 20°. Ghazalla et al. [84] suggested that 8° is the optimum diffuser angle to achieve maximum performance enhancement of the HDWT. Dessoky et al. [83], on the other hand, did a comprehensive numerical study to study the diffusers parameter influence on HDWT by testing diffusers angles of 9°, 19°, 29° and 46° at diffusers lengths of $0.5D$, $1.0D$ and $1.5D$ and found that the best diffusers parameters to be of length $1.0D$ with diffusers angle of 29°. Dessoky et al. also showed that the flow

characteristics for the same diffuser angle behave differently with different diffuser lengths, and it is the same the other way around [83]. Therefore, the first step of this parametric study was done on the cycloidal diffusers by varying the diffuser length, L_b (back length) and diffuser angle, ϕ (exit angle) at TSR 1.5. Based on the findings in past literature that have been highlighted here and in the literature review, the diffuser angles were chosen from 15° to 40°, and the diffuser lengths were chosen from $0.25D$ to $1.25D$ for the first step of this cycloidal diffuser parametric study.

Next, there are limited studies done to optimize the diffuser's shroud length in the literature. Only Dessoky et al. [83] and Kuang et al. [85] studied the influence of different shroud lengths of the flat-panel diffusers on the HDWT performance enhancement. In both these studies, it was reported that the shroud with a length of a quarter of the HDWT ($0.25D$) produced the best augmentation on the HDWT performance. To add to these studies, the second step of this parametric study was done for the shroud lengths from $0D$ to $0.48D$ at TSRs of 1.5 to 3.0. This is to investigate further the effect of not having a shroud ($0D$) up to the maximum possible shroud length for this cooling tower exhaust air energy extraction system ($0.48D$). The longest shroud length was chosen as $0.48D$ so that there is a clearance between the cycloidal diffusers and the cooling tower structure, as the HDWT was placed $0.5D$ away from the cooling tower outlet. Finally, the shroud angle (diffuser inlet) from the previous studies available in the literature showed the best angle to be between 0° and 4° for maximum performance enhancement [83]–[85]. Therefore, the final parametric study was done by choosing shroud angles from 0° to 10° to analyze how the different shroud angles behave and influence the HDWT performance under the cooling tower accelerated flow. The throat width and height of the diffusers were kept constant throughout the study. The flange width was also kept constant at $0.5D$ as this length produced a great performance, as shown in most diffuser studies [83]–[85].

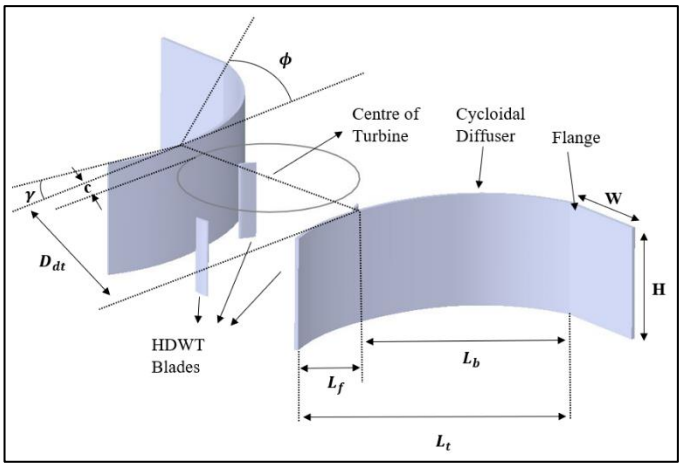

Figure 3.5. Proposed cycloidal diffuser design.

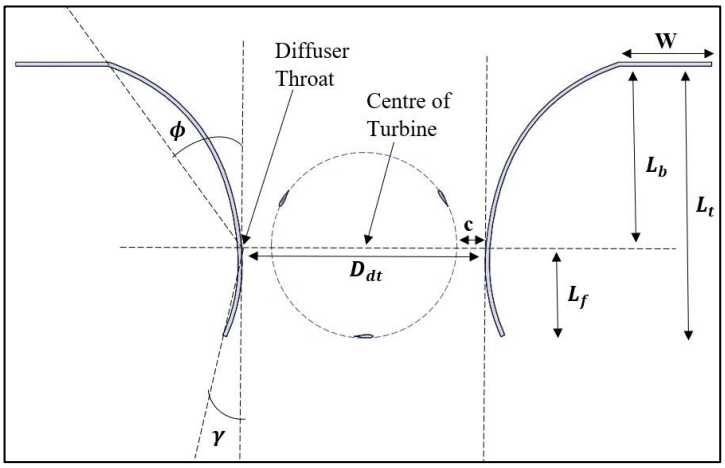

Figure 3.6. Two-dimensional view of cycloidal diffusers parameter and location.

Table 3.6. Cycloidal diffuser dimensions for parametric study.

Parameters	**Dimensions**
Shroud length (L_f)	0D, 0.25D (114 mm), 0.35D (156.6 mm), 0.48D (218 mm)
Diffuser's length (L_b)	0.25D (114 mm), 0.50D (228 mm), 0.75D (342 mm), 1.0D (456 mm), 1.25D (570 mm)
Shroud angle (γ)	0°, 2°, 4°, 7°,10°
Diffuser angle (ϕ)	15°, 20°, 30°, 35°,40°
Throat width (D_{dt})	486 mm
Clearance (c)	15 mm
Height (H_{df})	300 mm
Flange width (W)	0.5D (228 mm)

3.4.2 Steps for cycloidal diffusers parametric study

Firstly, the diffuser's length, L_b and diffuser angle, ϕ were studied at TSR 1.5. Five diffuser lengths at five different angles were tested, and the parameter that gives the best power coefficient was chosen for the next steps. Next, the shroud length, L_f was studied by testing four different lengths from TSR 1.5 to 3.0. In the final step, five shroud angles, γ were tested to improve the diffuser to achieve the highest possible power coefficient of the HDWT. All the cycloidal diffuser parametric study steps, with varying and constant parameters at each step, are shown in Table 3.7.

Table 3.7. Cycloidal diffusers parametric study steps.

Steps	Diffuser Length	Diffuser Angle	Shroud Length	Shroud Angle	TSR	Total Simulations
STEP 1	0.25 D	15, 20, 30, 35, 40	0.48 D	2	1.5	25
	0.50 D	15, 20, 30, 35, 40			1.5	
	0.75 D	15, 20, 30, 35, 40			1.5	
	1.0 D	15, 20, 30, 35, 40			1.5	
	1.25 D	15, 20, 30, 35, 40			1.5	
STEP 2	0.5 D	35	0 D 0.25 D 0.35 D 0.48 D	2	1.5, 2.0, 2.5, & 3.0	16
STEP 3	0.5 D	35	0.48 D	0 2 4 7 10	1.5, 2.0, 2.5, & 3.0	20

3.5 Analysis Methods

For the HDWT AR and solidity studies, the coefficient of moment report was generated in STAR CCM+ to measure the performance at a TSR of 1.5 to 3.5. Once the solution converges, the average coefficient of moment was obtained to calculate the coefficient of power. The moment and power coefficient graph was plotted against

the TSRs tested to evaluate the best HDWT performance. Next, the pressure and vorticity scalar contour scenes were produced and looked at to study the blade-fluid interaction at azimuthal angles of 0°, 30°, 60° and 90° for the reasoning behind the performance achieved. On top of that, the instantaneous moment coefficient plot against the azimuthal angle for the final 360° rotation of the HDWT was plotted to study the performance of HDWT by looking at which azimuthal angles the HDWT experienced low or high instantaneous moment coefficient values.

Once the best AR and solidity were achieved, a cycloidal diffuser was added to the cooling tower energy extractor system. The parameters of the cycloidal diffuser were then studied, as shown in Table 3.7 in Subsection 3.4.2. The moment coefficient of the final two rotations of the HDWT was averaged once the solution was converged. Then, the average power coefficient was calculated from the average moment. Graphs of the averaged moment and power coefficient against TSR were then plotted to compare the performance of the HDWT with every parameter of the cycloidal diffuser tested at each step. Analysis of the performance for selected diffuser parameters was done using pressure contours, streamlines, and velocity contours to discuss the reasons behind the difference in power coefficient produced by the diffuser parameters.

For the design optimization of the cycloidal diffusers, the method of the design of the experiment is described in Chapter 5. The analysis of variance (ANOVA) and response surface plots were used to analyse the results of response surface methodology (RSM), which is further discussed in Sections 5.1 and 5.2. After that, the velocity streamlines and pressure scene contour were obtained for the optimized diffuser to study the flow acceleration and blade-fluid interactions at certain azimuthal angles. The flow interaction near the diffuser walls was also looked at and discussed for flow separations.

Once the optimized design was obtained, the effect on the cooling tower was studied by obtaining the mass flow rate values at the cooling tower outlet with and without HDWT present. The effect of using different ARs, solidities, and cycloidal diffusers with different TSRs on the cooling tower flow was studied. Then, using the HDWT augmented with the optimized cycloidal diffusers, the possible energy recovery from an actual cooling tower was calculated. Lastly, the effect of the blockage on the cooling tower efficiency was also estimated.

3.5.1 Azimuthal angle discussion

This study's discussions mostly focused on the flow analysis of the HDWT blades under cooling tower exhaust air. One important parameter for HDWT discussion is the azimuth angle (θ), which is the relative angle between the HDWT's first blade or blade number 1 to the airflow direction. Since the cooling tower exhaust air is approaching the HDWT from the bottom, the azimuth angle is measured from the negative X-axis in an anti-clockwise direction, as shown in Figure 3.7. In this study, the HDWT blades at azimuth angles, θ=0° to 180°, which are facing the incoming exhaust air, resemble the upwind rotation of the blades, while the HDWT blades that are downstream to the exhaust air at θ=180° to 360° is the downwind rotation of the blades. The side of the HDWT blades approaching the wind source (on the left) is called windward, while the side of the HDWT moving away from the wind source is called leeward.

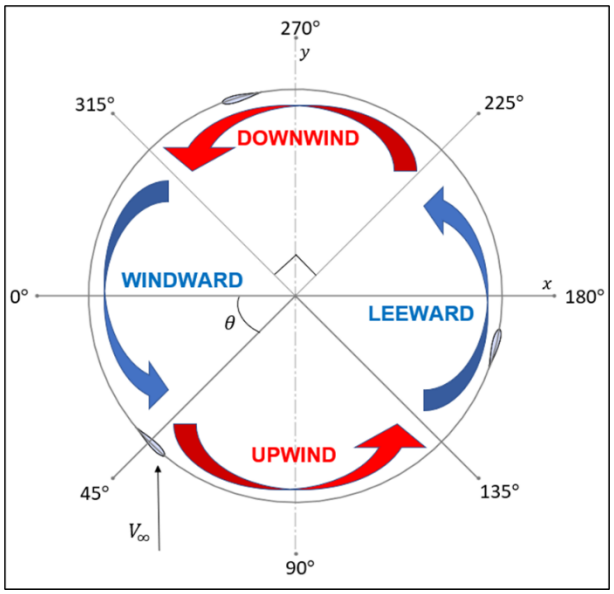

Figure 3.7. Wind turbine path relative to the direction of the wind.

3.6 Computational Methodology

CFD techniques have recently received many focuses and have been applied to study the aerodynamic behaviour of VAWTs. In the study presented in this thesis, STAR CCM+ was utilized for the 3-dimensional CFD simulation study and performance improvements of the 3-bladed HDWT under the accelerated nature of cooling tower exhaust air. Figure 3.8 shows the flow chart of the computational methodology from HDWT geometry preparation up to the discussion of results (post-processing).

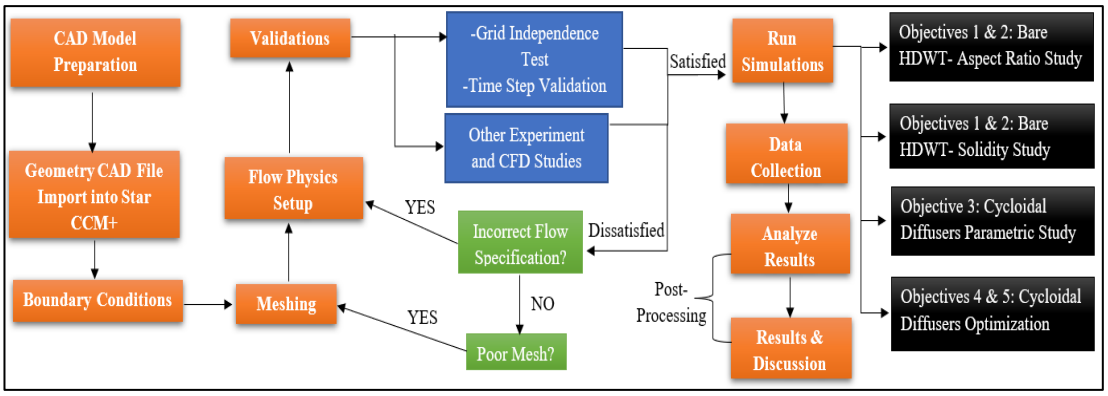

Figure 3.8. Computational methodology flow chart.

3.6.1 Boundary condition & flow physics setup

Three-dimensional Implicit URANS numerical simulations were carried out throughout this study using a CFD software called STAR CCM+ by employing the SST k-ω turbulence model. Additionally, a segregated flow solver and second-order temporal discretization were used. The semi-implicit method for the pressure-linked equations (SIMPLE) algorithm was used to realize the pressure-velocity coupling. Two regions were created for the computational domain in this study, namely a fixed region and a rotating region, which was modelled in STAR CCM+, as shown in Figure 3.9. The fixed region consists of a combined cuboidal-shaped and cooling tower-shaped domain. For this fixed region, the cooling tower dimensions were set as described in Section 3.2, whereas the cuboidal-shaped domain's length and width were set by scaling it to the cooling tower outlet diameter, D_o to be $8D_o$ and $6D_o$, respectively. This measurement of the fixed region is large enough to allow the effect of wake and avoid the blockage effect for this 3D study to achieve accurate results. Then, the HDWT, designed using Solidworks software, was imported into STAR CCM+ and aligned to the centre of the cooling tower outlet with the centre of HDWT placed $0.5D$ (D=HDWT's diameter) above the cooling tower outlet. A circular rotating region with a diameter of $1.5D$ was created around the HDWT that is large enough to minimize errors in the numerical model by maintaining the velocity and pressure continuity. An interface was created around the circular rotating region to distinguish between the two regions created, and a sliding mesh was used to rotate the circular rotating region.

The geometry of the whole domain was split into parts to create a few boundaries. Two velocity inlet boundaries were set. The first velocity inlet was set at the base of

the cooling tower with an inlet condition of 3.7 m/s. This was done to obtain an outlet velocity of 9 m/s at the cooling tower outlet, as described in Section 3.2 and Figure 3.2. The second velocity inlet was set at 2 m/s at the bottom side of the cuboidal domain, which surrounds the cooling tower outlet, to include the effect of natural atmospheric wind speed. The boundary at the top side of the cuboidal domain was set to pressure outlet with p= $0P_a$ as this is a large domain. The left and right sides of the cuboid domain were set as symmetry boundaries. The cooling tower geometry and the HDWT blades were set to no-slip wall boundaries. For objectives 3 to 5 of this study, the cycloidal diffuser geometry was imported into STAR CCM+ and positioned with the throat aligned to the centre of HDWT, as shown in Figure 3.6. The diffuser geometry was defined as no-slip wall boundaries. This study focuses on analyzing the aerodynamic performance of HDWT under accelerated wind conditions. Therefore, the effect of the exhaust air temperature was omitted since it is out of the scope of this study. The density of air, temperature, and dynamic viscosity values of the atmospheric air inlet and cooling tower inlet were set as 1.18415 kg/m^3, 27°C, and 1.85508 × 10^{-5} Pa.s, respectively, throughout this study. Other computational conditions assumptions made include turbulence intensity of 5%, turbulence viscosity of 10, and turbulent velocity scale of 1 m/s. To maintain small residuals for achieving quasi-static convergence, all of the residual convergence criterion variables were set to 1×10^{-5}, and the inner iteration of the simulation was kept at 20 [36], [85].

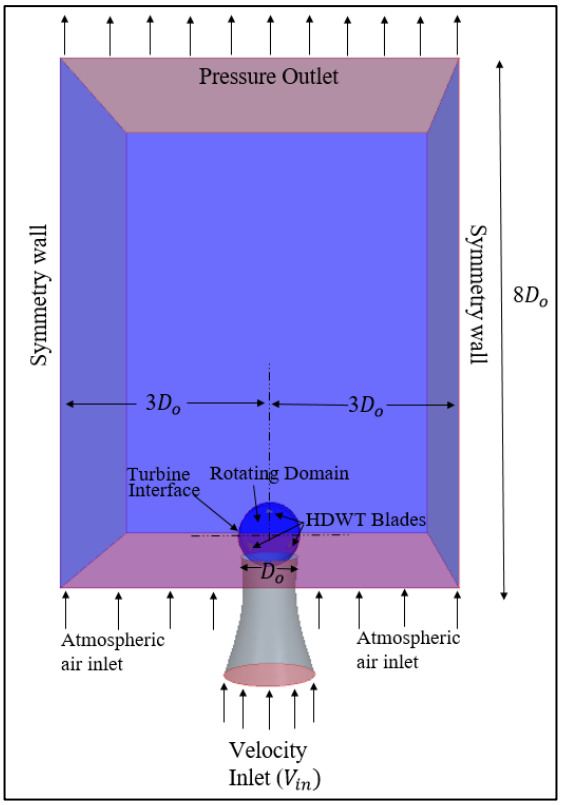

Figure 3.9. Three-dimensional view of the computational domain.

3.6.2 Governing equations and turbulence model

The turbulence model used in this study, SST k-ω is a two-equation eddy-viscosity model that provides adequate efficiency and accuracy and has been extensively used in many prior numerical studies involving VAWT [19], [37], [41], [129], [130]. This model was developed by Menter for flow with a low Reynolds number. This model assumes the flow in the entire domain to be turbulent, with the involvement of turbulent kinetic energy, k and the specific turbulent dissipation rate, ω in two transport equations. The benefit of this turbulence model over other models, such as the RANS k-epsilon (k-ϵ) or large eddy simulation equation (LES), is that it provides a good balance between the computational time and the accuracy of results. This is achieved due to the accurate formulation by blending the Wilcox k-ω at the near wall region, suitable for simulating flow in viscous sub-layer and blending of k-ϵ to predict the flow behaviour at the far field region. This element of the SST k-ω model makes it more reliable for flows with adverse pressure gradients, such as rotating flows and flow over airfoils, which is ideal for this study. Formulation of eddy viscosity is also incorporated in the SST k-ω turbulence model, which is highly preferred to simulate

separated boundary layers accurately. The mathematical formula associated with this turbulence model is presented below:

Continuity equation:

$$\frac{\partial \rho}{\partial t} + \frac{\partial (\rho U_i)}{\partial x_i} = 0 \tag{3.1}$$

Momentum equation:

$$\frac{\partial (\rho U_i)}{\partial t} + \frac{\partial (\rho U_i U_j)}{\partial x_j} = -\frac{\partial p}{\partial x_i} + \frac{\partial \left(\tau_{ij} - \rho \overline{U_\iota U_j}\right)}{\partial x} \tag{3.2}$$

Where the viscous tensor is expressed as:

$$\tau_{ij} = \mu \left(\frac{\partial U_j}{\partial x_i} + \frac{\partial U_i}{\partial x_j} - \frac{2}{3} \delta_{ij} \frac{\partial U_i}{\partial x_i} \right) \tag{3.3}$$

Transport equation for turbulent kinetic energy (k):

$$\frac{\partial (\rho k)}{\partial t} + \frac{\partial (\rho \overline{u_\iota} k)}{\partial x_i} = P_k + D_k + \frac{\partial}{\partial x_i} \left[(\mu + \sigma_k \mu_t) \frac{\partial k}{\partial x_i} \right] \tag{3.4}$$

Specific dissipation rate (ω):

$$\frac{\partial (\rho \omega)}{\partial t} + \frac{\partial (\rho \overline{u_\iota} \omega)}{\partial x_i} = P_\omega + D_\omega + \frac{\partial}{\partial x_i} \left[(\mu + \sigma_\omega \mu_t) \frac{\partial \omega}{\partial x_i} \right] \tag{3.5}$$

Where production terms are:

$$P_k = \mu_t \bar{S}^2 - \frac{2}{3} \rho k \frac{\partial (\overline{u_\iota})}{\partial x_i} - \frac{2}{3} \mu_t \left(\frac{\partial (\overline{u_\iota})}{\partial x_i} \right)^2 \tag{3.6}$$

$$P_\omega = \rho \gamma \bar{S}^2 - \frac{2}{3} \rho \gamma \omega \frac{\partial (\overline{u_\iota})}{\partial x_i} - \frac{2}{3} \rho \gamma \left(\frac{\partial (\overline{u_\iota})}{\partial x_i} \right)^2 \tag{3.7}$$

Where the term:

$$\bar{S}_{ij} = \frac{1}{2} \left(\frac{\partial \overline{u_\iota}}{\partial x_j} + \frac{\partial \overline{u_j}}{\partial x_i} \right) \tag{3.8}$$

Destruction terms:

$$D_k = -\rho \beta^* k \omega \tag{3.9}$$

$$D_\omega = -\rho \, \beta \omega^2 \tag{3.10}$$

Model coefficients are σ_k, σ_ω, β^*, and β, where μ is the dynamic viscosity of the fluid.

3.6.3 Mesh generation

An unstructured 3D polyhedral mesh was generated for this study with the fixed domain mesh set with a base size of 6cm and a minimum target size of 2.25cm. The mesh around the HDWT rotating region and the blades was refined by setting a minimum cell size of 2.2%D and 0.65%D, respectively, where D is the HDWT's diameter. Then, the resolution of mesh on the blade surface was further enhanced by employing a structured grid by using 15 prism layers with 1.2 growth rate, total thickness of 1%D, and a first-layer thickness of 3×10^{-5}m to keep the dimensionless wall distance, y+ value close to 1 as shown in Figure 3.14. These mesh settings and refinements around the rotating HDWT region and the blades were done to capture the flow around HDWT with high accuracy. The downstream region of the HDWT, which is facing towards the cuboidal domain pressure outlet boundary, was also refined to capture the wake flow by using the wake refinement function in the STAR CCM+ software by setting the isotropic size to 2cm with a growth rate of 1.2. Once all the mesh settings were defined, the mesh was generated and checked to ensure the cell concentration at the interface boundaries was uniform. Figures 3.10 and 3.11 show the mesh generated for this study. The mesh settings mentioned are chosen after conducting grid sensitivity analysis on the smallest (D=570mm) and biggest (D=285mm) AR HDWTs at TSR 2.0. The grid size sensitivity and time step size sensitivity tests are explained in Subsection 3.6.4. Once the study's objective for the HDWT AR and solidity is achieved, a cycloidal diffuser was added in the fixed region and meshed, as shown in Figures 3.12 and 3.13, to further enhance the HDWT performance under cooling tower air.

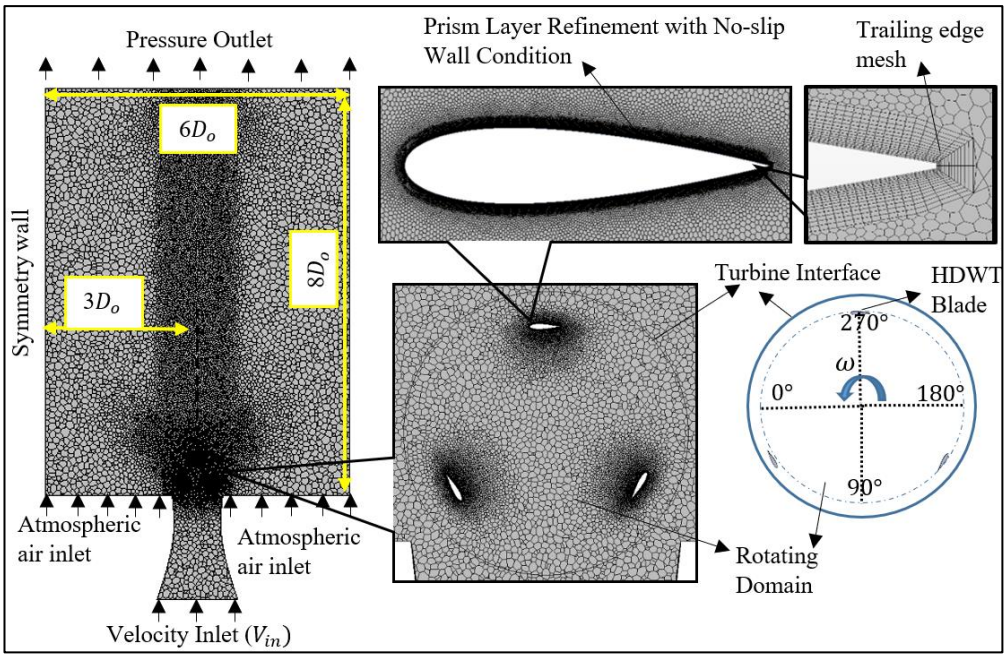

Figure 3.10. Two-dimensional view of the meshed computational domain.

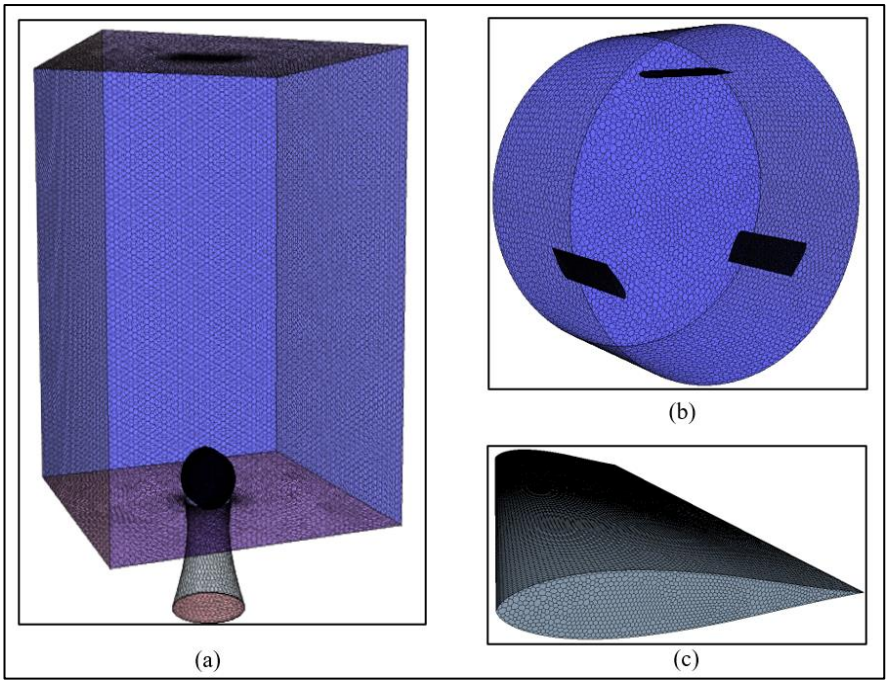

Figure 3.11. Three-dimensional mesh view for the (a) Whole computational domain, (b) HDWT rotating region, (c) HDWT blade.

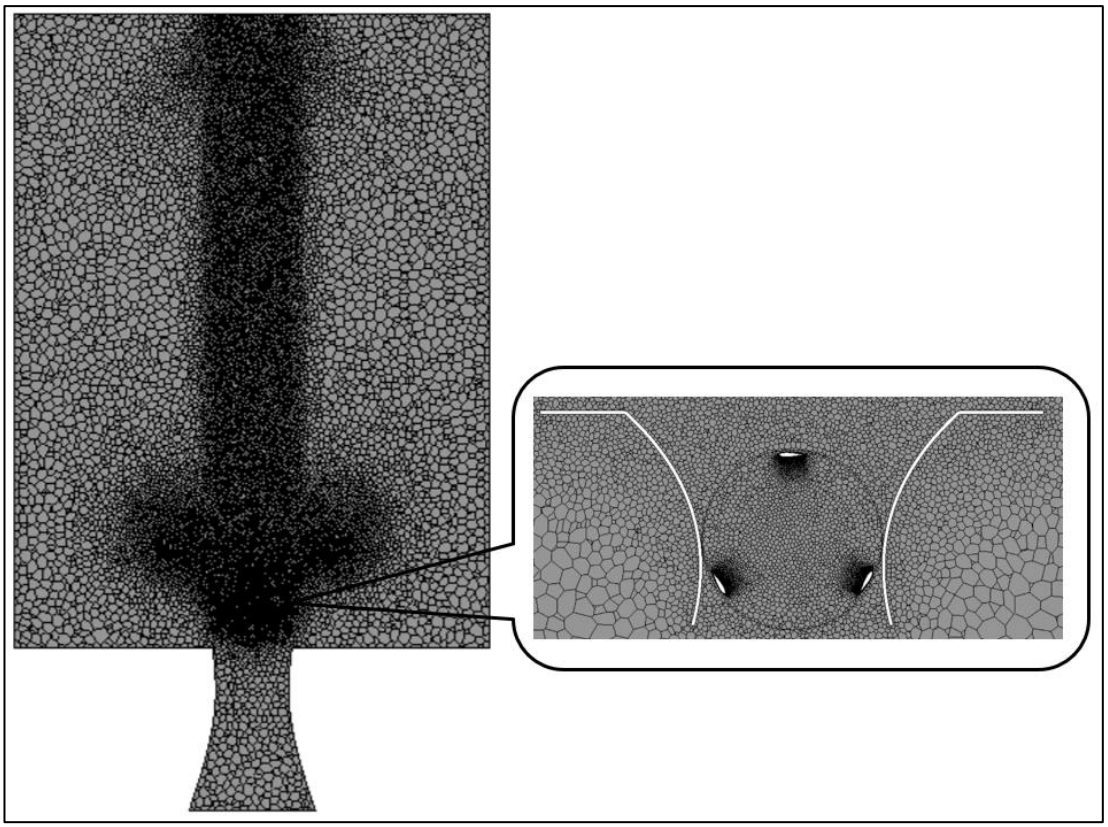

Figure 3.12. Two-dimensional view of the meshed computational domain with HDWT and cycloidal diffusers.

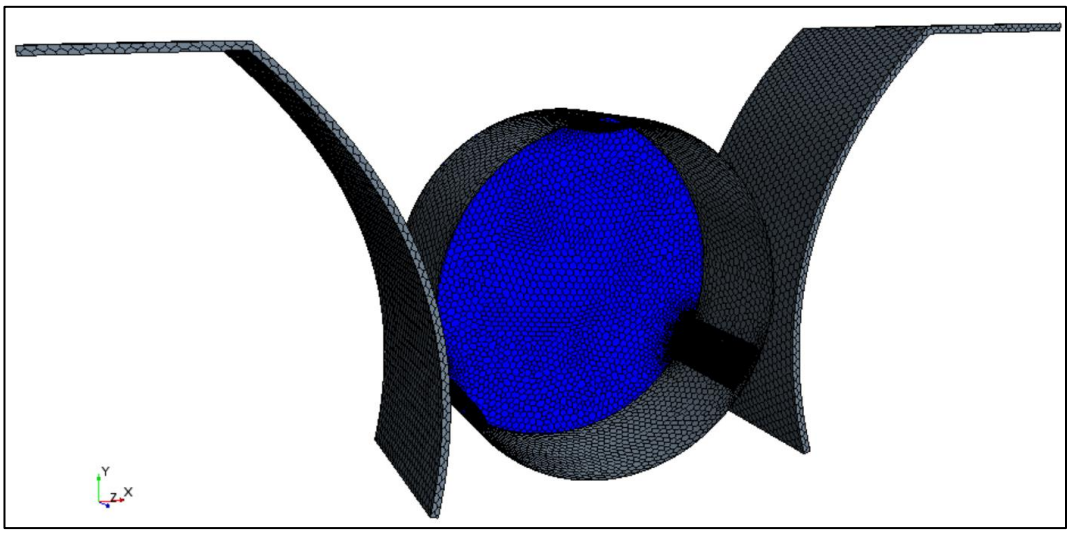

Figure 3.13. Three-dimensional view of the meshed diffusers around HDWT.

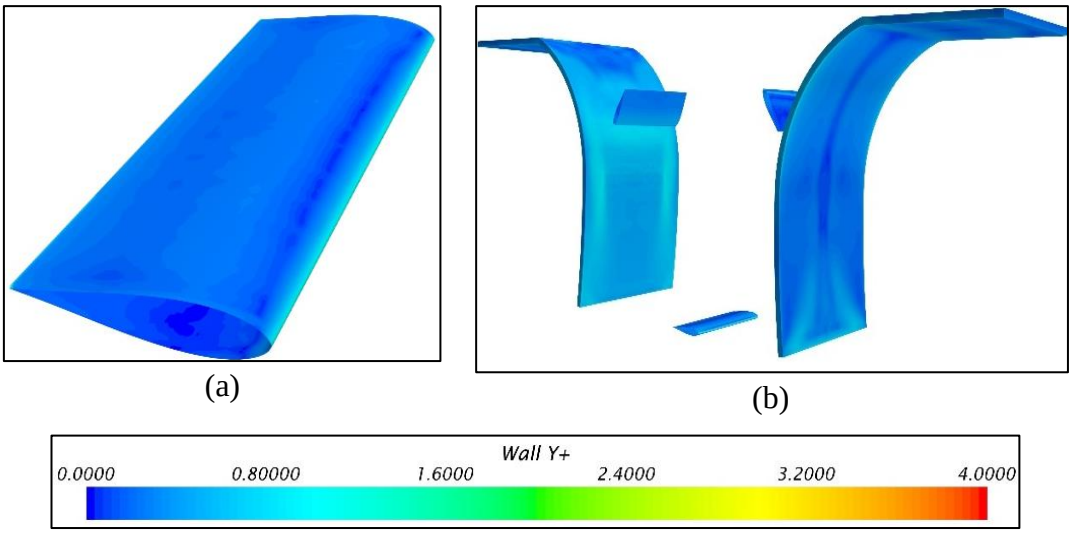

Figure 3.14. Contour of wall y+ value on the surface of (a) HDWT blade, (b) HDWT blades and cycloidal diffusers.

3.6.4 Grid sensitivity and time-step

The mesh sensitivity study for this study was done using the largest and smallest HDWT with a diameter of 570 mm and 285 mm, respectively, at a TSR of 2.0. The mesh for this study was generated as described in Subsection 3.6.3. Refinement was done around the HDWT blades and rotating region by reducing the mesh size by some percentage of the turbine's diameter. The coefficient of moment value of the HDWT at every refinement was obtained. The C_m value was calculated by averaging the value from the final two rotations (6^{th} and 7^{th} rotations) after the solution converged. The C_m was plotted for every refinement, as shown in Figures 3.15 and 3.16. The refinement results show that the same technique of setting the mesh sizes by using a percentage of the HDWT diameter for both the 570 mm and 285 mm HDWT is suitable to be used for this study as it gives less than 1% of C_m error compared to the finest grid tested for the HDWT tested. The final cell sizes are 5.6 million cells for the AR=0.35 HDWT (D=570mm), 5.1 million cells for AR=0.44 HDWT (D=456mm), 4.6 million cells for AR=0.54 HDWT (D=370.5mm), and 4.2 million cells for AR=0.70 HDWT (D=285mm).

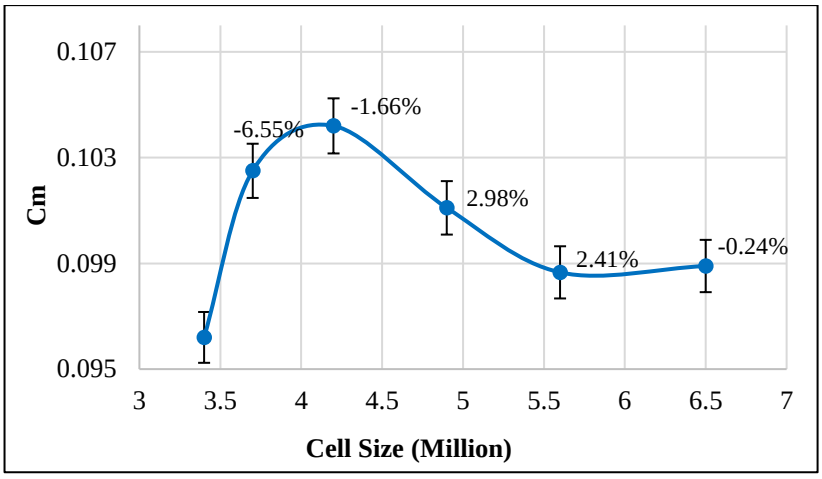

Figure 3.15. Grid independence study for AR 0.35 HDWT (D=570mm).

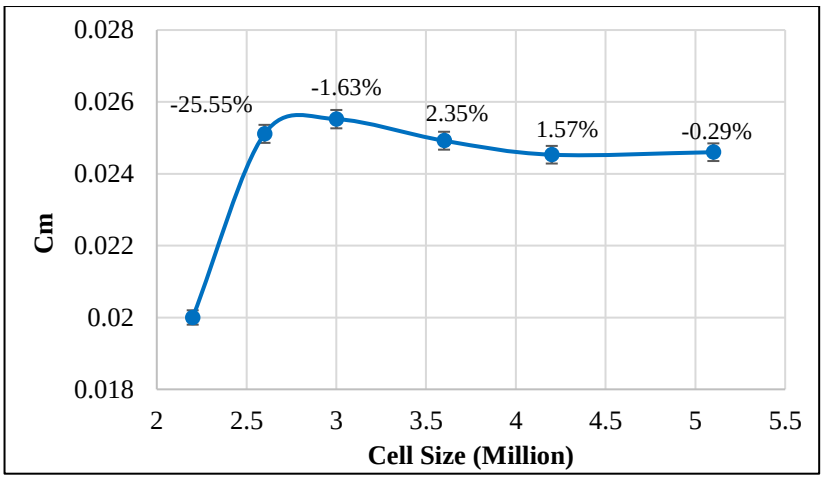

Figure 3.16. Grid independence study for AR 0.70 HDWT (D=285mm).

Next, the time step size test was conducted using the HDWT with a diameter of 570mm at TSR 1.5. Four values of time steps were set which are 3.68×10^{-4}, 9.21×10^{-4}, 1.84×10^{-3}, and 3.68×10^{-3} to rotate the HDWT by 1°, 2.5°, 5°, and 10° degrees, respectively. The instantaneous C_m value produced by a single blade over one converged rotation (360°) was compared, as shown in Figure 3.17. As seen in this figure, overprediction of the blade instantaneous C_m occurs at the upwind region of the HDWT in addition to the shifting of the peak blade C_m towards a higher azimuthal angle when bigger time steps are used. This result indicates that the smaller time step produces a more accurate result. As this is a 3D simulation study with a total of 40 simulations done to achieve the first two objectives with a further 91 simulations for cycloidal diffusers parametric and optimization study, the final time step chosen was $d\theta = 2.5°$ to balance computational time as it reaches quasi-static convergence after 72 hours (3 days), whereas the 1° time step converges after 180 hours, which is an

expensive computational time. Moreover, past studies on 3D VAWT CFD studies have shown that 2° and 2.5° are suitable for providing accurate results and balancing computational time for wind turbine studies [37], [85], [129].

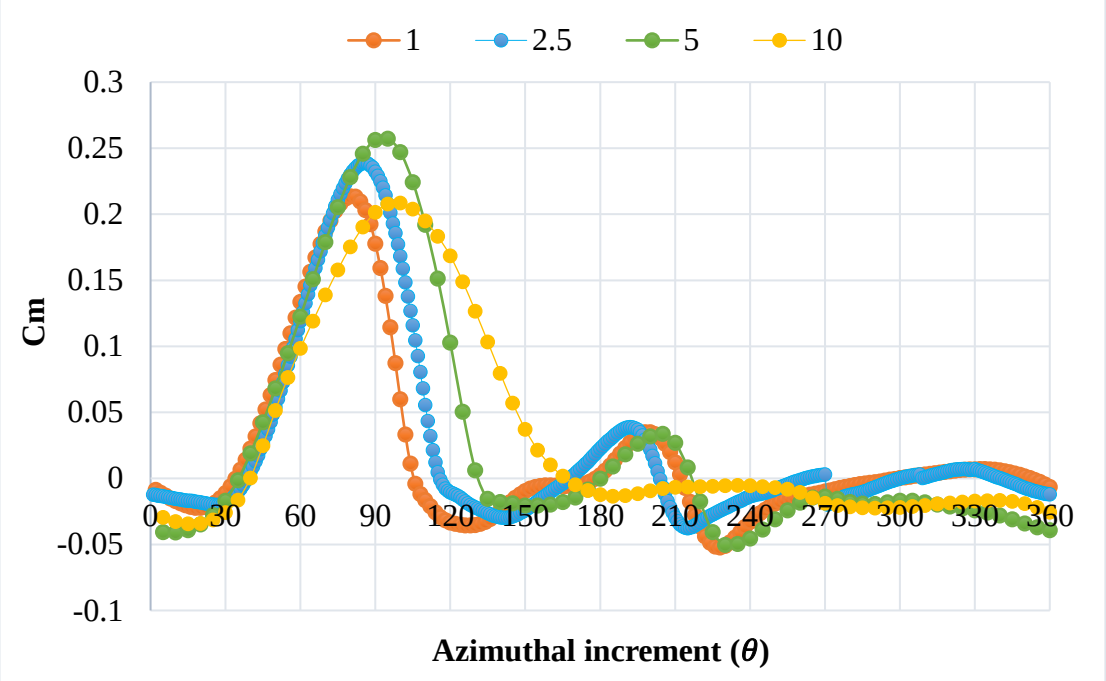

Figure 3.17. Time step size test.

3.7 Model Validation

To confirm the suitability of the CFD setup in this study, which includes the computational domain, generated mesh, and physics conditions, a validation study was done by using the HDWT with parameters shown in Table 3.8 and comparing the results to the previous experimental study conducted by Castelli et al. [131] and a 2D numerical study conducted by Rezaeiha et al. [132]. This validation was carried out using the same physics and mesh conditions described in Section 3.6. However, the computational domain shape was changed by removing the cooling tower-shaped part and extending the inlet side of the cuboidal domain so that it is $5D$ away from the centre of the HDWT, as shown in Figure 3.18. This was done to obtain the conventional rectangular shape domain with one constant velocity inlet boundary, as used in the validation reference cases. The measurements of the other sides of the cuboidal domain were also changed to scale with the HDWT's diameter used for this validation. Figure 3.19 shows the comparison of the HDWT coefficient of power from TSR of 1.44 to 3.31 between the present study and the reference cases. The result from

Rezaeiha et al. [132] overpredicts the experimental result of Castelli et al. [131] at higher TSRs as it is a 2D CFD study that does not consider the effects of blade tip losses in calculating the turbine performance. The present study uses 3D CFD and employs the k-ω turbulence model, showing a close pattern in the results compared to the experimental results of Castelli et al. [131]. The present study case shows similar characteristics with both the reference cases in terms of the HDWT performance as it shows an increase in C_p as TSR increases, reaching a maximum C_p at TSR of 2.63. Moreover, the C_p curve of the current study is close to the experimental data of [131] for all the TSRs tested. The difference in the coefficient of power values between the present validation case and the experiment case by Castelli et al. is below 10% at moderate TSR range and just slightly above 10% at high TSRs. Overall, the present 3D CFD results are in good agreement with the experimental reference case and the computational setup mentioned earlier is applicable to conduct this study.

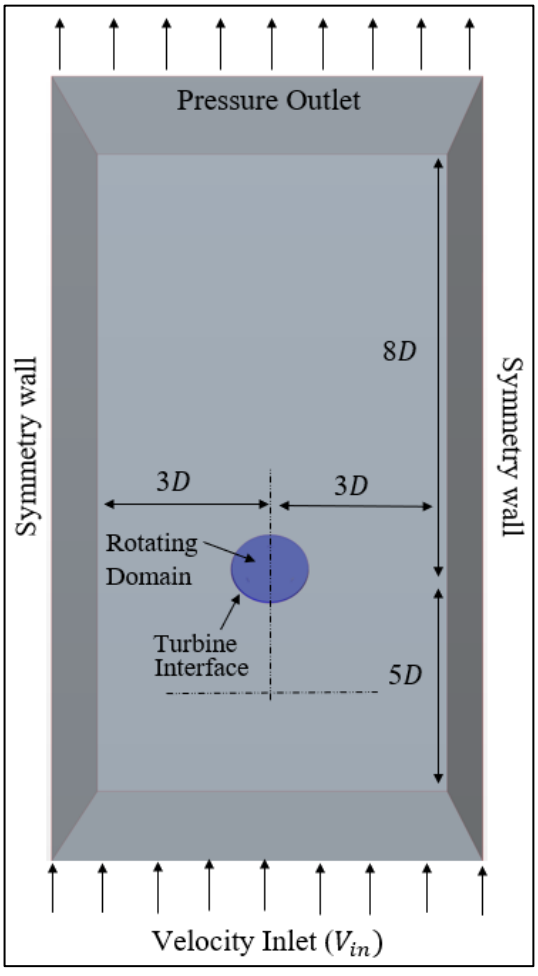

Figure 3.18. The boundary condition for the validation study.

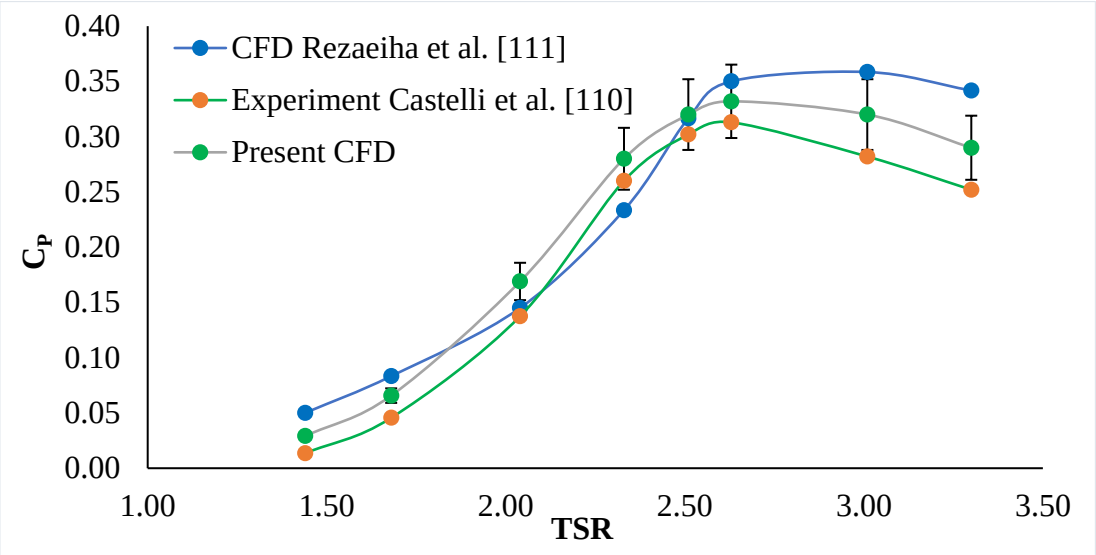

Figure 3.19. Validation of the current model against other studies.

Table 3.8. Validation reference parameters.

Parameter	**Value**
Airfoil profile	NACA 0021
Diameter, D (m)	1.030
Height, H (m)	1.456
Swept area, A (m^2)	1.236
Chord length, c (m)	0.0858
Solidity, σ	0.25
Freestream velocity, U_∞ (m/s)	9
Tip speed ratio (TSR)	1.44 to 3.31

CHAPTER 4: RESULTS & DISCUSSION

4.1 Effect of Aspect Ratio on HDWT Performance

After validating the computational model designed for this study, numerical simulations for four *AR*s using the three-bladed HDWT with S-1046 airfoils, as presented in Table 3.3 in Subsection 3.2.1, were conducted. In this section, the moment and power coefficient values of the HDWT are reported at a TSR range of 1.5 to 3.5. In Subsections 4.1.1, 4.1.2 and 4.1.3, the flow field visualization around the HDWT is presented to understand the aerodynamics of the different *AR*s of HDWT and TSR under the accelerated flow of cooling tower exhaust air.

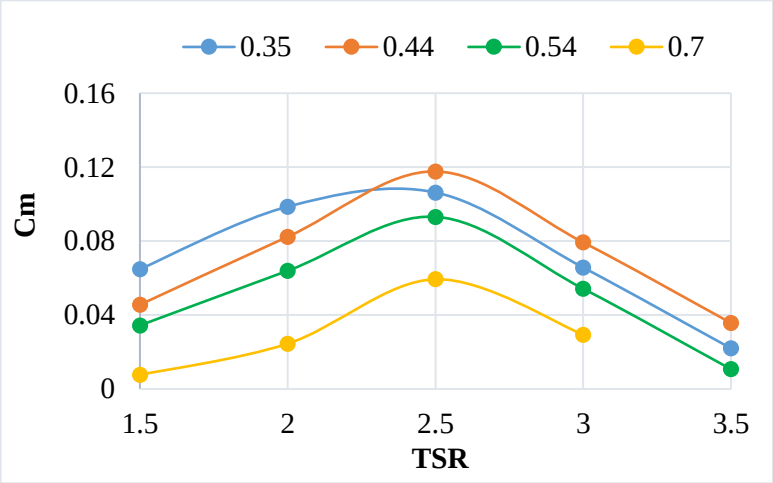

Figure 4.1. Effect of *AR* on HDWT moment coefficient under accelerated cooling tower exhaust air.

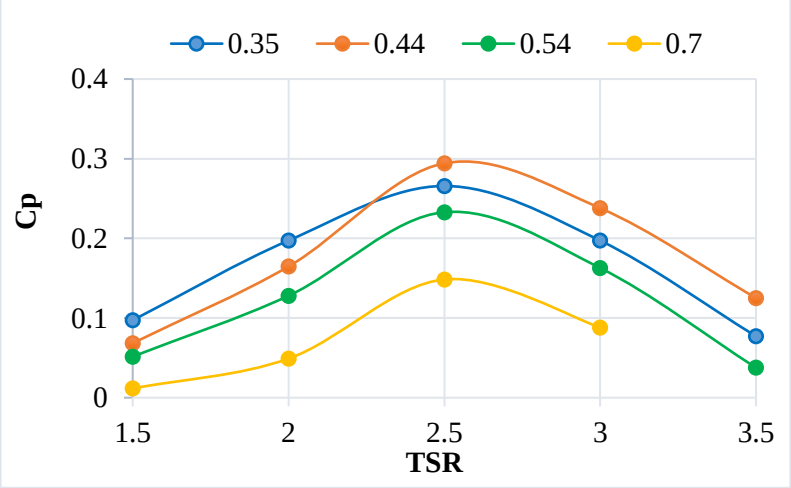

Figure 4.2. Effect of *AR* on HDWT power coefficient under accelerated cooling tower exhaust air.

In Figures 4.1 and 4.2, the moment coefficient and power coefficient plot for all four ARs of HDWT tested in accelerated flow conditions of the cooling tower are presented. Based on this data, case 2 HDWT, with an AR of 0.44, exhibited an outstanding performance at a TSR of 2.5, producing a C_m of 0.118 and a C_p of 0.294. Under the low TSR conditions of 1.5 and 2.0, the case 1 HDWT with the smallest AR of 0.35 demonstrated an enhanced performance compared to other HDWTs, while the case 2 HDWT presented the best performance at TSRs ranging from 2.5 to 3.5. Case 2 HDWT possesses a higher maximum C_p of 10.7% and 98.2% compared to case 1 and case 4 HDWTs at TSR of 2.5. The bigger AR HDWTs, which are the case 3 and case 4 HDWTs, exhibited unsatisfactory performance for all the TSR ranges, as shown in Figure 4.2. It is to be noted that each of the HDWT ARs reached peak C_p performance at a TSR of 2.5. Collectively, the HDWT ARs of the four cases presented similar patterns of increasing C_p values as TSR increases and achieves maximum C_p at TSR of 2.5 before decreasing at higher TSRs. These findings are similar to a study by Li et al. [23] in which it was shown that at fixed solidity, VAWT with different ARs achieved peak performances around the same TSR. To improve the comprehension of HDWTs' ARs under varying TSRs, instantaneous C_m values of the final rotation of the quasi-static HDWTs were extracted to produce a radar plot for a full 360° HDWT rotation as presented in Figures 4.3, 4.5, and 4.7 at 1.5, 2.5, and 3.5 TSRs, respectively. Figures 4.4, 4.6, and 4.8 show the instantaneous Cm against the single blade azimuthal angle, θ, at TSR 1.5, 2.5, and 3.5, respectively.

Based on the radar plots shown, the maximum instantaneous C_m performance of the HDWTs at TSR 1.5 for all the AR cases was obtained at 65° to 75°. Meanwhile, the HDWTs at TSRs of 2.5 and 3.5 reached the maximum instantaneous C_m at a higher θ of 90° and 100°, respectively. Case 2 HDWT showed the highest peak instantaneous C_m for all three TSRs shown. However, case 1 HDWT gives the best overall performance at TSR 1.5 as it contributes higher and more positive moments throughout the complete 360° rotation, especially from 0° to 15°, 90° to 120°, 210° to 240° and 330° to 360° where its instantaneous moment is significantly higher than the other HDWT as shown in Figure 4.3. Moreover, case 2 HDWT suffers from high negative instantaneous C_m from 0° to 20°, 100° to 140°, 225° to 260° and 345° to 360° which causes its overall performance to be lower than case 1 HDWT. As shown in Figures

4.5 and 4.7, case 2 HDWT at TSRs of 2.5 and 3.5 obtained the highest C_m and C_p as it achieved the highest instantaneous C_m for nearly all of the azimuthal angles. The plot of instantaneous C_m of a single blade in Figures 4.6 and 4.8 shows that the blade experiences continuous positive moment from 40° to 155° with the highest Cm values produced at the upwind side when the HDWT is facing the accelerated wind direction of the cooling tower exhaust.

The instantaneous C_m radar plot and single blade plot also show that the bigger AR HDWT (cases 3 and 4) produced lower C_m value compared to the smaller AR HDWT for almost the full rotation of the turbine, mainly at higher TSRs. The HDWT blades for this section of the study were designed to have constant solidity; hence, the bigger the AR of the HDWT, the shorter the length of the blade chord, as reflected in Equation 2.2. Consequently, shorter chord lengths and smaller diameters of HDWTs result in lower chord-based Reynolds' Numbers, as presented in Equations 2.6 and 2.7 of Subsection 2.1.3. This causes the lift coefficient to be reduced while increasing the drag coefficient, as reported by Zanforlin and Deluca [24]. Moreover, Zanforlin and Deluca [24] reported that for small VAWTs, the effect of Reynold's Number of blades on the turbine performance is stronger than that of tip losses. In the next few sections, flow analysis around the HDWT is also done to study the aerodynamic behaviour, which led to the results obtained. Since a similar pattern of the result was shown for all TSRs, in Subsection 4.1.1, the comparison between the smallest AR HDWT, case 1 and biggest AR HDWT, case 4 is done at TSR of 2.5 to analyse the effect of AR on the aerodynamic behaviour of HDWT under accelerated flow. In Subsection 4.1.2, the effect of TSR on HDWT is shown by analysing the flow field around the best AR HDWT, which is the case 2 HDWT at low TSR of 1.5, optimum TSR of 2.5 and high TSR of 3.5. Lastly, a comparison between case 1 and case 2 HDWT is made in Subsection 4.1.3 to discuss the reason behind the performance at TSR 1.5 and 2.5.

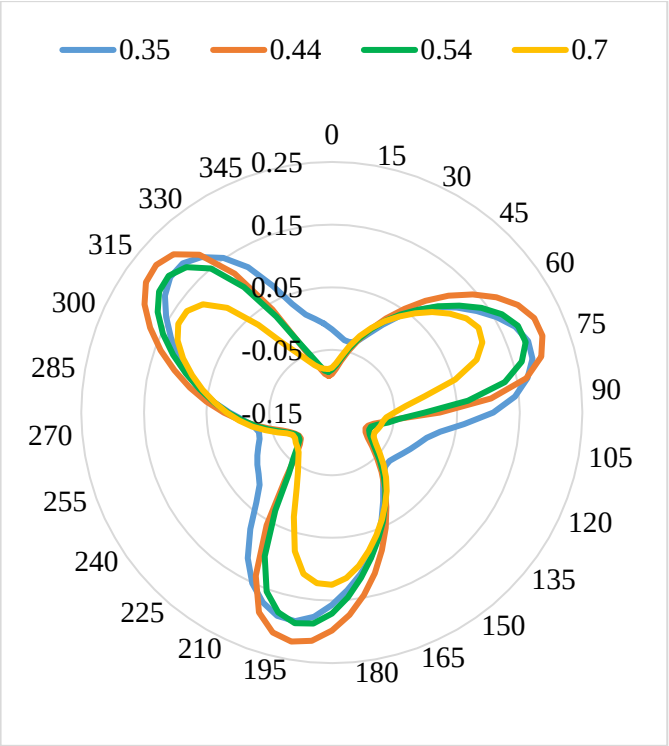

Figure 4.3. Instantaneous C_m against azimuthal angles of HDWT with ARs of 0.35, 0.44, 0.54 and 0.70 at TSR 1.5.

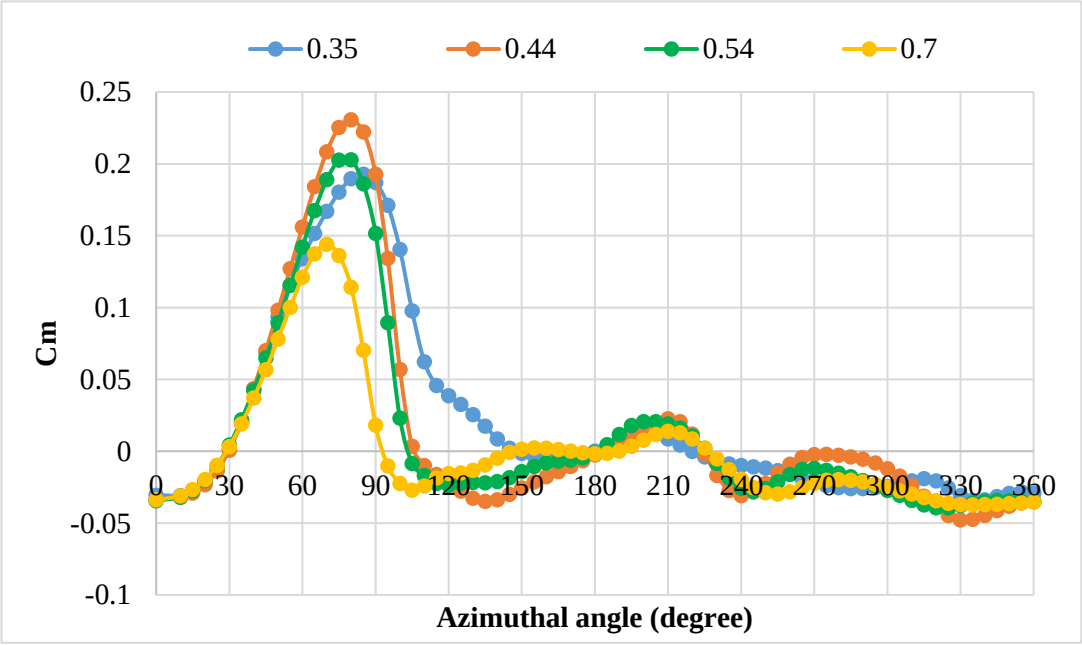

Figure 4.4. Single blade instantaneous C_m against azimuthal angles for HDWT with ARs of 0.35, 0.44, 0.54 and 0.70 at TSR 1.5.

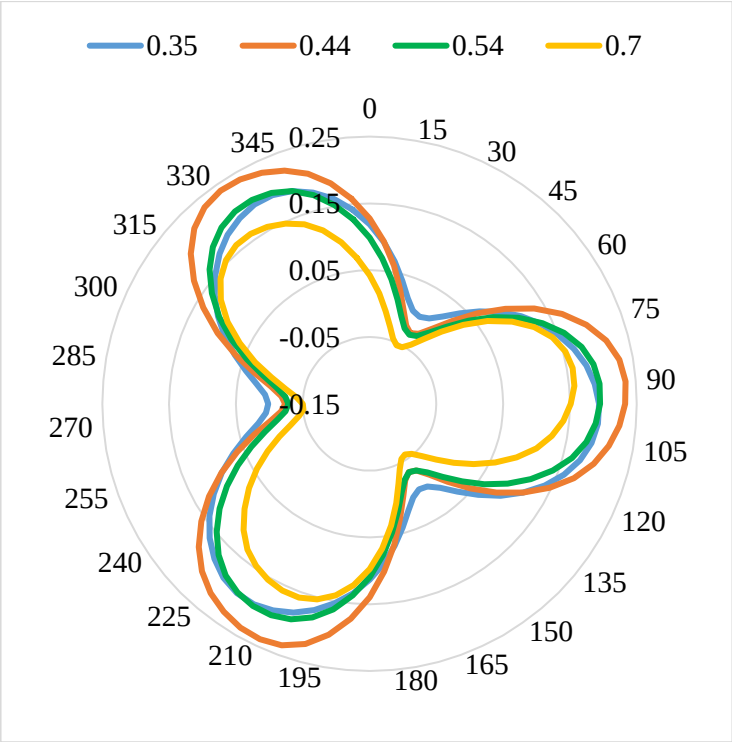

Figure 4.5. Instantaneous C_m against azimuthal angles of HDWT with ARs of 0.35, 0.44, 0.54 and 0.70 at TSR 2.5.

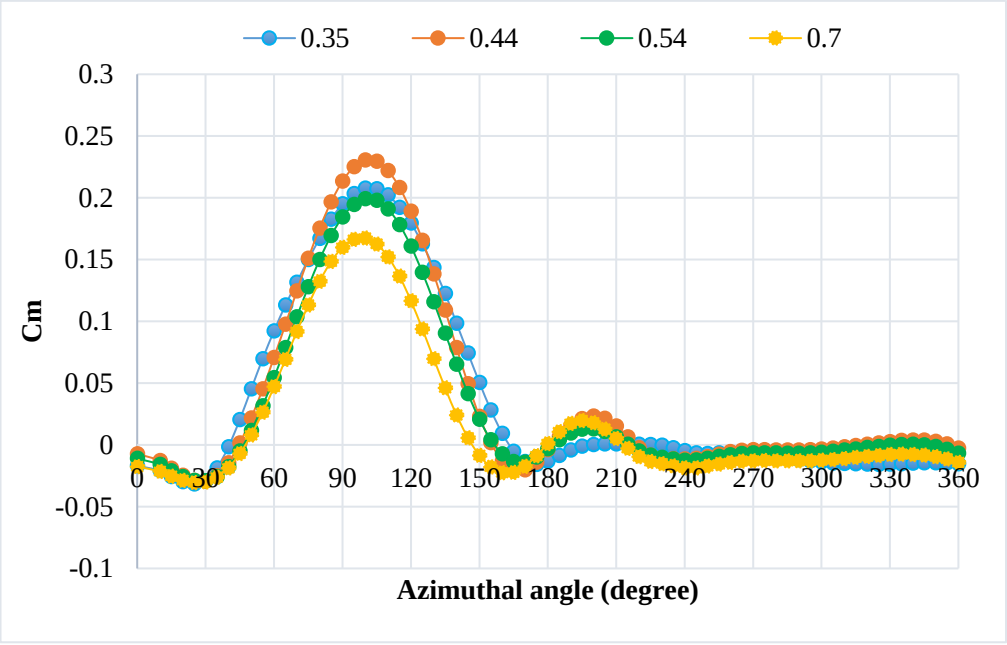

Figure 4.6. Single blade instantaneous C_m against azimuthal angles for HDWT with ARs of 0.35, 0.44, 0.54 and 0.70 at TSR 2.5.

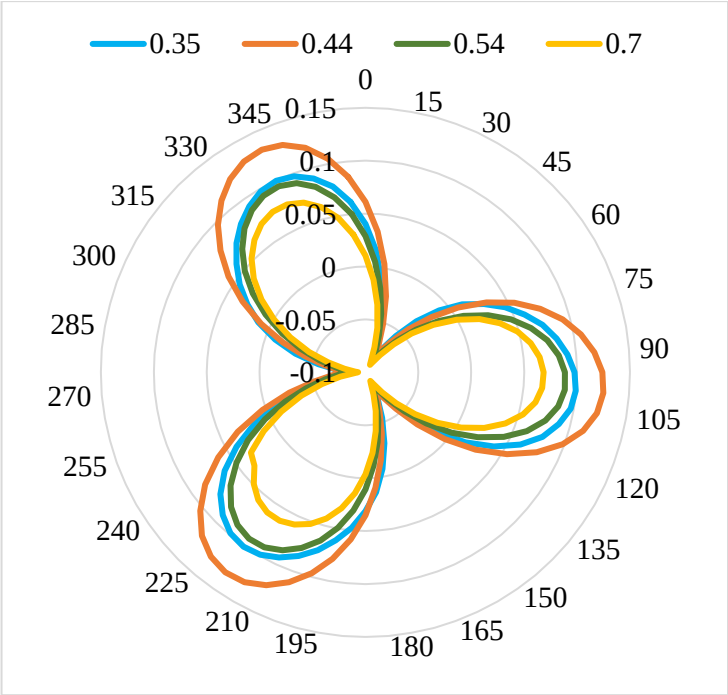

Figure 4.7. Instantaneous C_m against azimuthal angles of HDWT with ARs of 0.35, 0.44, 0.54 and 0.70 at TSR 3.5.

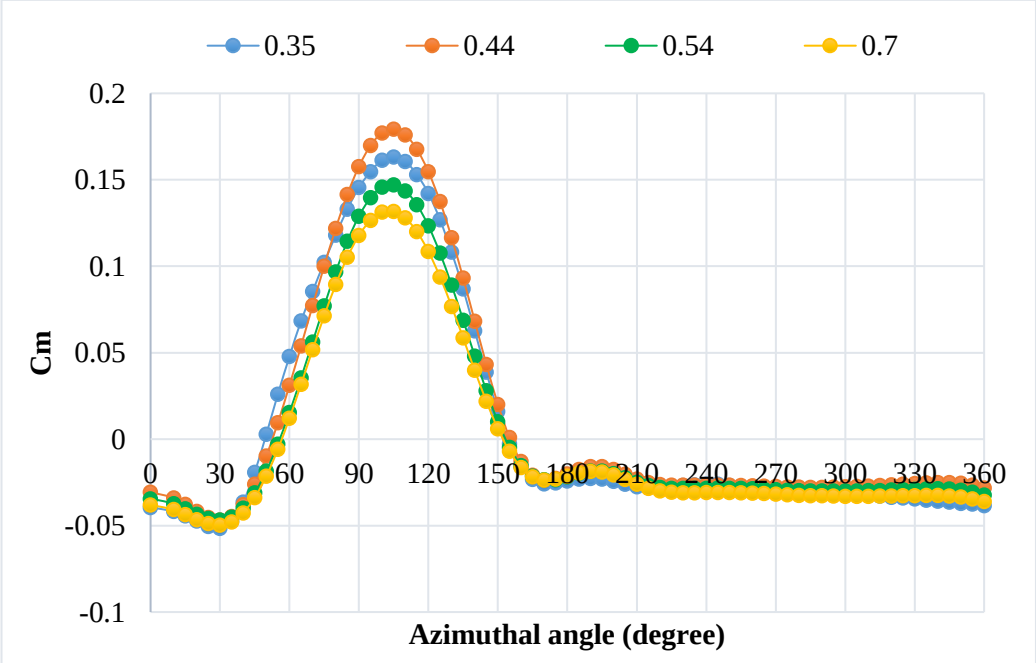

Figure 4.8. Single blade instantaneous C_m against azimuthal angles for HDWT with ARs of 0.35, 0.44, 0.54 and 0.70 at TSR 3.5.

4.1.1 The performance comparison of HDWT aerodynamics with aspect ratios of 0.35 and 0.70 at TSR of 2.5

The comparison of the blades' midplane vorticity contours for case 1 HDWT (AR=0.35) and case 4 HDWT (AR=0.70) at TSR 2.5 is shown in Figure 4.9 at rotation angles of θ=0°, 30°, 60° and 90° with respect to blade 1 position. It can be seen from the figure that for both cases, blade 1 at θ=60°, 90° and blade 2 at θ=0° experience attached flow for a long duration at the downwind region from 60° to 120° which explains the maximum moment being generated by the blades at these angles as confirmed by the instantaneous C_m plot in Figure 4.6. Then, a strong vortex began forming on the inner side of blade 2 (150°) at θ=30°, and this vortex continued to grow to the trailing edge of the blade as seen on blade 2 (180°) at θ=60° which resulted in lower C_m generated at these angles as confirmed in Figure 4.9. At θ=60°, for case 4's blade 2, the vortex formed on the blade at 180° shed more rapidly as the vortex was fully shed from blade 2 (210°) at θ=90°, whereas a small magnitude of the vortex is still attached to blade 2's trailing edge of the case 1 HDWT. This explains why the bigger AR HDWT blades give marginally higher C_m from 180° to 210°, as seen in Figure 4.6. However, once the vortex is shed from blade 2 of the case 4 HDWT, it travels towards the upwind direction and interacts with the oncoming blade as seen on blade 2 at a rotation angle of θ=90° and blade 3 at a rotation angle of θ=30°. As a result, the HDWT produced lower blade instantaneous C_m values ranging from 210° to 270° in contrast to case 1 HDWT, as shown in Figure 4.6. Additionally, the bigger AR HDWT in this study has a smaller diameter, which rotates faster than the smaller AR HDWT for the same TSR, resulting in the blades approaching and interacting with the oncoming vortex sooner. Moreover, for this case of cooling tower accelerated exhaust air, case 1 HDWT has the same diameter size as the outlet diameter of the cooling tower where the vortex is shed outwards from the HDWT region, which can be seen at θ=30° and 60°.

To further investigate the aerodynamic behaviour of the HDWT with different ARs under the cooling tower accelerated exhaust air, the pressure contour and streamlines around a single blade during its complete 360° rotation of case 1 and case 4 HDWTs is demonstrated as shown in Figures 4.10 and 4.11, respectively. For both cases, at the blade θ of 30°, positive pressure begins to build up at the leading edge of the blade

and grows until the blade reaches θ=90°. Concurrently, the blade experiences high negative pressure on the suction side, which starts from θ=60° to θ=120° and reaches maximum negative pressure at θ=90°. This results in significant pressure differences at the blade's leading edge at these angles, generating more lift force, contributing to positive tangential force and resulting in the highest blade C_m obtained during the HDWT rotation, as shown in Figure 4.6. The pressure characteristics around the blades for the biggest (case 4) and smallest (case 1) AR HDWT at all angles are similar except for the magnitude of pressure where the smaller AR HDWT shows a slightly higher pressure difference between the suction and pressure side of the blades at most angles, especially at θ=60° to 120°. The larger AR HDWT only shows slightly higher positive pressure at the leading edge of the blade at θ=180° to 210° and 270° to 330° which explains the result obtained in Figure 4.6 earlier that the larger HDWT AR gives a slightly better performance at these angles. The streamline from both these figures shows that vortex was formed on the blades starting at θ=210°, which grows on both sides of the blades until θ=270° and it starts to shrink until θ=0°, causing the instantaneous C_m of the blades at these angles to be mostly negative value. Apart from the slightly lower pressure difference shown by the larger AR HDWT at θ=90°, the streamlines display that the case 4 HDWT experiences a significantly large vortex on the suction side of the blade for a brief period that caused its instantaneous C_m to be much lower than the case 1 HDWT which affects the overall C_m and C_p greatly.

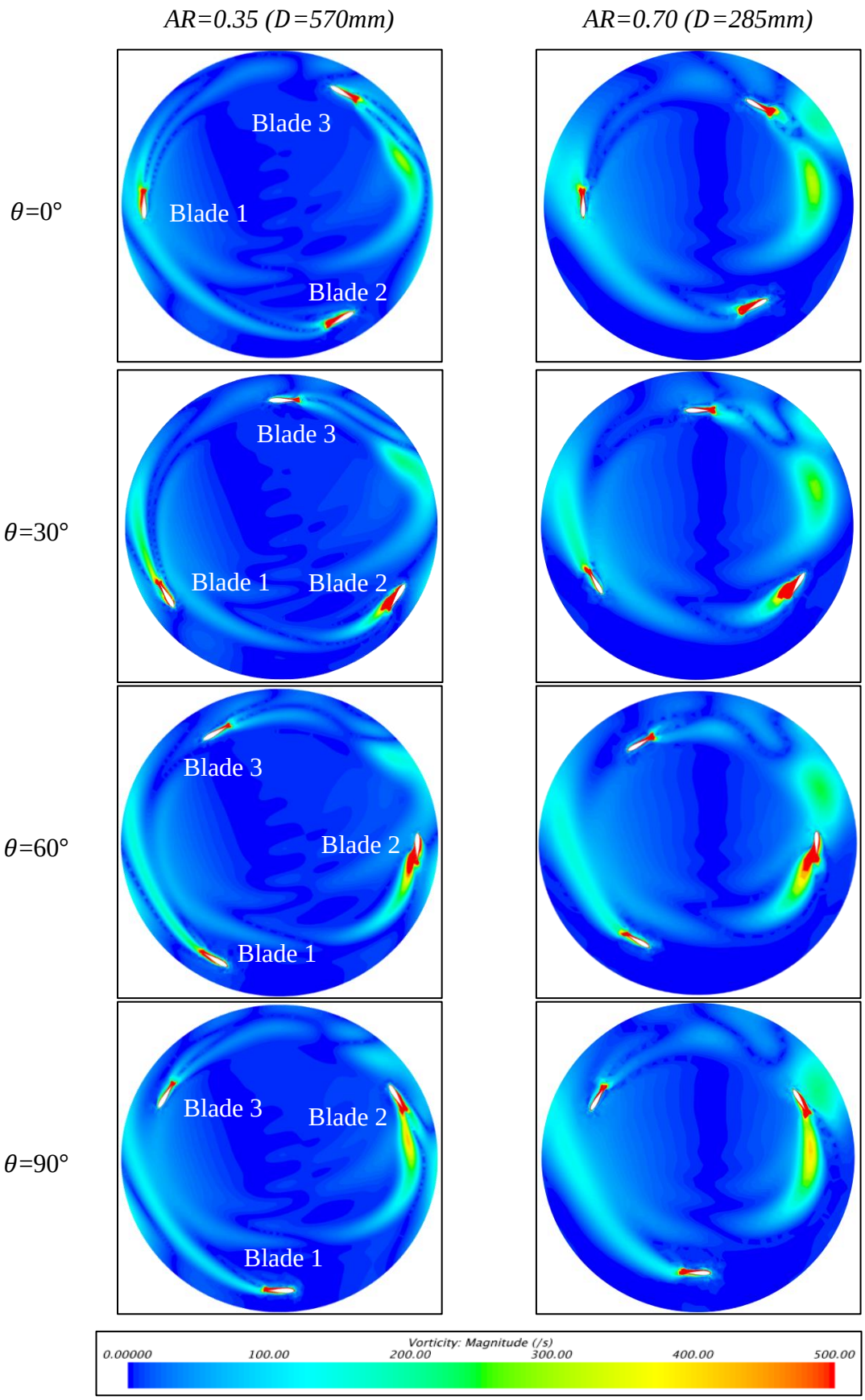

Figure 4.9. Vorticity contour comparison at a complete rotation between HDWT of aspect ratios 0.35 (left) and 0.70 (right) at TSR 2.5.

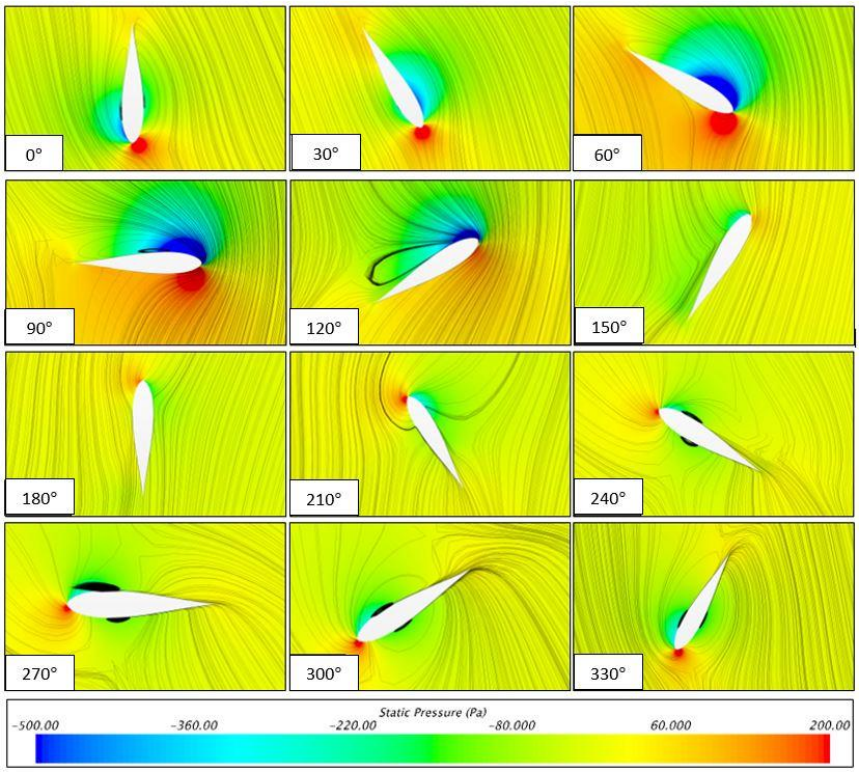

Figure 4.10. Static pressure contour and streamlines around a blade during one full rotation for HDWT of 0.35 AR at TSR 2.5.

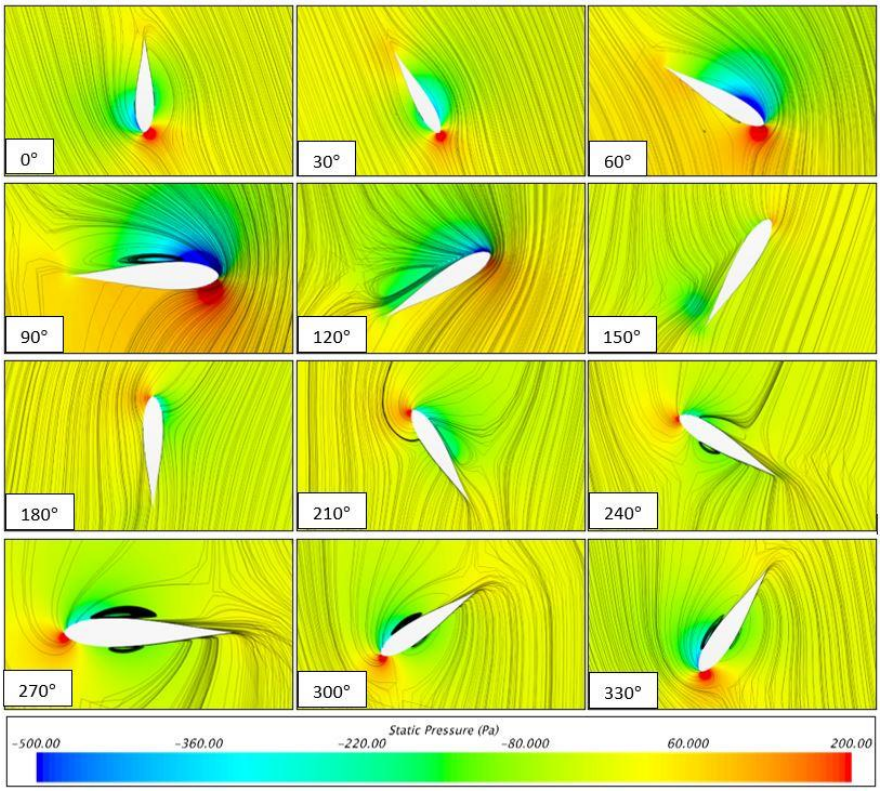

Figure 4.11. Static pressure contour and streamlines around a blade during one full rotation for HDWT of 0.70 AR at TSR 2.5.

4.1.2 Influence of TSR on the performance of HDWT with an aspect ratio of 0.44

In this section, the flow characteristics around the case 2 HDWT (AR=0.44) are analysed from low to high TSRs of 1.5, 2.5 and 3.5. Figure 4.12 exhibits the single-blade instantaneous C_m for a complete 360° rotation of case 2 HDWT at three different TSRs. Figures 4.13 and 4.14 provide the 2D midplane vorticity contour and 2D static pressure contour of the flow around HDWT under cooling tower exhaust air condition, at TSR 1.5 and 2.5, respectively, for comparison. It is evident that the vorticity-blade interaction at TSR 1.5 compared to TSR of 2.5 has significant differences, which suggests the behaviour of the HDWT at low TSR is dominated by the deep stall as confirmed by studies done by Sagharichi et al. [19], Rezaeiha et al. [20], Joo et al. [133] and Ali and Jang [134]. At a low TSR of 1.5, the HDWT demonstrates that blade 1 suffers from flow detachment at θ=0° while the vortex forming on the leading and trailing edge of blade 2 at θ=0° grows as seen at θ=30° and sheds gradually from the inner side of the blade at θ=60°. Furthermore, at θ=90°, the vortex formation is again observed near the leading edge on the outer side of blade 2, which detaches as seen on blade 3 at θ=0°. This separation of flow and vortex results in the reduction and discontinuity in the tangential force of the blades, hence decreasing its power generation at low TSR. The flow detachment can also be seen on the static pressure contour in Figure 4.14 at the stated azimuthal angles. The peak of the C_m for the blades at TSR 1.5 is achieved briefly as the difference of high pressure between the pressure and suction side of the blade occurs only on blade 1 from θ=60° to 90°. As a result, pressure is lost at low TSR due to the separation of the flow from the blade for long periods of the rotation.

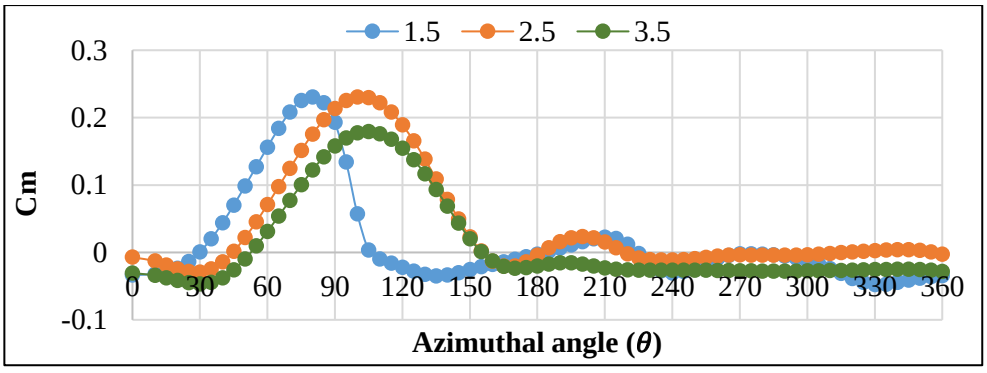

Figure 4.12. Single blade instantaneous C_m against azimuthal angles for HDWT with ARs of 0.44 at TSR 1.5, 2.5 and 3.5.

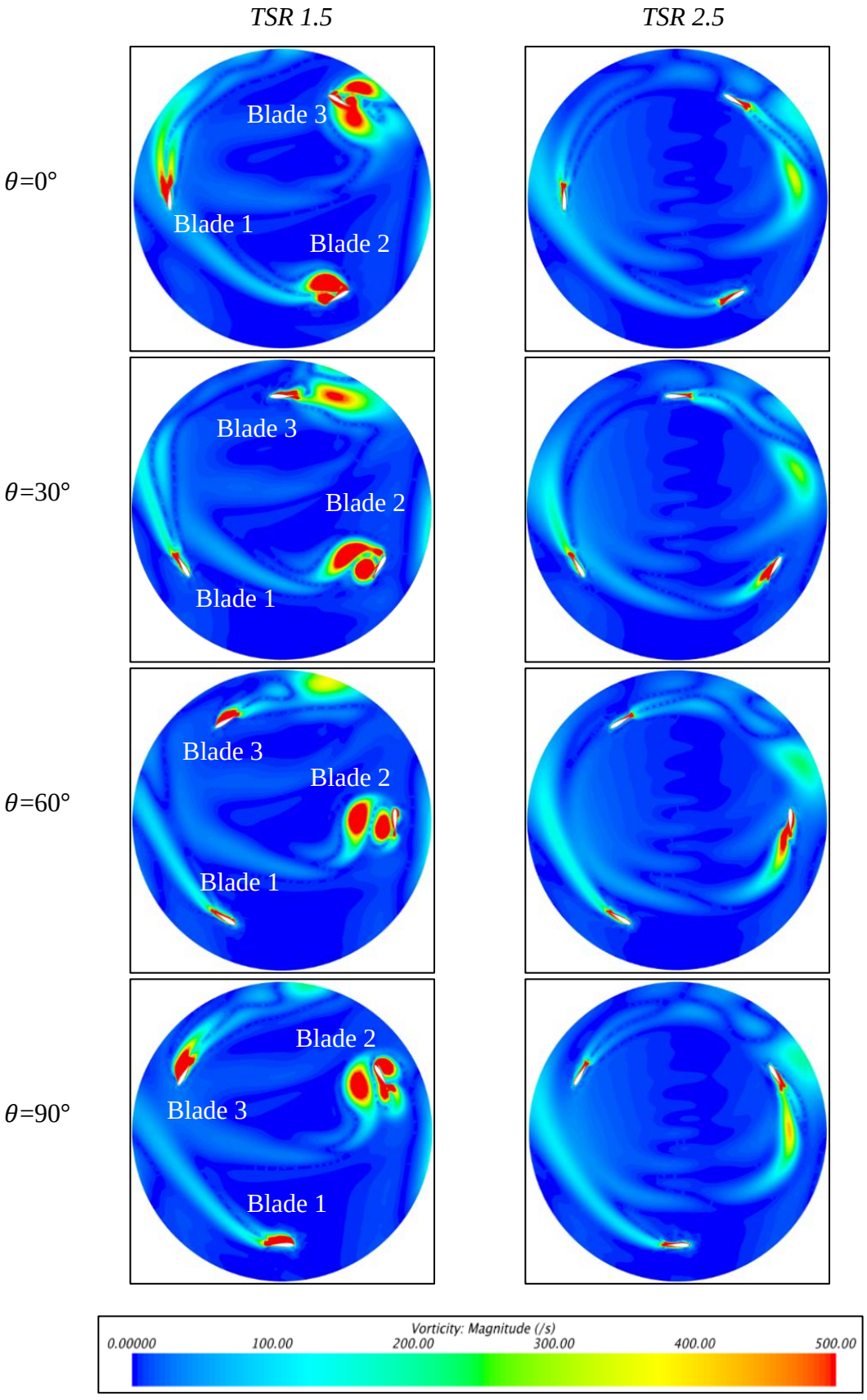

Figure 4.13. Vorticity contour comparison at a complete rotation for HDWT of AR=0.44 (D=456mm) at TSRs 1.5 and 2.5.

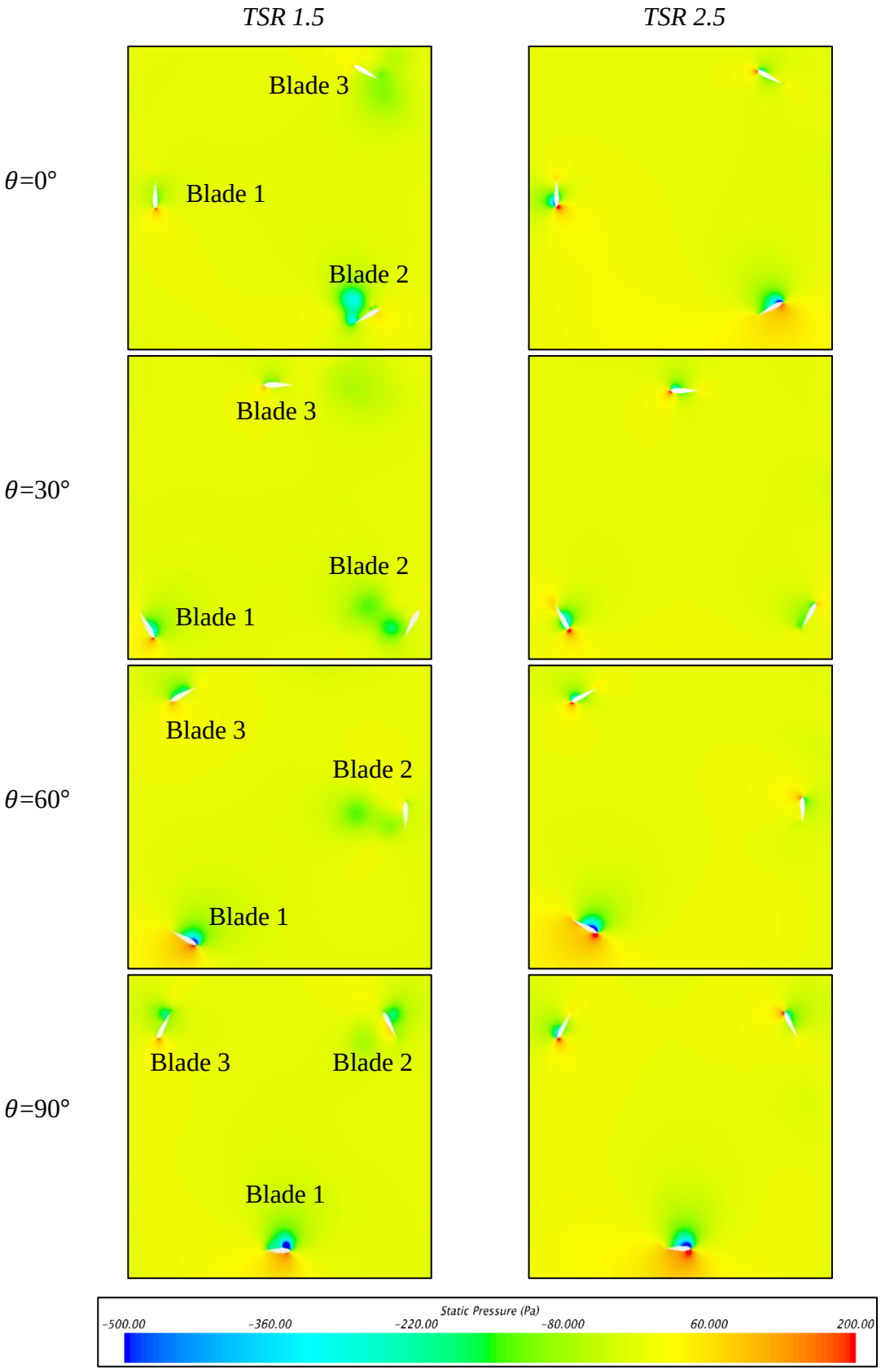

Figure 4.14. Static pressure comparison at a complete rotation for HDWT of AR=0.44 (D=456mm) at TSRs 1.5 and 2.5.

As TSR increases, the flow shows less chance of detaching from the blades, as shown in Figure 4.13, for the optimum TSR of 2.5. The extended period of attached flow on the blades for the complete rotation ensures the reduction of the drag force and increases lift force, resulting in the HDWT's production of a higher power as analyzed in many studies done in the past by Sagharichi et al. [19], Rezaeiha et al. [20], Joo et al. [133] and Ali and Jang [134]. The static pressure contour in Figure 4.14 also shows the pressure and suction side of the blades experience longer periods of high-pressure difference as observed on blade 1 from θ=60° to 90° and blade 2 at θ=0° which results in higher positive tangential force being obtained at TSR 2.5. However, from Figure 4.2, the HDWT at TSR of 3.5 shows lower C_p than that of TSR 2.5 due to the HDWT rotating faster at higher TSR, which increases the blades' relative velocity, resulting in a lower angle of attack and higher drag experienced by the blades as reported by Joo et al. [133] and Ali and Jang [134]. Figure 4.15 shows the plot of the drag coefficient, Cd against the angle of attack of the HDWT blade at TSR 2.5 and 3.5, which shows that at a high TSR of 3.5, the angle of attack of the HDWT blade is reduced and the drag coefficient increases. From Figure 4.16, the HDWT blades experience slightly higher shear stress along the whole length of the blade at TSR 3.5 compared to the HDWT blades at TSR 2.5. Therefore, HDWTs show characteristics of increasing power performance until an optimum TSR is reached (in this case, TSR=2.5) before losing power due to higher drag and reduction in angle of attack from higher rotating speed.

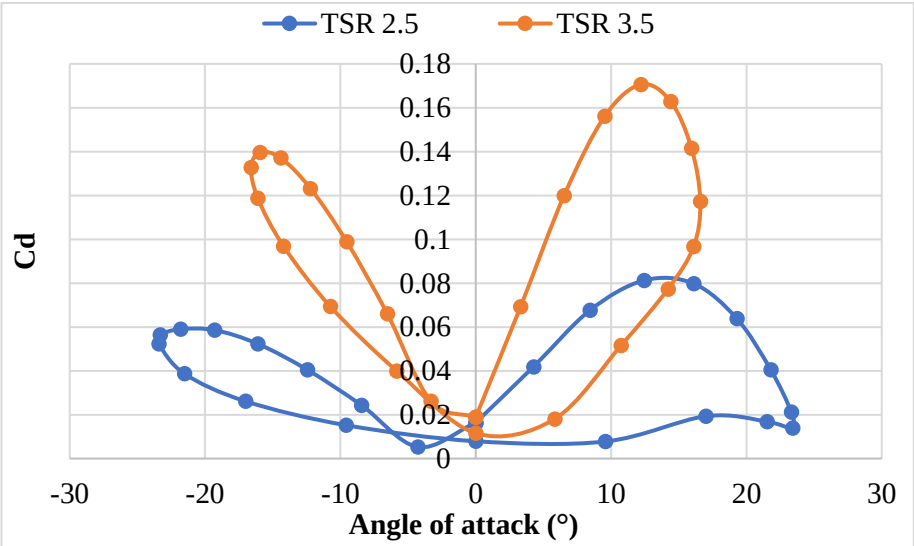

Figure 4.15. Drag coefficient versus angle of attack during a complete rotation of the *AR* 0.44 HDWT at TSRs 2.5 and 3.5.

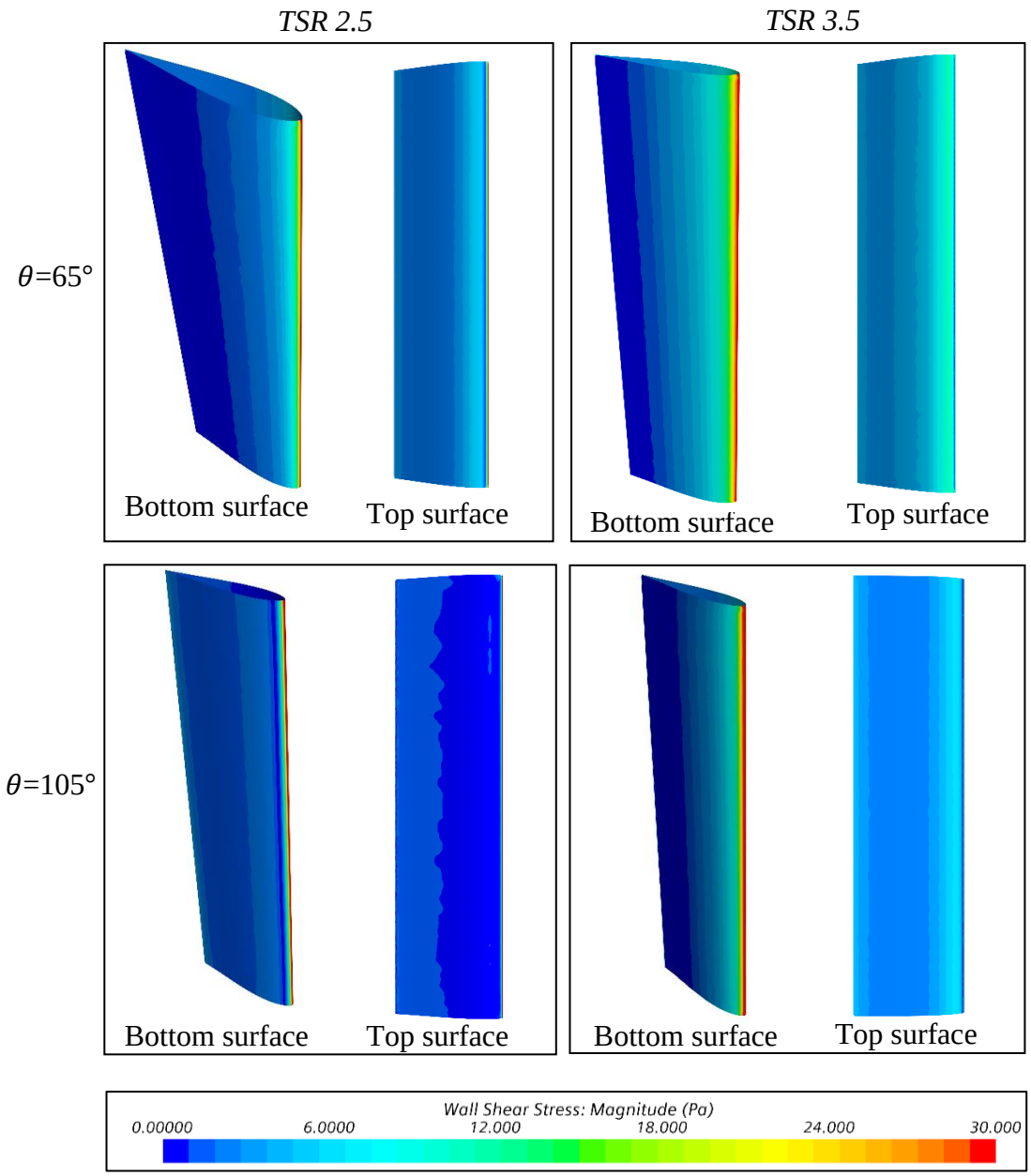

Figure 4.16. Wall shear stress contour comparison for AR 0.44 HDWT blades at blade azimuth angles of θ=65° and 105° at TSRs 2.5 and 3.5.

4.1.3 Analysis of the aerodynamic performance between HDWT of aspect ratio 0.35 and 0.44 at TSR 1.5 & 2.5

As described earlier, the discussion in Figure 4.2 case 1 HDWT (AR=0.35) provides an improved C_p compared to case 2 HDWT (AR=0.44) at TSR 1.5 and 2.0. However, case 2 HDWT produces a higher C_p at TSR ranges of 2.5 to 3.5. To investigate the differences in these results, the volumetric vorticity contour of case 1 and case 2 HDWTs is shown in Figures 4.17 and 4.18, respectively. For the case of TSR 1.5, the

case 2 HDWT blades experience more vortex shedding and flow detachment compared to the case 1 HDWT. Both HDWTs exhibit the formation of the vortex at the leading edge on blade 2 (120°) at θ=0°; however, only case 2 HDWT has vortex generation at the trailing edge throughout the blade span, while case 1 HDWT has several tip vortices at this azimuthal angle. Then, at θ=30°, case 2 HDWT experiences the detachment of these vortices in larger magnitudes compared to case 1 HDWT, as observed on blade 2 (150°). The shed vortex from the trailing edge remains on the case 2 HDWT blade 2 (180°) at θ=60° while the case 1 HDWT vortex diminishes. The extended period of flow detachment and vortex shedding explains the long period of negative instantaneous C_m experienced by the case 2 HDWT blades at these angles, as shown in Figure 4.4. Case 1 HDWT's favourable flow characteristics with fewer vortex production and rapid shedding experienced by its blade resulted in a wider period of positive instantaneous C_m at θ ranging from 30° to 150° as seen on blades 1 and 2 for all the HDWT azimuthal angles in Figure 4.17. However, case 2 HDWT provided a higher Cm ranging from θ=60° to 90° as at this azimuthal angle, case 2 blade 1 demonstrated attached flow. In contrast, case 1 HDWT showed some detached flow at the tip of the blade.

Next, at a TSR of 2.5, the vorticity of case 2 HDWT shows better flow characteristics, resulting in higher power production. This can be seen in Figure 4.18, where case 2 HDWT shows fully attached flow at the tip of the blades and along the blade span on blades 1 and 3 for all the azimuthal angles (θ=0° to 90°). It is observed that only a small magnitude of flow is detached at the trailing edge of blade 2 from θ=30° to 90°. Simultaneously, for the case 1 HDWT, there is detached flow is observed at the tip of blade 1 at θ=60° to 90° and at the tip of blade 2 at θ= 0° to 60°, resulting in a lower performing HDWT. It is important to note that case 1 HDWT has a similar diameter as the cooling tower outlet diameter, which contributes to the formation of tip vortices in both TSR 1.5 and 2.5 cases. Although a smaller diameter-based AR (bigger diameter) produces higher power, it is restricted by the size of the cooling tower outlet, as case 1 HDWT presented the formation of tip vortices at the optimum TSR, leading to the degradation of its performance. Ergo, the second smallest AR, case 2 HDWT (AR=0.44), demonstrated better C_p at the optimal TSR of 2.5.

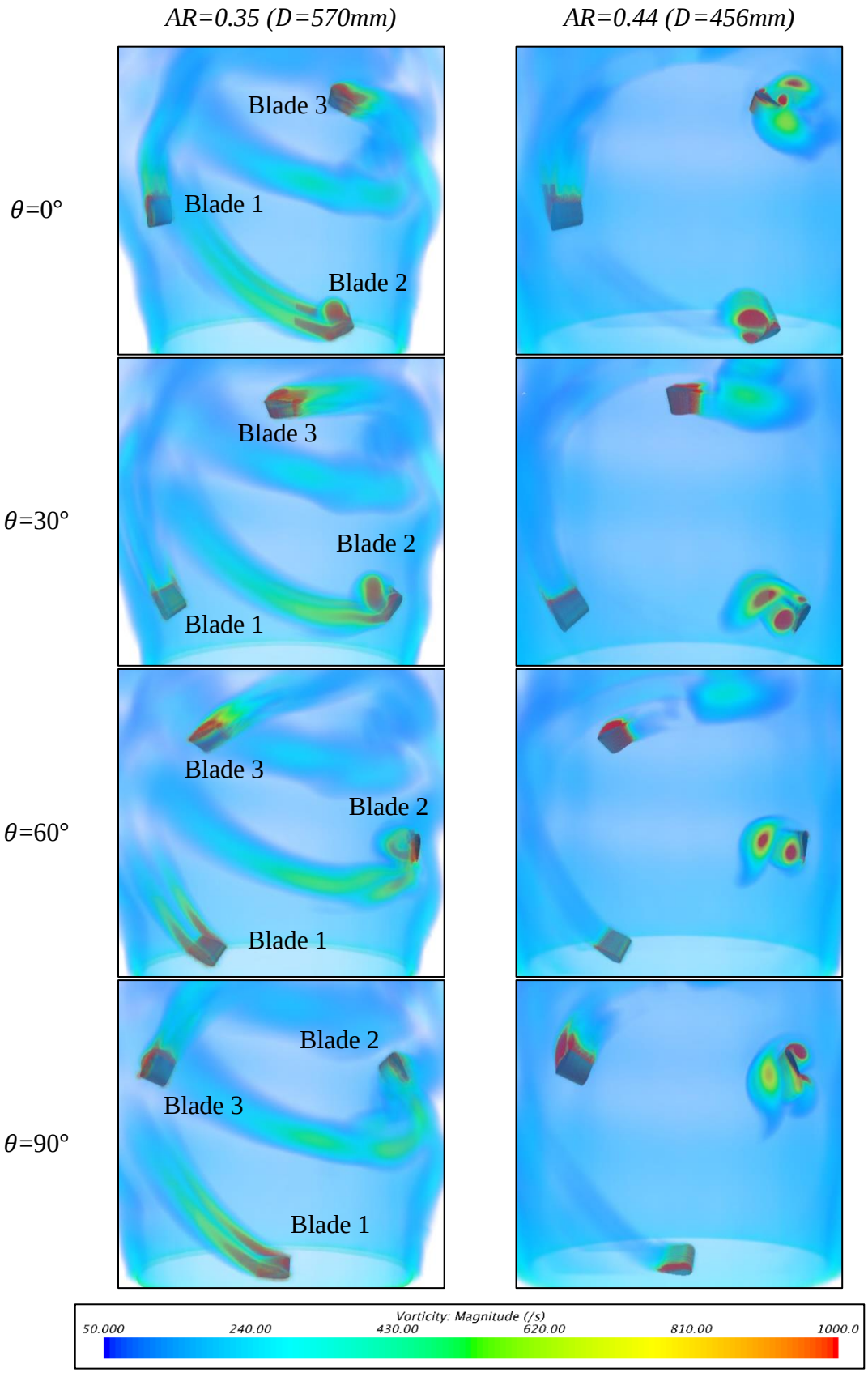

Figure 4.17. Three-dimensional volumetric vorticity contour at a complete rotation for HDWT of AR=0.35 (left) and AR=0.44 (right) at TSR 1.5.

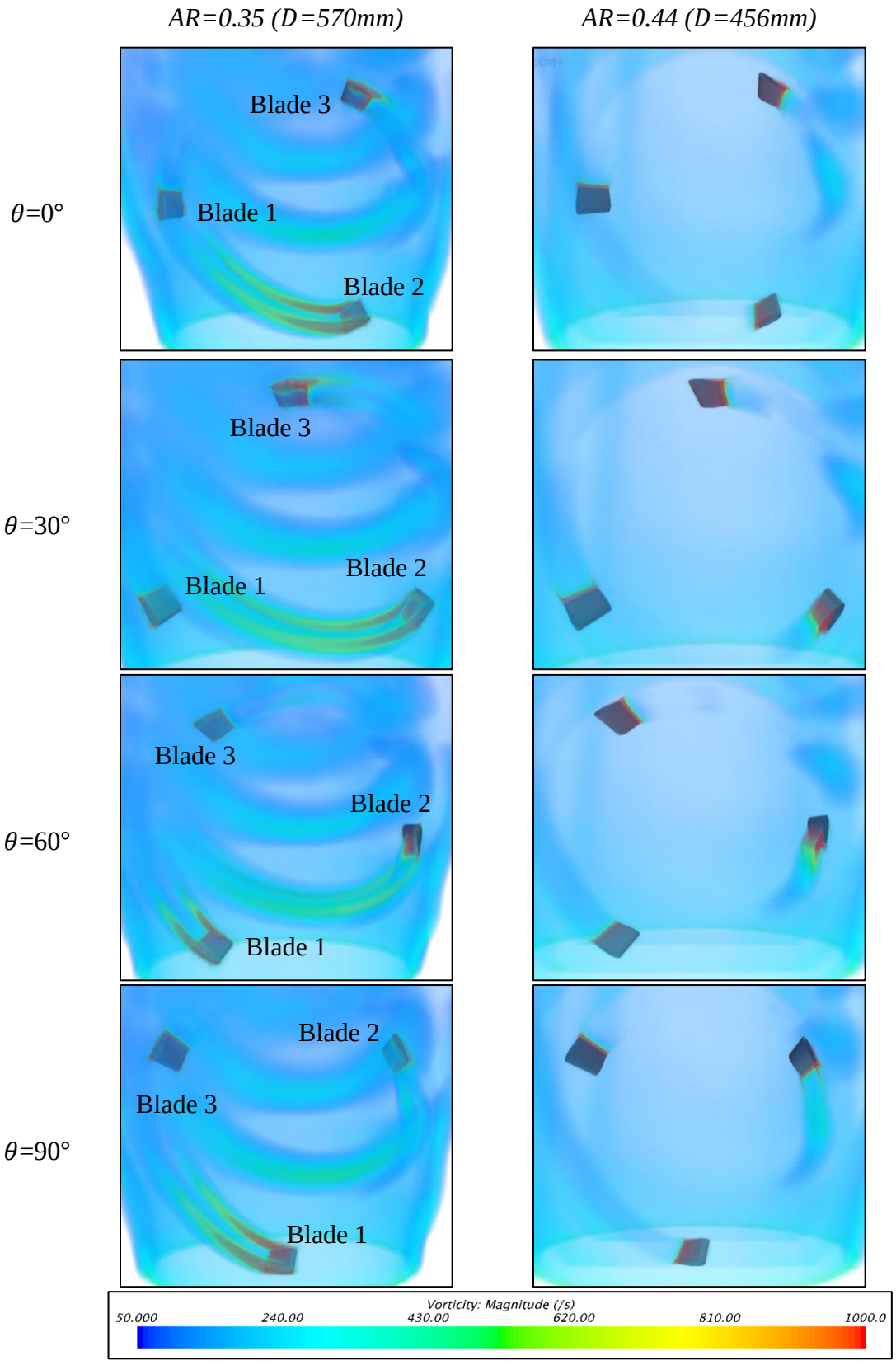

Figure 4.18. Three-dimensional volumetric vorticity contour at a complete rotation for HDWT of AR=0.35 (left) and AR=0.44 (right) at TSR 2.5.

4.1.4 Comparative study between the present HDWT to past studies

Figure 4.19 compares the drag coefficient between the HDWT used in this study to the studies done by Sengupta et al. [35] and Rezaeiha et al. [135]. The HDWT used for this comparison has an aspect ratio of 0.44 with a solidity of 0.3 at TSR 2.5, the best-performing HDWT among all aspect ratios and TSR investigated. It is shown in all studies that the blades experience drag as the angle of attack increases; a similar observation can be seen in the current study. The discrepancies in the stall angle is due to the different parameters used in each of the study. The study by Rezaeiha et al. [135] was done at TSR 4.0 using NACA 0015 blades. The higher TSR reduces the angle of attack on the blades, which causes the drag to increase. However, the drag experienced by Rezaiha et al.'s [135] blades is not that high, as the NACA 0015 has a thinner airfoil design, which is suitable for high TSR conditions. Next, the blades used by Sengupta et al. are the S815 and EN0005, with a solidity of 0.51 at TSR of 1.48 and 1.52, respectively [35]. The low TSR condition allows the high-solidity blades to reach a higher angle of attack and experience lower drag.

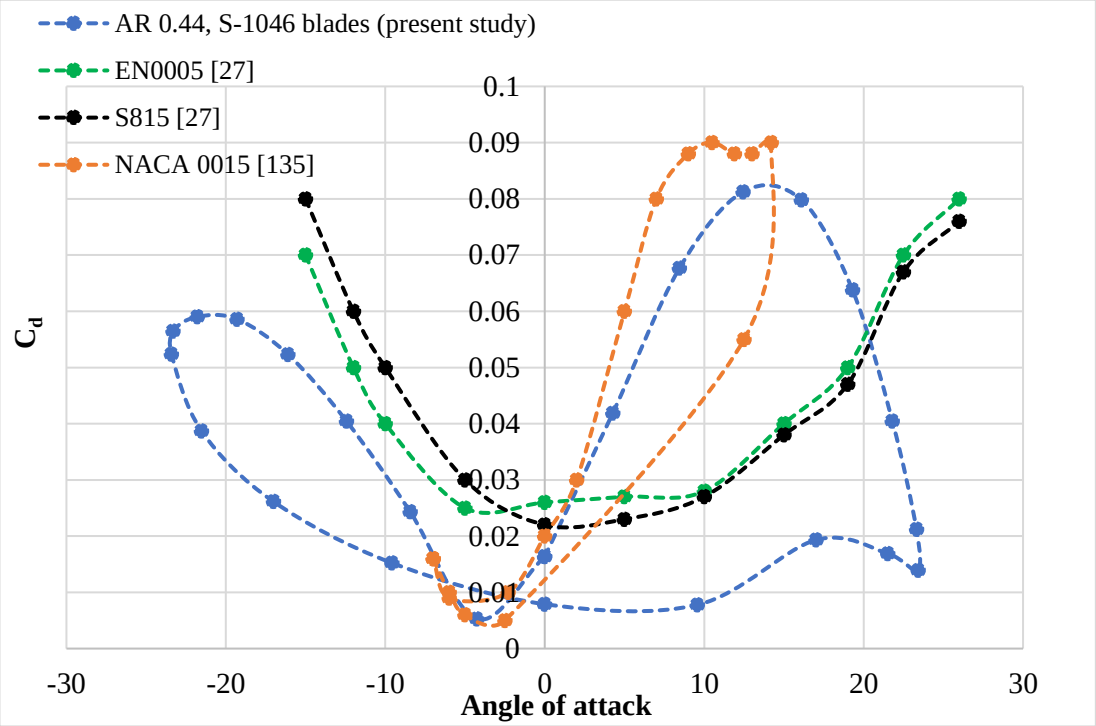

Figure 4.19. Comparative study on the drag coefficients produced by the turbine blades with other studies

4.2 Effect of Solidity on HDWT Performance for Cooling Tower Exhaust Air Energy Extraction

The HDWT of AR 0.44 (D=456mm) is the best turbine to harvest the cooling tower exhaust air in this study as it produced the highest power coefficient at TSR 2.5, as shown and discussed in Section 4.1. In this section, further optimization was done, this time on the HDWT's solidity to find out the best solidity for cooling tower exhaust air energy extractions. Figure 4.20 and Figure 4.21 show the moment and power coefficient plot against TSR, respectively, for HDWT with four solidities tested. The result shows that the HDWT, with a solidity of 0.45 at TSR 2.0, achieved the highest performance with a moment coefficient of 0.16 and a power coefficient of 0.32. This is an 8.71% increase in power coefficient compared to the best HDWT, with a solidity of 0.3 from Section 4.1. It is observed that higher solidity HDWT performs better at lower TSR. In comparison, lower solidity HDWT achieves peak performance at higher TSR, which corroborates with previous work by Sagharichi et al. [19] and Rezaeiha et al. [20]. The lowest solidity HDWT of 0.225 reached its peak C_p of 0.214 at TSR 3.0. At low TSRs of 1.5 and 2.0, the HDWT with the highest solidity (σ=0.45) produced the best C_p. At TSRs of 2.5 and 3.0, the HDWT with the solidity of 0.3 produced the best C_p. At a high TSR of 3.5, the lowest solidity HDWT (σ=0.225) produced the highest C_p of 0.179. There is a big difference in C_p value between the highest and lowest solidity HDWTs at low TSRs; this difference gets smaller at higher TSRs, as observed in Figure 4.21. Overall, the higher solidity HDWT is more desirable for cooling tower exhaust air energy extractions in this study.

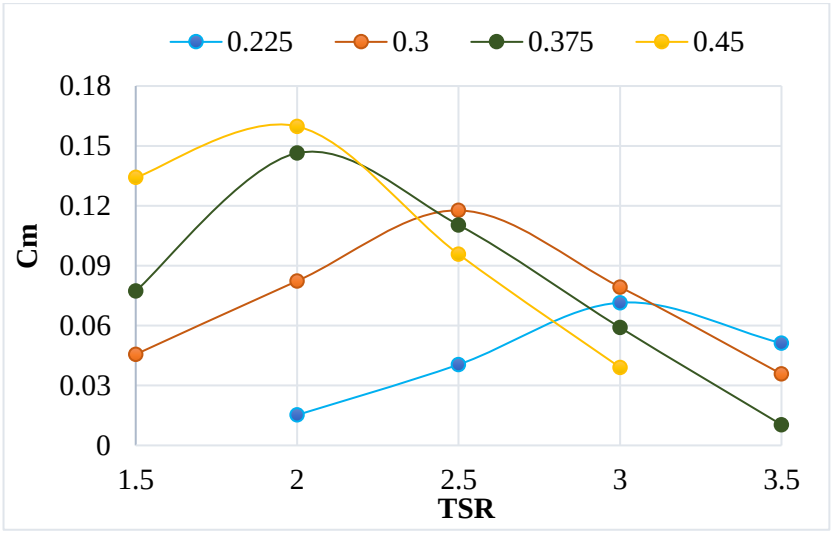

Figure 4.20. Effect of solidity on HDWT moment coefficient under accelerated cooling tower exhaust air.

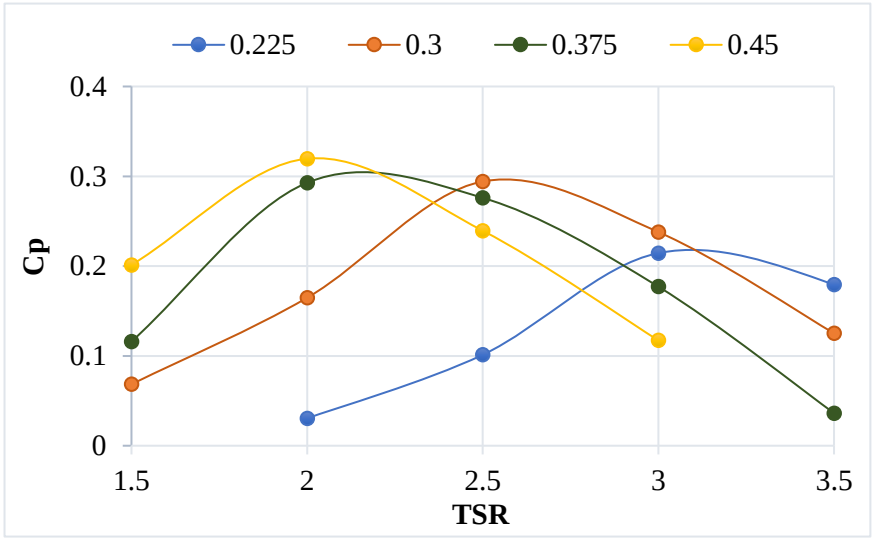

Figure 4.21. Effect of solidity on HDWT power coefficient under accelerated cooling tower exhaust air.

Figures 4.21 and 4.22 show the radar plot of the instantaneous coefficient of moment for a full 360° of the HDWT rotation at TSR 2.0 and 3.0, respectively. The values for the instantaneous coefficient of moment are taken from the final rotation of the HDWT once the solution converges. The plot of the instantaneous coefficient of the moment of a single HDWT blade against azimuthal angle, θ, is also provided, as shown in Figures 4.24 and 4.25 for TSR 2.0 and 3.0, respectively. At TSR 2.0, the radar plot in Figure 4.22 shows that the highest solidity HDWT (σ=0.45) gives the highest instantaneous C_m for almost the full turbine revolution, and Figure 4.24 shows

the blade of this HDWT produces a higher positive C_m compared to other HDWT of lower solidities. The HDWT of solidity 0.225 gave an unsatisfactory performance at TSR 2.0 as it produced a much lower instantaneous C_m values compared to other higher solidity HDWT, and it has a high negative C_m from azimuthal angle of 0° to 35° and 345° to 360° as seen in Figure 4.22. At TSR 3.0, the higher solidity blades show the highest maximum instantaneous C_m for a single blade, as shown in Figure 4.25. However, the power coefficient obtained in Figure 4.21 suggests that the lower solidity HDWTs perform better. This is because the overall C_m for the higher solidity, HDWT, suffers from a higher negative Cm, as shown in the radar plot in Figure 4.23. Also, the lowest solidity HDWT (σ=0.225) blades produce a higher average C_m for the complete 360° as seen in Figure 4.25. Additional observation of the result shows that at TSR 2.0, the lower solidity HDWTs reach peak instantaneous C_m at lower azimuthal angles. The HDWT with the solidity of 0.225 reached peak instantaneous C_m at θ=80° while the highest solidity HDWT (σ=0.45) reached peak instantaneous C_m at θ=105°. At a higher TSR of 3.0, the peak instantaneous C_m of the lower solidity HDWT shifts to a higher azimuthal angle. The HDWT of 0.225 solidity peak instantaneous C_m shifts to 95° whereas the other 3 HDWTs peak instantaneous C_m is at 105°.

In the next two sections, flow analysis around the HDWT is done to study the aerodynamic characteristics behind the results obtained. Since higher solidity HDWT perform better at lower TSR while lower solidity HDWT performs better at higher TSR, the comparison between HDWT with the largest (σ=0.450) and smallest (σ=0.225) solidities is done. In Subsection 4.2.1, the two-dimensional comparison of the scalar scene of the pressure and streamlines on an airfoil is presented and discussed at a low TSR of 2.0 and high TSR of 3.0. In Subsection 4.2.2, the three-dimensional vorticity comparison at TSR 2.0 is presented and discussed.

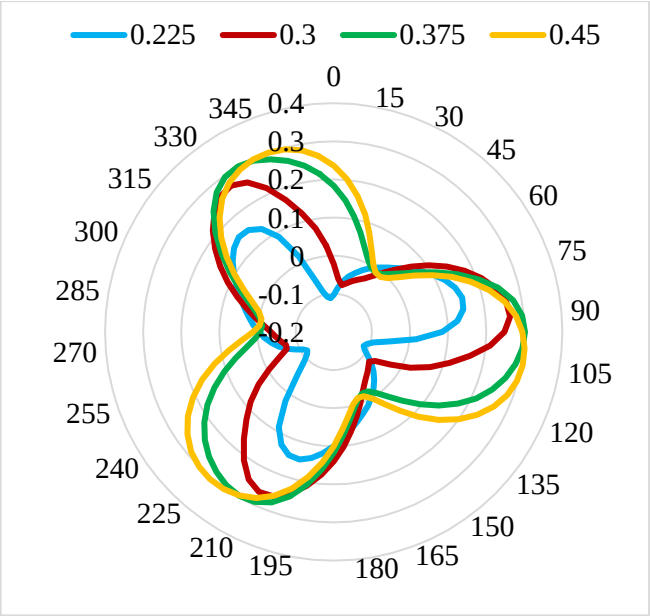

Figure 4.22. Instantaneous C_m against azimuthal angles for HDWT of solidities 0.225, 0.3, 0.375, 0.45 at TSR 2.0.

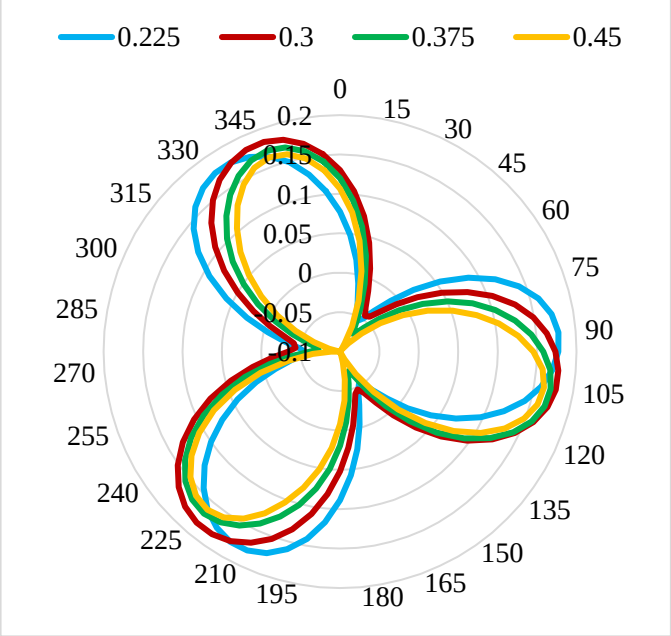

Figure 4.23. Instantaneous C_m against azimuthal angles for HDWT of solidities 0.225, 0.3, 0.375, 0.45 at TSR 3.0.

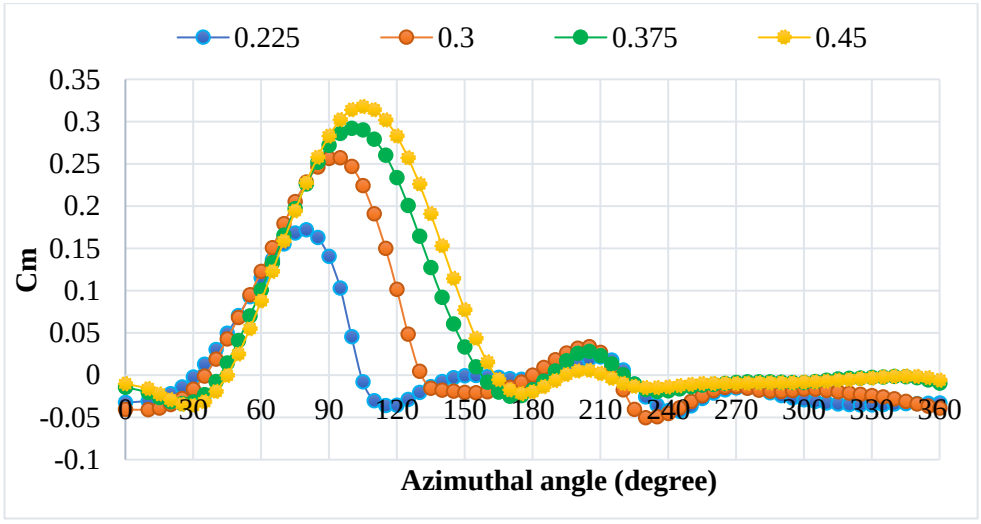

Figure 4.24. Single blade instantaneous C_m against azimuthal angles for HDWT of solidities 0.225, 0.30, 0.375 and 0.45 at TSR 2.0.

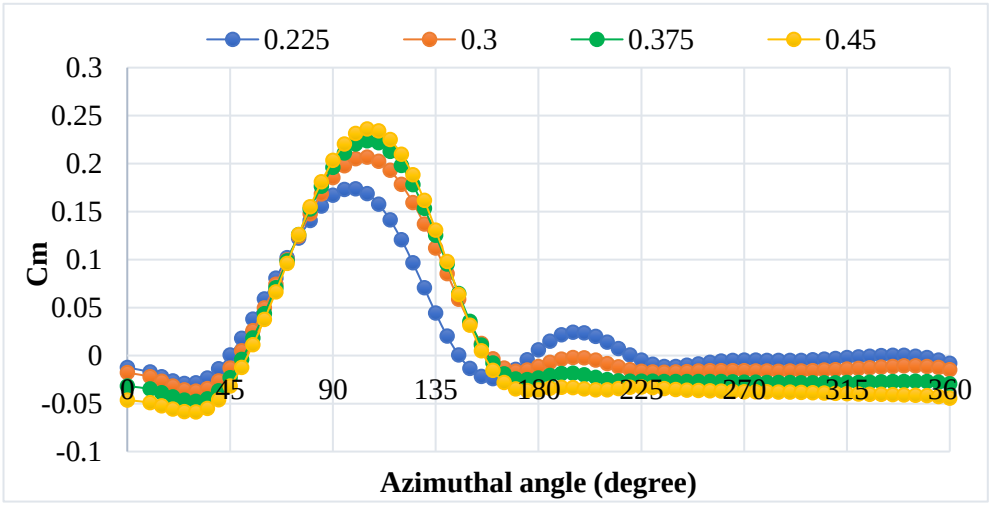

Figure 4.25. Single blade instantaneous C_m against azimuthal angles for HDWT of solidities 0.225, 0.30, 0.375 and 0.45 at TSR 3.0.

4.2.1 Pressure and streamlines comparison between HDWT of solidity 0.225 and 0.450 at TSR 2.0 and TSR 3.0

Figure 4.26 compares the pressure contour and flow streamlines around the blades between HDWT with a low solidity of 0.225 and a high solidity of 0.450 at TSR 2.0 for one complete rotation. From the pressure distribution, the solidity 0.225 HDWT starts experiencing significant pressure difference build-up between the suction and pressure side of the airfoil beginning from 30°, reaching maximum pressure difference at about 90°. Therefore, most of the lift is generated at these azimuth angles, as observed from the instantaneous C_m curve in Figure 4.24. The HDWT blade only

experiences pressure difference for a short period during one complete rotation as after 120°, there is a very small pressure difference as the flow above the airfoil is interfered by the exhaust air at blade position 120°. The solidity 0.450 HDWT shows better flow characteristics at TSR 2.0. Near the upwind region at 60°, a significant pressure difference between the pressure and suction side of the airfoil occurs, which lasts till 120° as observed in Figure 4.26. Then, at 120°, the vortex formed can be seen on the surface of the airfoil, which delays flow separation, causing the HDWT blade to have a high lift until 150°. This can also be observed in the instantaneous C_m plot in Figure 4.24. This corroborates with the findings of Subramaniam et al. [37], which discussed that higher solidity HDWT performs better at low TSR due to the longer duration of attached flow. Therefore, the longer high lift and moment produced during the rotation results in the higher solidity HDWT producing higher C_p at TSR 2.0.

Figure 4.27 shows the comparison of the pressure contour and flow streamlines around the blades of HDWT of solidity 0.225 and 0.450, respectively, at TSR 3.0 during one complete rotation. The blades of σ=0.225 HDWT experience a slight pressure difference between the suction and pressure side from 270° to 330° and 0° to 30°, which gives a small positive instantaneous C_m at these azimuth angles. The σ=0.45 HDWT have a very small pressure difference between the top and bottom side of the blades, which hinders it from generating any positive moment from 270° to 360° (0°). It can be seen from Figure 4.27 that at 30° to 120°, both the HDWTs experience growing pressure differences at the top and bottom sides of the blades, which is good for lift generation, hence producing high instantaneous C_m at these angles. This is also shown by the graph in Figure 4.25. From 180° to 210°, the 0.225 solidity blade has high pressure at the leading edge and some pressure difference between the top and bottom of the blade, which gives a positive performance. Therefore, the performance of the lower solidity HDWT is better at a high TSR of 3.0 as the shed vortices dissipate much faster than the high solidity HDWT, with similar findings reported by Subramaniam et al. [37] in their study. Even though low solidity HDWT showed excellent characteristics at TSR 3.0, the high solidity HDWT produced higher C_p at TSR 2.0, as Zanforlin and Deluca [24] and Rezaeiha et al. [20] have discussed in their studies that shorter chord length results in lower chord-based Reynolds' Number as shown in Equation 2.7, which causes reduced lift and increases drag coefficient.

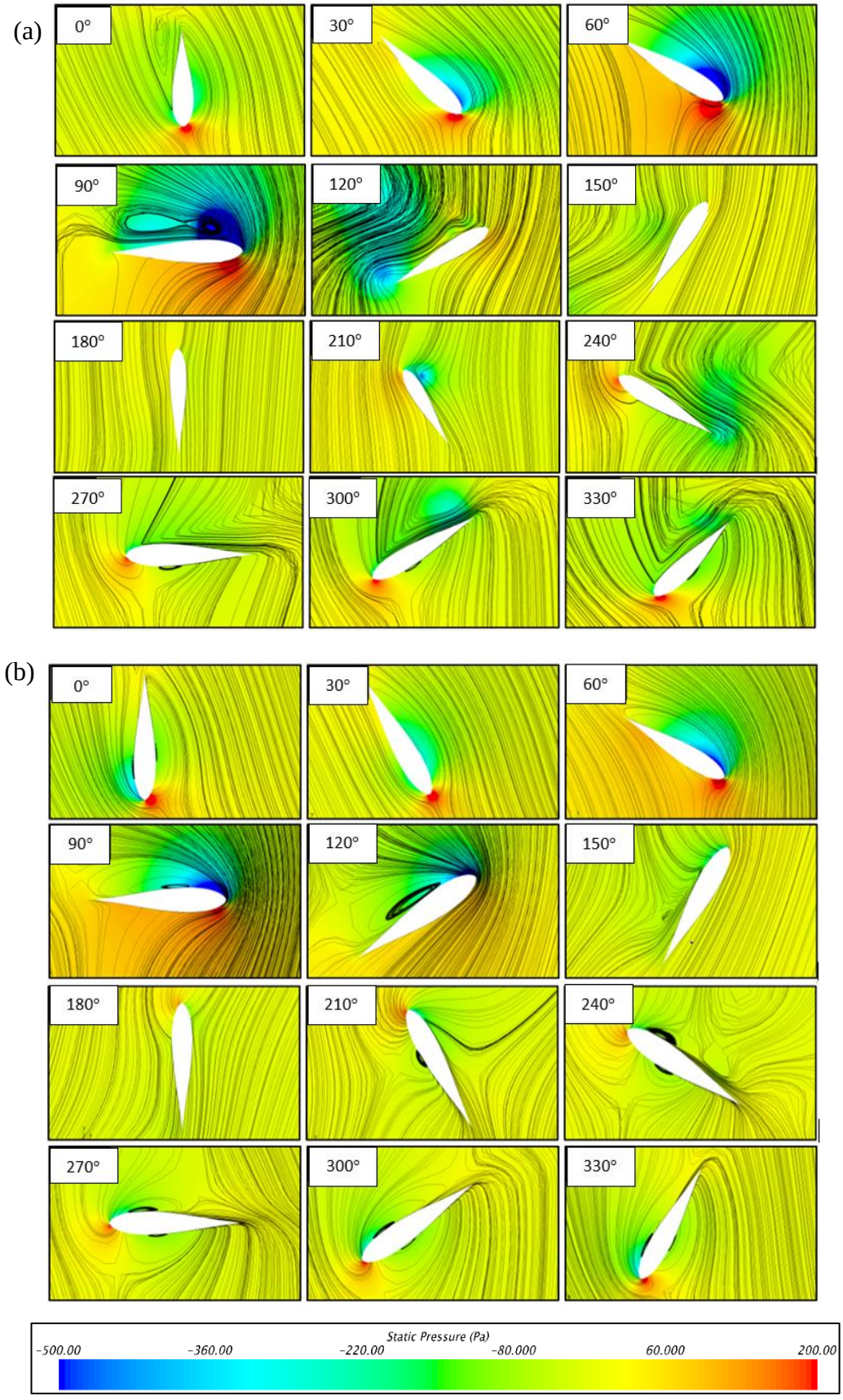

Figure 4.26. Static pressure contour and streamlines around the blade during one full rotation at TSR 2.0 for HDWT of solidity: (a) 0.225 & (b) 0.450.

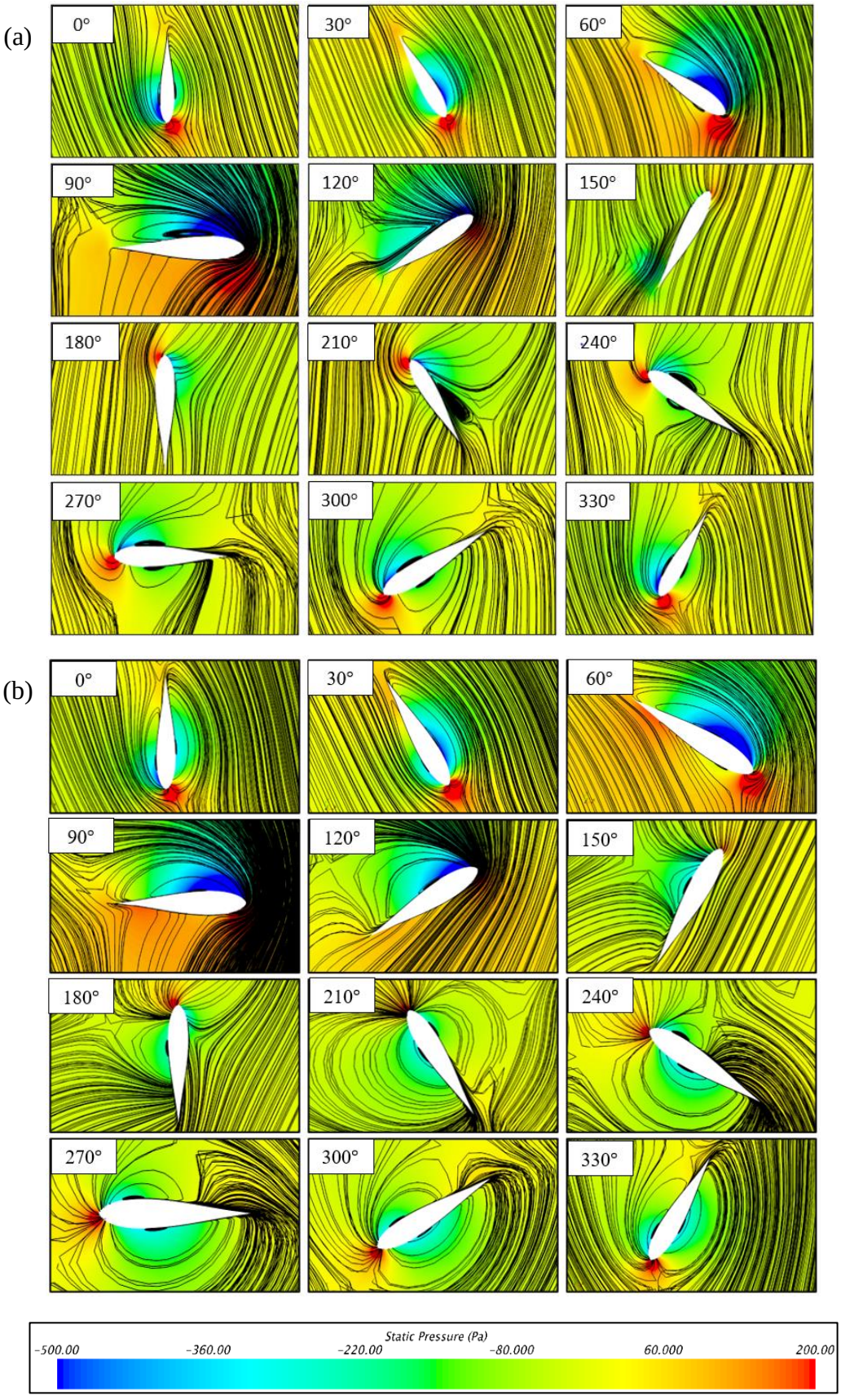

Figure 4.27. Static pressure contour and streamlines around the blade during one full rotation at TSR 3.0 for HDWT of solidity: (a) 0.225 & (b) 0.450.

4.2.2 Vorticity comparison between HDWT of solidity 0.225 and 0.450 at TSR 2.0

Figure 4.28 shows the vorticity comparison between HDWT of solidity 0.225 and 0.450 at TSR 2.0. It can be seen from the figure that the smaller solidity HDWT experiences vortex shedding and flow detachment. The 0.450 solidity HDWT shows good flow characteristics, with the flow near the blades being attached for the full rotation, producing the highest power coefficient value among all the HDWT tested.

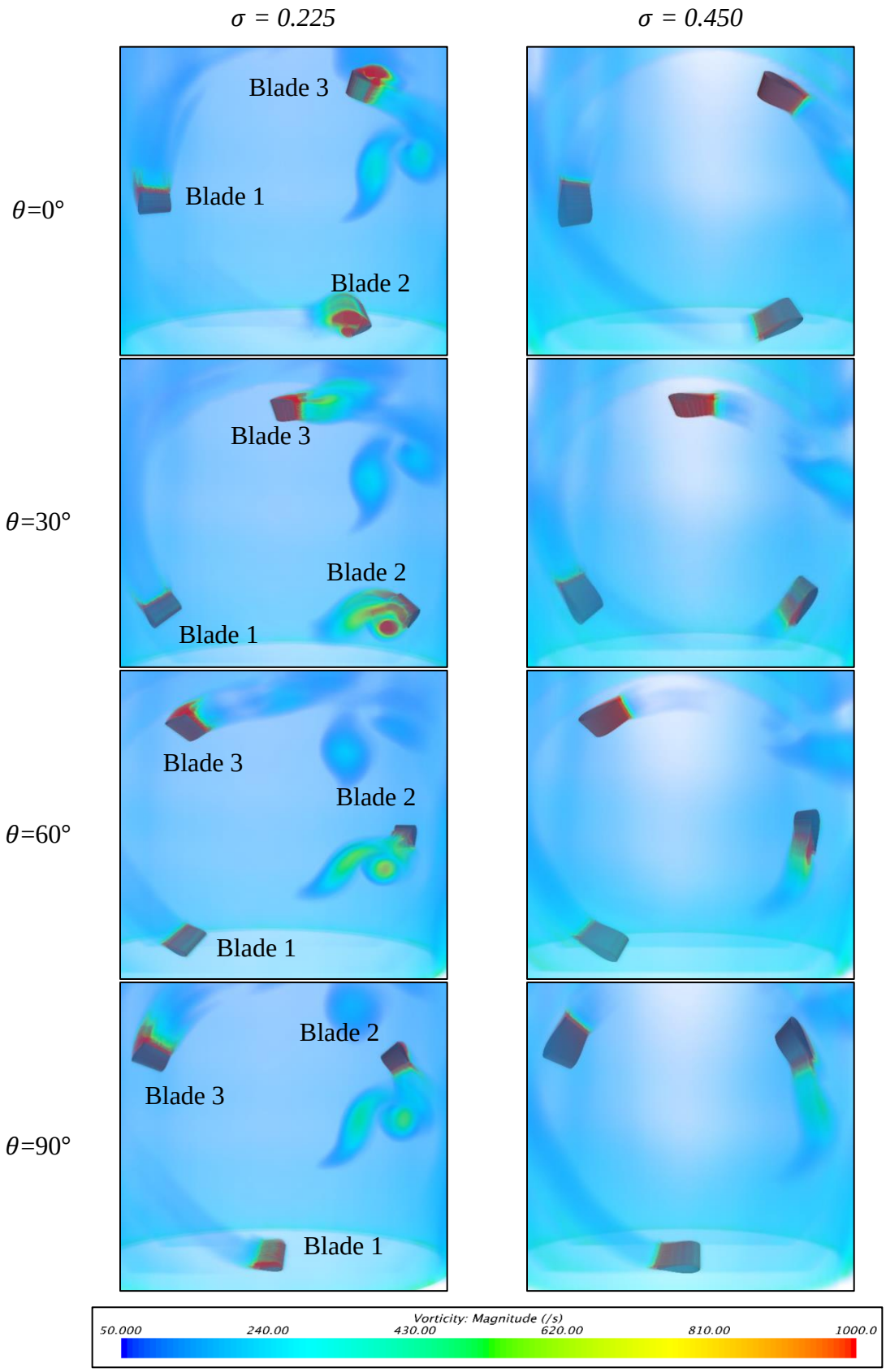

Figure 4.28. Three-dimensional volumetric vorticity contour at a complete rotation for HDWT of σ=0.225 (left) and σ= 0.450 (right) at TSR 2.0

4.3 Cycloidal Diffusers Parametric Study for HDWT Performance Enhancement under Cooling Tower Exhaust Air

HDWT with an AR of 0.44 and solidity of 0.45, which is the best parameter as discussed in Sections 4.1 and 4.2, was used for this part of the study. Three-dimensional CFD simulations were carried out to further enhance the performance of the HDWT by adding a cycloidal diffuser to the current exhaust air energy extractor system. The cycloidal diffuser parametric study is done in three steps, as discussed in Subsection 3.4.2, to find the best diffuser length, diffuser angle, shroud length and shroud angle. The coefficient of moment was obtained, and the coefficient of power was calculated for each cycloidal diffuser design. This parametric study was first done by investigating the effect of the cycloidal diffusers' length and diffuser angle, and the results are discussed in Subsection 4.3.1. The cycloidal diffuser shroud length was then studied in the second step, and the results are shown in Subsection 4.3.2. Lastly, the third step of this parametric study involves the shroud angle, the results of which are presented in Subsection 4.3.3.

4.3.1 Parametric study of diffuser length and diffuser angle

The cycloidal diffuser was added, and the HDWT performance was measured while optimizing the diffuser length and angle at TSR 1.5. The diffuser lengths of $1.25D$, $1.0D$, $0.75D$, $0.5D$ and $0.25D$ were tested with diffuser angles of 15°, 20°, 30°, 35° and 40°. For this first optimisation step, the shroud angle and shroud length of the cycloidal diffuser were kept constant at 2° and $0.48D$, respectively. The cycloidal diffuser parameters and optimization step were discussed in detail in Subsection 3.4.2. The moment and power coefficients of the HDWT using each diffuser length and angle were calculated and presented in Figures 4.29 and 4.30, respectively. The percentage difference in power coefficient between the HDWT augmented by cycloidal diffuser and bare HDWT was also calculated, as shown in Table 4.1.

From the results obtained, the diffuser length of $0.50D$ with a diffuser angle of 35° gave the highest performance enhancement with C_p of 0.2234, which is equivalent to a 10.98% increase compared to the bare HDWT design. At the smallest diffuser angle of 15°, most diffuser lengths decreased the HDWT performance. At 20°, the $1.25D$ diffuser caused a reduction in performance, but $1.0D$ $0.75D$ and $0.25D$ diffusers

showed slight performance improvements, while the 0.5D diffuser gave the highest performance improvements of 6.51%. The diffuser angles of 30° and 35° are the preferred design as they produced the highest C_p increase for the HDWT except for the diffuser with length 1.25D, where the angle of 35° decreased the HDWT performance. For diffusers of lengths 1.25D, the optimum diffuser angle is 30°, while for diffusers of length 1.0D, 0.75D, 0.50D and 0.25D, the optimum diffuser angle is 35°. Overall, a shorter diffuser length with a bigger diffuser angle enhanced HDWT performance the most. Using the 0.50D length diffusers with a diffuser angle of 35° produced the highest C_p among all configurations tested.

Table 4.1. Moment and power coefficients of HDWT using cycloidal diffusers with different diffuser lengths and diffuser angles at TSR 1.5.

Diffuser Design		C_m	C_p	**Percentage Deviation from Bare HDWT (%)**
Diffuser Length, L_b	**Diffuser Angle, ϕ**			
No Diffuser (Bare HDWT)		0.1342	0.2013	-
1.25D	15°	0.1307	0.1961	-2.583
	20°	0.1336	0.2004	-0.447
	30°	0.1385	0.2078	3.229
	35°	0.1339	0.2009	-0.199
	40°	0.1300	0.1950	-3.130
1.0D	15°	0.1332	0.1998	-0.745
	20°	0.1361	0.2042	1.441
	30°	0.1409	0.2114	5.017
	35°	0.1422	0.2133	5.961
	40°	0.1383	0.2075	3.080
0.75D	15°	0.1326	0.1989	-1.192
	20°	0.1386	0.2079	3.279
	30°	0.1454	0.2181	8.346
	35°	0.1456	0.2184	8.495
	40°	0.1432	0.2148	6.706
0.50D	15°	0.1376	0.2064	2.534
	20°	0.1429	0.2144	6.508

	30°	0.1471	0.2207	9.637
	35°	0.1489	0.2234	10.979
	40°	0.1464	0.2196	9.091
0.25*D*	15°	0.1341	0.2012	-0.050
	20°	0.1392	0.2088	3.726
	30°	0.1422	0.2133	5.961
	35°	0.1485	0.2228	10.681
	40°	0.1478	0.2217	10.134

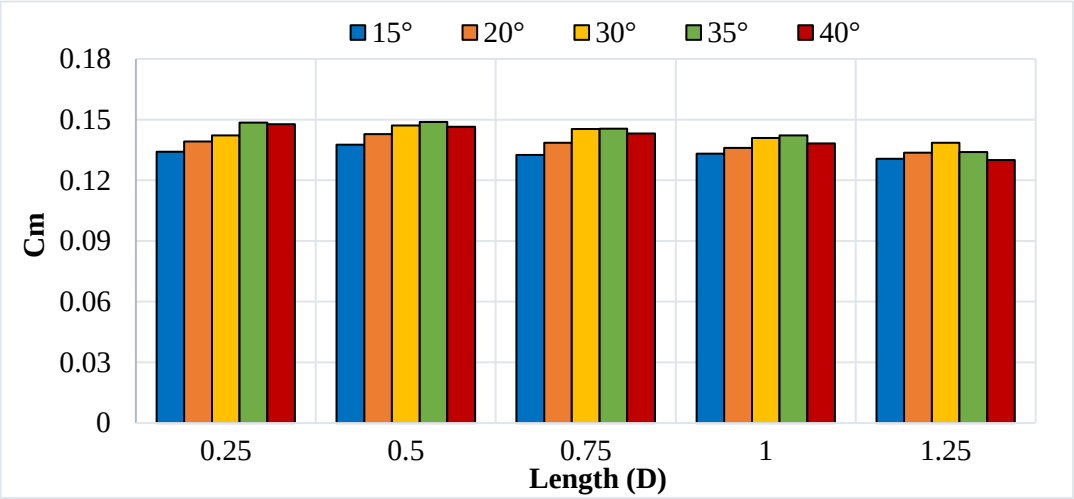

Figure 4.29. Moment coefficient for HDWT using cycloidal diffusers of different diffuser lengths and with diffuser angles of 15°, 20°, 30°, 35° and 40° at TSR 1.5.

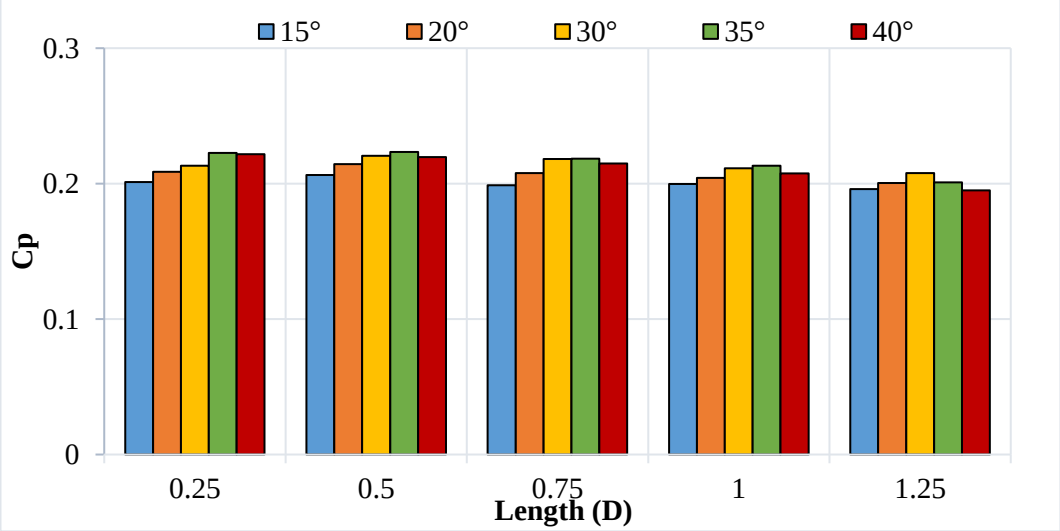

Figure 4.30. Power coefficient for HDWT using cycloidal diffusers of different diffuser lengths and with diffuser angles of 15°, 20°, 30°, 35° and 40° at TSR 1.5.

4.3.1.1 Flow analysis of the cycloidal diffusers with diffuser angles of 15°, 35°, and 40° with constant diffuser length of 0.5D

Figures 4.31 to 4.34 are presented to discuss the effect of using varying diffuser angles on the HDWT's moment and power coefficient while keeping the diffuser length constant at $0.5D$. The diffuser angles chosen for this analysis are 15°, which produced the lowest C_m, 35°, which produced the highest C_m, and 40°, to show how increasing the diffuser's angle above the optimum angle starts to deteriorate the HDWT performance. It can be seen from Figure 4.31 that the differences between the blade's instantaneous moment throughout the rotation are minimal, with the 35° diffuser angle generating just a slightly higher instantaneous C_m for most of the blade azimuthal angles. The radar plot in Figure 4.32 depicts that the 35° diffuser angle notably produces higher C_m than the other two cases from azimuthal angles of 75° to 90°. To study the reason behind this, the velocity contours and the pressure contours with velocity streamlines at θ=90° are presented as shown in Figures 4.33 and 4.34, respectively. From the streamlines, it is evident that the diffuser angles of 35° and 40° create higher velocity towards the upwind side (45° to 135°) and the windward side (0° to 45°) and (315° to 360°) of the HDWT, where wind turbines generate the most torque [48], [60]. This creates a higher pressure difference between the blade surfaces, as shown by blades 1 & 3 for the diffuser angles of 35° and 45° in Figure 4.34, consequently increasing the blade's positive instantaneous moments at these positions, as shown in Figure 4.31.

Diffusers are used in many VAWT studies to further increase their performance by using the flange's ability to generate vortices, which helps to decrease the pressure downstream, resulting in higher pressure differences between the upwind and downwind regions [78]. The higher pressure difference between the two regions will then cause the air to be accelerated through the diffuser, increasing the velocity of the air interacting with the VAWT [79]. From Figure 4.34, the 15° diffuser angle creates more vortices. Even though the 15° diffuser has more vortices, it still has a lower overall C_m as compared to the other two cases. This is because the vortices are smaller and detach further from the HDWT near the wake region. In contrast, the vortices created by the flanges at the left diffusers of 35° and 40° are bigger and closer to the diffuser surface, which creates a lower pressure region closer to the downwind region of the HDWT. This, in turn, increases the exhaust air velocity flowing through the

diffuser and HDWT. Hashem and Mohamed [42] reported similar findings on the effect of the vortex size and location downstream of the flange on the wind turbine performance. They reported that the flange fades in effect as the vortex is further away from the flanged diffuser.

Figure 4.34 illustrates that for the 35° diffuser angle, the low-pressure vortices, which are attached to the left diffuser close to blade 3, reduce the pressure on the blade suction side. This causes the blade's instantaneous moment at that position (330°) to be higher than the other two cases, contributing to the overall higher performance at θ=90°. The 40° diffuser follows this, with a slightly lower instantaneous moment due to a larger opening angle that reduces the strength of the opposite-direction vortices behind the flange. These observations are in line with the study done by Dessoky et al. [83], where it was communicated that increasing the diffuser angle improves the VAWT performance due to the strength of vortices generated until a certain angle, where increasing it further deteriorates the vortices formation and strength.

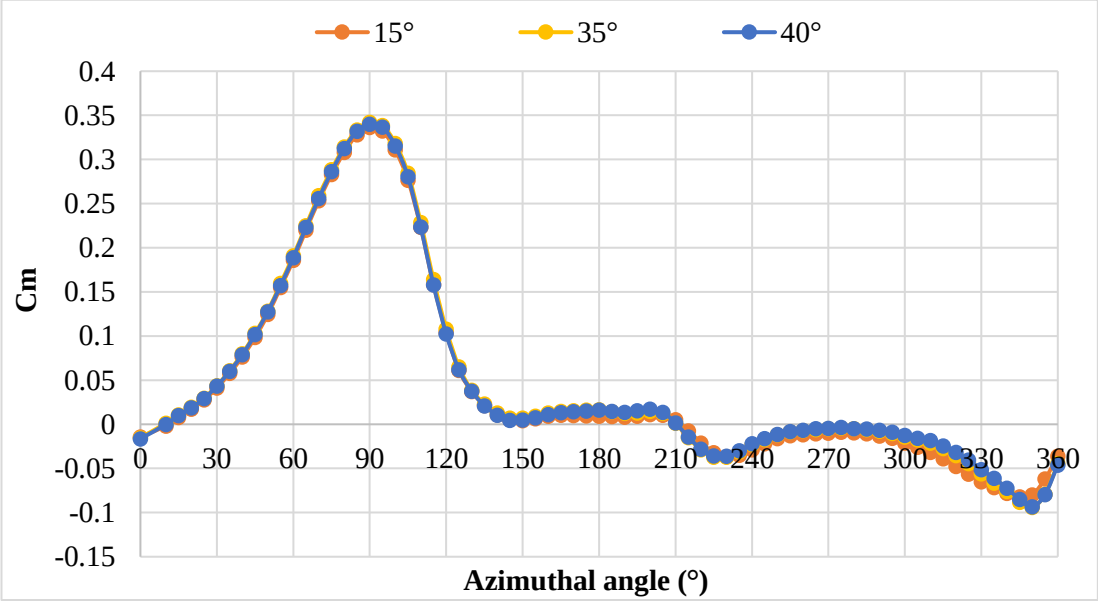

Figure 4.31. Single blade instantaneous C_m against azimuthal angles for HDWT using cycloidal diffusers with diffuser angles of 15°, 35°, and 40° with a constant diffuser length of 0.5D.

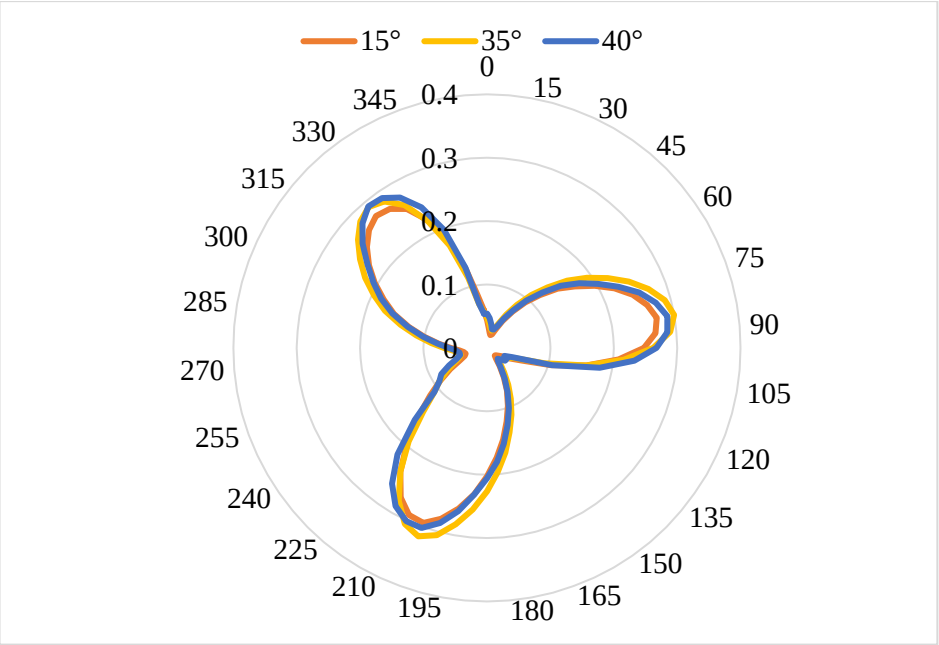

Figure 4.32. Instantaneous C_m against azimuthal angles for HDWT using cycloidal diffusers with diffuser angles of 15°, 35°, and 40° with a constant diffuser length of $0.5D$.

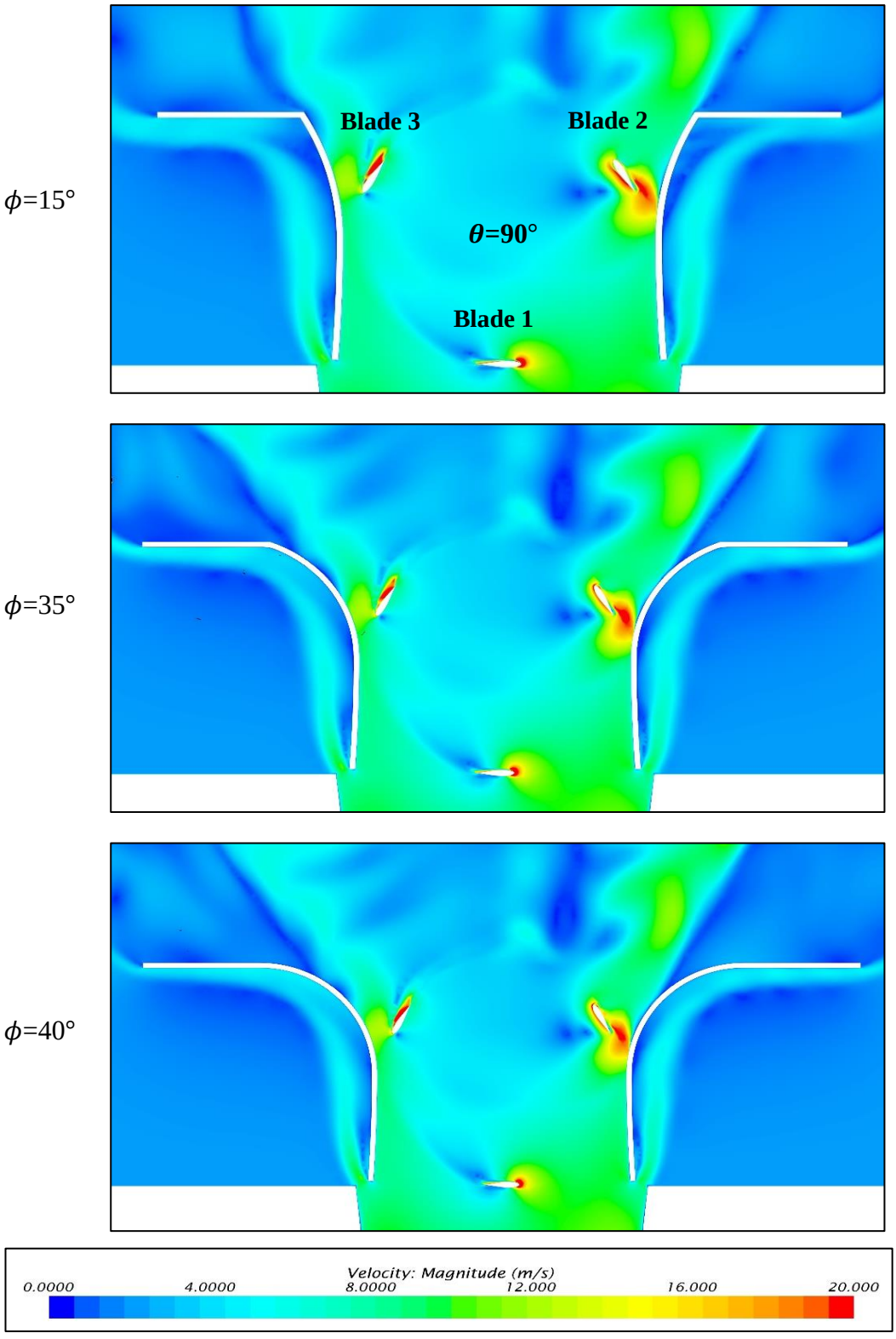

Figure 4.33. Velocity contour comparison around the augmented HDWT using cycloidal diffusers with angles of 15°, 30°, and 45° with a constant diffuser length of 0.5D at θ = 90°.

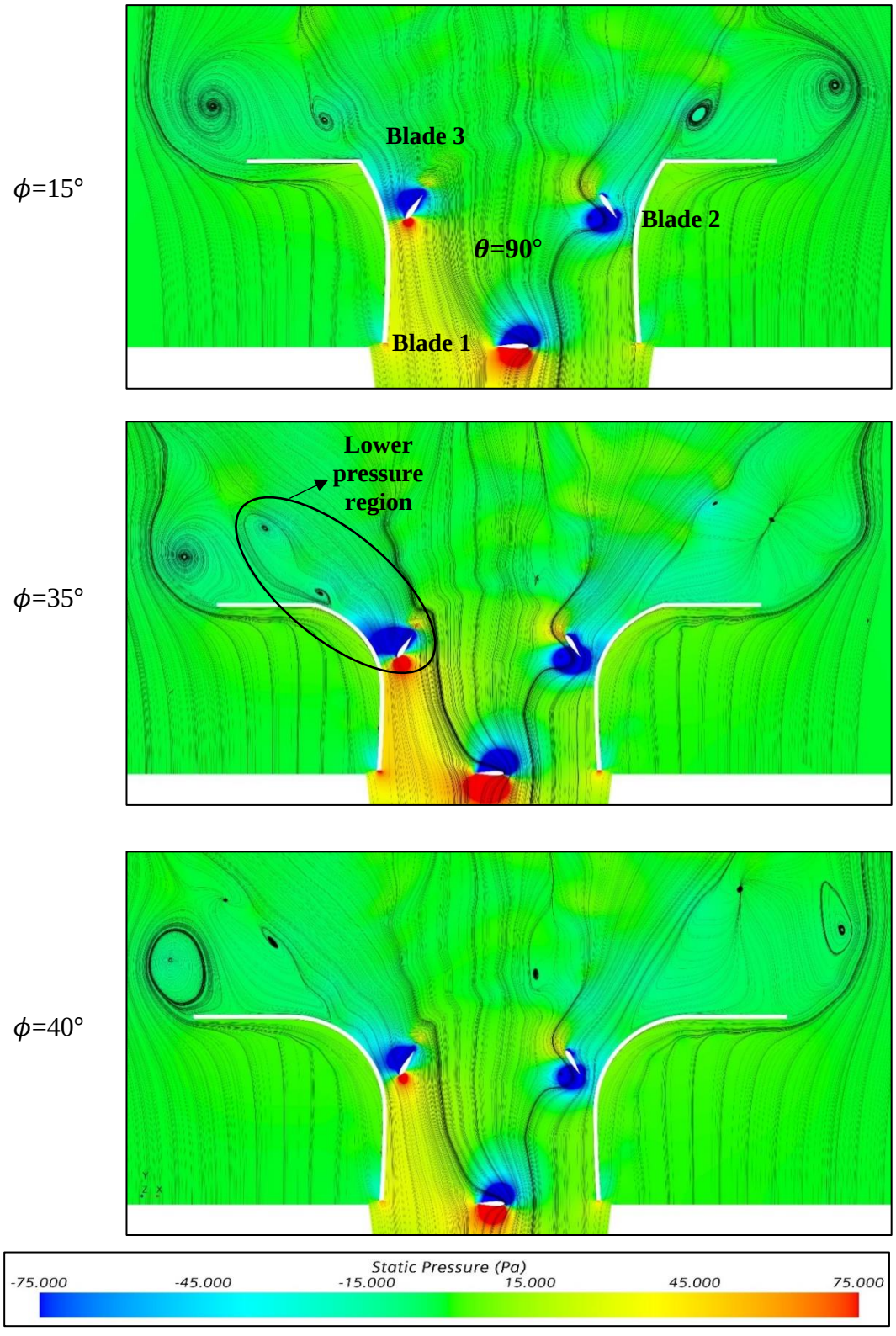

Figure 4.34. Pressure contour with velocity streamline comparison around the augmented HDWT using cycloidal diffusers with angles of 15°, 30°, and 45° with a constant diffuser length of 0.5D at θ = 90°.

4.3.1.2 Flow analysis of the cycloidal diffusers with diffuser lengths of 0.25D, 0.5D, and 1.25D with constant diffuser angle of 35°

It was shown in Figures 4.29 and 4.30 that the performance enhancement capability of the cycloidal diffusers decreases with increasing diffuser lengths. The cycloidal diffusers with lengths of 0.25D and 0.5D perform much better than the longer diffuser lengths. Figures 4.35 to 4.38 are presented to discuss the variation in the HDWT's moment and power coefficient using cycloidal diffusers with varying diffuser lengths while keeping the diffuser's angle constant at 35°. The diffuser lengths chosen for this analysis are 0.25D, 0.5D, and 1.25D to show the deviation in HDWT performance between different lengths of the diffusers. It can be seen from Figures 4.35 and 4.36 that the diffuser of lengths 0.25D and 0.5D produced the highest C_m throughout the entire HDWT rotation, while the 1.25D diffuser has a lower overall C_m. The difference between the C_p produced by the cycloidal diffuser of diffuser lengths 0.25D (C_p=0.1485) and 0.5D (C_p=0.1489) with a diffuser angle of 35° is very minimal as shown earlier in Table 4.1. The cycloidal diffuser with a diffuser length of 1.25D only produced a C_p of 0.1339 using the same diffuser angle of 35°.

The radar plot in Figure 4.36 depicts that the HDWT using 1.25D diffuser length has a relatively lower C_m compared to the other two cases from azimuthal angles of 60° to 90°. To study the reason behind this, the velocity contours and the pressure contours with velocity streamlines at θ=90° are presented as shown in Figures 4.37 and 4.38, respectively. From Figure 4.38, the diffusers with lengths of 0.25D and 0.5D have vortex formations near the flanges, but this is not the case for the diffuser of 1.25D length. This clearly shows that the 0.25D and 0.5D diffuser lengths create lower pressure at the HDWT's downwind region, which increases the velocity of the air passing through the HDWT and diffusers, as shown in Figure 4.37. The increased velocity is the main reason for the greater HDWT power coefficients produced by 0.25D and 0.5D diffusers. Hashem and Mohamed [42], Ohya et al. [78], and Krishnan and Paraschivoiu [79] have previously shown that the low-pressure vortex helps accelerate the wind through the diffuser, improving turbine performances.

The 1.25D length diffuser does not produce vortices due to the longer and wider design guiding the air for a longer and wider distance before approaching the flanges, resulting in less obstacle effect. Therefore, the 1.25D diffuser length cancels out the effectiveness of the flange in forming vortices. In contrast, the shorter diffusers result

in more air flowing directly to the flanges, creating a more blockage effect that forms more low-pressure vortices. This finding corroborates with the work by Hashem and Mohamed [42], where it was highlighted that the flanges can only cause significant improvement to the VAWT performance if the flanges shield enough air to form vortices.

The 0.25D diffuser has bigger vortices compared to the 0.5D diffuser. However, they are far away from the flanges, which limits the ability to create a low-pressure region at the downwind region of HDWT. In the case of the 0.5D diffuser, the high-velocity air is created by the combination of vortices on the flanges and the longer diffuser length, which is more convergent. Moreover, the air flows more smoothly into the 0.5D length diffuser than the 0.25D diffuser. The same observation was communicated by Dessoky et al. [83], where the diffuser length of 1D gives smoother flow that accelerates the wind more, compared to the shorter length (0.5D) and longer length (1.5D) diffusers in their study. The difference in the best diffuser length between their study and this study could be the type of diffuser used, as their study uses a flat-panel diffuser.

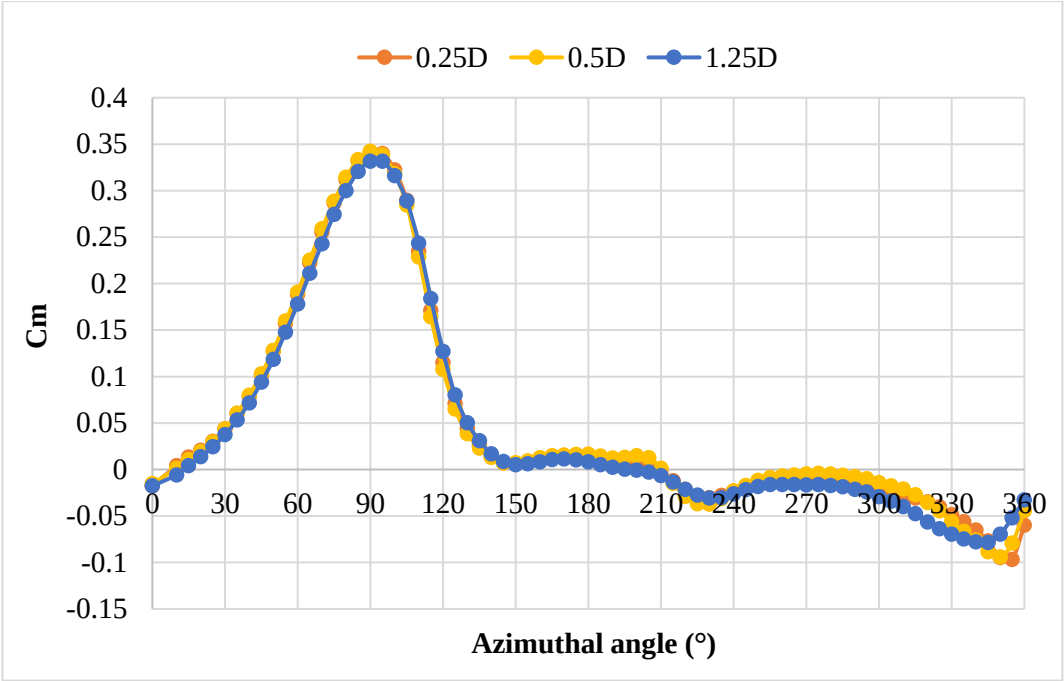

Figure 4.35. Single blade instantaneous C_m against azimuthal angles for HDWT using cycloidal diffusers with diffuser lengths of $0.25D$, $0.5D$, and $1.25D$ with a constant diffuser angle of 35°.

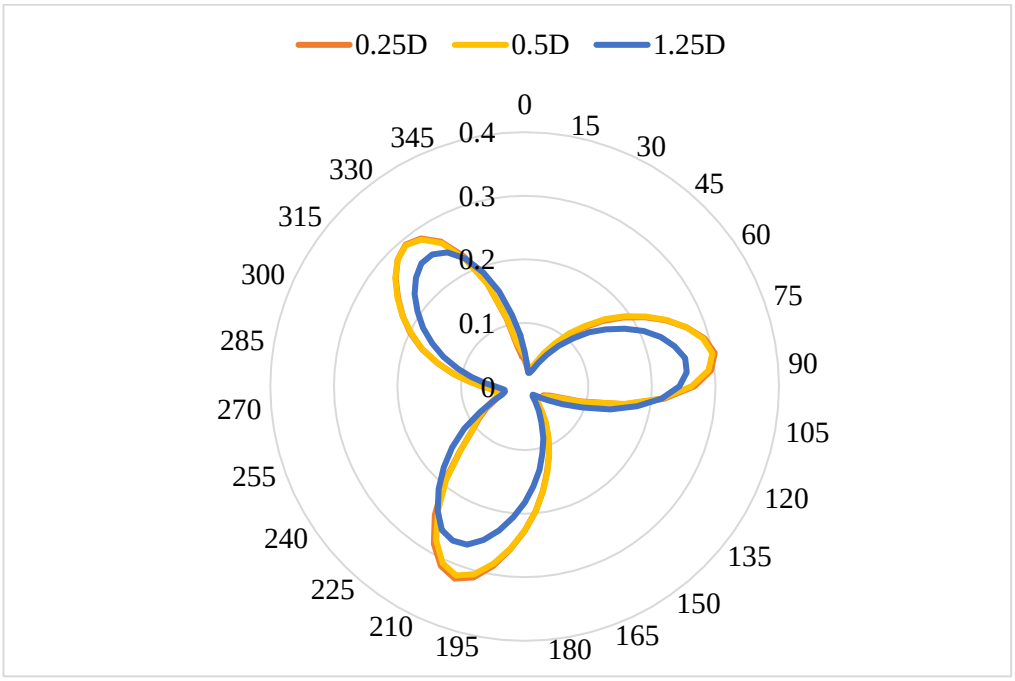

Figure 4.36. Instantaneous C_m against azimuthal angles for HDWT using cycloidal diffusers with diffuser lengths of $0.25D$, $0.5D$, and $1.25D$ with a constant diffuser angle of 35°.

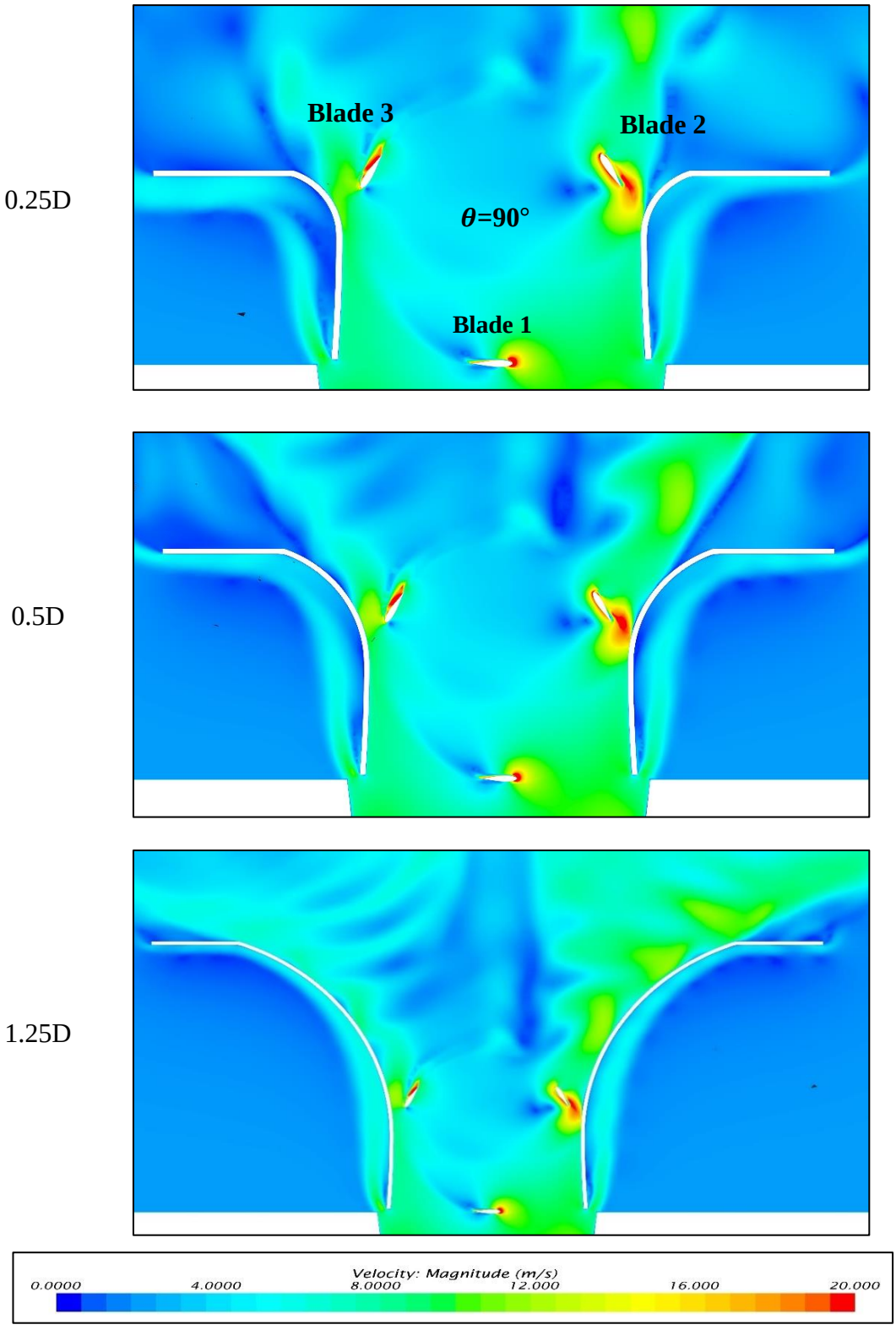

Figure 4.37. Velocity contour comparison around the augmented HDWT using cycloidal diffusers with diffuser lengths of 0.25D, 0.5D, and 1.25D with a constant diffuser angle of 35° at θ = 90°.

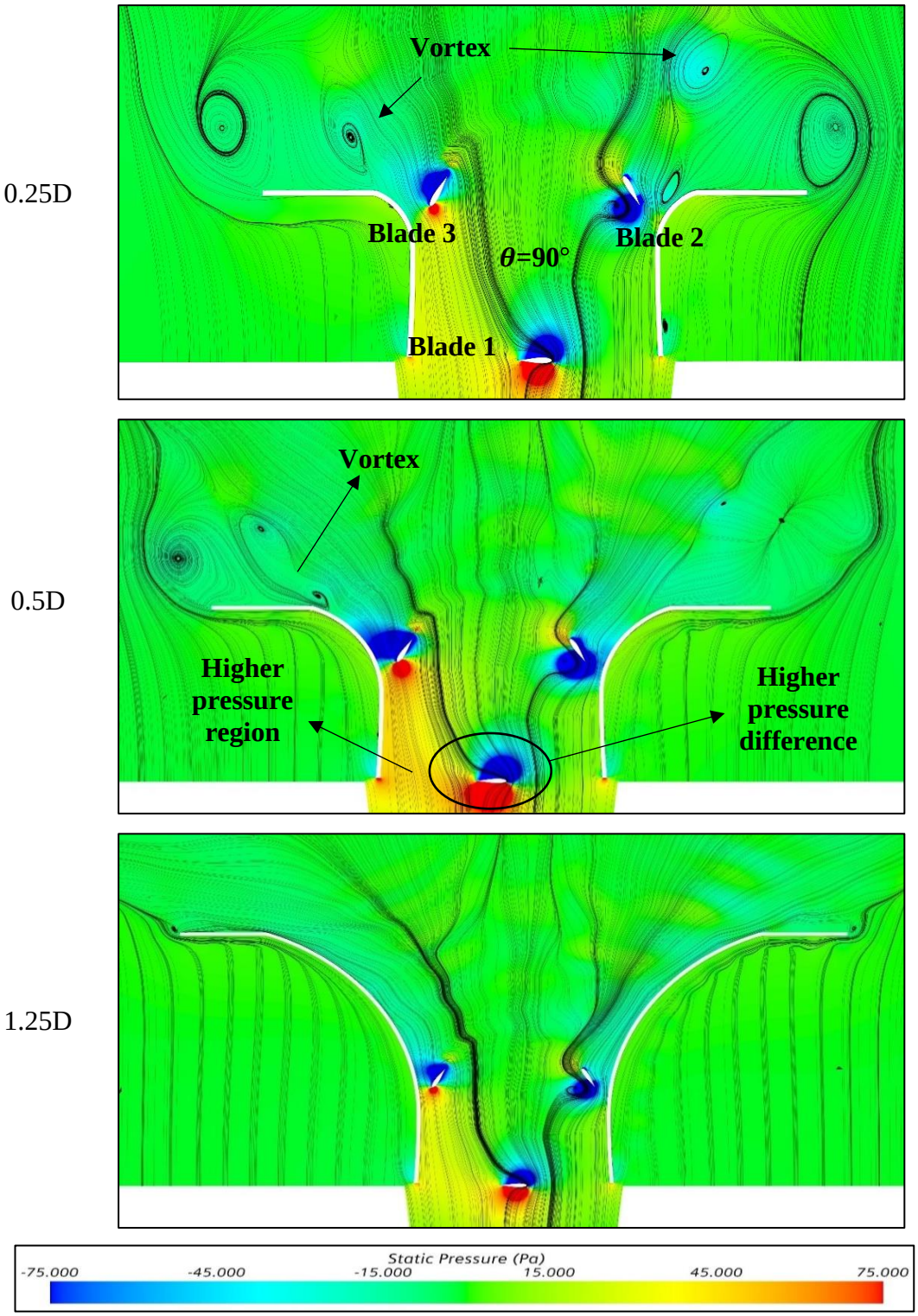

Figure 4.38. Pressure contour with velocity streamlines comparison around the augmented HDWT using cycloidal diffusers with diffuser lengths of 0.25D, 0.5D, and 1.25D with a constant diffuser angle of 35° at θ = 90°.

4.3.2 Parametric study of shroud length

Efforts to further improve the cycloidal diffuser design were made by testing four different shroud lengths at TSRs of 1.5, 2.0, 2.5 and 3.0 to study the effects of shroud lengths on the HDWT performance under cooling tower exhaust air. For this step, the shroud angle was kept constant at 2° while the diffuser length and angle were set using the best result obtained from Subsection 4.3.1, which are $0.50D$ and 35°, respectively. The results are shown in the moment and power coefficient plots in Figure 4.39 and 4.40, respectively. The diffuser with a shroud length of $0.48D$ gave the highest HDWT moment and power coefficient at all TSRs tested. The peak performance of the HDWT was achieved at TSR 2.0 for all shroud lengths, similar to the case of bare HDWT. At TSR 2.0, the diffuser with a shroud length of $0.48D$ improves the HDWT performance by 27.85% compared to the bare HDWT design. The diffuser without any shroud ($\gamma = 0D$) and shroud length of $0.25D$ achieved the lowest performance, giving lower moment and power coefficients than the case of bare HDWT.

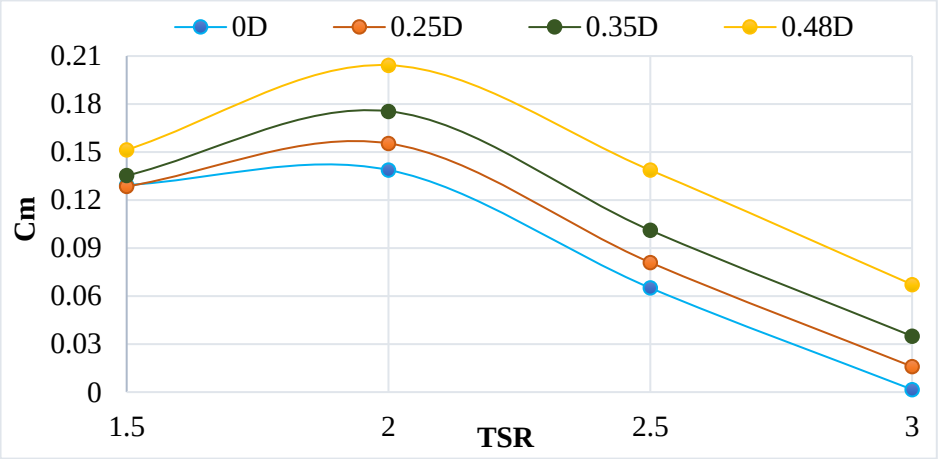

Figure 4.39. Moment coefficient of HDWT using cycloidal diffusers with shroud lengths of 0D, 0.25D, 0.35D and 0.48D.

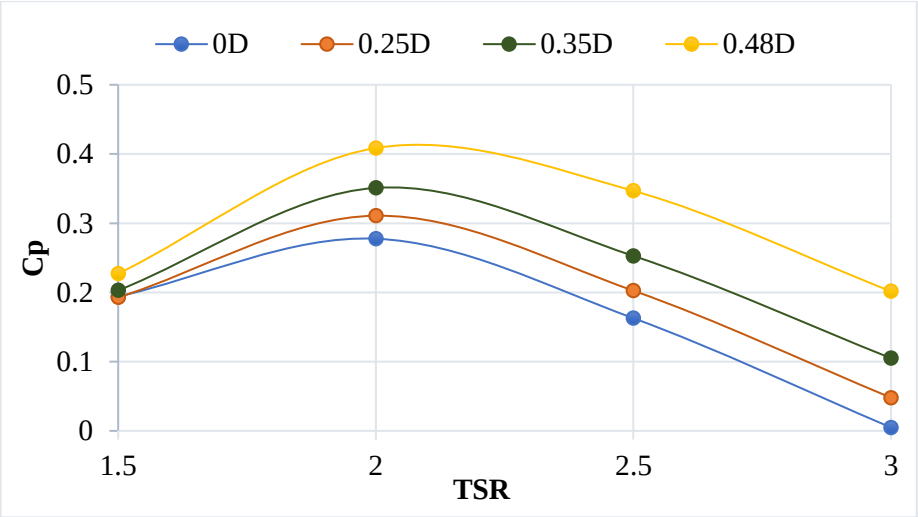

Figure 4.40. Power coefficient of HDWT using cycloidal diffusers with shroud lengths of 0D, 0.25D, 0.35D and 0.48D.

Figures 4.41 to 4.44 are presented to discuss the variation in the moment and power coefficient using cycloidal diffusers of different shroud lengths with a constant diffuser length and diffuser angle of $0.5D$ and 35°, respectively. It can be seen from Figure 4.42 that the $0D$ shroud length produces the least C_m for the full 360° rotation of the HDWT. This shows that including a shroud plays a vital role in further enhancing the power augmentation ability of the cycloidal diffusers. Comparing the two cases of using shrouds of lengths $0.35D$ and $0.48D$, the longer shroud increased the HDWT performance more, especially by exhibiting much higher instantaneous C_m for almost the full upwind rotation (0° to 180°).

Figures 4.43 and 4.44 are presented to discuss the reason behind the greater performance of using the cycloidal diffuser with a longer shroud length ($0.48D$). The velocity contour in Figure 4.43 shows that the presence of a shroud allows the diffusers to guide and accelerate more of the exhaust air through it, resulting in the HDWT interacting with much higher air velocity. This directly causes the HDWT blades to experience a much higher pressure difference between the pressure and suction side of the blades, as shown in Figure 4.44. The pressure difference is highest at the upwind location, as seen in the pressure contour presented, justifying the plots in Figures 4.41 and 4.42. The presence of a longer shroud helps create a converging shape and guides more exhaust air, increasing its velocity towards the HDWT, especially at azimuthal angles of 0° to 180°.

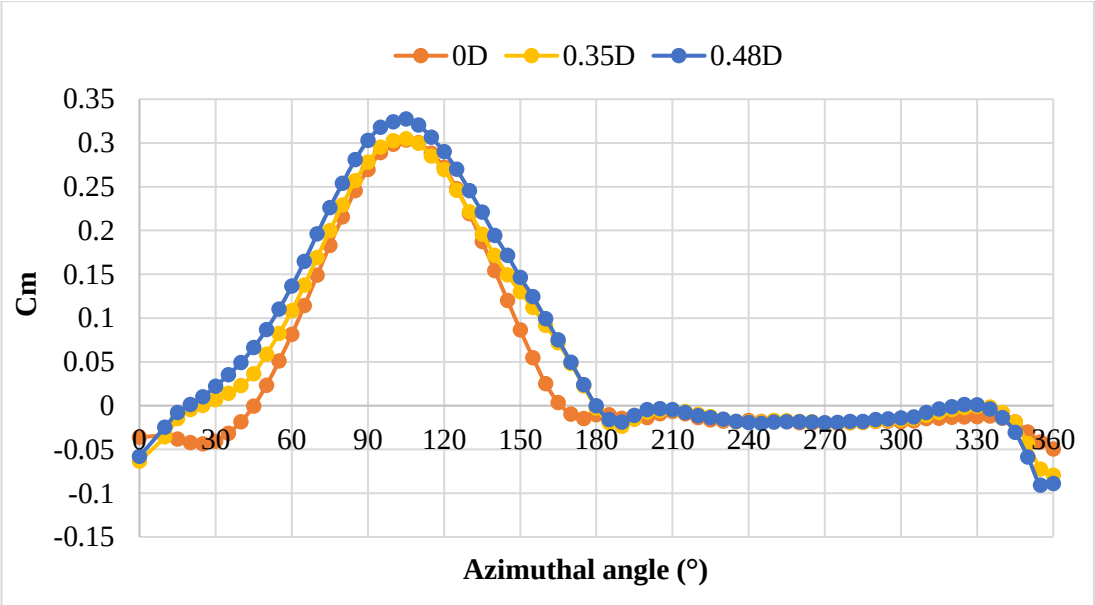

Figure 4.41. Single blade instantaneous C_m against azimuthal angles for HDWT using cycloidal diffusers with shroud lengths of $0D$, $0.35D$, and $0.48D$.

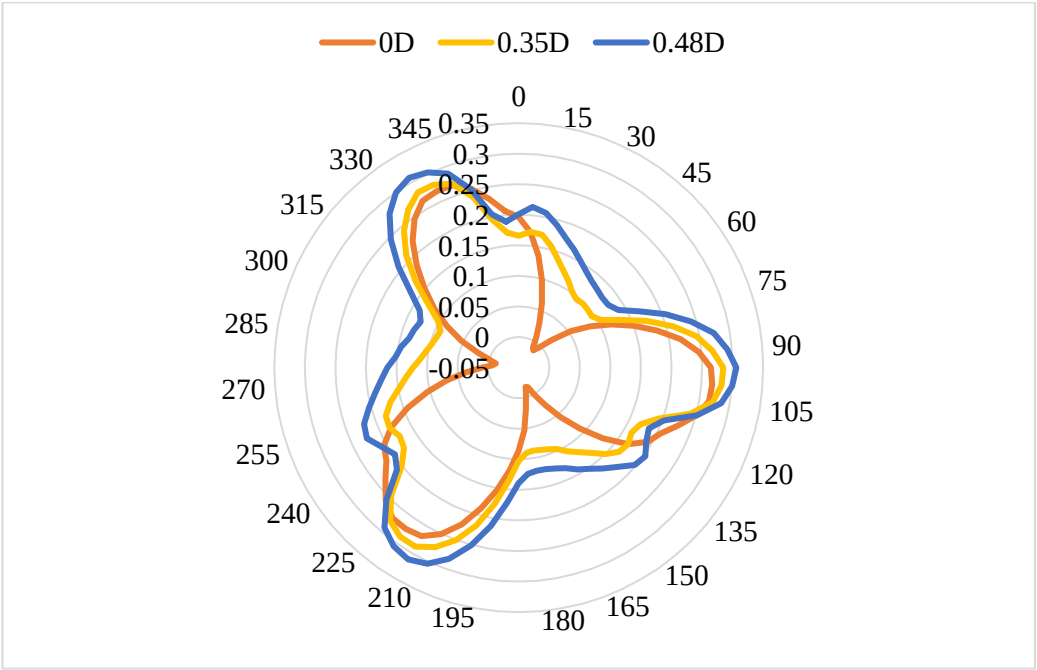

Figure 4.42. Instantaneous C_m against azimuthal angles for HDWT using cycloidal diffusers with shroud lengths of $0D$, $0.35D$, and $0.48D$.

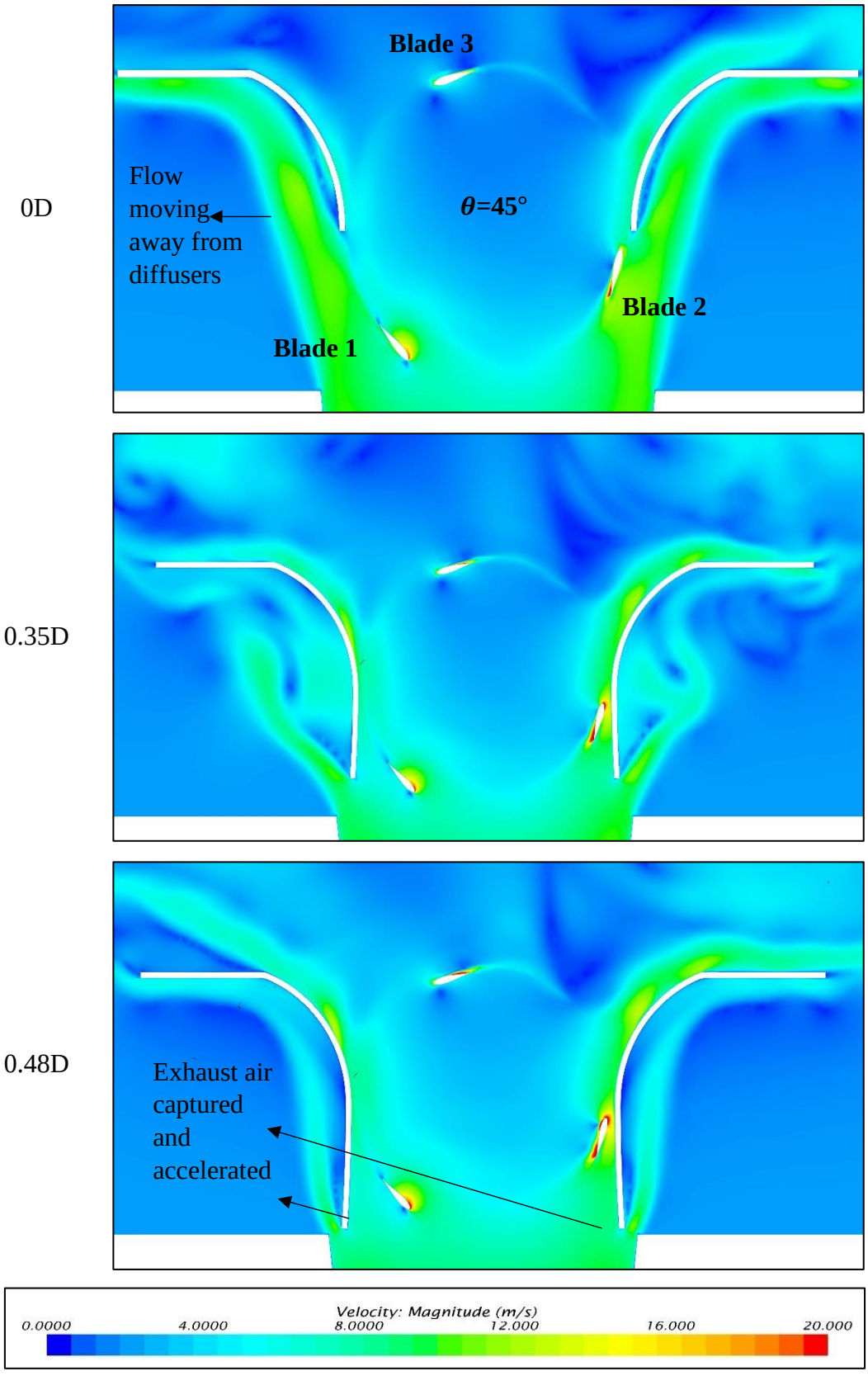

Figure 4.43. Velocity contour comparison around the augmented HDWT using cycloidal diffusers with shroud lengths of $0D$, $0.35D$, and $0.48D$ at θ = 45°.

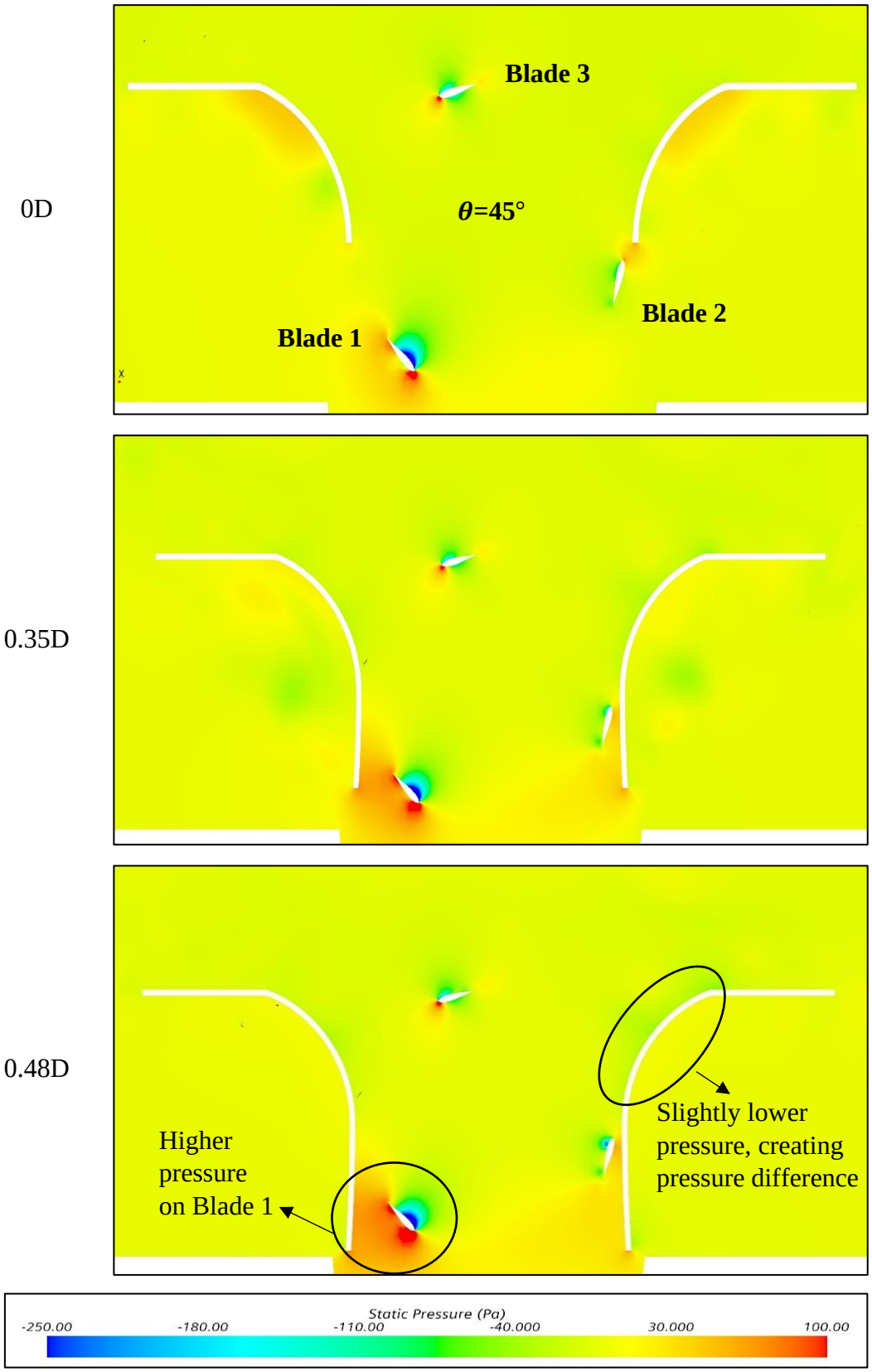

Figure 4.44. Pressure contour comparison around the augmented HDWT using cycloidal diffusers with shroud lengths of $0D$, $0.35D$, and $0.48D$ at θ = 45°.

4.3.3 Parametric study of shroud angle

Once the best diffuser length, diffuser angle and shroud length have been determined from the previous two parametric study steps, the parametric study on the cycloidal diffusers' shroud angle is done by testing five different angles of 0°, 2°, 4°, 7°, and 10° at TSRs of 1.5 to 3.0 to obtain the best performance for the HDWT under cooling tower exhaust air. The diffuser length was kept at $0.5D$, the diffuser angle kept at 35°, and the shroud length kept at $0.48D$, which are the best parameters from Subsections 4.3.1 and 4.3.2. Figures 4.45 and 4.46 show the moment and power coefficient plots, respectively, for the diffuser with different shroud angles. The shroud angle of 7° produced the highest performance increase at all TSRs, giving the highest C_p of 0.4118 at TSR 2.0. This is equivalent to a 28.85% increase in performance compared to the bare HDWT.

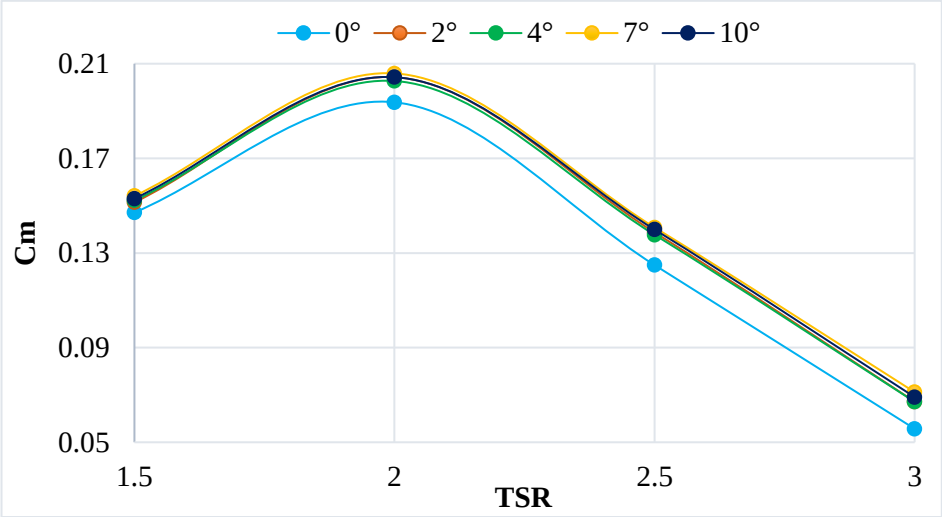

Figure 4.45. Moment coefficient of HDWT using cycloidal diffusers with shroud angles of 0°, 2°, 4°, 7° and 10°.

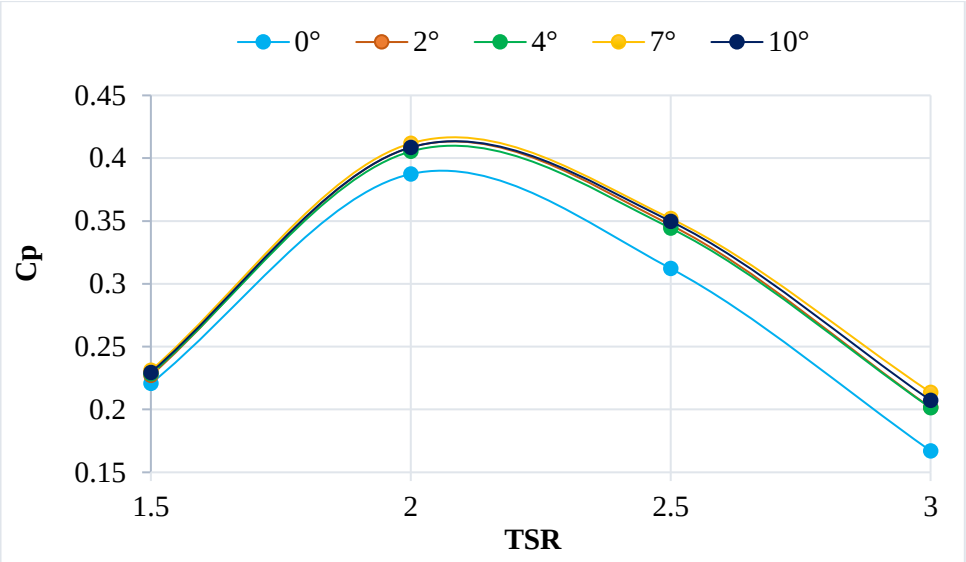

Figure 4.46. Power coefficient of HDWT using cycloidal diffusers with shroud angles of 0°, 2°, 4°, 7° and 10°.

It can be seen from Figure 4.47 that the difference in C_p produced by the shrouds of angles 2° to 10° is very small and barely noticeable. The diffuser with a shroud angle of 0° produced a noticeably lower C_p compared to the other shroud angles mentioned at all the TSRs tested. Figures 4.47 to 4.49 are presented to discuss the variation in the moment and power coefficient produced by the cycloidal diffusers of shroud angles 0° and 7° with a constant diffuser length, diffuser angle, and shroud length of $0.5D$, 35°, and $0.48D$, respectively. The instantaneous moment graph in Figure 4.47 shows that the diffuser with a shroud angle of 7° outperforms the 0° shroud for the first half of the cycle.

Figure 4.49 shows the pressure contour and streamlines comparison of the 0° and 7° diffuser angles. The flow is captured and guided smoothly by the wider shroud angle diffuser. Moreover, the flow is also accelerated due to the curved shaped exhibited by the 7° shrouded diffuser, as shown by the streamlines, resulting in the blades rotating in the windward direction to experience higher velocity air. This increases the pressure on the pressure side of the blade, resulting in a higher pressure difference between the blades' pressure and the suction side. The blade then contributes to more lift force and moment, increasing the coefficient of power of the HDWT. In contrast, the diffuser with a 0° shroud angle experiences a slightly lower pressure difference due to lesser acceleration.

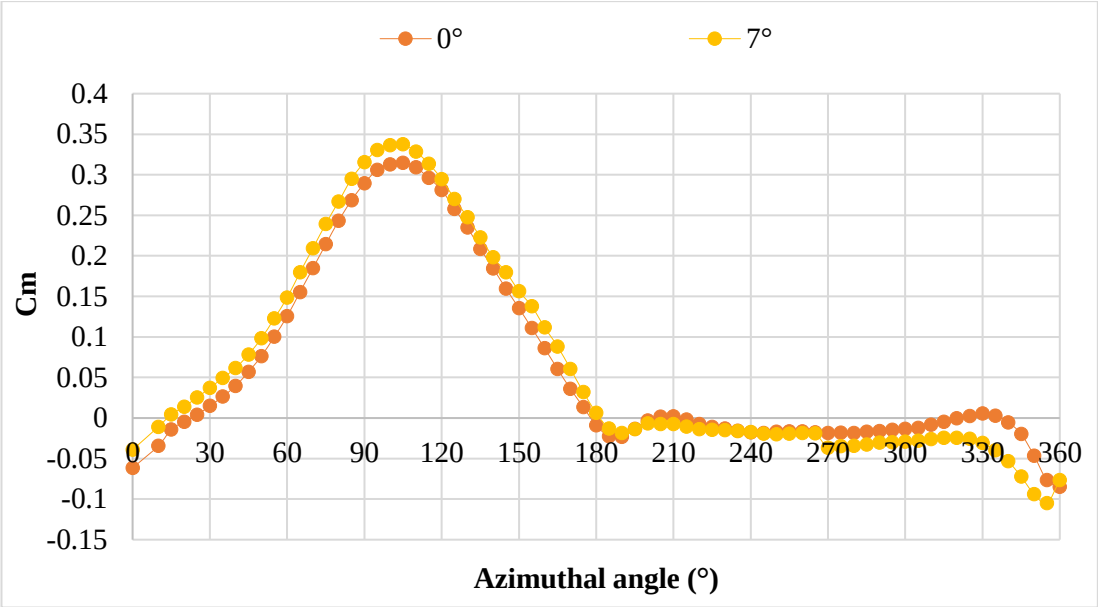

Figure 4.47. Single blade instantaneous C_m against azimuthal angles for HDWT using cycloidal diffusers with shroud angles of 0° and 7°.

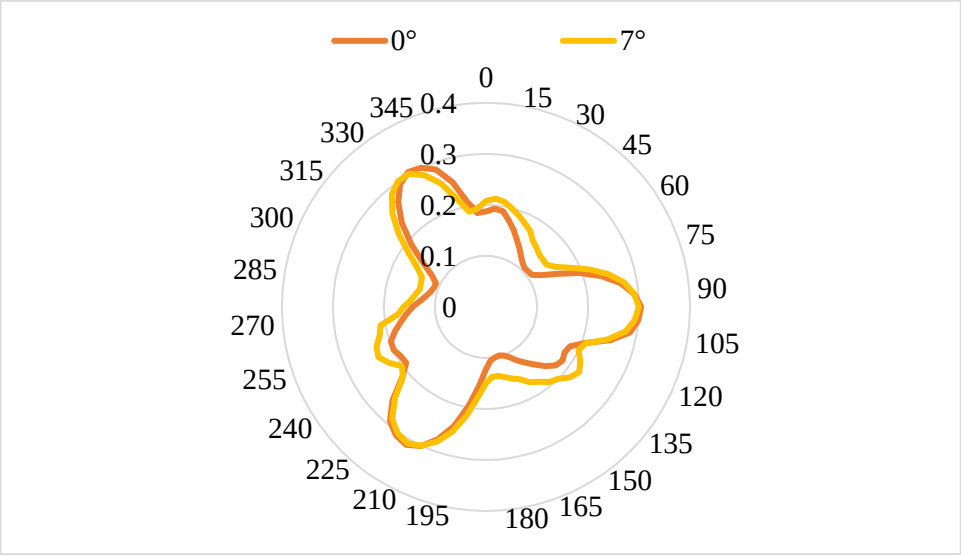

Figure 4.48. Instantaneous C_m against azimuthal angles for HDWT using cycloidal diffusers with shroud angles of 0° and 7°.

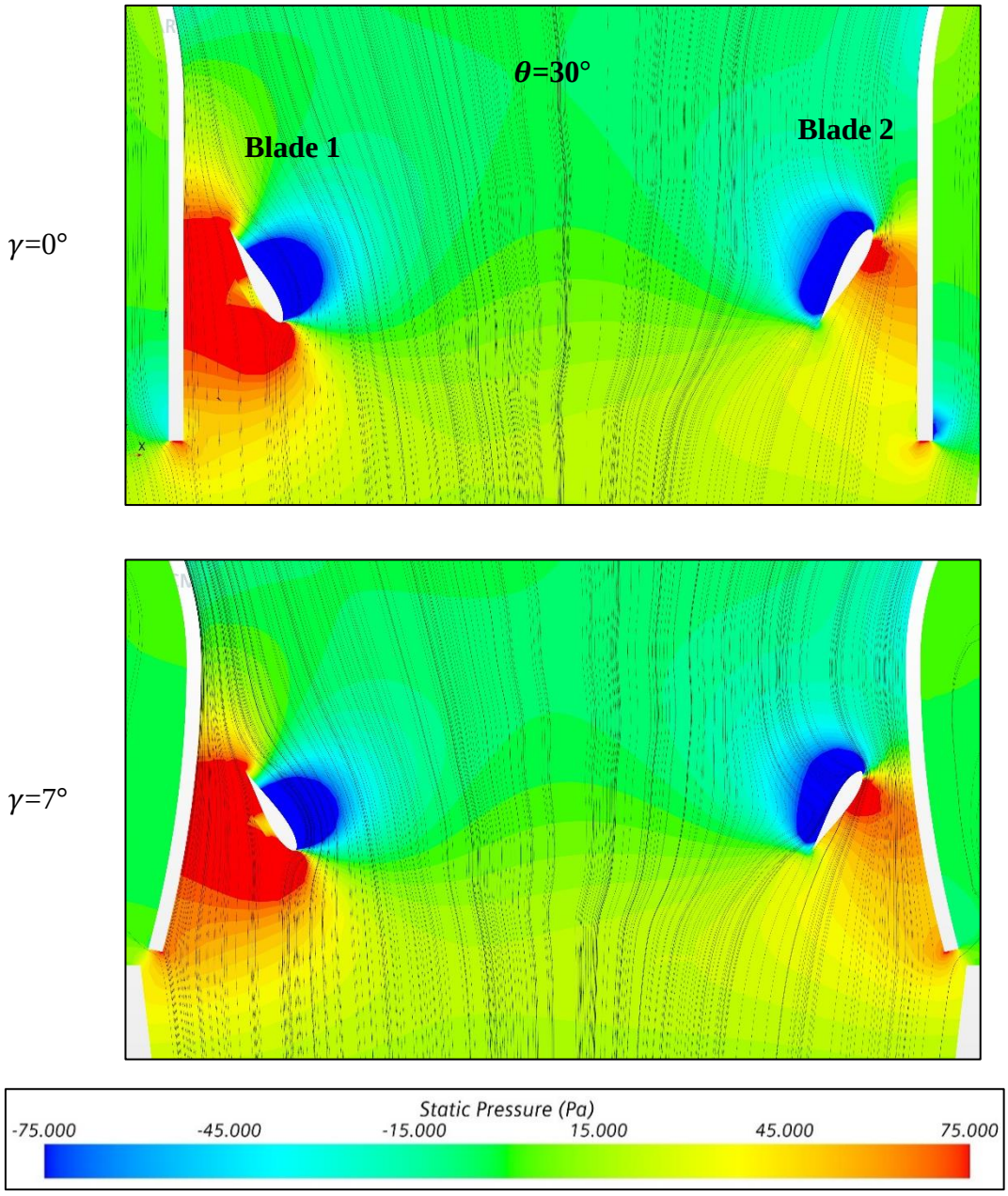

Figure 4.49. Pressure contour with velocity streamline comparison around the augmented HDWT using cycloidal diffusers with shroud angles of 0° and 7° at θ = 30°.

CHAPTER 5: DESIGN OPTIMIZATION OF CYCLOIDAL DIFFUSERS FOR EXHAUST AIR ENERGY EXTRACTIONS

5.1 Optimization using Response Surface Methodology

In this chapter, design optimization on the cycloidal diffuser design parameters is done to obtain the best design for maximizing the power coefficient of the cooling tower exhaust air energy recovery system. This optimization is carried out by 3D simulation using parameters generated by a design of experiment software, Design Expert. The design method used was RSM with an Optimal Design of 4 numeric factors, including diffuser length, diffuser angle, shroud length and shroud angle. The levels of each numeric factor are described in Subsection 5.1.1. Optimal Design was chosen to spread the design throughout the design space as this is desirable for computational study. Fifteen lack of fit were added to the design to maximize the combination of each factor and spread the design space to improve the precision of the design. Since this is a computational study, no replicates were added, as repeating the same simulation with the same parameter condition will result in the same response. The type of design space search was set as both exchanges, as this is the best combination of point exchange and coordinate exchange. I-optimality or integrated variance design was chosen as this is desired for RSM to minimize the integral of prediction variance across the design space to improve precision for the optimization process. The quadratic model was chosen as the base model. The response for this study is the coefficient of power of the HDWT. Applying these conditions resulted in 30 runs, as shown in Table 5.2.

Once the simulations were done, the response was input into the design table, and an analysis was performed using ANOVA to evaluate the contribution of each factor and the interactions between them. A regression model was used to fit the data with a quadratic polynomial equation. Then, response surface plots were used to study the interactions between the numeric factors. Lastly, numerical optimization was done to identify the most optimum design for achieving the highest coefficient of power from the cooling tower exhaust air energy recovery system, and extra computational runs validated this design.

5.1.1 Diffuser design parameters selection

As shown in Figure 3.5, Figure 3.6 and Table 3.6, the cycloidal diffuser parameters for this study have been defined by a front inlet section named shroud and a back exit part named diffuser. In Section 4.3, the effect of the diffuser length, diffuser angle, shroud length, and shroud angle was studied individually by varying it one at a time while keeping other design parameters constant. To maximize the power coefficient of the HDWT under cooling tower exhaust air, the cycloidal diffuser design needs to be further improved by optimization to study the effect and interaction that may occur between the parameters mentioned. These four parameters mentioned are the independent variables for this optimization study. In Subsection 4.3.1, the diffuser length was optimized with the diffuser angle. The results showed that the HDWT power coefficient reduces as the diffuser length is increased beyond $1.0D$ (D= HDWT diameter). So, the range of the diffuser length selected for this optimization study is from $0.25D$ (114mm) to $0.75D$ (342mm). The diffuser angle study in Subsection 4.3.1 showed that at angles below 20°, a low power coefficient was obtained, while at angles of 30°, 35° and 40°, the HDWT gives a high power coefficient. Therefore, for this optimization study, the diffuser angles are set to 4 levels (25°, 32°, 38° and 45°). Next, the shroud length parametric study in Subsection 4.3.2 clearly shows that the longer shroud length (218mm) is the best length to maximize the power coefficient of the HDWT. However, since the interaction between the cycloidal diffuser parameters needs to be studied, three levels of the shroud length (114mm, 166mm, 218mm) were chosen as one of the independent variables. Lastly, four levels of shroud angles, 2°, 5°, 8°, and 11°, were chosen to optimize the HDWT power coefficient. The summary of the independent variables of this optimization study is shown in Table 5.1.

Table 5.1. Independent variables and their levels.

Independent Variable	Symbol	Levels
Diffuser Length (mm)	A	114, 228, 342
Diffuser Angle (°)	B	25, 32, 38, 45
Shroud Length (mm)	C	114, 166, 218
Shroud Angle (°)	D	2, 5, 8, 11

5.1.2 Computational fluid dynamics study

STAR-CCM+ was used to simulate the 30 design points obtained from the custom design. The CFD conditions are the same as the ones used for parametric study, as described in Subsection 3.6.1. The time step for this optimization study was set to achieve TSR 2.0 as this is the TSR where the best performing HDWT with AR of 0.44 and solidity of 0.45 produced the highest coefficient of power for both the studies done on the bare HDWT in Sections 4.1 and 4.2 and on the cycloidal diffusers parametric study in Section 4.3. Therefore, SST k-ω is used as the turbulence model with a time step size of 5.53×10^{-4} s to set the TSR to 2.0 and rotate the HDWT by 2.5° per time step with a meshing strategy identical to the one used for the parametric study as described in Subsections 3.6.3 and 3.6.4.

5.2 Optimization Results And Discussion

The independent factors to be optimized were inserted into the Design Expert® software, with the conditions stated in Section 5.1; 30 simulation runs were needed to do the optimization. These 30 runs were done using CFD in Star CCM+ software. The parameters of each run are shown in Table 5.2. Once the values of all the responses (coefficient of power) are obtained, they are recorded and input into the design space table in Design Expert to be analyzed and optimized. The actual C_p value in the table is the observed values from CFD simulations. The analysis of the accuracy of the results, the independent factors, and the optimization process are presented and discussed in Subsection 5.2.1 to Subsection 5.2.5.

Table 5.2. Optimal RSM runs conditions with the observed and predicted responses.

Run	**Independent Variables**				**Coefficient of Power (C_p)**	
	A: Diffuser Length (mm)	**B: Diffuser Angle (°)**	**C: Shroud Length (mm)**	**D: Shroud Angle (°)**	**Actual**	**Predicted**
1	342	32	218	11	0.4064	0.4062
2	228	38	166	11	0.3438	0.3488
3	342	45	166	11	0.3382	0.3375

4	342	25	166	2	0.3274	0.3289
5	342	38	166	5	0.3574	0.3505
6	114	32	166	11	0.3572	0.3589
7	342	25	166	8	0.3436	0.3459
8	114	25	166	2	0.3434	0.3416
9	228	32	166	8	0.3566	0.3553
10	342	38	114	11	0.2990	0.2977
11	228	25	114	8	0.3006	0.2998
12	228	25	218	11	0.4094	0.4070
13	342	38	218	8	0.4076	0.4091
14	342	25	218	5	0.3986	0.3985
15	342	45	114	5	0.2968	0.3005
16	114	45	166	8	0.3614	0.3573
17	114	38	218	5	0.4200	0.4217
18	342	32	114	2	0.2930	0.2932
19	228	38	114	2	0.3022	0.2990
20	114	38	114	8	0.3126	0.3141
21	114	45	166	2	0.3492	0.3514
22	114	45	218	5	0.4190	0.4164
23	114	25	114	11	0.3048	0.3028
24	228	38	218	2	0.4038	0.4018
25	228	32	166	5	0.3506	0.3526
26	114	25	114	5	0.3016	0.3038
27	114	32	218	8	0.4212	0.4224
28	228	32	114	5	0.3046	0.3048
29	228	45	218	2	0.3954	0.3984
30	228	45	114	8	0.3014	0.3010

5.2.1 Statistical analysis

The statistical significance of the second-order polynomial model to predict the coefficient of power (C_p) of the HDWT using a cycloidal diffuser under cooling tower exhaust air was tested using ANOVA and in Design Expert®. The ANOVA results of the regression model for the quadratic response surface are shown in Table 5.3. The

significance of the coefficients was determined by Fisher's *F*-test and values of probability > *F*. The model term can be treated to be statistically significant if the p-value is less than 0.05. For this study, the model shows an *F*-value of 331.70 and a small probability value (p<0.0001), which shows that the model is statistically significant. This means there can only be a 0.01% chance that noise contributes to this large *F*-value. Since there are no replicates in this study because it is a computational study where repeating the same simulation parameter condition will result in the same response (coefficient of power), the quadratic ANOVA results did not include the lack-of-fit values. Table 5.4 shows the goodness of fit values. The adequate precision ratio of the quadratic model of this analysis is 53.03, which is desirable since it is well above 4, which indicates an adequate signal to navigate the design space. Next, a high coefficient of determination (R_2), adjusted R_2 and predicted R_2 values of 0.9968, 0.9938 and 0.9860 were obtained, respectively. The difference between the predicted R_2 and adjusted R_2 is less than 0.2. This shows that the quadratic model is very reliable in correlating the predicted response and the obtained result from the study.

Table 5.3. ANOVA for power coefficient response of the optimal RSM design using a quadratic model.

Source	**Sum of Squares**	**df**	**Mean Square**	**F-value**	**p-value**	**Remark**
Model	0.0568	14	0.0041	331.70	< 0.0001	Significant
A-Diffuser Length	0.0006	1	0.0006	49.04	< 0.0001	Significant
B-Diffuser Angle	0.0000	1	0.0000	1.10	0.3116	
C-Shroud Length	0.0427	1	0.0427	3489.21	< 0.0001	Significant
D-Shroud Angle	0.0001	1	0.0001	8.92	0.0092	Significant
AB	1.975E-09	1	1.975E-09	0.0002	0.9900	
AC	0.0000	1	0.0000	1.48	0.2426	

AD	6.929E-07	1	6.929E-07	0.0566	0.8151	
BC	5.206E-06	1	5.206E-06	0.4255	0.5241	
BD	0.0001	1	0.0001	7.03	0.0181	Significant
CD	0.0000	1	0.0000	1.46	0.2450	
A^2	0.0000	1	0.0000	3.36	0.0866	
B^2	0.0003	1	0.0003	20.78	0.0004	Significant
C^2	0.0002	1	0.0002	12.32	0.0032	Significant
D^2	0.0004	1	0.0004	31.27	< 0.0001	Significant
Residual	0.0002	15	0.0000			
Total	0.0570	29				

Table 5.4. The goodness of fit for the regression model of the quadratic model.

Parameter	**Response Value**
Adequate Precision	53.0267
R^2	0.9968
Adjusted R^2	0.9938
Predicted R^2	0.9860
Std. Dev.	0.0035
Mean	0.3510

Figure 5.1 shows the normal probability plot of the residuals. The points mostly lie on or near the straight line, as seen on the graph, which shows that the residuals are normally distributed. This means that statistical assumptions for this model are appropriate and align with the obtained simulation data. Figure 5.2 shows the predicted value against the actual value graph for the coefficient of power of the HDWT. The linear distributions of the points along the ideal straight trend line indicate that the predicted and observed values have low discrepancies. This means the predicted value gives good accuracy in predicting the response value. Figure 5.3 shows the externally studentized residuals against the predicted graph, while Figure 5.4 shows the externally studentized residuals against the run graph. It can be seen in both these diagnostic plots that the data are randomly scattered and do not show any clear

distribution pattern, which shows that the quadratic model is acceptable and provides a good representation of the data.

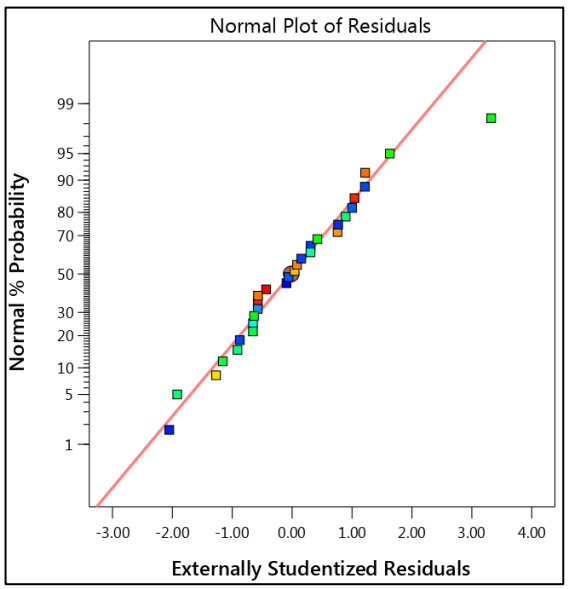

Figure 5.1. Normal probability plot of externally studentized residuals for the coefficient of power of the quadratic model.

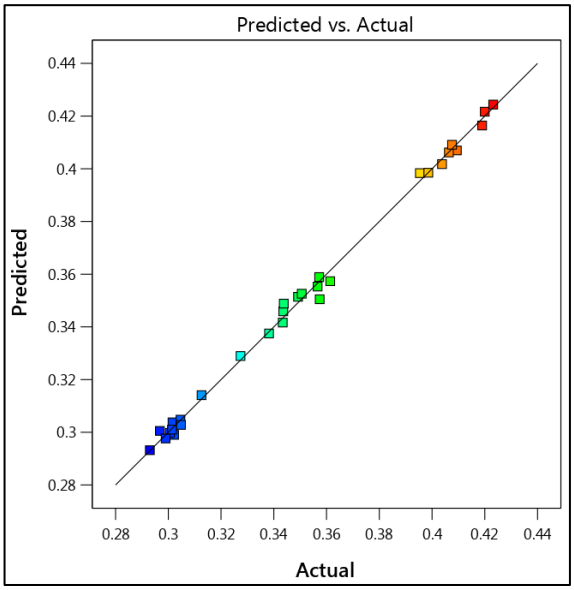

Figure 5.2. Predicted values against actual values for the coefficient of power of the quadratic model.

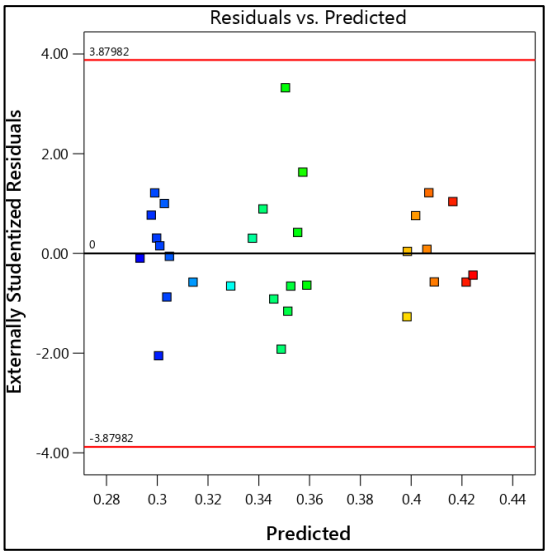

Figure 5.3. Externally studentized residuals vs. predicted values diagnostic plot for the coefficient of power of the quadratic model.

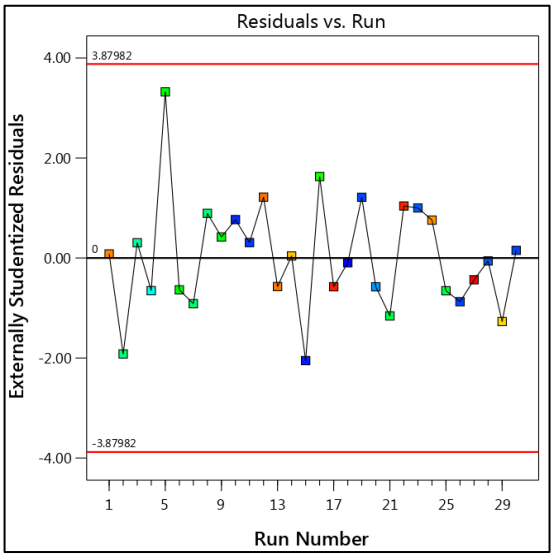

Figure 5.4. Externally studentized residuals vs. runs diagnostic plot for the coefficient of power of the quadratic model.

5.2.2 Prediction equation

The optimization process provides prediction equations as one of the outputs, which can be very useful for future studies as it can be used to predict the response value without running any experiments. This can save a good amount of cost and time. For this study, the prediction equation for the coefficient of power of the quadratic model is as follows:

$$\boldsymbol{Coefficient\ of\ Power} = (0.121791) - (0.000112307\ A) + (0.00574255\ B) + (0.000458261\ C) + (0.00784161\ D) + (1.30608e^{-08}\ AB) - (2.26257e^{-07}\ AC) + (5.58624e^{-07}\ AD) - (1.64346e^{-06}\ BC) - (8.55581e^{-05}\ BD) + (6.71924e^{-06}\ CD) + (2.03249e^{-07}\ A^2) - (6.87422e^{-05}\ B^2) + (1.8986e^{-06}\ C^2) - (0.000418358\ D^2) \quad (5.1)$$

However, the quadratic model equation can be reduced to consider only the significant factors. From Table 5.3, the model terms (*AB*, *AC*, *AD*, *BC*, and *CD*) are statistically insignificant. Therefore, these terms can be removed from the equation to increase accuracy. The model was reselected by modifying the automatic model selection using the AICc criterion and backward selection to remove the statistically insignificant model terms mentioned earlier. This results in the prediction equation below:

$$\boldsymbol{Coefficient\ of\ Power} = (0.124622) - (0.000145872\ A) + (0.00584152\ B) + (0.00040037\ C) + (0.00891751\ D) - (8.17687e^{-05}\ BD) + (2.10827e^{-07}\ A^2) - (7.39685e^{-05}\ B^2) + (1.87654e^{-06}\ C^2) - (0.000417789\ D^2) \quad (5.2)$$

In the equations above, A is the diffuser length, B is the diffuser angle, C is the shroud length, and D is the shroud angle. Equation 5.2 was validated by computational methods and is presented in Subsection 5.2.5.

5.2.3 Interaction effect between independent variables

To study the interactions between the independent variables (diffuser length, diffuser angle, shroud length and shroud angle) and the effect it has on the response (HDWT power coefficient), a 3-dimensional response surface plot of the quadratic model is presented as shown in Figure 5.5 to 5.10. It is seen from Figures 5.6, 5.8 and 5.10 that the shroud length has the strongest effect on the response as all three of the response surface plots containing shroud length have the steepest plot. From Figure 5.6, it is apparent that the highest response (C_p=0.42) can be obtained when the diffuser length is reduced to a minimum length (114mm), and the shroud length is increased to a maximum length (218mm). From Table 5.3, it was shown that the individual factors of diffuser length (*A*) and shroud length (*C*) have the most significant effect on the design response as the *p*-values are less than 0.0001. The strongest interaction is shown between the diffuser angle (*B*) and shroud angle (*D*) as it produces a quadratic curve

for the 3D response surface plot, as seen in Figure 5.9. It is also apparent from Table 5.3 that the interaction between independent variables *B* and *D* was the most significant as it gives the lowest *p*-value. Figure 5.9 shows that the best diffuser and shroud angles to achieve the highest coefficient of power are around 35° and 7°, respectively.

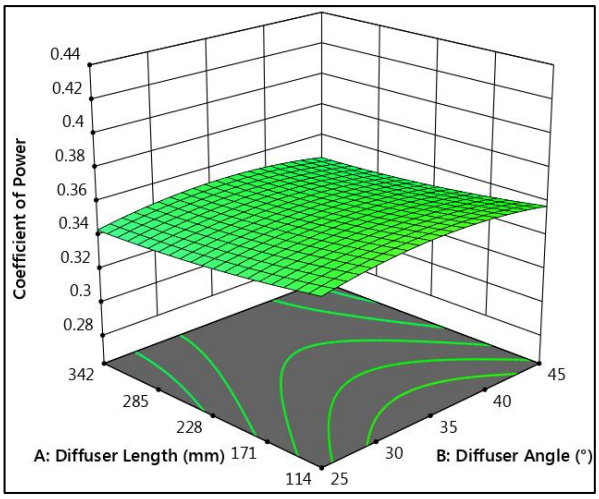

Figure 5.5. Three-dimensional surface response plot of the effect of interaction between diffuser length (A) and diffuser angle (B) on the coefficient of power.

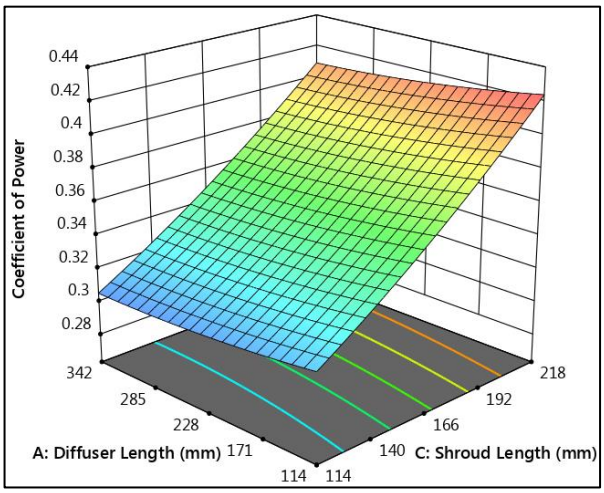

Figure 5.6. Three-dimensional surface response plot of the effect of interaction between diffuser length (A) and shroud length (C) on the coefficient of power.

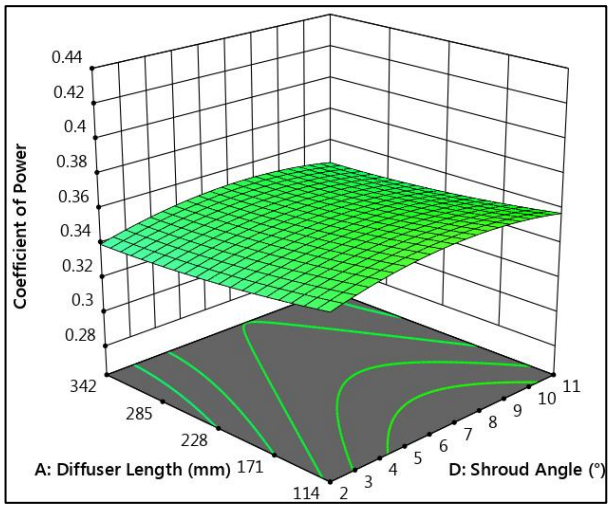

Figure 5.7. Three-dimensional surface response plot of the effect of interaction between diffuser length (A) and shroud angle (D) on the coefficient of power.

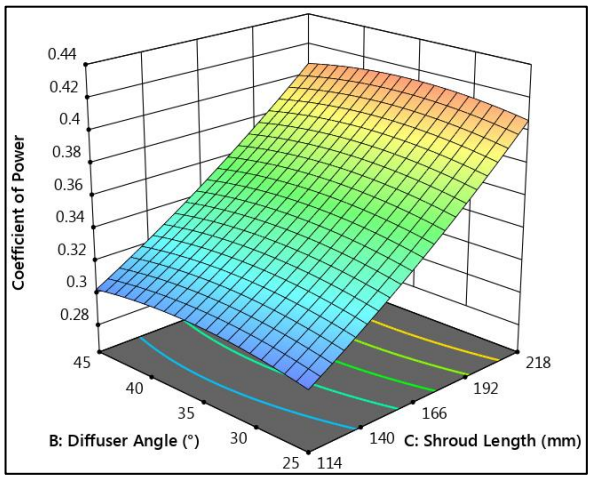

Figure 5.8. Three-dimensional surface response plot of the effect of interaction between diffuser angle (B) and shroud length (C) on the coefficient of power.

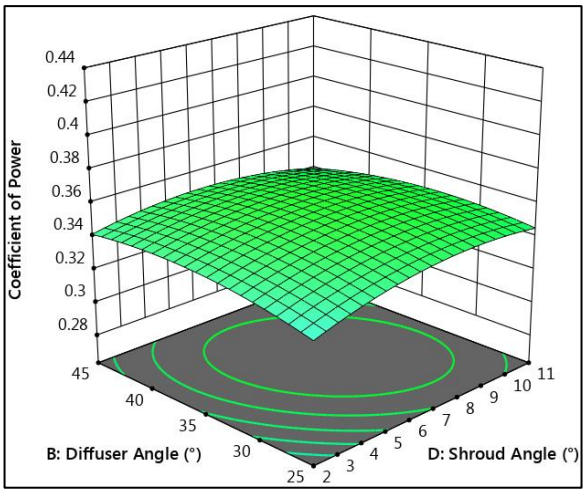

Figure 5.9. Three-dimensional surface response plot of the effect of interaction between diffuser angle (B) and shroud angle (D) on the coefficient of power.

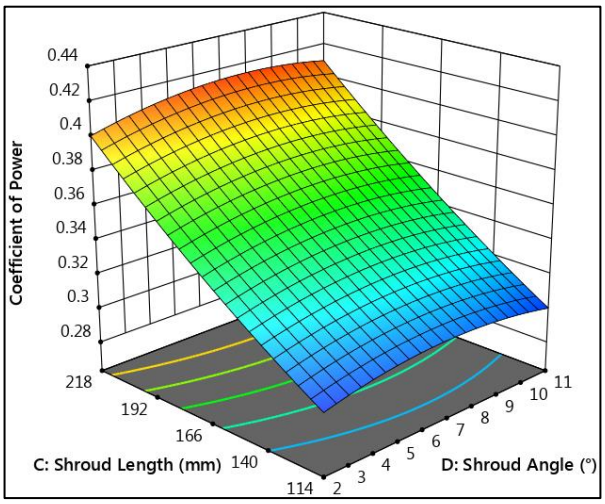

Figure 5.10. Three-dimensional surface response plot of the effect of interaction between shroud length (C) and shroud angle (D) on the coefficient of power.

5.2.4 Optimized design

Once the statistical analysis of the model was done, the prediction equation of the quadratic model and reduced model was obtained, and 3D surface response plots were presented, the numerical optimization was carried out using the built-in function in Design Expert® to find the very best cycloidal diffuser parameters to achieve the maximum possible response (coefficient of power). The optimum design parameters were obtained using the reduced model prediction equation (Equation 5.2). Table 5.5 shows the criteria used for the optimization process. Figure 5.11 shows the best solution to achieve the maximum possible power coefficient. From the optimization

result, a predicted C_p of 0.4230 can be obtained when the diffuser length is 114mm, the diffuser angle is 35.5°, the shroud length is 218mm, and the shroud angle is 7.2°. This would be a 32.35% increment in C_p compared to the baseline design shown in Section 4.2 and a 0.43% increment compared to the best run (Run 27) in the optimal design table as seen in Table 5.2.

Table 5.5. Criteria for the numerical optimization constraints.

Variable	Goal	Lower Limit	Upper Limit	Importance
A: Diffuser Length	In range	114	342	+++
B: Diffuser Angle	In range	25	45	+++
C: Shroud Length	In range	114	218	+++
D: Shroud Angle	In range	2	11	+++
Coefficient of Power	Maximize	0.293	0.43	+++++

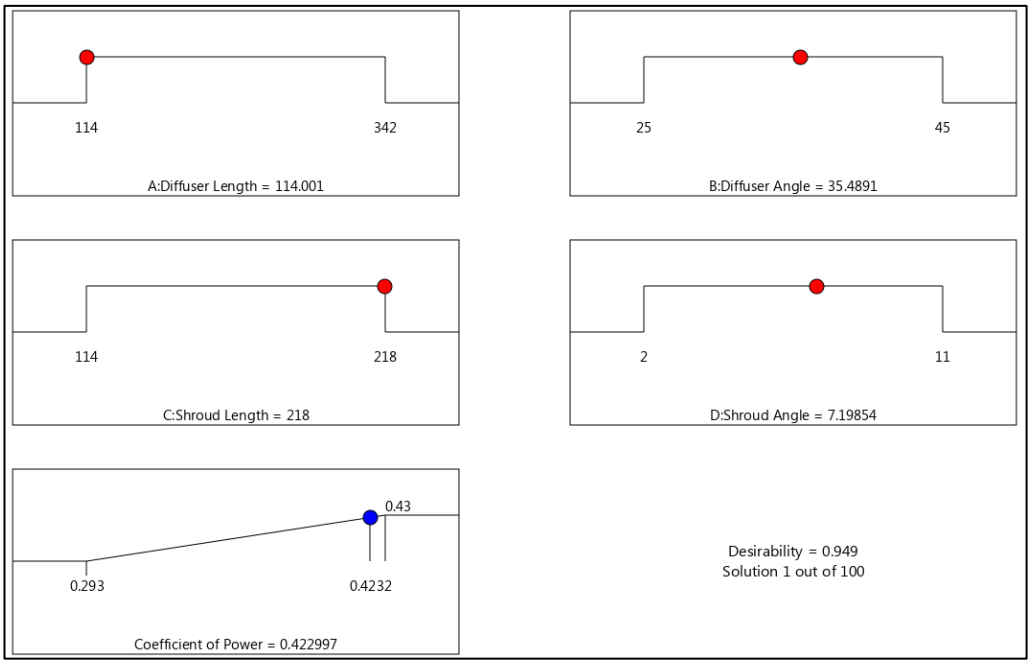

Figure 5.11. Suggested optimum design based on numerical optimization.

5.2.5 Validation of optimization result

In this section, the numerical optimization results were validated by a computational method. Based on the reduced model prediction equation (Equation 5.2) in Subsection 5.2.2, there was a total of 30 designs suggested as the optimized design, producing a

predicted C_p of 0.423. From this, five designs were selected to validate the predicted C_p value. Table 5.6 shows the parameters of each design and their predicted and computational C_p. The computational study used the same meshing strategy and flow physics setup discussed in previous sections. The result shows an acceptable deviation between the predicted C_p and computational C_p. The error for all 5 cases tested is small, less than 0.15%. These validation results showed that the developed model shows good accuracy. Therefore, this optimization study can be concluded to be valid and can be used for further studies if needed.

Table 5.6. Validation of the numerical optimization predicted results by the computational result.

Design No.	A (mm)	B (°)	C (mm)	D (°)	Predicted C_p	Computational C_p	Error (%)
1	114	35.5	218	7.2	0.4230	0.4228	0.05
2	114	36.1	218	7.4	0.4230	0.4232	0.05
3	114	35.1	218	7.5	0.4229	0.4223	0.14
4	114	36.8	218	7.4	0.4229	0.4226	0.07
5	114	33.6	218	7.2	0.4227	0.4224	0.07

5.3 Flow Analysis of Optimized Design

From the optimization study, it was found that the cycloidal diffusers with a diffuser length of 114mm, diffuser angle of 36.1°, shroud length of 218mm, and shroud angle of 7.4° resulted in the highest HDWT performance with C_p of 0.4232 under the cooling tower exhaust air. For the bare HDWT case, as studied in Subsections 4.1 and 4.2, the HDWT with the solidity of 0.45 and AR of 0.44 produces C_p of 0.3196. The optimized cycloidal diffusers enhanced the power coefficient of the HDWT under cooling tower exhaust air by 32.42%. To understand how the cycloidal diffusers help increase the performance of the HDWT, the instantaneous coefficient of moment plots of the bare HDWT and the HDWT with cycloidal diffusers are plotted and shown in Figure 5.12 and Figure 5.13 to compare the performances. The radar plot in Figure 5.12 shows that the HDWT with optimized cycloidal diffusers (wind-augmented HDWT) outperforms the bare HDWT as it continuously produces high C_m throughout the complete rotation.

The wind-augmented HDWT excels from θ=15° to 65° as it produces much higher instantaneous C_m than the bare HDWT. The bare HDWT only produced higher instantaneous C_m than the augmented HDWT from 110° to 120°. This repeats three times during a complete cycle since it is a 3-bladed HDWT.

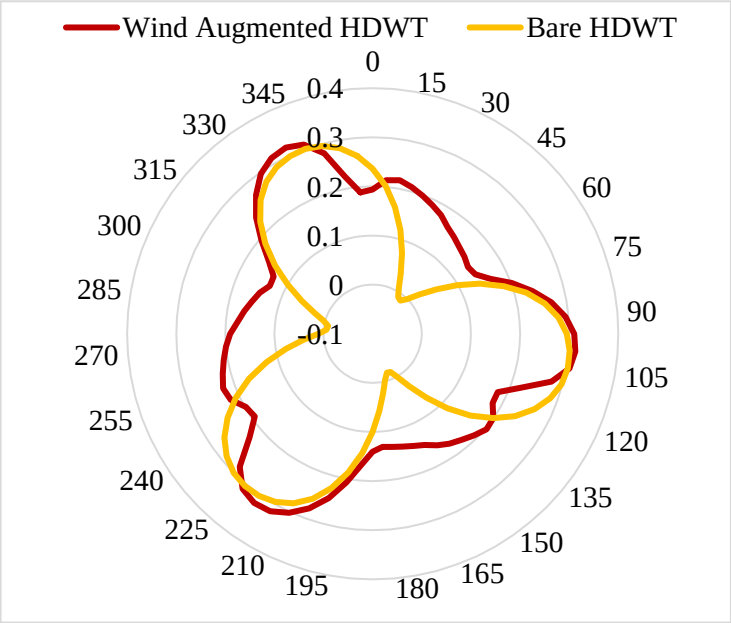

Figure 5.12. Radar plot of instantaneous C_m against azimuthal angles of Bare HDWT and HDWT with optimized cycloidal diffusers at TSR 2.0.

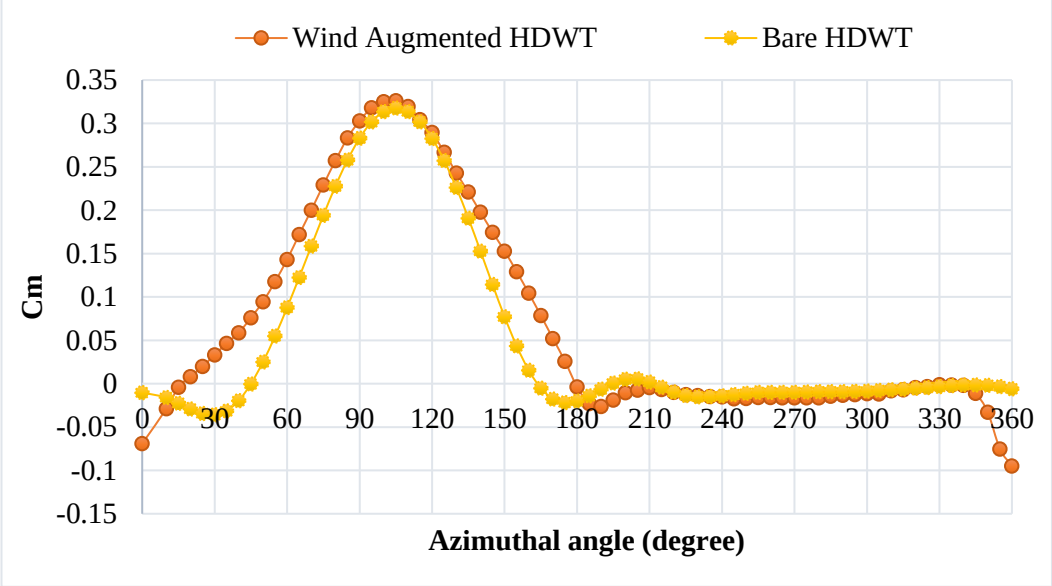

Figure 5.13. Single blade instantaneous C_m against azimuthal angles of Bare HDWT and HDWT with optimized cycloidal diffusers at TSR 2.0.

To study how the flow behaves and affects the HDWT performance with and without the cycloidal diffusers, the streamlines of velocity and pressure contour of the HDWT blades are shown in Figures 5.14 to 5.16 for HDWT at azimuthal angles of 30° and 0° respectively. With respect to the blade 1 position, at an azimuthal angle of 30°, the wind-augmented HDWT outperforms the bare HDWT, as seen in Figure 5.12. This is because at θ=30°, the wind-augmented blade 1 experiences much higher pressure on its pressure side and much lower pressure on its suction side than the bare HDWT blade, as seen in Figure 5.14 (b). The higher-pressure difference created between the pressure and suction side of the blade results in more lift being created and, hence, higher C_m. The same observation can be seen on blade 2 (150°) in Figure 5.14, which confirms the observation of the blade's instantaneous Cm in Figure 5.13, which shows that the wind-augmented HDWT produces much higher C_m while the bare HDWT produces a lower C_m at this azimuthal angle. This is due to the higher velocity of air flowing around the suction side of blades 1 and 2, which is helped by the converging shape of the diffuser. It is shown in Figure 5.16 that the flanges of the diffusers create a low-pressure region at the downwind of the HDWT by the formation of low-pressure vortices, which also causes the wind from the cooling tower to accelerate.

However, at θ=0°, the bare HDWT blades give a slightly higher positive instantaneous C_m while the wind-augmented HDWT blades produce negative C_m as seen in the plot in Figure 5.12. This is because when the blade of the augmented turbine is at an azimuthal angle of 0°, it is close and adjacent to the wall of the cycloidal diffuser. This increases the flow on both sides of the blade, resulting in the pressure side of the blade having low pressure, as seen in Figure 5.15 (b), which prevents any lift from being generated. In the case of the bare HDWT, the pressure difference between the blade's suction side and pressure side is still low but still manages to create a small lift force, resulting in a positive C_m. Therefore, it is observed from the plot in Figure 5.13 that at blade positions θ=0° to 15° and 345° to 360° (back to 0°), the augmented HDWT suffers from low or negative instantaneous C_m. Overall, the augmented HDWT outperforms the bare HDWT. Still, this analysis provides opportunities for further improvement to the exhaust air energy extractor system, especially at the blade positions where the HDWT suffers from negative performance.

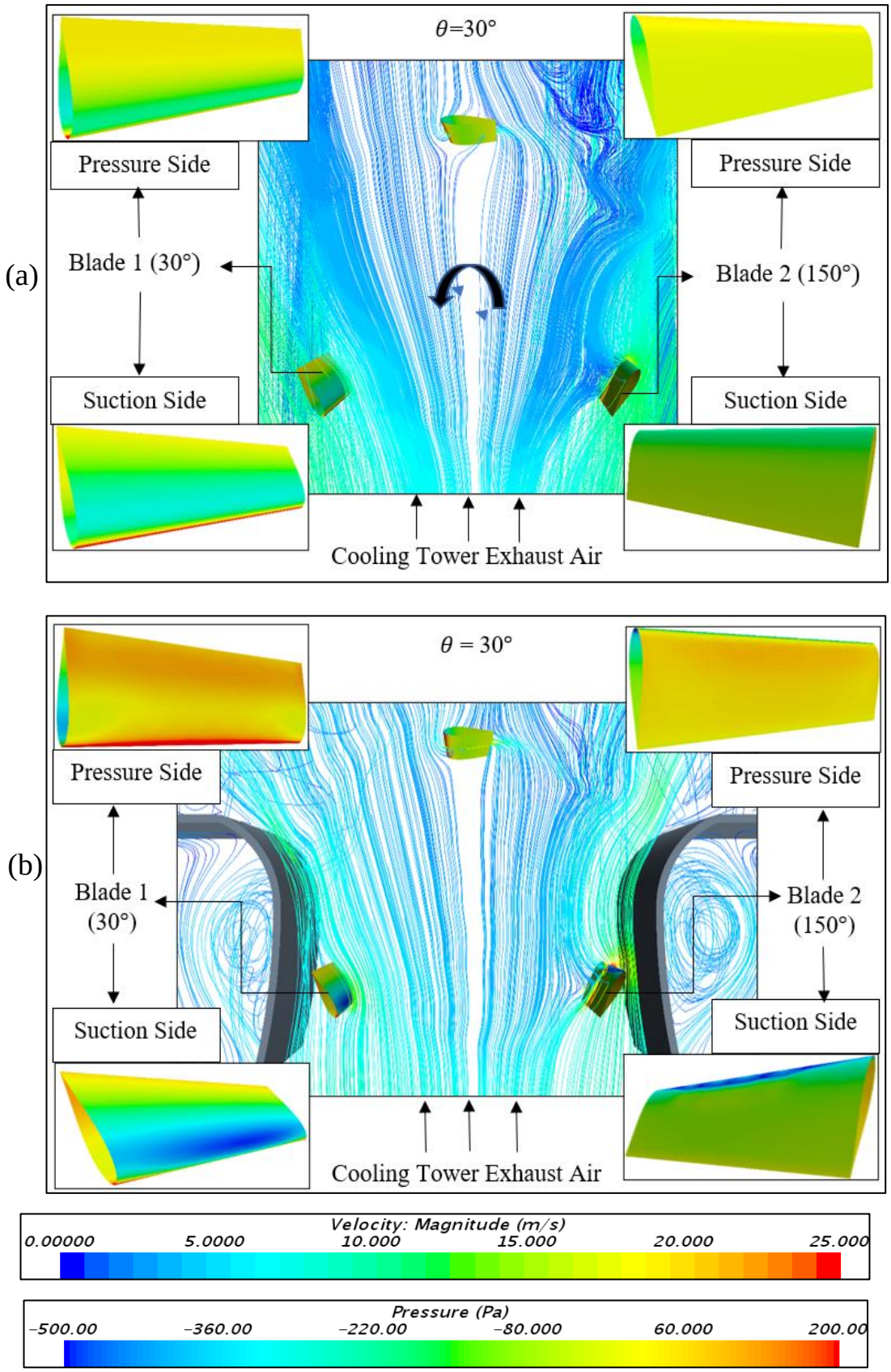

Figure 5.14. Streamlines coloured by velocity magnitude and 3D pressure contour on blade surfaces at θ=30° of the (a) Bare HDWT and (b) HDWT with optimized cycloidal diffusers.

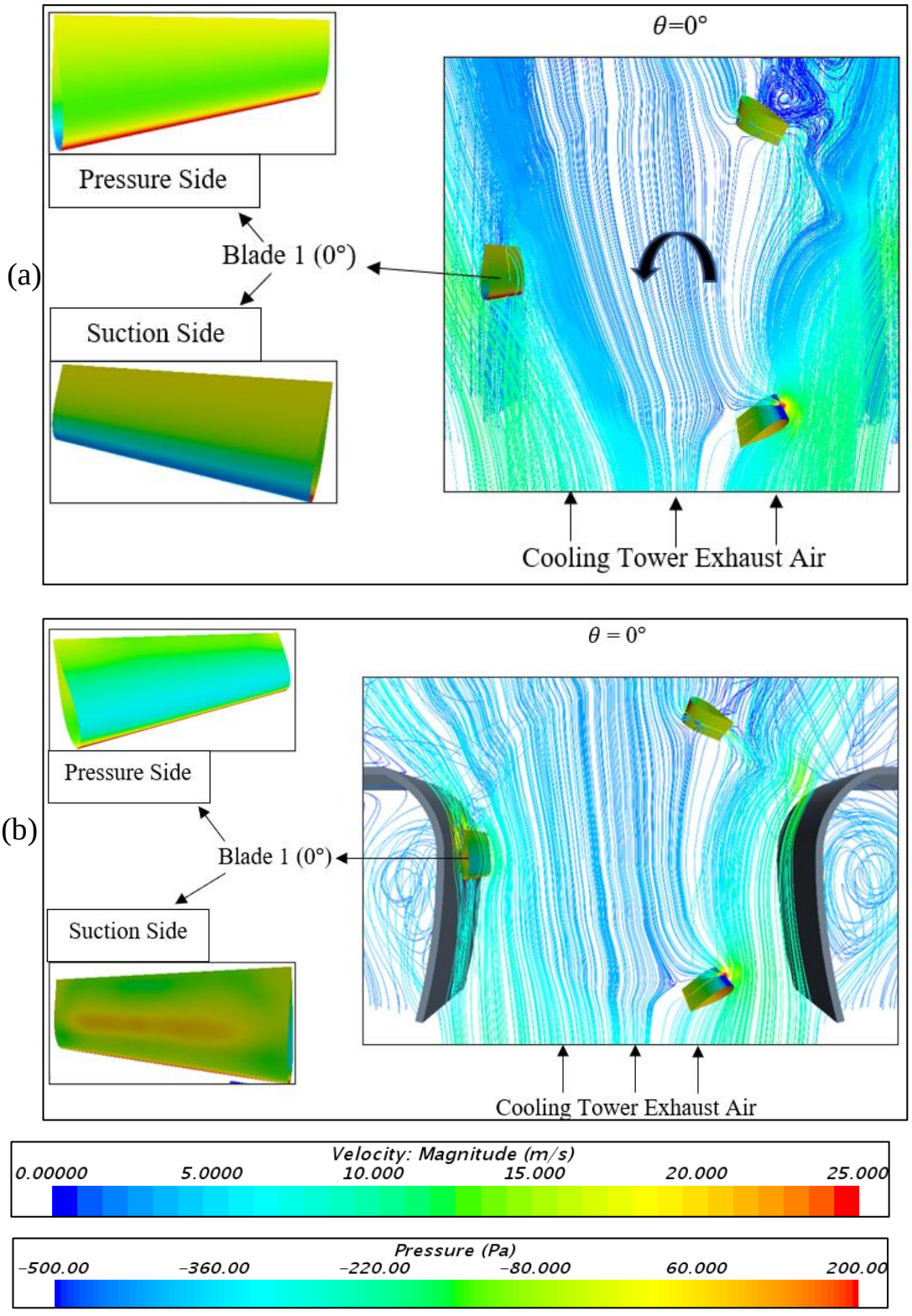

Figure 5.15. Streamlines coloured by velocity magnitude and 3D pressure contour on blade surfaces at θ=0° of the (a) Bare HDWT and (b) HDWT with optimized cycloidal diffusers.

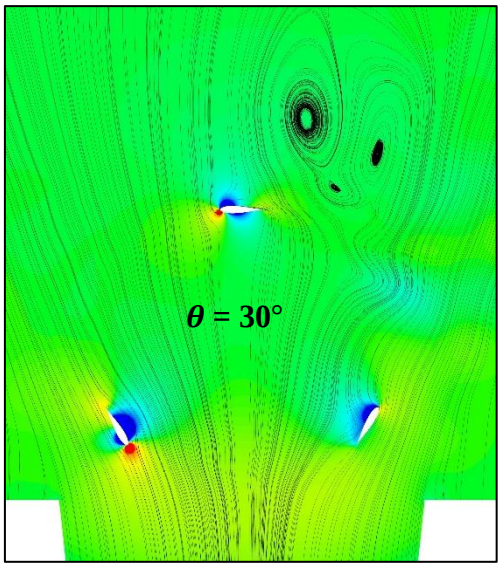

(a)

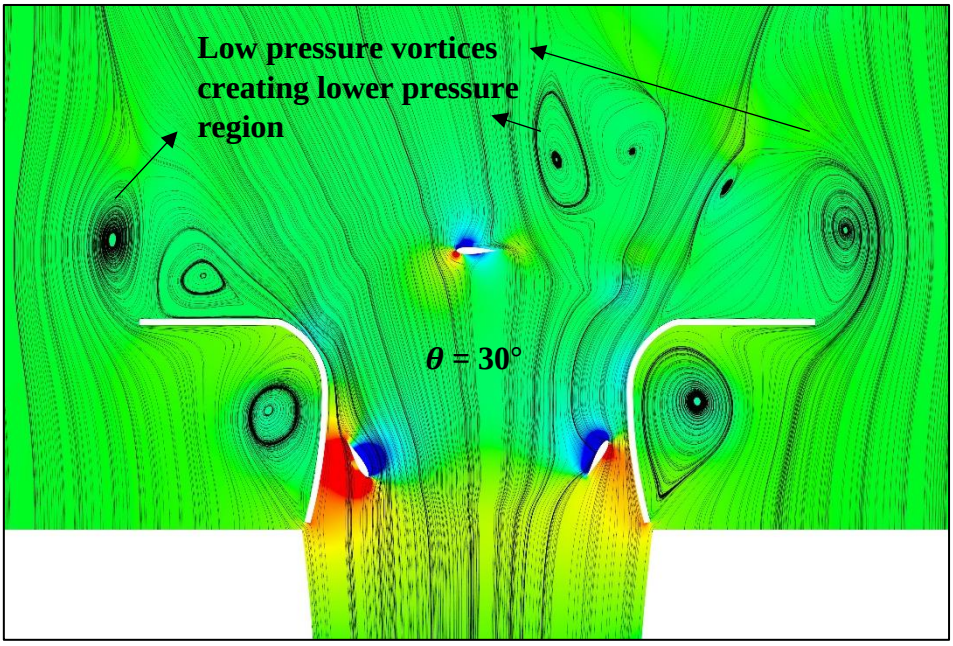

(b)

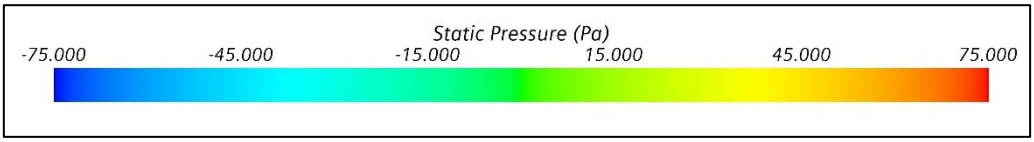

Figure 5.16. The pressure contour and streamlines comparison at θ=30° between (a) Bare HDWT and (b) HDWT with optimized cycloidal diffusers.

5.4 Analysis of the Cooling Tower Velocity Profile with Energy Recovery System for Performance Evaluation

The comparison of the exhaust airflow between the empty cooling tower and the cooling tower with the HDWT and the optimized cycloidal diffusers is shown in Figure 5.17. The velocity vector is used to analyse how the presence of the HDWT and the cycloidal diffusers affects the cooling tower flow. Since experimental work was not done in this study, this analysis provides a rough idea of how the cooling tower performance is affected by the addition of the optimized exhaust air recovery system in this study. In addition to the velocity vector, a report was created to obtain the air velocity at various points throughout the cooling tower. Figure 5.17 (a) shows the measuring points 1 to 6 (P1 to P6) on the XY plane, while Figure 5.17 (b) shows the measuring points 7 (P7) and 8 (P8) on the YZ plane. The velocities at these points were taken for HDWT at azimuthal angles of θ=30° and θ=90° for the case of the HDWT with diffusers. The values of the velocities obtained from the simulation are recorded in Table 5.7. From the result, point 1 exhibited higher velocity when an HDWT was positioned at the cooling tower's outlet. Since point 1 is located close to the bottom of the cooling tower, it is assumed as the intake air. Tabatabaeikia et al. [59] demonstrated in their study that the air intake of the cooling tower can increase by up to 8.9% when an HDWT and separator plates are optimally positioned at the cooling tower outlet. However, because the HDWT is centred at the exit, it creates a blockage effect, which causes the velocity of the exhaust air to reduce as it moves upwards through the centre, as reflected by the velocities at points 2 and 3. The presence of the HDWT, rotating at the outlet of the cooling tower, causes an increase in the air velocity near the cooling tower wall from the throat (point 4) to the outlet, as seen in Figure 5.17 (b)

The HDWT for this comparison has a diameter of 456mm, comparable to 0.8 of the cooling tower outlet size ($0.8D_o$). As a result, the velocity at the outlet, measured at points 5 and 6 on the XY plane, decreases compared to the case of the empty cooling tower. Nonetheless, to reduce the blockage effect, the blades used in this study have a length of 200mm, which covers only a small area of the cooling tower outlet ($0.35D_o$), causing the velocities at points 7 and 8 to increase dramatically, as seen from the YZ plane in Figure 5.17 (b) and as shown in Table 5.7. Moreover, the rotating HDWT creates a low-pressure region at the cooling tower outlet, which forces the air at the

high-pressure region inside the cooling tower out of the cooling tower, as reported in a study by Tabatabaeikia et al. [59]. Overall, no backflow is seen in Figure 5.17 (b), indicating that the HDWT has no significant detrimental impact on the performance of the cooling tower.

Table 5.7. The velocity of the air in the cooling tower at various positions, with and without the exhaust air energy extraction system.

Measuring points	**Velocity, v (m/s)**				
	Without HDWT	**HDWT at θ=30°**	**% difference compared to without HDWT**	**HDWT at θ=90°**	**% difference compared to without HDWT**
Point 1	3.89	3.96	1.80	3.96	1.80
Point 2	6.39	6.61	3.44	6.61	3.44
Point 3	10.29	10.23	-0.58	10.22	-0.68
Point 4	11.25	11.50	2.22	11.58	2.93
Point 5	9.48	7.82	-17.51	7.09	-25.21
Point 6	9.53	7.71	-19.10	9.10	-4.51
Point 7	9.49	11.83	24.66	11.98	26.24
Point 8	9.49	11.81	24.45	11.97	26.13

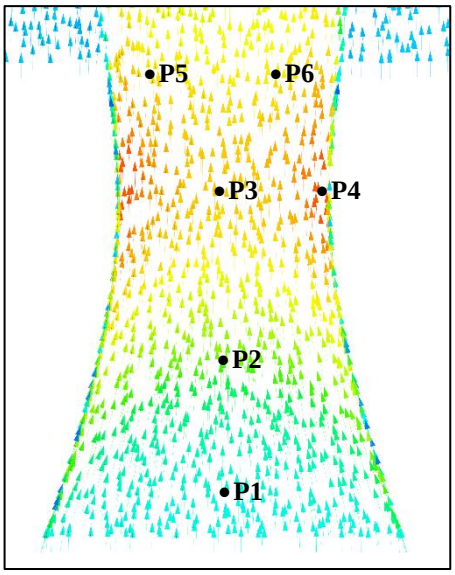

(a) Cooling tower without HDWT

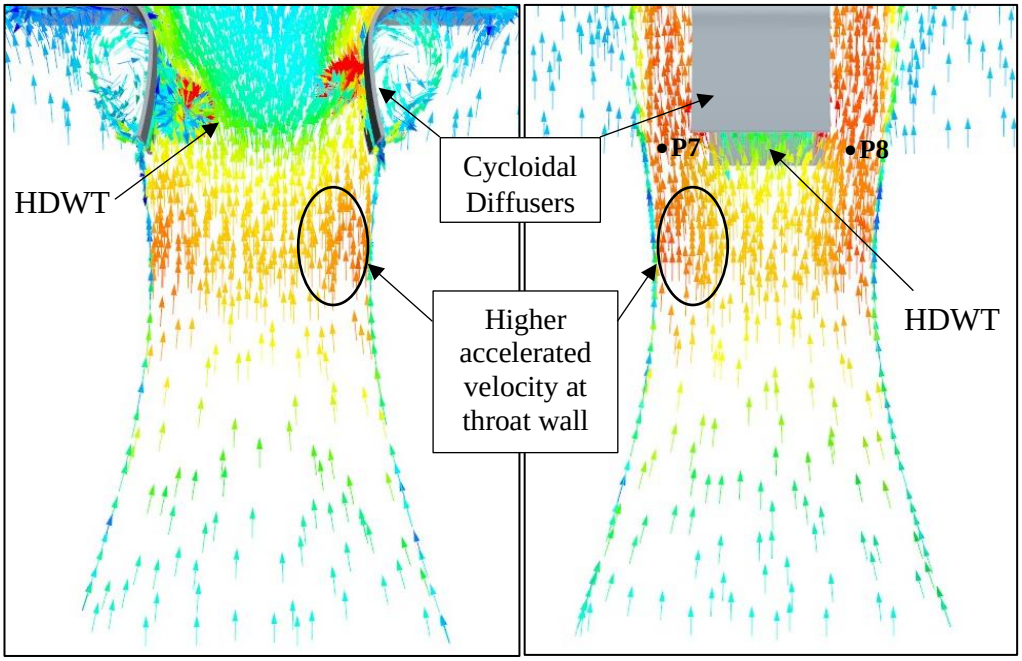

(b) Cooling tower with HDWT and optimized diffusers placed at its outlet

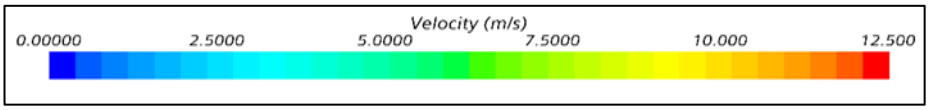

Figure 5.17. Characteristics of the airflow in the cooling tower with and without HDWT placed at the outlet.

5.5 Analysis of the Power Produced by the HDWT Exhaust Air Energy Recovery and its Effect on the Cooling Tower Performance

The cooling tower airflow characteristics from the inlet to the outlet between the empty cooling tower and the cooling tower with the best HDWT parameters, augmented with the optimized cycloidal diffuser (ϕ=36.1°, L_b=114 mm, γ=7.4°, and L_f= 218mm) placed at the tower's outlet at TSR 2.0 has been analyzed in Section 5.4. In this section, the performance of the HDWT in terms of power generation and the effect of the HDWT on the air mass flow rate of the cooling tower flow are analysed. The HDWT of different AR, solidities, and the HDWT augmented with the cycloidal diffusers at different TSRs are chosen to calculate how much power can be generated by each of the HDWT and to study how each of the HDWT affects the cooling tower mass flow rate flow. The HDWT of AR 0.35, 0.44, and 0.70 at TSR 2.5 (from Section 4.1) were chosen to study the effect of different HDWT AR on the cooling tower flow. TSR 2.5 was chosen for the different AR HDWT as all the AR tested gave a peak C_p at this TSR. Next, the HDWT with a solidity of 0.225 and 0.450 at TSRs 2.0 and 3.0 (from Section 4.2) were chosen to study the effect of different solidities on the cooling tower flow. These HDWTs and TSRs were chosen as the bigger solidity HDWT (σ=0.450) gave the highest C_p at a TSR of 2.0, while the smaller solidity HDWT (σ=0.225) performed better at a higher TSR of 3.0. Then, to study the effect of integrating cycloidal diffusers with the HDWT on the cooling tower at different TSRs, the best cycloidal diffuser (ϕ=35°, L_b=228mm, γ=7°, L_f= 218mm) from the parametric study in Section 4.3 was chosen at TSRs of 1.5, 2.0, and 3.0.

5.5.1 HDWT exhaust air power generation and its effect on the cooling tower mass flow rate

The cooling tower outlet mass flow rate for all the HDWT cases selected is obtained, and the power generated is calculated and presented in Table 5.8. The effect on the cooling tower flow is studied by obtaining the mass flow rate from the cooling tower outlet, $\dot{m}_a$ (kg/s). This was done by creating a mass flow rate report in the CFD software, STAR CCM+, and choosing the horizontal plane section created at the cooling tower outlet as the target part to obtain the mass flow rate at the cooling tower outlet. The HDWT's power is calculated using Equation 2.10 and the C_p obtained from

the numerical simulations. An example calculation using the HDWT of AR 0.44 and solidity 0.450, augmented by the optimized cycloidal diffuser design, is presented below:

$$P_{turbine} = 0.5 C_p \rho A U_\infty{}^3$$

Where the density used in the numerical simulations is 1.18415 kg/m^3, A is the swept area of the HDWT, which is the product of the blade length and the HDWT's diameter. The HDWT used for the optimization study has a blade length of 0.2m and a diameter of 0.456m. The optimized cycloidal diffuser design integrated with the HDWT in this study produced a C_p of 0.4232. The cooling tower and inlet velocity conditions were modelled to achieve a wind velocity of 9m/s at the cooling tower outlet. Substituting these values in the above equation provides the HDWT power as follows:

$$P_{turbine} = 0.5(0.4232)(1.18415)(0.2 \times 0.456)(9^3)$$

$$P_{turbine} = 16.66\ W$$

Table 5.8. Cooling tower outlet mass flow rate and the power generated by the HDWT for selected HDWT cases.

Cases	**Mass flow rate (kg/s)**	**Difference in mass flow rate (%)**	C_p	**Power generated (W)**
Empty CT	2.8504	-	-	-
Optimized Cycloidal Diffusers with HDWT at TSR 2.0	2.8356	-0.519	0.4232	16.66
Bare HDWT Cases				
Different Aspect Ratios at TSR = 2.5				
AR=0.35 (D = 570mm)	2.8413	-0.319	0.2658	13.08
AR=0.44 (D = 456mm)	2.8414	-0.316	0.2943	11.58
AR=0.70 (D = 285mm)	2.8435	-0.242	0.1485	3.65
Different Solidities at TSR = 2.0				
σ = 0.225	2.8428	-0.267	0.0305	1.20

σ = 0.450	2.8403	-0.354	0.3196	12.58
Different Solidities at TSR = 3.0				
σ = 0.225	2.8420	-0.295	0.2145	8.44
σ = 0.450	2.8399	-0.368	0.1172	4.61
Best Diffuser Design from the Parametric Study at a few TSRs				
TSR 1.5	2.8377	-0.446	0.2312	9.10
TSR 2.0	2.8357	-0.516	0.4118	16.21
TSR 3.0	2.8337	-0.586	0.2136	8.41

The blockage effect on the cooling tower caused by the HDWT can be evaluated using the outlet mass flow rate obtained. It can be seen that the presence of HDWT at the cooling tower outlet reduces the mass flow rate for all the selected cases. Including a cycloidal diffuser further increases the blockage compared to a bare HDWT. The highest blockage is caused by the integration of diffusers at TSR 3.0, while the HDWT with the smallest diameter has a minimal blockage effect. Higher solidity HDWT also causes more blockage than lower solidity HDWT cases. However, the bigger solidity HDWT generates more power than the lower solidity HDWT due to a higher C_p. Further analysis of the blockage by the different HDWT cases is discussed in Subsection 5.5.2.

This blockage caused by the HDWT may cause a reduction in the cooling tower's efficiency in rejecting heat and increase the cooling tower fan power consumption for a mechanical draft tower. However, the blockage effect is minimal, with the optimized design causing only a 0.519 % reduction in the mass flow rate. An example calculation is presented in Subsection 5.5.4 to estimate the impact on cooling tower efficiency. It is recommended that an experimental investigation be conducted to measure the possible impact on cooling tower fan power consumption. Since the fan power input is neglected in this study, the estimated percentage of energy that can be recovered from cooling tower exhaust air cannot be calculated. However, using an actual cooling tower with exhaust air velocity close to 9m/s, the expected recovery of the HDWT in this study can be estimated. This is presented in Subsection 5.5.3 using a real cooling tower specification.

5.5.2 Analysis of the cooling tower flow

Based on the mass flow rates in Table 5.8, the smallest aspect ratio HDWT (biggest diameter) shows more blockage than the smaller AR HDWT (smallest diameter) as it covers a bigger area at the cooling tower outlet. Figure 5.18 and Figure 5.19 shows the midplane velocity contour comparison of the cooling tower flow for HDWT of AR 0.35, 0.44, and 0.70 at TSR 2.5 on the XY and YZ plane, respectively. The figures show that more air flows out of the cooling tower on the left and right sides of the 0.70 AR HDWT, as seen on the XY plane. No clear difference can be observed in the flow inside the cooling tower between the 3 AR cases. From the YZ plane contour in Figure 5.19, the HDWT of AR 0.44 exhibits higher velocity discharge air on the front and back areas of the turbine. The 0.35 AR HDWT reduced cooling tower mass flow by 0.319% but recovered 13.08 W. The 285mm HDWT gave the least blockage, with only a 0.242% reduction in the mass flow of the exhaust air. However, the small HDWT only manages to produce 3.65 W of power. The HDWT with the highest C_p from the aspect ratio study in Section 4.1, the AR 0.44 HDWT can produce 11.58 W of power but with a 0.316% reduction in mass flow. Therefore, the 570mm HDWT is the most suitable choice of standalone HDWT for maximizing exhaust air energy recovery without the use of any augmentation device, as it gives the highest power while exhibiting only 0.077% higher blockage compared to the AR 0.70 HDWT. Since power is proportional to area, and area for HDWT is the product of the height and diameter of the HDWT, the 570mm produced higher power due to its bigger diameter despite the lower C_p, compared to the AR 0.44 HDWT. Even though the AR 0.35 HDWT generates more power than the AR 0.44 HDWT, it has a diameter equal to the cooling tower outlet size. The AR 0.44 HDWT has a diameter of 456mm, which is 0.8D of the cooling tower outlet, allowing room for diffusers to be placed in the high-velocity region of the cooling tower exhaust air. Therefore, the AR 0.44 HDWT was chosen for the subsequent solidities and cycloidal diffuser optimization studies.

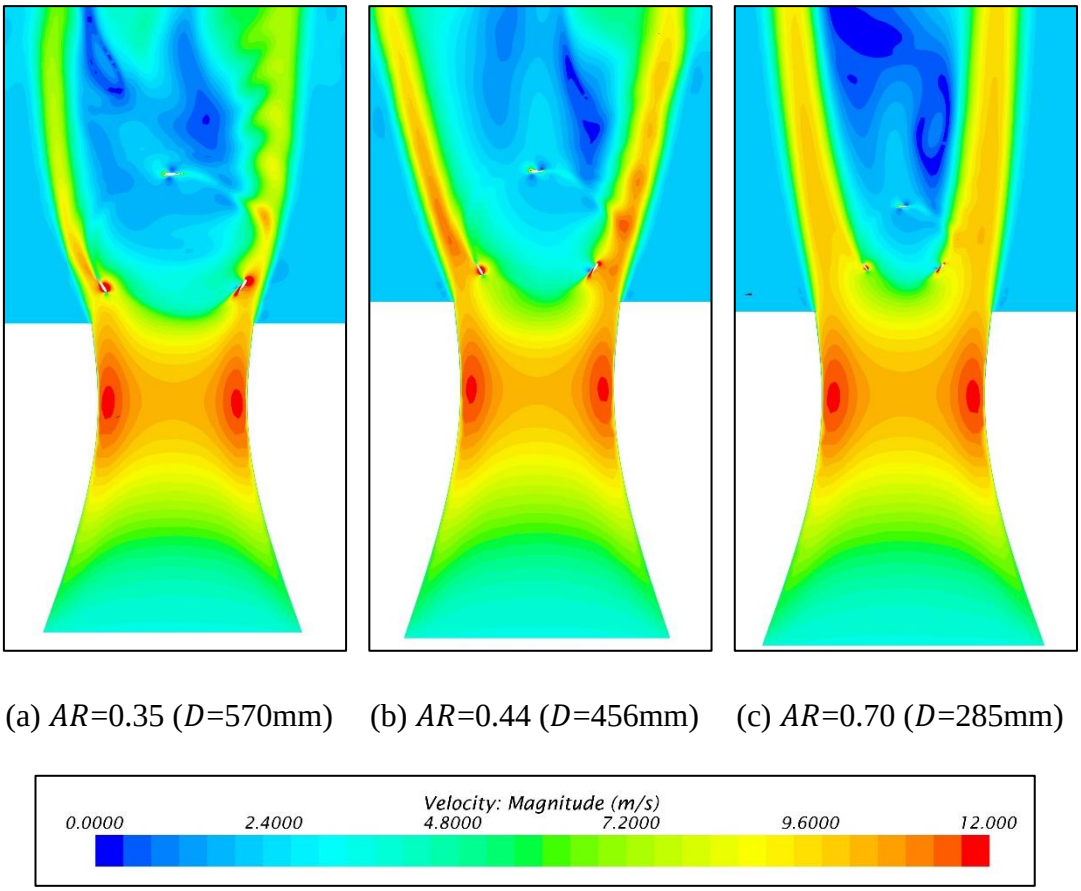

(a) AR=0.35 (D=570mm) (b) AR=0.44 (D=456mm) (c) AR=0.70 (D=285mm)

Figure 5.18. XY-midplane velocity contour comparison for the cooling tower air flow with HDWT of (a) AR=0.35, (b) AR=0.44, and (c) AR=0.70 placed at the outlet at TSR 2.5.

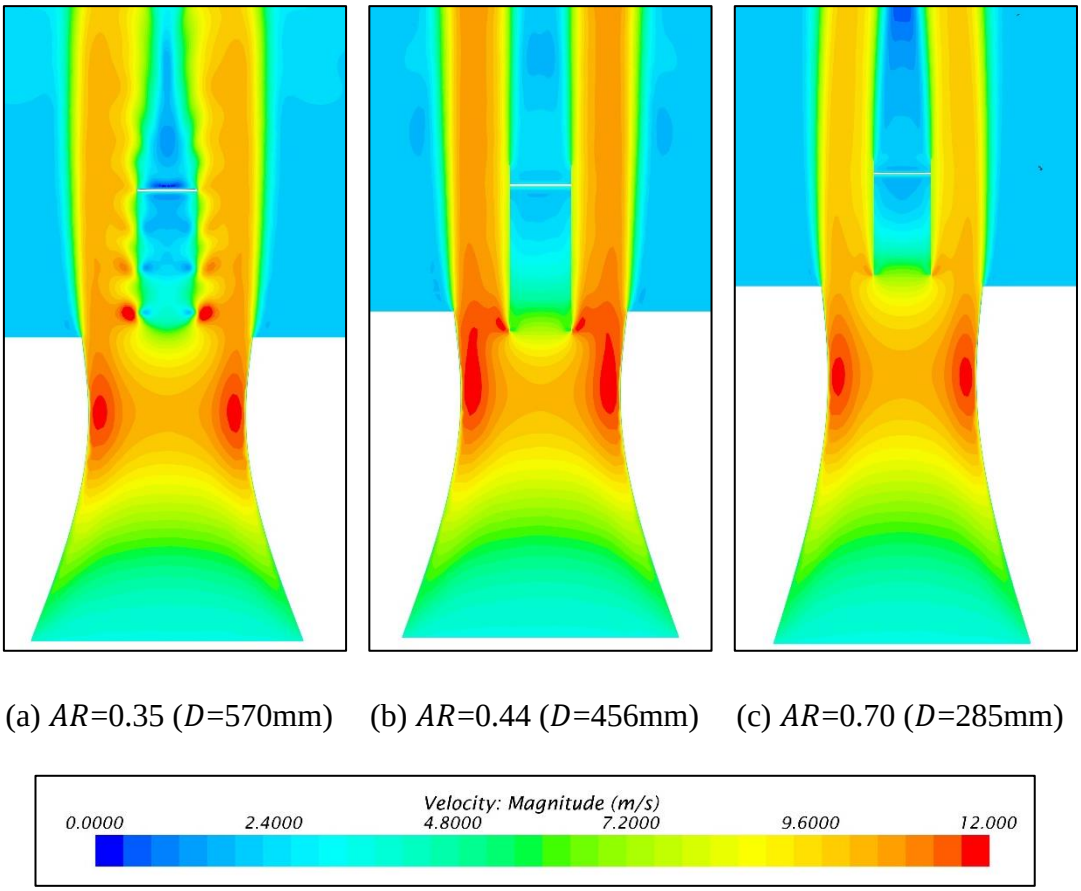

(a) AR=0.35 (D=570mm) (b) AR=0.44 (D=456mm) (c) AR=0.70 (D=285mm)

Figure 5.19. YZ-midplane velocity contour comparison for the cooling tower air flow with HDWT of (a) AR=0.35, (b) AR=0.44, and (c) AR=0.70 placed at the outlet at TSR 2.5.

The effect of different HDWT solidities on the cooling tower performance was also studied to compare the differences at TSR 2.0 & 3.0. It has been communicated in Section 4.2 that the lower solidity HDWT performs better at higher TSR, while the higher solidity works better at lower TSR. Regarding blockage, the HDWT with a solidity of 0.450 showed 0.354% and 0.368% reduction in the cooling tower outlet mass flow rates at TSR 2.0 and TSR 3.0, respectively. On the other hand, the HDWT with a solidity of 0.225 only showed 0.267% and 0.295% lower mass flow rates for TSR 2.0 and TSR 3.0, respectively. Figure 5.20 and Figure 5.21 show the midplane velocity contour comparison of the cooling tower flow for HDWT of solidity 0.225 and 0.450 at TSR 2.0 on the XY and YZ planes, respectively. Figure 5.22 and Figure 5.23 show the midplane velocity contour comparison of the cooling tower flow for HDWT of solidity 0.225 and 0.450 at TSR 3.0 on the XY and YZ planes, respectively. These figures show that the higher solidity HDWT blocks a significant amount of

exhaust air in the middle region of the cooling tower, compared to the lower solidity HDWT, as seen in the XY plane for both the TSRs studied. However, from the YZ velocity contour plane, it is observed that the higher solidity HDWT causes a higher velocity of exhaust air being discharged on the front and back sides of the HDWT. However, the reduced mass flow in the middle part of the tower caused by the high solidity HDWT dominates the increased mass flow on the front and back sides of the HDWT, resulting in an overall reduced mass flow rate of the cooling tower air. Next, for both the HDWT solidities studied, TSR 3.0 showed lower mass flow rates, indicating that the cooling tower experiences more blockage as the HDWT rotates faster, regardless of its solidity. Overall, the 0.450 solidity HDWT boasts a superior performance by producing 12.58 W of power at TSR 2.0, 32.91% higher than the power production capability of the 0.225 solidity HDWT at TSR 3.0. On top of that, the 0.450 solidity HDWT at TSR 2.0 only shows 0.059% higher blockage compared to the 0.225 solidity HDWT at TSR 3.0. Choosing the right balance between solidity and TSR is important to maximize the energy recovery from the exhaust air while keeping the blockage at a minimum so as not to cause any significant impact on the cooling tower performance and fan power usage.

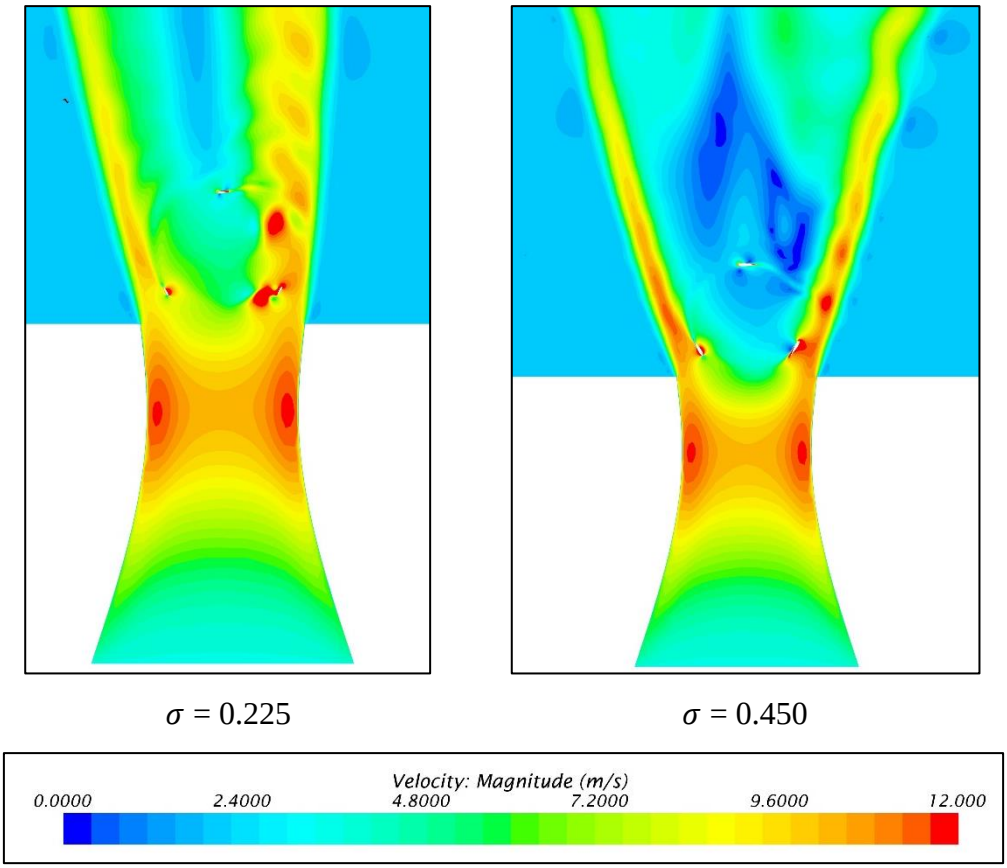

Figure 5.20. XY-midplane velocity contour comparison for the cooling tower air flow with AR 0.44 HDWT of σ = 0.225 (left) and σ = 0.450 (right) placed at the outlet at TSR 2.0.

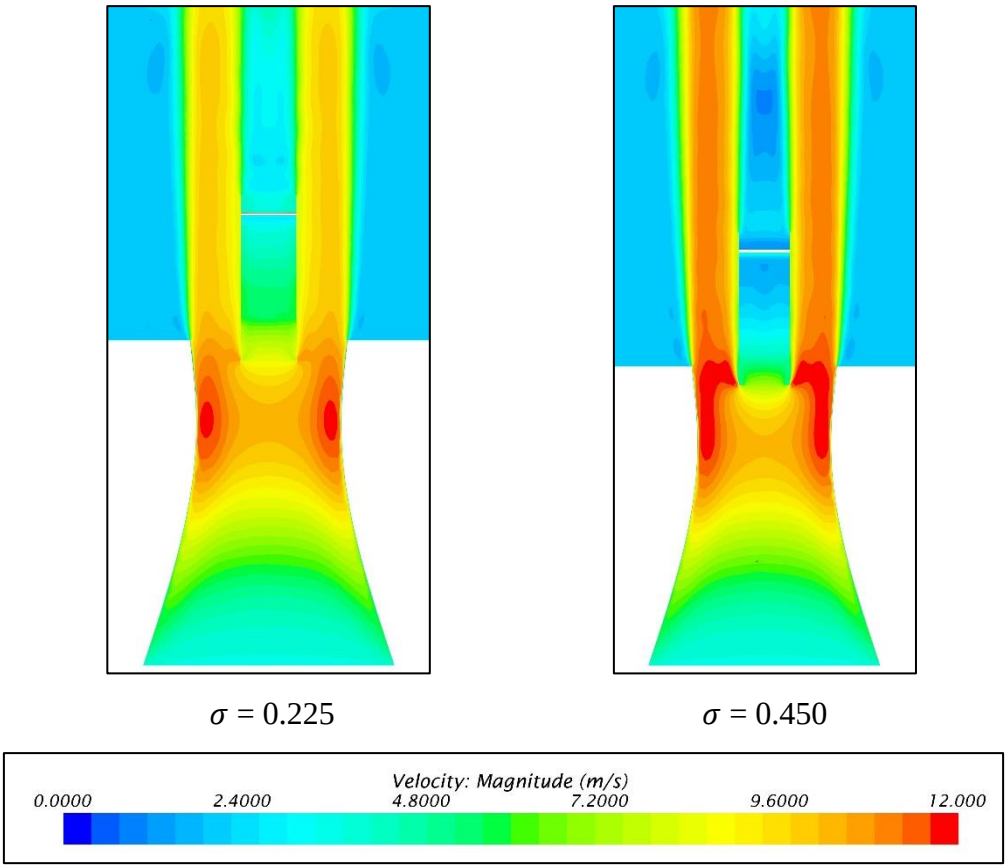

Figure 5.21. YZ-midplane velocity contour comparison for the cooling tower air flow with AR 0.44 HDWT of σ = 0.225 (left) and σ = 0.450 (right) placed at the outlet at TSR 2.0.

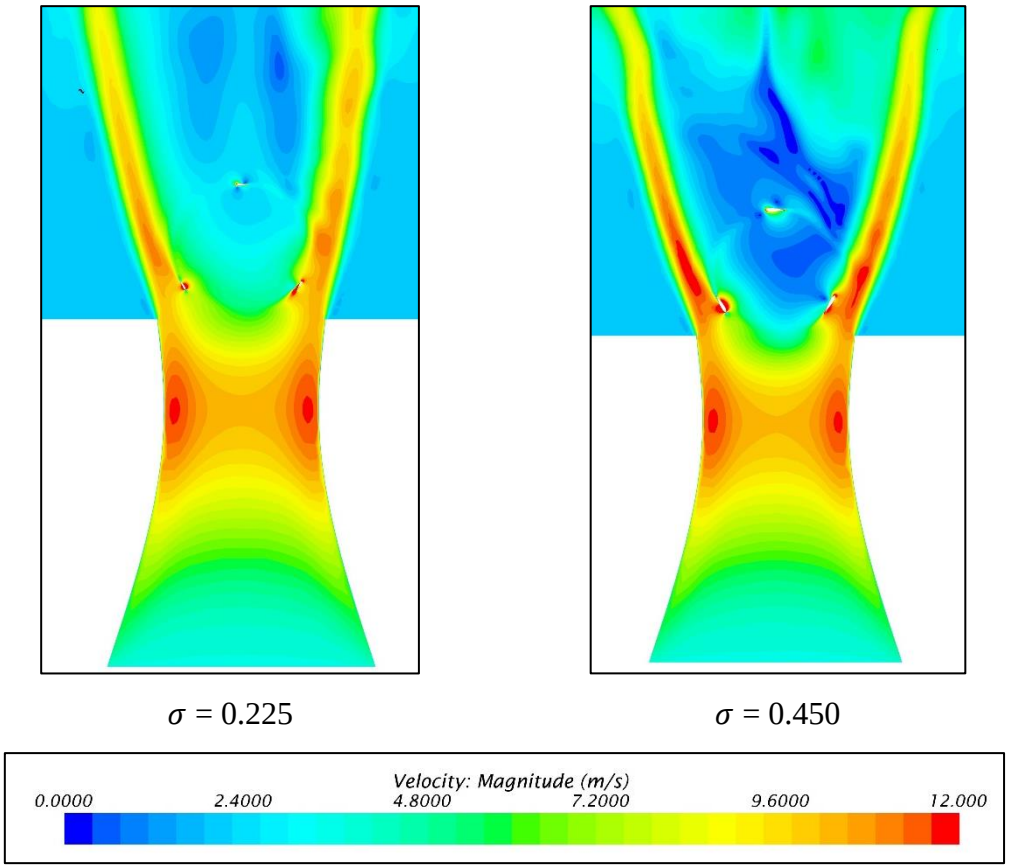

Figure 5.22. XY-midplane velocity contour comparison for the cooling tower air flow with AR 0.44 HDWT of σ = 0.225 (left) and σ = 0.450 (right) placed at the outlet at TSR 3.0.

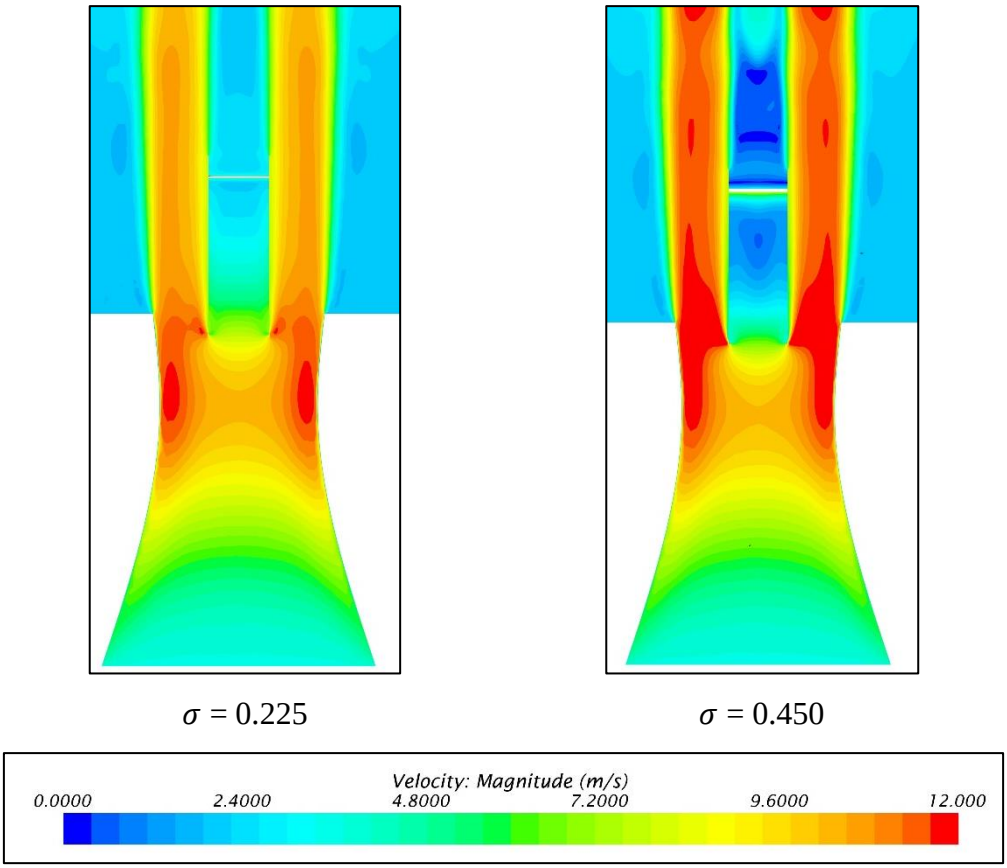

Figure 5.23. YZ-midplane velocity contour comparison for the cooling tower air flow with AR 0.44 HDWT of σ = 0.225 (left) and σ = 0.450 (right) placed at the outlet at TSR 3.0.

Figures 5.24 and 5.25 show the midplane velocity contour comparison for the cooling tower air flow with HDWT of AR 0.44 and solidity of 0.450 augmented by cycloidal diffusers placed at the outlet at TSR 1.5, TSR 2.0, and TSR 3.0 on the XY plane and YZ plane, respectively. The best cycloidal diffusers after the parametric study done in Section 4.3 are used in this analysis. Integrating cycloidal diffusers further increased the blockage compared to the bare HDWT cases. It is seen from the velocity contour presented that the blockage increases with TSR. The higher blockage experienced at TSR 3.0 is because less flow goes through the turbine as the turbine acts like an obstacle, the faster it spins, as discussed by Peng et al. [74]. The HDWT with the cycloidal diffuser integrated produces a maximum power of 16.21 W at its optimum TSR of 2.0.

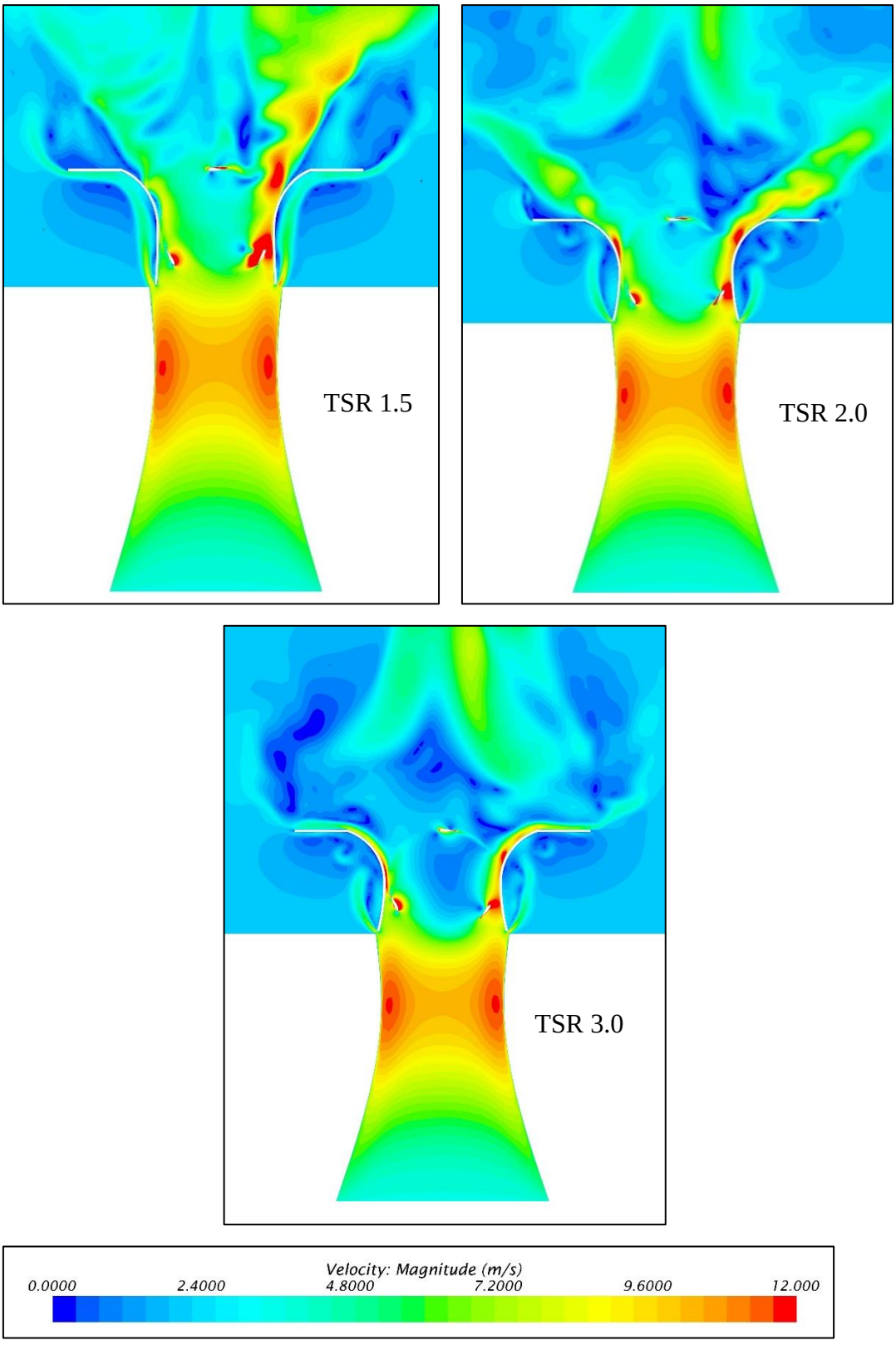

Figure 5.24. XY-midplane velocity contour comparison for the cooling tower air flow with HDWT of AR 0.44 and solidity of 0.450 augmented by cycloidal diffusers placed at the outlet at (a) TSR 1.5, (b) TSR 2.0, and (c) TSR 3.0.

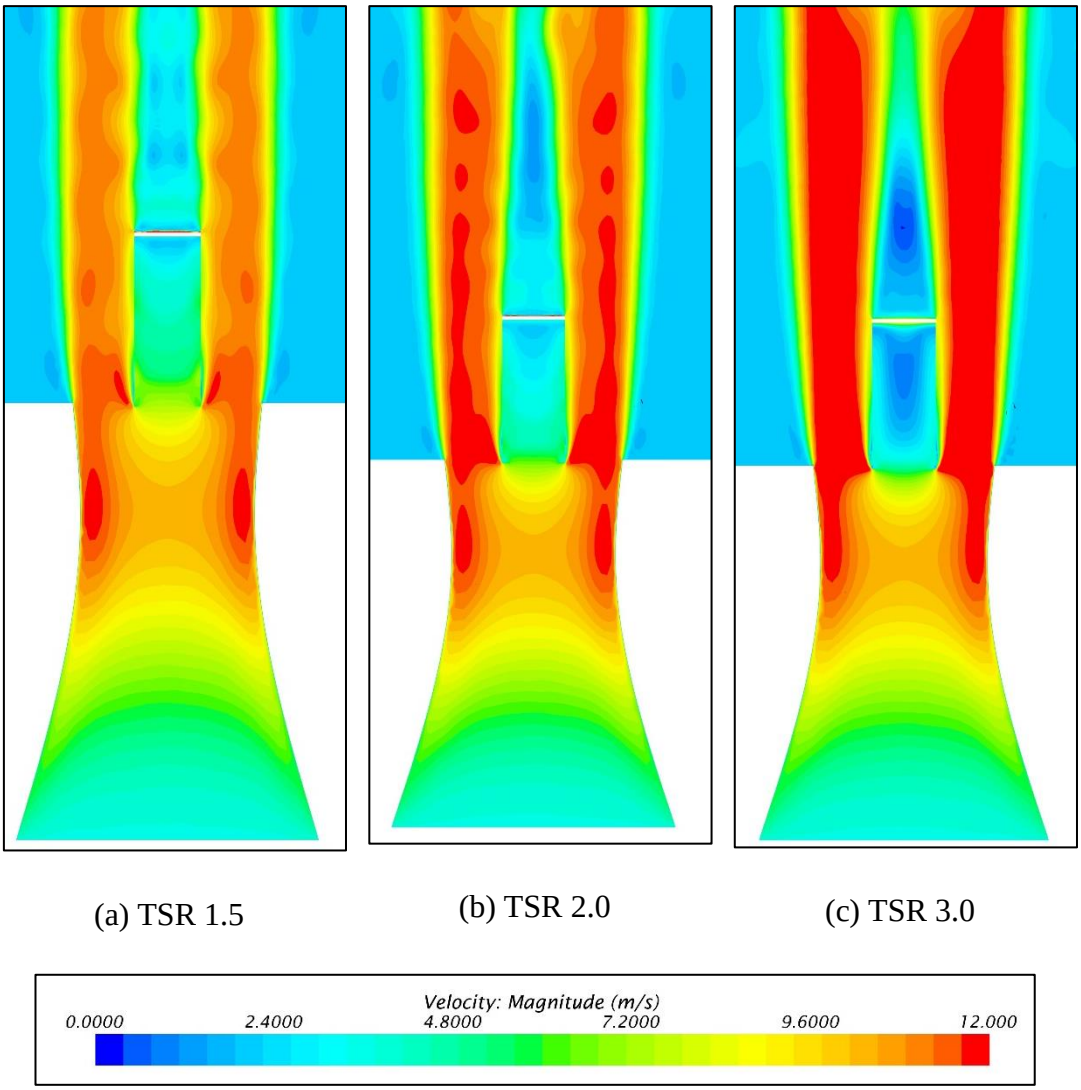

Figure 5.25. YZ-midplane velocity contour comparison for the cooling tower air flow with HDWT of AR 0.44 and solidity of 0.450 augmented by cycloidal diffusers placed at the outlet at (a) TSR 1.5, (b) TSR 2.0, and (c) TSR 3.0.

5.5.3 Expected energy recovery from cooling tower exhaust air

An actual cooling tower with an exhaust air speed close to 9m/s is used to calculate the expected energy that can be recovered using the optimized HDWT and cycloidal diffuser design from this study. The specification of the cooling tower model, T-2800 from Cooling Tower Systems, Inc., is shown in Appendix A1. The cooling tower has a diameter of 3.381 m, a nominal air flow rate of 82.591 m^3/s, an exhaust outlet wind speed of 9.2 m/s, and a fan-rated power of 14914 W. The calculations to obtain these values are shown in Appendix A2. The diameter of the T-2800 cooling tower is about 5.93 times bigger than the cooling tower size used for the numerical simulations in this

study. So, the HDWT diameter and other parameters such as blade length and chord length from this study are also scaled up by 5.93 times to maintain the AR, solidity, and ratio of the HDWT diameter to the cooling tower outlet diameter. This results in an HDWT with a diameter of 2.704 m with a blade length of 1.186 m. In their study, Tong et al. [136] showed that as the diameter of HDWT increases, it produces higher C_p when the solidity is kept the same at the same TSR. Therefore, at TSR 2.0, with a bigger diameter, the HDWT of this study can provide a higher C_p. However, assuming the same C_p is produced at the same wind speed of 9 m/s and the same density, the expected power generated by the HDWT with the optimized cycloidal diffuser under the exhaust air of the T-2800 cooling tower from Cooling Tower Systems, Inc. is calculated as below:

$$P_{turbine} = 0.5 C_p \rho A U_\infty^{\,3}$$

$$P_{turbine} = 0.5(0.4232)(1.18415)(2.704 \times 1.186)(9^3)$$

$$P_{turbine} = 585.79\ W$$

Therefore, the percentage of energy recovered from the reference case cooling tower is:

$$Percentage\ of Energy\ recovered = \frac{P_{turbine}}{Cooling\ tower\ fan\ rated\ power} \times 100$$

$$Energy\ recovered = \frac{585.79\ W}{14914\ W} \times 100$$

$$= 3.928\% \approx 3.93\%$$

5.5.4 Impact of the blockage caused by the exhaust air energy recovery on cooling tower performance

To evaluate the impact of placing the HDWT with the optimized cycloidal diffuser design on the cooling tower performance, an example calculation is done below by assuming some parameters of the cooling tower to find the outlet water temperature difference with two different air mass flow rates. This is done to estimate the impact of the reduced air mass flow rate (0.519% reduction) from the optimized HDWT and cycloidal diffuser design in this study on the cooling tower efficiency.

Assume:

Mass flow rate of water, $\dot{m}_w$ = 60,000 kg/h

Initial mass flow rate of air, $\dot{m}_w$ = 164,183.04 kg/h

Dry-bulb temperature, T_{db}= 35°C

Wet-bulb temperature, T_{wb} = 26°C

Inlet water temperature, T_{wi} = 35°C

Temperature at cooling tower outlet, T_{ao} = 31°C

Relative humidity = 80%

With the given wet-bulb temperature, dry-bulb temperature, and the temperature of the air at the cooling tower outlet, the specific enthalpy and humidity ratio of the air entering and exiting the cooling tower can be found using the Psychrometric Chart obtained from Perry's Chemical Engineer's Handbook (Seventh Edition) as shown in Appendix B.

For the air entering the cooling tower:

$$Specific\ enthalpy, h_1 = 80\ KJ/Kg$$

$$Specific\ humidity\ ratio\ of\ air, \omega_1 = 0.0172$$

For air exiting the cooling tower:

$$Specific\ enthalpy, h_2 = 89.5\ KJ/Kg$$

$$Humidity\ ratio, \omega_2 = 0.0225$$

Then, the outlet water temperature can be calculated using the mass transfer equation as shown in Equation 2.23 where:

$$\dot{m}_a = \frac{\dot{m}_w c_{pw}(T_{wi} - T_{wo})}{(h_2 - h_1) - (\omega_2 - \omega_1)c_{pw}T_{wo}}$$

$$164{,}183.04 = \frac{60{,}000(4.184)(35 - T_{wo})}{(89.5 - 80) - (0.0225 - 0.0172)(4.184)(T_{wo})}$$

$$1{,}559{,}738.88 - 3{,}640.7917\ T_{wo} = 8{,}786{,}400 - 251{,}040\ T_{wo}$$

$$247{,}399.2081\ T_{wo} = 7{,}226{,}661.12$$

$$T_{wo} = 29.21°C$$

Next, for the case of the cooling tower with HDWT and the optimized cycloidal diffusers placed at the outlet, assuming all the conditions stay the same but with a reduced airflow rate of 0.519% due to the integration of the HDWT and cycloidal diffusers:

$$\dot{m}_a = \frac{\dot{m}_w c_{pw}(T_{wi} - T_{wo})}{(h_2 - h_1) - (\omega_2 - \omega_1)c_{pw}T_{wo}}$$

$$163{,}330.56 = \frac{60{,}000(4.184)(35 - T_{wo})}{(89.5 - 80) - (0.0225 - 0.0172)(4.184)(T_{wo})}$$

$$1{,}551{,}640.32 - 3{,}621.8878\,T_{wo} = 8{,}786{,}400 - 251{,}040\,T_{wo}$$

$$247{,}418.1122\,T_{wo} = 7{,}234{,}759.68$$

$$T_{wo} = 29.24°C$$

Percentage difference between the two inlet water temperatures:

$$= \frac{29.24 - 29.21}{29.21} * 100$$

$$= 0.103\%$$

The cooling tower efficiency difference can be calculated as shown below, where η_{CT} is the empty cooling tower efficiency, and η_{AWT} is the cooling tower efficiency with the augmented HDWT placed at the outlet:

$$= \frac{\eta_{AWT} - \eta_{CT}}{\eta_{CT}} * 100$$

From Equation 2.15:

$$\eta_{CT} = \frac{35 - 29.21}{35 - 26}$$

$$\eta_{CT} = 0.6433\ or\ 64.33\%$$

$$\eta_{AWT} = \frac{35 - 29.24}{35 - 26}$$

$$\eta_{AWT} = 0.6400\ or\ 64.0\%$$

Therefore, the difference in the efficiency is:

$$64\% - 64.33\% = -0.33\%$$

The air mass flow rate blockage of 0.519% only causes the cooling tower to drop by 0.33% in efficiency. From Subsection 5.5.3, it was estimated that a scaled-up HDWT used on an actual cooling tower can recover 3.93% (585.79 W) of the cooling tower fan power consumed. This shows that the percentage of energy recovered is way higher than the negative impact on the cooling tower. However, a more comprehensive study in the form of an experimental setup can be done to measure and validate the performance of the HDWT and its impact on cooling tower efficiency and fan performance.

CHAPTER 6: CONCLUSIONS AND RECOMMENDATIONS

6.1 Findings and Contributions

In this study, a three-dimensional URANS study has been carried out on the HDWT to optimize the energy extraction from cooling tower exhaust air. The best diameter-based AR and the solidity of the HDWT were investigated before adding and optimizing the cycloidal diffusers to increase the performance of the turbine. The main findings obtained from this study are:

- At equal solidity (σ) of 0.30, smaller diameter-based AR HDWTs (AR=0.35 and 0.44) produced higher C_p at all TSRs (1.5 to 3.5) compared to the bigger AR HDWTs (AR=0.54 and 0.70). This is because the smaller AR HDWT (bigger diameter) has a longer blade chord length, which benefits from a longer period of attached flow on the blades. Besides, the smaller AR HDWT in this study has a higher chord-based Reynolds' number, Re_c which is directly proportional to the blade's chord length as shown in Equation 2.7, has a significant effect on small HDWT performance as it promotes a higher lift coefficient and lowers drag coefficient.

- The bigger AR HDWT experiences larger vortex formation on the blade's surface and a slightly lower pressure difference between the pressure and suction side of the blade at most of the azimuthal angle, which results in a lower C_p. Moreover, at TSR 2.5, it was observed that the bigger AR blade interacts with the detached flow from the advancing blade from 270° to 300°, whereas the smaller AR HDWT does not. The effect of TSR was also studied, and it was shown that the performance at lower TSR values was unsatisfactory due to the pressure loss at deep stalls from the consistent vortex formation and detached flow. The optimum TSR for the solidity 0.3 HDWT is 2.5 since the flow over the HDWT blades was mostly attached, producing the highest pressure difference between the suction side and pressure side of the blade. At a higher TSR of 3.5, the blade rotates faster, and the relative velocity on the blade increases to a point where the blade's angle of attack decreases and the drag force increases, which reduces the HDWT performance.

- The solidity was also optimized, and the HDWT of $\sigma = 0.450$ has given the highest power coefficient of 0.3196 at TSR 2.0. The HDWT blades with a solidity of 0.450

interact better with the cooling tower flow, exhibiting a longer duration of attached flow and the high-pressure difference between the blades' pressure and suction side, generating higher lift force and moment at TSR 2.0.

- A cycloidal diffuser was added to the current cooling tower exhaust air energy extraction system. The diffuser length, diffuser angle, shroud length and shroud angle were optimized, which resulted in the diffuser with a length of $0.25D$ (114mm), diffuser angle of 36.1°, shroud length of $0.48D$ (218mm) and shroud angle of 7.4° provided maximum power enhancement as it successfully improved the HDWT power coefficient by 32.42% compared to the bare HDWT design at TSR 2.0.

- Optimal design method for RSM design of experiment can provide accurate results for optimizing wind augmenter designs in wind turbine applications. It is shown that using wind augmenters, in this case, the cycloidal diffuser with optimized parameters can enhance the HDWT performance for cooling tower exhaust air energy extractions.

- The effect of using HDWT with different AR, solidities, and integration of cycloidal diffusers at different TSRs on the cooling tower mass flow rate and flow behaviour was done. It was shown that all the cases reduced the mass flow rate of the cooling tower exhaust air, with the optimized design causing a 0.519 % reduction in the mass flow rate. Analysis of the cooling tower flow shows that the blockage occurred in the middle area of the outlet where the HDWT was placed. The smaller AR (bigger diameter), higher solidity, and higher TSR caused the most blockage on the cooling tower exhaust air.

- Estimated power produced by the HDWT, augmented with the optimized cycloidal diffuser design, was calculated using specification from an actual cooling tower (Model T-2800) from Cooling Tower Systems, Inc. The HDWT in this study was scaled up based on the diameter of the actual cooling tower while keeping other parameters the same. It was estimated that 3.93% of cooling tower fan motor energy can be recovered from the exhaust air. Furthermore, the effect of the blockage caused by the optimized HDWT setup on the cooling tower efficiency was also estimated, where a reduction of 0.33% efficiency was shown.

6.2 Recommendations for Future Work

The present study only focuses on one type of cooling tower with a constant size and shape. Therefore, the parameter optimized to maximize the cooling tower exhaust air energy is only valid for this specific geometry and wind condition of the cooling tower. Many varieties of cooling towers are available in many configurations that produce different wind characteristics. However, the methods presented in this study can be used to study the feasibility of using wind augmenters and optimize the system for exhaust air energy extractions on different types and sizes of cooling towers. Moreover, the mesh and boundary conditions of the present study were validated using free stream flow conditions studies available in the open literature. To properly validate the results and performance of the HDWT for this study, an experimental set-up needs to be done for this cooling tower. The power recovery of the present HDWT augmented by the optimized cycloidal diffuser has been estimated using specifications from an actual cooling tower. In addition, the effect of the blockage caused by the exhaust air energy recovery system has also been evaluated, showing minimal negative impact on the cooling tower efficiency. However, it is recommended that a further study using an experimental setup be done to measure the impact of blockage on the cooling tower efficiency and fan motor power consumption before implementation. Investigating the performances of the exhaust air recovery systems at different distances from the cooling tower outlet can be done for future research to minimize the blockage effect on the cooling tower.

REFERENCES

[1] BP, “bp Statistical Review of World Energy 2022,” London, 2022. [Online]. Available: https://www.bp.com/content/dam/bp/business-sites/en/global/corporate/pdfs/energy-economics/statistical-review/bp-stats-review-2022-full-report.pdf.

[2] H. Ritchie, M. Roser, and P. Rosada, “Fossil Fuels,” *Our World in Data*, 2022. https://ourworldindata.org/fossil-fuels.

[3] International Energy Agency, “Global Energy Review 2021,” Paris, 2021. [Online]. Available: https://iea.blob.core.windows.net/assets/d0031107-401d-4a2f-a48b-9eed19457335/GlobalEnergyReview2021.pdf.

[4] International Energy Agency, “CO2 Emissions in 2022,” Paris, 2022. [Online]. Available: https://www.iea.org/news/global-co2-emissions-rebounded-to-their-highest-level-in-history-in-2021.

[5] A. Kibria, S. B. Akhundjanov, and R. Oladi, “Fossil fuel share in the energy mix and economic growth,” *Int. Rev. Econ. Financ.*, vol. 59, no. August 2018, pp. 253–264, 2019, doi: 10.1016/j.iref.2018.09.002.

[6] BP, “bp Statistical Review of World Energy 2021,” London, 2021. [Online]. Available: https://www.bp.com/content/dam/bp/business-sites/en/global/corporate/pdfs/energy-economics/statistical-review/bp-stats-review-2021-full-report.pdf.

[7] REN21, “Renewables 2022 Global Status Report,” Paris, 2022. [Online]. Available: https://www.ren21.net/gsr-2022/.

[8] W. Liu, X. Zhang, and S. Feng, “Does renewable energy policy work? Evidence from a panel data analysis,” *Renew. Energy*, vol. 135, pp. 635–642, 2019, doi: 10.1016/j.renene.2018.12.037.

[9] A. Savaresi, “The Paris agreement: A new beginning?,” *J. Energy Nat. Resour. Law*, vol. 34, no. 1, pp. 16–26, 2016, doi: 10.1080/02646811.2016.1133983.

[10] H. Ritchie, M. Roser, and P. Rosado, “CO_2 and Greenhouse Gas Emissions,” *Our World in Data*, 2020. https://ourworldindata.org/co2-and-greenhouse-gas-emissions.

[11] J. Lee and F. Zhao, “GWEC Global Wind Report,” Brussels, 2022. [Online]. Available: https://gwec.net/wp-content/uploads/2022/04/Annual-Wind-Report-2022_screen_final_April.pdf.

[12] IRENA, “World Energy Transitions Outlook 2023: 1.5°C Pathway,” Abu Dhabi, 2023. [Online]. Available: https://irena.org/Digital-Report/World-Energy-Transitions-Outlook-2022%0Ahttps://irena.org/publications/2021/March/World-Energy-Transitions-Outlook.

[13] V. Nelson, “Vertical Axis Wind Turbines,” *Innov. Wind Turbines*, no. February, pp. 63–90, 2019, doi: 10.1201/9781003010883-4.

[14] N. Ma *et al.*, “Airfoil optimization to improve power performance of a high-solidity vertical axis wind turbine at a moderate tip speed ratio,” *Energy*, vol. 150, pp. 236–252, 2018, doi: 10.1016/j.energy.2018.02.115.

[15] S. Roy and A. Ducoin, “Unsteady analysis on the instantaneous forces and moment arms acting on a novel Savonius-style wind turbine,” *Energy Convers. Manag.*, vol. 121, pp. 281–296, 2016, doi: 10.1016/j.enconman.2016.05.044.

[16] R. Kumar, K. Raahemifar, and A. S. Fung, “A critical review of vertical axis wind turbines for urban applications,” *Renew. Sustain. Energy Rev.*, vol. 89, no. April, pp. 281–291, 2018, doi: 10.1016/j.rser.2018.03.033.

[17] W. Hao, Q. Ding, and C. Li, “Optimal performance of adaptive flap on flow separation control,” *Comput. Fluids*, vol. 179, pp. 437–448, 2019, doi: 10.1016/j.compfluid.2018.11.010.

[18] A. Bianchini, G. Ferrara, and L. Ferrari, “Design guidelines for H-Darrieus wind turbines: Optimization of the annual energy yield,” *Energy Convers. Manag.*, vol. 89, pp. 690–707, 2015, doi: 10.1016/j.enconman.2014.10.038.

[19] A. Sagharichi, M. Zamani, and A. Ghasemi, “Effect of solidity on the performance of variable-pitch vertical axis wind turbine,” *Energy*, vol. 161, pp. 753–775, 2018, doi: 10.1016/j.energy.2018.07.160.

[20] A. Rezaeiha, H. Montazeri, and B. Blocken, “Towards optimal aerodynamic design of vertical axis wind turbines: Impact of solidity and number of blades,” *Energy*, vol. 165, pp. 1129–1148, 2018, doi: 10.1016/j.energy.2018.09.192.

[21] Q. Li, T. Maeda, Y. Kamada, J. Murata, K. Furukawa, and M. Yamamoto, “Effect of number of blades on aerodynamic forces on a straight-bladed Vertical Axis Wind Turbine,” *Energy*, vol. 90, pp. 784–795, 2015, doi: 10.1016/j.energy.2015.07.115.

[22] Z. Wang, Y. Wang, and M. Zhuang, “Improvement of the aerodynamic performance of vertical axis wind turbines with leading-edge serrations and helical blades using CFD and Taguchi method,” *Energy Convers. Manag.*, vol. 177, no. September, pp. 107–121, 2018, doi: 10.1016/j.enconman.2018.09.028.

[23] Q. Li *et al.*, “Effect of rotor aspect ratio and solidity on a straight-bladed vertical axis wind turbine in three-dimensional analysis by the panel method,” *Energy*, vol. 121, pp. 1–9, 2017, doi: 10.1016/j.energy.2016.12.112.

[24] S. Zanforlin and S. Deluca, “Effects of the Reynolds number and the tip losses on the optimal aspect ratio of straight-bladed Vertical Axis Wind Turbines,” *Energy*, vol. 148, pp. 179–195, 2018, doi: 10.1016/j.energy.2018.01.132.

[25] O. S. Mohamed, A. A. Ibrahim, A. K. Etman, A. A. Abdelfatah, and A. M. R. Elbaz, “Numerical investigation of Darrieus wind turbine with slotted airfoil blades,” *Energy Convers. Manag. X*, vol. 5, no. November 2019, p. 100026, 2020, doi: 10.1016/j.ecmx.2019.100026.

[26] X. Sun, J. Zhu, A. Hanif, Z. Li, and G. Sun, “Effects of blade shape and its

corresponding moment of inertia on self- starting and power extraction performance of the novel bowl-shaped floating straight-bladed vertical axis wind turbine," *Sustain. Energy Technol. Assessments*, vol. 38, no. December 2019, p. 100648, 2020, doi: 10.1016/j.seta.2020.100648.

[27] Y. Celik, L. Ma, D. Ingham, and M. Pourkashanian, "Aerodynamic investigation of the start-up process of H-type vertical axis wind turbines using CFD," *J. Wind Eng. Ind. Aerodyn.*, vol. 204, no. November 2019, p. 104252, 2020, doi: 10.1016/j.jweia.2020.104252.

[28] S. B. Qamar and I. Janajreh, "Investigation of Effect of Cambered Blades on Darrieus VAWTs," *Energy Procedia*, vol. 105, pp. 537–543, 2017, doi: 10.1016/j.egypro.2017.03.353.

[29] H. Zhu, W. Hao, C. Li, and Q. Ding, "Numerical study of effect of solidity on vertical axis wind turbine with Gurney flap," *J. Wind Eng. Ind. Aerodyn.*, vol. 186, no. January, pp. 17–31, 2019, doi: 10.1016/j.jweia.2018.12.016.

[30] H. Wang *et al.*, "Effects of leading edge slat on flow separation and aerodynamic performance of wind turbine," *Energy*, vol. 182, pp. 988–998, 2019, doi: 10.1016/j.energy.2019.06.096.

[31] I. C. M. Lositaño and L. A. M. Danao, "Steady wind performance of a 5 kW three-bladed H-rotor Darrieus Vertical Axis Wind Turbine (VAWT) with cambered tubercle leading edge (TLE) blades," *Energy*, vol. 175, pp. 278–291, 2019, doi: 10.1016/j.energy.2019.03.033.

[32] S. Brusca, R. Lanzafame, and M. Messina, "Design of a vertical-axis wind turbine: how the aspect ratio affects the turbine's performance," *Int. J. Energy Environ. Eng.*, vol. 5, no. 4, pp. 333–340, 2014, doi: 10.1007/s40095-014-0129-x.

[33] J. U. Parakkal, K. El Kadi, A. El-Sinawi, S. Elagroudy, and I. Janajreh, "Numerical analysis of VAWT wind turbines: Joukowski vs classical NACA rotor's blades," *Energy Procedia*, vol. 158, pp. 1194–1201, 2019, doi: 10.1016/j.egypro.2019.01.306.

[34] H. Y. Peng, H. F. Lam, and H. J. Liu, "Power performance assessment of H-rotor vertical axis wind turbines with different aspect ratios in turbulent flows via experiments," *Energy*, vol. 173, pp. 121–132, 2019, doi: 10.1016/j.energy.2019.01.140.

[35] A. R. Sengupta, A. Biswas, and R. Gupta, "Comparison of low wind speed aerodynamics of unsymmetrical blade H-Darrieus rotors-blade camber and curvature signatures for performance improvement," *Renew. Energy*, vol. 139, pp. 1412–1427, 2019, doi: 10.1016/j.renene.2019.03.054.

[36] J. Su, Y. Chen, Z. Han, D. Zhou, Y. Bao, and Y. Zhao, "Investigation of V-shaped blade for the performance improvement of vertical axis wind turbines," *Appl. Energy*, vol. 260, no. December 2019, p. 114326, 2020, doi: 10.1016/j.apenergy.2019.114326.

[37] A. Subramanian *et al.*, "Effect of airfoil and solidity on performance of small scale vertical axis wind turbine using three dimensional CFD model," *Energy*, vol. 133, pp. 179–190, 2017, doi: 10.1016/j.energy.2017.05.118.

[38] S. B. Qamar and I. Janajreh, “A comprehensive analysis of solidity for cambered darrieus VAWTs,” *Int. J. Hydrogen Energy*, vol. 42, no. 30, pp. 19420–19431, 2017, doi: 10.1016/j.ijhydene.2017.06.041.

[39] A. Bianchini, F. Balduzzi, D. Di Rosa, and G. Ferrara, “On the use of Gurney Flaps for the aerodynamic performance augmentation of Darrieus wind turbines,” *Energy Convers. Manag.*, vol. 184, no. January, pp. 402–415, 2019, doi: 10.1016/j.enconman.2019.01.068.

[40] A. Meana-Fernández, I. Solís-Gallego, J. M. Fernández Oro, K. M. Argüelles Díaz, and S. Velarde-Suárez, “Parametrical evaluation of the aerodynamic performance of vertical axis wind turbines for the proposal of optimized designs,” *Energy*, vol. 147, pp. 504–517, 2018, doi: 10.1016/j.energy.2018.01.062.

[41] J. Chen, L. Chen, H. Xu, H. Yang, C. Ye, and D. Liu, “Performance improvement of a vertical axis wind turbine by comprehensive assessment of an airfoil family,” *Energy*, vol. 114, pp. 318–331, 2016, doi: 10.1016/j.energy.2016.08.005.

[42] I. Hashem and M. H. Mohamed, “Aerodynamic performance enhancements of H-rotor Darrieus wind turbine,” *Energy*, vol. 142, pp. 531–545, 2018, doi: 10.1016/j.energy.2017.10.036.

[43] I. Ostos, I. Ruiz, M. Gajic, W. Gómez, A. Bonilla, and C. Collazos, “A modified novel blade configuration proposal for a more efficient VAWT using CFD tools,” *Energy Convers. Manag. J.*, vol. 180, no. August 2018, pp. 733–746, 2019, doi: 10.1016/j.enconman.2018.11.025.

[44] M. M. Aslam Bhutta, N. Hayat, A. U. Farooq, Z. Ali, S. R. Jamil, and Z. Hussain, “Vertical axis wind turbine - A review of various configurations and design techniques,” *Renew. Sustain. Energy Rev.*, vol. 16, no. 4, pp. 1926–1939, 2012, doi: 10.1016/j.rser.2011.12.004.

[45] W. Tjiu, T. Marnoto, S. Mat, M. H. Ruslan, and K. Sopian, “Darrieus vertical axis wind turbine for power generation I: Assessment of Darrieus VAWT configurations,” *Renew. Energy*, vol. 75, pp. 50–67, 2015, doi: 10.1016/j.renene.2014.09.038.

[46] M. Ghasemian, Z. N. Ashrafi, and A. Sedaghat, “A review on computational fluid dynamic simulation techniques for Darrieus vertical axis wind turbines,” *Energy Convers. Manag.*, vol. 149, pp. 87–100, 2017, doi: 10.1016/j.enconman.2017.07.016.

[47] B. Hand, G. Kelly, and A. Cashman, “Aerodynamic design and performance parameters of a lift-type vertical axis wind turbine: A comprehensive review,” *Renew. Sustain. Energy Rev.*, vol. 139, no. December 2019, p. 110699, 2021, doi: 10.1016/j.rser.2020.110699.

[48] Z. Zhao, D. Wang, T. Wang, W. Shen, H. Liu, and M. Chen, “A review: Approaches for aerodynamic performance improvement of lift-type vertical axis wind turbine,” *Sustain. Energy Technol. Assessments*, vol. 49, no. November 2021, p. 101789, 2022, doi: 10.1016/j.seta.2021.101789.

[49] I. Renewable Energy Agency, “Renewable capacity highlights (31 March

2020)," 2020. Accessed: Jan. 13, 2021. [Online]. Available: www.irena.org/publications.

[50] R. Nobile, M. Vahdati, J. F. Barlow, and A. Mewburn-Crook, "Unsteady flow simulation of a vertical axis augmented wind turbine: A two-dimensional study," *J. Wind Eng. Ind. Aerodyn.*, vol. 125, pp. 168–179, 2014, doi: 10.1016/j.jweia.2013.12.005.

[51] A. Dilimulati, T. Stathopoulos, and M. Paraschivoiu, "Wind turbine designs for urban applications: A case study of shrouded diffuser casing for turbines," *J. Wind Eng. Ind. Aerodyn.*, vol. 175, no. November 2017, pp. 179–192, 2018, doi: 10.1016/j.jweia.2018.01.003.

[52] K. H. Wong *et al.*, "The design and flow simulation of a power-augmented shroud for urban wind turbine system," *Energy Procedia*, vol. 61, pp. 1275–1278, 2014, doi: 10.1016/j.egypro.2014.11.1080.

[53] W. T. Chong *et al.*, "Design of an exhaust air energy recovery wind turbine generator for energy conservation in commercial buildings," *Renew. Energy*, vol. 67, pp. 252–256, 2014, doi: 10.1016/j.renene.2013.11.028.

[54] S. A. Salih, S. Mat, K. Sopian, E. Saleh, and M. Alkhair, "Simulation analysis of Venturi-Vertical Axis Wind Turbine (V-VAWT)," in *Proceeding of the 8th International Conference on Renewable Energy Sources (RES'14)*, 2014, no. November, pp. 191–196, doi: 10.13140/2.1.2290.9122.

[55] H. W. Stanford III, - *Cooling Tower Fundamentals*. 2012.

[56] W. T. Chong, S. C. Poh, A. Fazlizan, S. Y. Yip, C. K. Chang, and W. P. Hew, "Early development of an energy recovery wind turbine generator for exhaust air system," *Appl. Energy*, vol. 112, pp. 568–575, 2013, doi: 10.1016/j.apenergy.2013.01.042.

[57] W. T. Chong *et al.*, "The experimental study on the wind turbine's guide-vanes and diffuser of an exhaust air energy recovery system integrated with the cooling tower," *Energy Convers. Manag.*, vol. 87, pp. 145–155, 2014, doi: 10.1016/j.enconman.2014.07.009.

[58] A. Fazlizan, W. T. Chong, S. Y. Yip, W. P. Hew, and S. C. Poh, "Design and experimental analysis of an exhaust air energy recovery wind turbine generator," *Energies*, vol. 8, no. 7, pp. 6566–6584, 2015, doi: 10.3390/en8076566.

[59] S. Tabatabaeikia *et al.*, "Computational and experimental optimization of the exhaust air energy recovery wind turbine generator," *Energy Convers. Manag.*, vol. 126, pp. 862–874, 2016, doi: 10.1016/j.enconman.2016.08.039.

[60] Z. Zhao *et al.*, "Variable pitch approach for performance improving of straight-bladed VAWT at rated tip speed ratio," *Appl. Sci.*, vol. 8, no. 6, 2018, doi: 10.3390/app8060957.

[61] C. Zhu, Y. Qiu, Y. Feng, T. Wang, and H. Li, "Combined effect of passive vortex generators and leading-edge roughness on dynamic stall of the wind turbine airfoil," *Energy Convers. Manag.*, vol. 251, no. November 2021, p. 115015, 2021, doi: 10.1016/j.enconman.2021.115015.

[62] J. Liu, R. Chen, Y. You, and Z. Shi, “Numerical investigation of dynamic stall suppression of rotor airfoil via improved co-flow jet,” *Chinese J. Aeronaut.*, 2021, doi: 10.1016/j.cja.2021.07.041.

[63] W. J. McCroskey, L. W. Carr, and K. W. McAlister, “Dynamic stall experiments on oscillating airfoils,” *AIAA J.*, vol. 14, no. 1, pp. 57–63, 1976.

[64] J. G. Leishman, “Dynamic stall experiments on the NACA 23012 aerofoil,” *Exp. Fluids*, vol. 9, no. 1–2, pp. 49–58, 1990, doi: 10.1007/BF00575335.

[65] J. G. Leishman and G. L. Martin, “Challenges in Modelling the Unsteady Aerodynamics of Wind Turbines †,” *Wind Energy*, vol. 132, no. January, pp. 85–132, 2002, doi: 10.1002/we.62.

[66] Y. Celik, D. Ingham, L. Ma, and M. Pourkashanian, “Design and aerodynamic performance analyses of the self-starting H-type VAWT having J-shaped aerofoils considering various design parameters using CFD,” *Energy*, vol. 251, p. 123881, 2022, doi: 10.1016/j.energy.2022.123881.

[67] A. Abdolahifar and S. M. H. Karimian, “A comprehensive three-dimensional study on Darrieus vertical axis wind turbine with slotted blade to reduce flow separation,” *Energy*, vol. 248, p. 123632, 2022, doi: 10.1016/j.energy.2022.123632.

[68] J. Joseph and A. Sathyabhama, “Leading edge tubercle on wind turbine blade to mitigate problems of stall, hysteresis, and laminar separation bubble,” *Energy Convers. Manag.*, vol. 255, no. February, p. 115337, 2022, doi: 10.1016/j.enconman.2022.115337.

[69] Y. Yan, E. Avital, J. Williams, and J. Cui, “Aerodynamic performance improvements of a vertical axis wind turbine by leading-edge protuberance,” *J. Wind Eng. Ind. Aerodyn.*, vol. 211, no. January, p. 104535, 2021, doi: 10.1016/j.jweia.2021.104535.

[70] Z. Yi-Nan, C. Hui-Jing, and Z. Ming-Ming, “A calculation method for modeling the flow characteristics of the wind turbine airfoil with leading-edge protuberances,” *J. Wind Eng. Ind. Aerodyn.*, vol. 212, no. September 2020, p. 104613, 2021, doi: 10.1016/j.jweia.2021.104613.

[71] Y. Zhang *et al.*, “Investigation of aerodynamic forces and flow field of an H-type vertical axis wind turbine based on bionic airfoil,” *Energy*, vol. 242, p. 122999, 2022, doi: 10.1016/j.energy.2021.122999.

[72] Y. N. Zhang, H. J. Cao, and M. M. Zhang, “Investigation of leading-edge protuberances for the performance improvement of thick wind turbine airfoil,” *J. Wind Eng. Ind. Aerodyn.*, vol. 217, no. January, p. 104736, 2021, doi: 10.1016/j.jweia.2021.104736.

[73] X. Zhu *et al.*, “Numerical study of aerodynamic characteristics on a straight-bladed vertical axis wind turbine with bionic blades,” *Energy*, vol. 239, p. 122453, 2022, doi: 10.1016/j.energy.2021.122453.

[74] H. Y. Peng, B. W. Zhong, G. Hu, and H. J. Liu, “Optimization analysis of straight-bladed vertical axis wind turbines in turbulent environments by wind tunnel testing,” *Energy Convers. Manag.*, vol. 257, no. December 2021, 2022,

doi: 10.1016/j.enconman.2022.115411.

[75] M. Maalouly, M. Souaiby, A. ElCheikh, J. S. Issa, and M. Elkhoury, "Transient analysis of H-type Vertical Axis Wind Turbines using CFD," *Energy Reports*, vol. 8, pp. 4570–4588, 2022, doi: 10.1016/j.egyr.2022.03.136.

[76] K. H. Wong, W. T. Chong, N. L. Sukiman, S. C. Poh, Y. C. Shiah, and C. T. Wang, "Performance enhancements on vertical axis wind turbines using flow augmentation systems: A review," *Renew. Sustain. Energy Rev.*, vol. 73, no. January, pp. 904–921, 2017, doi: 10.1016/j.rser.2017.01.160.

[77] T. A. Khamlaj and M. P. Rumpfkeil, "Analysis and optimization of ducted wind turbines," *Energy*, vol. 162, pp. 1234–1252, 2018, doi: 10.1016/j.energy.2018.08.106.

[78] Y. Ohya, T. Karasudani, A. Sakurai, K. ichi Abe, and M. Inoue, "Development of a shrouded wind turbine with a flanged diffuser," *J. Wind Eng. Ind. Aerodyn.*, vol. 96, no. 5, pp. 524–539, 2008, doi: 10.1016/j.jweia.2008.01.006.

[79] A. Krishnan and M. Paraschivoiu, "3D analysis of building mounted VAWT with diffuser shaped shroud," *Sustain. Cities Soc.*, vol. 27, pp. 160–166, 2016, doi: 10.1016/j.scs.2015.06.006.

[80] X. H. Wang, K. H. Wong, W. T. Chong, J. H. Ng, X. B. Xiang, and C. T. Wang, "Experimental investigation of a diffuser-integrated vertical axis wind turbine," *IOP Conf. Ser. Earth Environ. Sci.*, vol. 463, no. 1, 2020, doi: 10.1088/1755-1315/463/1/012153.

[81] A. M. El-zahaby, A. E. Kabeel, S. S. Elsayed, and M. F. Obiaa, "CFD analysis of flow fields for shrouded wind turbine ' s diffuser model with different flange angles," *Alexandria Eng. J.*, vol. 56, no. 1, pp. 171–179, 2017, doi: 10.1016/j.aej.2016.08.036.

[82] K. Watanabe, S. Takahashi, and Y. Ohya, "Application of a diffuser structure to vertical-axis wind turbines," *Energies*, vol. 9, no. 6, 2016, doi: 10.3390/en9060406.

[83] A. Dessoky, G. Bangga, T. Lutz, and E. Krämer, "Aerodynamic and aeroacoustic performance assessment of H-rotor darrieus VAWT equipped with wind-lens technology," *Energy*, vol. 175, pp. 76–97, 2019, doi: 10.1016/j.energy.2019.03.066.

[84] R. A. Ghazalla, M. H. Mohamed, and A. A. Hafiz, "Synergistic analysis of a Darrieus wind turbine using computational fluid dynamics," *Energy*, vol. 189, 2019, doi: 10.1016/j.energy.2019.116214.

[85] L. Kuang, J. Su, Y. Chen, Z. Han, and D. Zhou, "Wind-capture-accelerate device for performance improvement of vertical-axis wind turbines : External diffuser system," *Energy*, vol. 239, p. 122196, 2022, doi: 10.1016/j.energy.2021.122196.

[86] A. G. Refaie, H. S. Abdel Hameed, M. A. A. Nawar, Y. A. Attai, and M. H. Mohamed, "Qualitative and quantitative assessments of an Archimedes Spiral

Wind Turbine performance augmented by A concentrator," *Energy*, vol. 231, p. 121128, 2021, doi: 10.1016/j.energy.2021.121128.

[87] A. G. Refaie, H. S. A. Hameed, M. A. A. Nawar, Y. A. Attai, and M. H. Mohamed, "Comparative investigation of the aerodynamic performance for several Shrouded Archimedes Spiral Wind Turbines," *Energy*, vol. 239, p. 122295, 2022, doi: 10.1016/j.energy.2021.122295.

[88] A. M. Kamal, M. A. A. Nawar, Y. A. Attai, and M. H. Mohamed, "Blade design effect on Archimedes Spiral Wind Turbine performance: Experimental and numerical evaluations," *Energy*, vol. 250, p. 123892, 2022, doi: 10.1016/j.energy.2022.123892.

[89] N. Kumar Thakur, R. Thakur, K. Kashyap, and B. Goel, "Efficiency enhancement in Archimedes screw turbine by varying different input parameters – An experimental study," *Mater. Today Proc.*, vol. 52, pp. 1161–1167, 2022, doi: 10.1016/j.matpr.2021.11.020.

[90] M. Takao, H. Kuma, T. Maeda, Y. Kamada, M. Oki, and A. Minoda, "A straight-bladed vertical axis wind turbine with a directed guide vane row - Effect of guide vane solidity on the performance," *J. Therm. Sci.*, vol. 18, no. 1, pp. 414–418, 2009, doi: 10.1299/jsmekyushu.2008.199.

[91] W. T. Chong, A. Fazlizan, S. C. Poh, K. C. Pan, W. P. Hew, and F. B. Hsiao, "The design, simulation and testing of an urban vertical axis wind turbine with the omni-direction-guide-vane," *Appl. Energy*, vol. 112, pp. 601–609, 2013, doi: 10.1016/j.apenergy.2012.12.064.

[92] B. Shahizare, N. Nik-Ghazali, W. T. Chong, S. Tabatabaeikia, N. Izadyar, and A. Esmaeilzadeh, "Novel investigation of the different Omni-direction-guide-vane angles effects on the urban vertical axis wind turbine output power via three-dimensional numerical simulation," *Energy Convers. Manag.*, vol. 117, pp. 206–217, 2016, doi: 10.1016/j.enconman.2016.03.034.

[93] M. H. Mohamed, G. Janiga, E. Pap, and D. Thèvenin, "Optimization of Savonius turbines using an obstacle shielding the returning blade," *Renew. Energy*, vol. 35, no. 11, pp. 2618–2626, 2010, doi: 10.1016/j.renene.2010.04.007.

[94] B. D. Altan and M. Atilgan, "The use of a curtain design to increase the performance level of a Savonius wind rotors," *Renew. Energy*, vol. 35, no. 4, pp. 821–829, 2010, doi: 10.1016/j.renene.2009.08.025.

[95] M. Tartuferi, V. D'Alessandro, S. Montelpare, and R. Ricci, "Enhancement of savonius wind rotor aerodynamic performance: A computational study of new blade shapes and curtain systems," *Energy*, vol. 79, no. C, pp. 371–384, 2015, doi: 10.1016/j.energy.2014.11.023.

[96] W. A. El-Askary, M. H. Nasef, A. A. AbdEL-hamid, and H. E. Gad, "Harvesting wind energy for improving performance of savonius rotor," *J. Wind Eng. Ind. Aerodyn.*, vol. 139, pp. 8–15, 2015, doi: 10.1016/j.jweia.2015.01.003.

[97] E. Fatahian, F. Ismail, M. Hafifi Hafiz Ishak, and W. Shyang Chang, "An innovative deflector system for drag-type Savonius turbine using a rotating

cylinder for performance improvement," *Energy Convers. Manag.*, vol. 257, no. March, p. 115453, 2022, doi: 10.1016/j.enconman.2022.115453.

[98] M. Eshagh Nimvari, H. Fatahian, and E. Fatahian, "Performance improvement of a Savonius vertical axis wind turbine using a porous deflector," *Energy Convers. Manag.*, vol. 220, no. March, p. 113062, 2020, doi: 10.1016/j.enconman.2020.113062.

[99] K. Qasemi and L. N. Azadani, "Optimization of the power output of a vertical axis wind turbine augmented with a flat plate deflector," *Energy*, vol. 202, p. 117745, 2020, doi: 10.1016/j.energy.2020.117745.

[100] K. Hoe *et al.*, "Experimental and simulation investigation into the effects of a flat plate deflector on vertical axis wind turbine," *Energy Convers. Manag.*, vol. 160, no. January, pp. 109–125, 2018, doi: 10.1016/j.enconman.2018.01.029.

[101] K. Hoe, W. Tong, S. Chew, Y. Shiah, N. Liana, and C. Wang, "3D CFD simulation and parametric study of a flat plate deflector for vertical axis wind turbine," *Renew. Energy*, vol. 129, pp. 32–55, 2018, doi: 10.1016/j.renene.2018.05.085.

[102] W. H. Chen, J. S. Wang, M. H. Chang, J. K. Mutuku, and A. T. Hoang, "Efficiency improvement of a vertical-axis wind turbine using a deflector optimized by Taguchi approach with modified additive method," *Energy Convers. Manag.*, vol. 245, no. May, p. 114609, 2021, doi: 10.1016/j.enconman.2021.114609.

[103] W. H. Chen *et al.*, "Optimization of a vertical axis wind turbine with a deflector under unsteady wind conditions via Taguchi and neural network applications," *Energy Convers. Manag.*, vol. 254, no. January, p. 115209, 2022, doi: 10.1016/j.enconman.2022.115209.

[104] Y. Li, S. Zhao, K. Tagawa, and F. Feng, "Starting performance effect of a truncated-cone-shaped wind gathering device on small-scale straight-bladed vertical axis wind turbine," *Energy Convers. Manag.*, vol. 167, no. 600, pp. 70–80, 2018, doi: 10.1016/j.enconman.2018.04.062.

[105] Y. Li *et al.*, "Aerodynamic characteristics of Straight-bladed Vertical Axis Wind Turbine with a curved-outline wind gathering device," *Energy Convers. Manag.*, vol. 203, no. September 2019, p. 112249, 2020, doi: 10.1016/j.enconman.2019.112249.

[106] W. Hu, J. E, Y. Tan, F. Zhang, and G. Liao, "Modified wind energy collection devices for harvesting convective wind energy from cars and trucks moving in the highway," *Energy*, vol. 247, p. 123454, 2022, doi: 10.1016/j.energy.2022.123454.

[107] I. J. T. Matias, L. A. M. Danao, and B. E. Abuan, "Numerical investigation on the effects of varying the arc length of a windshield on the performance of a highway installed Banki wind turbine," *Fluids*, vol. 6, no. 8, 2021, doi: 10.3390/FLUIDS6080285.

[108] M. Heragy, T. Kono, and T. Kiwata, "Investigating the effects of wind concentrator on power performance improvement of crossflow wind turbine,"

Energy Convers. Manag., vol. 255, no. June 2021, p. 115326, 2022, doi: 10.1016/j.enconman.2022.115326.

[109] A. A. Nimje and N. M. Gandhi, "Design and development of small wind turbine for power generation through high velocity exhaust air," *Renew. Energy*, vol. 145, pp. 1487–1493, 2020, doi: 10.1016/j.renene.2019.06.065.

[110] J. H. Park, M. H. Chung, and J. C. Park, "Development of a small wind power system with an integrated exhaust air duct in high-rise residential buildings," *Energy Build.*, vol. 122, pp. 202–210, 2016, doi: 10.1016/j.enbuild.2016.04.037.

[111] H. Berhanu, D. Gudeta, A. Haiter Lenin, and B. Karthikeyan, "Numerical and experimental investigation of an exhaust air energy recovery Savonius wind turbine for power production," *Mater. Today Proc.*, vol. 46, no. 9, pp. 4142–4152, 2021, doi: 10.1016/j.matpr.2021.02.675.

[112] I. Sutton, "Equipment and Buildings," in *Plant Design and Operations*, 2017, pp. 73–137.

[113] J. Yu, Z. Qu, J. Zhang, S. Hu, J. Song, and Y. Chen, "A comprehensive energy efficiency assessment indicator and grading criteria for natural draft wet cooling towers," *Energy*, vol. 254, p. 124375, 2022, doi: 10.1016/j.energy.2022.124375.

[114] R. Javadpour, S. Zeinali Heris, and J. P. Meyer, "Experimental study of the effect of filled bed type on the performance of a cross-flow cooling tower with the approach of using nanofluids," *Energy Reports*, vol. 8, pp. 8346–8360, 2022, doi: 10.1016/j.egyr.2022.06.027.

[115] S. El Marazgioui and A. El Fadar, "Impact of cooling tower technology on performance and cost-effectiveness of CSP plants," *Energy Convers. Manag.*, vol. 258, no. February, p. 115448, 2022, doi: 10.1016/j.enconman.2022.115448.

[116] J. H. Yu, Z. G. Qu, J. F. Zhang, S. J. Hu, and J. Guan, "Comprehensive coupling model of counter-flow wet cooling tower and its thermal performance analysis," *Energy*, vol. 238, 2022, doi: 10.1016/j.energy.2021.121726.

[117] N. Karimi Bakhtiyar, R. Javadpour, S. Zeinali Heris, and M. Mohammadpourfard, "Improving the thermal characteristics of a cooling tower by replacing the operating fluid with functionalized and non-functionalized aqueous MWCNT nanofluids," *Case Stud. Therm. Eng.*, vol. 39, no. June, p. 1DUMMY, 2022, doi: 10.1016/j.csite.2022.102422.

[118] K. A. Abed, E. E. Khalil, A. M. Abouel-Fotouh, G. El-Hariry, and L. O. Abd El Salam, "Optimal design of a counter flow cooling tower using PSO algorithm for operating cost minimization," *Appl. Therm. Eng.*, vol. 143, no. March, pp. 149–159, 2018, doi: 10.1016/j.applthermaleng.2018.07.057.

[119] Hensley John C., *Cooling Tower Fundamentals*, 2nd ed. Overland Park, Kansas USA: SPX Cooling Technologies, Inc, 2009.

[120] S. Suranjan Salins, S. Kumar, A. T. González, and S. Shetty, "Influence of

packing configuration and flow rate on the performance of a forced draft wet cooling tower," *J. Build. Eng.*, vol. 72, no. April, 2023, doi: 10.1016/j.jobe.2023.106615.

[121] S. Li and M. R. Flynn, *Cooling tower plume abatement and plume modeling: a review*, vol. 21, no. 3. Springer Netherlands, 2021.

[122] A. Zargar *et al.*, "Numerical analysis of a counter-flow wet cooling tower and its plume," *Int. J. Thermofluids*, vol. 14, no. December 2021, 2022, doi: 10.1016/j.ijft.2022.100139.

[123] Z. Yu *et al.*, "Analysis of a novel combined heat exchange strategy applied for cooling towers," *Int. J. Heat Mass Transf.*, vol. 169, p. 120910, 2021, doi: 10.1016/j.ijheatmasstransfer.2021.120910.

[124] J. Ruiz, P. Navarro, M. Hernández, M. Lucas, and A. S. Kaiser, "Thermal performance and emissions analysis of a new cooling tower prototype," *Appl. Therm. Eng.*, vol. 206, p. 118065, 2022, doi: 10.1016/j.applthermaleng.2022.118065.

[125] T. Castiglione, F. Nicoletti, V. Ferraro, and C. M. Sangineto, "CFD analysis of Part-Load operation of an Open-Circuit Induced-Draft cooling tower," *Appl. Therm. Eng.*, vol. 229, no. March, p. 120636, 2023, doi: 10.1016/j.applthermaleng.2023.120636.

[126] S. Mokhatab, W. A. Poe, and J. Y. Mak, "Utility and Offsite Systems in Gas Processing Plants," in *Handbook of Natural Gas Transmission and Processing*, Fourth., S. Mokhatab, W. A. Poe, and J. Y. Mak, Eds. Gulf Professional Publishing, 2019, pp. 537–578.

[127] W. Deng, F. Sun, K. Chen, and X. Zhang, "New retrofit method to cooling capacity improvement of mechanical draft wet cooling tower group," *Int. J. Heat Mass Transf.*, vol. 188, p. 122589, 2022, doi: 10.1016/j.ijheatmasstransfer.2022.122589.

[128] Z. Liu, C. Zhang, and T. Ishihara, "Numerical study of the wind loads on a cooling tower by a stationary tornado-like vortex through LES," *J. Fluids Struct.*, vol. 81, pp. 656–672, 2018, doi: 10.1016/j.jfluidstructs.2018.06.001.

[129] M. M. S. R. S. Bhargav, V. Ratna Kishore, and V. Laxman, "Influence of fluctuating wind conditions on vertical axis wind turbine using a three dimensional CFD model," *J. Wind Eng. Ind. Aerodyn.*, vol. 158, no. August, pp. 98–108, 2016, doi: 10.1016/j.jweia.2016.10.001.

[130] Y. Guo, X. Li, L. Sun, Y. Gao, Z. Gao, and L. Chen, "Aerodynamic analysis of a step adjustment method for blade pitch of a VAWT," *J. Wind Eng. Ind. Aerodyn.*, vol. 188, no. October 2018, pp. 90–101, 2019, doi: 10.1016/j.jweia.2019.02.023.

[131] M. Raciti Castelli, A. Englaro, and E. Benini, "The Darrieus wind turbine: Proposal for a new performance prediction model based on CFD," *Energy*, vol. 36, no. 8, pp. 4919–4934, 2011, doi: 10.1016/j.energy.2011.05.036.

[132] A. Rezaeiha, I. Kalkman, and B. Blocken, "Effect of pitch angle on power performance and aerodynamics of a vertical axis wind turbine," *Appl. Energy*,

vol. 197, pp. 132–150, 2017, doi: 10.1016/j.apenergy.2017.03.128.

[133] S. Joo, H. Choi, and J. Lee, “Aerodynamic characteristics of two-bladed H-Darrieus at various solidities and rotating speeds,” *Energy*, vol. 90, pp. 439–451, 2015, doi: 10.1016/j.energy.2015.07.051.

[134] S. Ali and C. M. Jang, “Effects of tip speed ratios on the blade forces of a small h-darrieus wind turbine,” *Energies*, vol. 14, no. 13, pp. 1–18, 2021, doi: 10.3390/en14134025.

[135] A. Rezaeiha, I. Kalkman, and B. Blocken, “Effect of pitch angle on power performance and aerodynamics of a vertical axis wind turbine,” *Appl. Energy*, vol. 197, pp. 132–150, 2017, doi: 10.1016/j.apenergy.2017.03.128.

APPENDICES

A1) Cooling tower specifications for model T-2800 by Cooling Tower Systems, Inc.

CTS Cooling Tower Systems, Inc.

TOWER SPECIFICATIONS: MODEL T-2800

Design and Operating Conditions		Water Distribution System Construction Materials	
Tower Type:	Counter Flow Induced Draft	Stand Pipe:	PVC
Water Flow Rate (GPM):	2,370 GPM	Sprinkler Head:	AC
Entering Water Temperature	95°F	Sprinkler Pipes:	PVC
Leaving Water Temperature	85°F	**Mechanical Equipment**	
Wet Bulb Temperature:	75°F	Fan Unit:	One Unit per Tower
Total Fan BHP:	30 HP	Type:	Axial Flow
Total Pump Head:	20'	Manufacturer:	CTS
Drift Loss of Water Flow:	0.1%	Diameter:	133 1/8"
Evaporation Loss of Water Flow:	0.93%	Blade Material:	AC
Design Wind Load:	41 lbs/sq. ft.	Hub Material:	AC
Structural Details		Nominal Air Volume:	175,000 CFM
Overall Diameter:	299.25"	**Fan Motor**	
Overall Height:	194 11/16"	Number of motors:	One Unit per Tower
Dry Weight:	9,656 lbs.	Type:	Induction
Operating Weight:	41,349 lbs.	Manufacturer:	CTS
Basic Tower Construction Materials		F	E Class
Tower Support Frame Assembly	HDGS	Rated HP:	20 HP
Casing:	FRP	Voltage and phase:	220/440V/3
Casing Supporters	HDGS	**Piping Connections**	
Cold Water Basin	FRP	Primary Water Inlet Diameter	12"
Filling:	PVC	Primary Water Outlet Diameter:	12"
Filling Supports:	HDGS	Auto fill inlet diameter:	2"
Fan Guard	HDGS	Quick fill inlet diameter:	2"
Mechanical Equipment Supports:	HDGS	Overflow outlet diameter:	4"
Inlet Louvers:	PVC	Drain diameter:	3"
Bolts, Nuts & Washers:	STS	Water Flow (GPM):	2,370 GPM

Materials Key			
FRP	Fiberglass Reinforced Polyester	STS	Stainless Steel
HDGS	Hot Dipped Galvanized Steel	AC	Aluminum Alloy Cast

Cooling Tower Systems, Inc.
196 Lower Cherry Street Macon, GA 31201
TF: 800.752.1905 F: 478.755.8304 www.coolingtowersystems.com info@coolingtowersystems.com

A2) Conversion and calculation for cooling tower estimated power recovery

From the cooling tower specifications in Appendix A1:

Given:

1) The nominal air volume of the cooling tower fan = 175 000 CFM

2) Fan diameter = 133 1/8”

3) Cooling tower rated power = 20 Horsepower (HP)

Converting CFM to m^3/s:

$$1\ CFM\ =\ 4.71947 \times 10^{-4}\ m^3/s$$

$$175\ 000\ CFM\ =\ 82.591\ m^3/s$$

Converting fan diameter from inch to m:

$$1\ inch\ =\ 0.0254\ m$$

$$133\ 1/8”\ =\ 3.381\ m$$

Area of the cooling tower fan = πr^2:

$$= \pi \times \left(\frac{3.381}{2}\right)^2$$

$$= 8.978 m^2$$

The volume of air flowing from the cooling tower fan = Area of cooling tower fan x exhaust air velocity:

$$82.591 m^3/s = 8.978 m^2 \times exhaust\ air\ velocity$$

$$wind\ speed = 9.2\ m/s$$

Converting the cooling tower-rated power from HP to Watts (W):

$$1\ Horsepower\ (HP) =\ 745.7\ W$$

$$20\ HP\ =\ 14914\ W$$

B) Psychometry chart from Perry's Engineer Handbook (Seventh Edition)

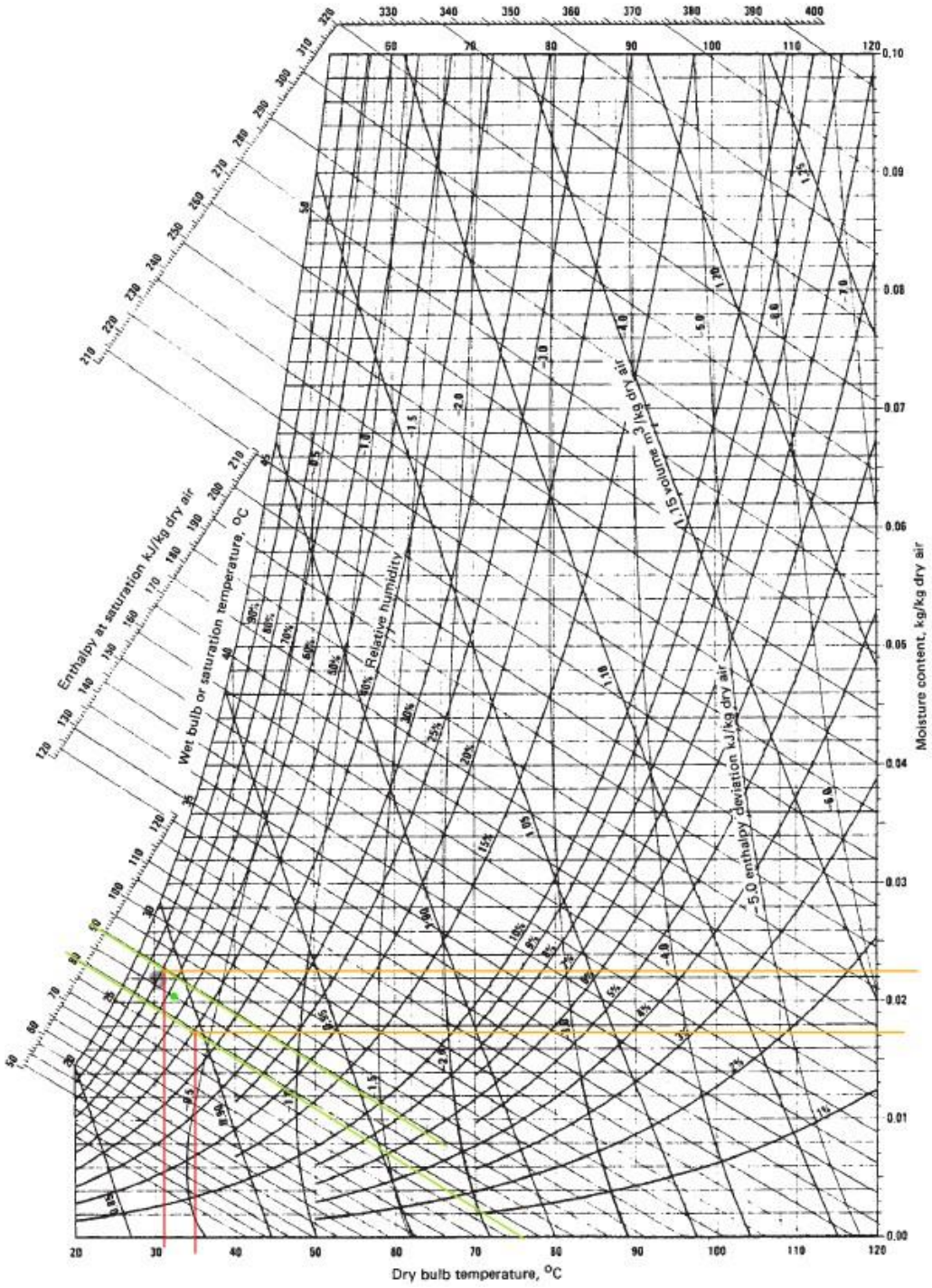

C) Publications resulting from this study

Published Journal Paper:

Singh, E., Roy, S., San Yam, K., & Law, M. C. (2023). Numerical analysis of H-Darrieus vertical axis wind turbines with varying aspect ratios for exhaust energy extractions. *Energy*, *277*, 127739.

Published Conference Papers:

Singh, E., Roy, S., San, Y. K., & Chiat, L. M. (2023). Performance Enhancement of VAWT using Diffuser for Energy Extraction from Cooling Tower Exhaust Air. In *MATEC Web of Conferences* (Vol. 377, p. 01022). EDP Sciences.

Singh, E., Roy, S., San, Y. K., & Chiat, L. M. (2022). Optimisation of H-Darrieus VAWT Solidity for Energy Extraction in Cooling Tower Exhaust Systems. *Journal of Advanced Research in Fluid Mechanics and Thermal Sciences*, *91*(2), 51-61. (Presented at the 11th International Conference in Mechanical and Manufacturing Engineering (ICME ’21) (Won the best presenter award)

Published Book Chapter:

Singh, E., Roy, S., Ke San, Y., Law, M. C., & Kumar, P. (2022). Computational Analysis of Air Energy Extractors for Guided Flow Exhaust Applications. In *Advances in Smart Energy Systems* (pp. 185-204). Singapore: Springer Nature Singapore.

D) Author copyright statement

In this thesis, some of the work (tables and figures) in the paper titled "Numerical analysis of H-Darrieus vertical axis wind turbines with varying aspect ratios for exhaust energy extractions," published in Energy, was used. Below is the author rights statement from Elsevier.

Author rights

The below table explains the rights that authors have when they publish with Elsevier, for authors who choose to publish either open access or subscription. These apply to the corresponding author and all co-authors.

Author rights in Elsevier's proprietary journals	Published open access	Published subscription
Retain patent and trademark rights	√	√
Retain the rights to use their research data freely without any restriction	√	√
Receive proper attribution and credit for their published work	√	√
Re-use their own material in new works without permission or payment (with full acknowledgement of the original article): 1. Extend an article to book length 2. Include an article in a subsequent compilation of their own work 3. Re-use portions, excerpts, and their own figures or tables in other works.	√	√
Use and share their works for scholarly purposes (with full acknowledgement of the original article): 1. In their own classroom teaching. Electronic and physical distribution of copies is permitted 2. If an author is speaking at a conference, they can present the article and distribute copies to the attendees 3. Distribute the article, including by email, to their students and to research colleagues who they know for their personal use 4. Share and publicize the article via Share Links, which offers 50 days' free access for anyone, without signup or registration 5. Include in a thesis or dissertation (provided this is not published commercially) 6. Share copies of their article privately as part of an invitation-only work group on commercial sites with which the publisher has a hosting agreement	√	√
Publicly share the preprint on any website or repository at any time.	√	√
Publicly share the accepted manuscript on non-commercial sites	√	√ using a CC BY-NC-ND license and usually only after an embargo period (see Sharing Policy for more information)
Publicly share the final published article	√ in line with the author's choice of end user license	×
Retain copyright	√	×

E) Best presenter award